UNIVERSITY OF CALIFORNIA

Los Angeles

Dynamic Shake Testing of a Model Levee on Peaty Organic Soil in the Sacramento-San Joaquin Delta

A dissertation submitted in partial satisfaction of the requirements for the degree Doctor of Philosophy in Civil and Environmental Engineering

by

Edward Thomas Reinert

2014

ABSTRACT OF THE DISSERTATION

Dynamic Shake Testing of a Model Levee on
Peaty Organic Soil in the Sacramento-San Joaquin Delta

by

Edward Thomas Reinert

Doctor of Philosophy in Civil and Environmental Engineering
University of California, Los Angeles, 2014
Professor Scott Brandenberg, Chair

The Sacramento-San Joaquin Delta is the hub of California's water distribution system, which consists of below sea-level islands surrounded by levees. Delta levees are constructed of local fill, have typically been unengineered and are notorious for breaching, causing flooding of the islands inside. One major concern is the seismic performance of Delta levees, which have not experienced a significant seismic event in over a century. Many of these levees are founded on local peaty organic soils, and the seismic performance of these levees is poorly understood.

As part of a collaborative research investigation to study to study the seismic performance of Delta levees, a series of dynamic field tests were performed on a model levee constructed on very soft and compressible peaty organic soils on Sherman Island. This first-of-its-kind test applied dynamic loads to the model levee-peat system using the large

NEES@UCLA MK-15 eccentric mass shaker mounted on the levee crest. Two sets of tests were performed in 2011 and 2012.

Geotechnical and geophysical investigations performed at the site found a 11m thick peat deposit rests atop permeable Pleistocene sand. The peaty soils consist of 9m of soft saturated peat with a Vs of 30 m/ and a 2m stiff desiccated crust with a Vs of 60 m/s lying atop the soft peat. Artesian pressures exist in the soft saturated peat due to hydraulic connection with the nearby Sacramento River, with a zero effective stress condition existing at the peat-sand interface. Remote data monitoring measured settlement and pore pressure dissipation of the levee using embedded piezometers and a slope inclinometer. The remote monitoring found fast dissipation of pore pressures underneath the levee and continued settlement of the levee due to a high rate of secondary compression. Prior to the 2012 tests, a berm was constructed around the levee and the ground was flooded, to create more realistic soil conditions in the unsaturated crust.

Dynamic base shear-displacement and moment-rotation relations were made for the levee. The model levee translated and rotated visibly during testing, demonstrating a response that differs from the one-dimensional wave propagation assumption used to analyze seismic levee response. High radiation damping was observed, and translation of the levee was found to go out-of-phase at peak shaker frequencies. Complex-valued stiffness of the levee-peat system was analyzed and compared to analytical solutions for a rigid foundation on an elastic halfspace. Little agreement was found between the field test results and the analytic solution, suggesting that the levee-peat foundation is flexible.

Dynamic shear strains measured underneath the levee crest and toe measured an average value of shear strains at the bottom of the stiff crust and top of the soft peat. Peak shear strains

measured during testing went up to 0.4%, with higher shear strains occurring underneath the levee toe, due to the rocking behavior. Comparison of residual pore pressure ratios generated during testing show a trend in increasing residual pore pressure with increasing shear strain. Comparison of field test results with dynamic laboratory testing showed very little increase in residual pore pressures from field tests, suggesting that pore pressures underneath the levee dissipated quickly due to high horizontal permeability.

A series of finite element simulations were performed with elastic isotropic materials to compare different hypothetical soil conditions and loading scenarios. Good agreement in shear strains between the field test and the finite element simulations were found. Higher shear strains were found to exist beneath the levee for softer soils and uniform base excitation. A study investigated the development of shear stresses within the levee fill, and found an increase in peak shear stresses compared to shear stresses calculated for a simple shear case. This has implications for liquefaction triggering analysis, and the finite element simulations suggest that the current methodology used in evaluating seismic demand may be underestimating shear stresses within the levee fill.

The dissertation of Edward Thomas Reinert is approved.

Jonathan P. Stewart

Anne Lemnitzer

David D. Jackson

Daniel Pradel

Scott J. Brandenberg, Committee Chair

University of California, Los Angeles

2014

To my parents, family, and friends.

Table of Contents

Acknowledgments

As I approach the end of my long career as a student at UCLA, I would like to acknowledge the help, support, and guidance I received from a number of people over the last four and a half years. The research and this dissertation would not have been possible without them, and I am simultaneously humbled and grateful for all of the assistance they have provided.

First of all, I would like to thank my advisor, Professor Scott Brandenberg, for helping me with all stages of this project and supported me throughout my doctoral studies. It has been an honor and pleasure to work with him throughout the entire duration of this project. He has worn many hats during the last four and a half years: performing as a teacher, a researcher, a project manager, and a mentor, and he has done all of these superbly. He has helped me to become a better engineer and has helped guide me through all of the various technical challenges that have come up in the duration of this project. His ability as a mentor has been second-to-none, and I come away from my time with a greater understanding and heightened passion for this career field.

I would like to acknowledge the help of the various researchers and state officials that have been gotten their hands dirty with me and have been instrumental in putting this project together. First, I would like to thank the entire staff of the NEES@UCLA team that provided the muscle and man hours during the construction and field testing of our model levee. Without the help of Bob Nigbor, Steve Keowen, Alberto Salamanca, Andrey Kozhukovskiy, Erica Eskes, Sophia Poulos, Jackson English, Estefan Garcia, Charys Clay, and Jasmin Sadegh, none of this would have been remotely possible. I would like to thank the tireless efforts of the staff at Gornto Ditching in providing excellent contracting services in building the model levee. State of

California Department of Water Resources staffers Bryan Brock and Michael driller have been of tremendous help in letting us use the Sherman Island site for our model levee. I would like to thank Professor Robb Moss of Cal Poly, San Luis Obispo, for providing enormous help in our site investigations, along with Doug Wahl, Andrew Makdisi, and Chris Krage from UC Davis in helping us use the NEES CPT rig. I would furthermore like to thank UCLA undergraduate interns and researchers Nicky Galloway, Jay Merani, Pavlo Chrysovergis, and Sean Ahdi in their help with my research and field testing. I would also like to thank John Lemke of GEODAQ in his tireless efforts to construct and provide the remote data acquisition system we used for levee monitoring.

I would like to thank the funding provided by the National Science foundation in funding this project. This research was supported by the National Science Foundation under award number 0830081 through the George E. Brown Network for Earthquake Engineering Simulation Research (NEESR) program in coordination with cognizant program official for this grant, Richard J. Fragaszy.

I would like to thank the NEEShub team for their assistance in the massive data archiving work performed as part of this project. DOI's for the various experiment for this project are listed in the table below:

Experiment	DOI
2: Geophysical Study	N/A
3: Field Testing with MK-15 Shaker	10.4231/D3SF2MB89
4: SASW Array	10.4231/D3J09W43H
5: Shaker Testing with Atom Ant Shaker	10.4231/D3D795994
6: Continuous Raw Data Files	10.4231/D34Q7QQ2B
7: Field Testing with MK-15 Shaker (2012 Re-Test)	10.4231/D38G8FH6G
8: SASW Array (2012 Re-Test)	10.4231/D30Z70W8Z
9: Continuous Raw Data Files (2012 Re-Test)	10.4231/D3NP1WJ45

I would like to thank my committee members for their tireless assistance with this project and their help in allowing me to graduate. First, I would like to thank Dept. chair and co-PI Jonathan Stewart for taking so much time out of his busy schedule to provide assistance, guidance, and feedback with this project. I would like to thank Prof. Daniel Pradel for being on my committee and encouraging me to pursue my doctoral studies. I would also like to thank Prof. David Jackson of UCLA and Prof. Anne Lemnitzer of UC Irvine for serving on my committee and providing valuable feedback.

I would like to thank the family and friends that have enthusiastically and unwaveringly supported my decision to pursue a doctoral degree. My brothers at Triangle Fraternity have been especially helpful during my time at UCLA. My grandmother, Virginia Herron, has provided essential material and personal support during my time at UCLA.

Finally, I would like to thank my parents, Kathleen and Ted Reinert, for their constant moral support and encouragement during my entire time at UCLA, especially during my doctoral studies. I'd first like to acknowledge my mother's help and encouragement even during the most stressful times of my doctoral career, and her never-ending optimism that I would succeed. I would finally like to thank my father for his encouragement in my studies, as well as his cheerful attendance at my prospectus, field tests, and my defense. I am eternally grateful for the help of my parents, and my wish is that I have done them proud during my research.

Vita

Edward Reinert earned his Bachelor's degree in 2008 and his Master's degree in 2009 at the University of California, Los Angeles. He is a member of the American Society of Civil Engineers (ASCE), the Earthquake Engineering Research Institute (EERI), the California Geoprofessionals Association (CalGeo), and the Chi Epsilon honor society. He earned his EIT in the state of California in 2008 (No. 130989). He has been a Teaching Assistant at the UCLA for undergraduate Introductory Soil Mechanics, Soil Mechanics Laboratory, and Advanced Geotechnical Design classes. He has worked as a student intern at the Los Angeles Department of Water and Power (2007) and at Praad Geotechnical (2008-2009). He has been a graduate student researcher at UCLA from April 2009 to March 2014.

His published work is listed below:

Brandenberg, S.J., Nigbor, R.L., Reinert, E.T., Levulett, D., Stewart, J.P., Moss, R. (2010). "Geophysical testing to determine safe vibration limits and spatial attenuation of vibrations on Sherman Island",Report prepared for NEES@UCLA, http://www.nees.ucla.edu/neesrii/ShermanGeophysicalReport.pdf,14 pp.

Reinert, E.T., Brandenberg, S.J., Stewart, J.P., and Moss, R.E.S. (2012). "Dynamic field test of a model levee founded on peaty organic soil using an eccentric mass shaker." 15th World Conference on Earthquake Engineering, Lisbon, Portugal.

Reinert, E.T., Lemke, J., Stewart, J.P., Brandenberg, S.J. (2013). "Remote monitoring of a model levee constructed on soft peaty organic soil." 2013 Geo Congress, San Diego.

Reinert, E.T., Brandenberg, S.J., Stewart, J.P. (2013). "Measurements of Translational and Rotational Dynamic Stiffness for a Model Levee on Peat." 10th International Conference on Urban Earthquake Engineering, Tokyo, Japan.

Reinert, E.T., Brandenberg, S.J., Stewart, J.P., Moss, R.E.S. (2013) "Destructive Cyclic Field Testing of Model Levee on Peaty Organic Soil: Data Report for Field Tests." Report No. UCLA SGEL 2013/01, Structural and Geotechnical Engineering Laboratory, University of California, Los Angeles.

Reinert, E.T., Stewart, J.P., Moss, R.E.S., Brandenberg. S.J. “Dynamic Response of a Model Levee on Sherman Island Peat: A Curated Dataset.” Submitted to Earthquake Spectra on Oct. 19, 2013. Accepted for publication on Feb. 19, 2014.

Chapter 1. Introduction

1.1. Introducing the Delta

The Sacramento-San Joaquin Delta is a low-lying fresh water estuary located at the confluence of the Sacramento and San Joaquin Rivers in Northern California, in between the cities of Sacramento, Antioch, and Stockton (Figure 1.1). Today, the Delta consists of an area of roughly 1,300 square miles of meandering channels that enclose over 50 reclaimed "islands," many of which are below sea level. These islands are enclosed by more than 1,100 miles of levees; with approximately 400 miles of project levees that were part of an authorized federal flood control project, and 700 miles of non-project levees that were constructed and maintained by local reclamation districts.

The Delta is a very important to the state of California for a number of reasons. First, the Delta lies at the center of an important water distribution hub for the state. Roughly one-half of all stream flow in the state flows through the Delta, which is at the end of California's largest watershed (Isenberg et al. 2008). As seen in Fig. 1.2, this watershed covers over 40% of California's land area. Water is distributed across the state from irrigation projects such as the Central Valley Project and State Water Project, and many areas of the state depend on exported water from the Delta to survive. For example, Southern California receives roughly one-third of its water from Delta exports (Isenberg et al. 2008), and the Delta is the sole source of water for many communities in the Central Valley. Besides being an important water source for many Californians, the Delta is also an important agricultural region for the state. Farming continues to dominate the Delta's land use, and large ports in the cities of Stockton and Sacramento are used to ship crops grown there, which contribute to over $650 million in sales. Finally, the Delta is an

important ecological and recreational area, and many species, such as the endangered Delta Smelt, are unique to the Delta.

1.2. Historical Background

The past 160 years have seen the Delta transform from an inland freshwater marsh to an important water distribution and agricultural area for California, and much of this activity depends on the stability and performance of the Delta's levees. In order to understand the current state of the Delta and the levees, it is important to understand the history of the Delta and how the development of the region has led to the current state of the Delta and the levees.

The pre-Gold Rush Delta was much different than it is today. Instead of farms and islands, it was originally a mainly freshwater marsh. According to Lund et al. (2007), over 60% of the Delta's area was submerged by daily tides, and spring tides could completely submerge the Delta. The Delta was not entirely a freshwater marsh, as saltwater intrusion typically happened in the summer months or during dry years, when low outflow occurred. Natural levees in the Delta had formed from sediments deposited by repeated flooding, and many natives built settlements on these levees. Tules were the main types of plants that existed in the marshy areas of the Delta, and they survived in both fresh and brackish water. As seen in Fig. 1.3, the combination of sediment deposits and growth/death of marsh tules led to the formation of thick deposits of extremely compressible peaty organic soils, a process that had happened during the approximately 6,000 years before the European settlement and reclamation of the Delta.

The Gold Rush of the late 1840's led to the first large-scale European settlement of California and the Delta. Many of these first settlers saw farming as being a more profitable

alternative to mining gold, and the nutrient-rich organic soils in the Delta were considered a good place to farm. The first farms were located on the natural levees, and once that space ran out, farmers directed their efforts toward reclamation of lowlands for farming. The passage of the Swampland act in 1850 transferred ownership of Delta lands to the State of California, who began selling the Delta lands for $1 an acre in 1858 to encourage reclamation. Local reclamation districts formed as an organizational mechanism for this widespread reclamation effort, which helped facilitate the rapid development of delta into farmland. The first attempts at reclamation were little more than crudely constructed levees built on top of the natural levees that had already existed, mostly as part of a "levee war" in which farmers would try to build their levee higher than their neighbor's levee in order to preserve their farm when flooding occurred. Many of these original levees, therefore, were not built to any engineered standard, and were composed of uncompacted to poorly compacted sands, clays, and organic fill, and were often built directly on top of the peaty organic soil. Improvements in construction technology, such as mechanized fill placement and dredging, helped accelerate construction of levees and thus reclamation of Delta lands to farmland. Between 1860 and 1930, over 441,000 acres had been reclaimed by over 1,100 miles of levees.

Towards the end of the 1920's much of the Delta lands had been reclaimed, and attention began to focus on delivering Delta water to more arid regions of the State. Other large-scale public works projects for water distribution, such as the Los Angeles Aqueduct, had been completed by this time, and many saw the Sacramento and San Joaquin rivers as good water sources for distribution across the State. The first major project to use the Delta was the Central Valley Project (CVP) in the 1930's and 1940's, which sought to deliver water and reduce salinity intrusion to the agriculturally productive San Joaquin Valley. These main goals were achieved by

expelling salt water in the Delta through controlled releases from the Shasta Reservoir and construction of canals which could deliver water to irrigators in the San Joaquin Valley. The CVP fundamentally changed the Delta from a mostly freshwater estuary, subject to seasonal saltwater intrusion, to a freshwater only area, where salinity would be controlled by upstream water releases. The second major project to use the Delta as a water distribution hub was the State Water Project (SWP) in the 1960's and 70's, which resulted in the creation of the California Aqueduct to deliver water to Southern California. This project brought the construction of large pumping plants, such as the Harvey Banks pumping facility in Tracy, to the Delta, thus increasing reliance on the stability of the current levees to keep the Delta an exclusively fresh water area.

Around the same time as the construction of the State Water Project, the emergence of environmental concerns and the shift of public opinion on such issues as pollution and species protection would eventually impact the direction of the SWP. For example, a peripheral canal was proposed to divert water around the Delta and directly to the pumping plants, but increasing concern about the environmental problems of the Delta led to a failed statewide referendum to approve the construction of the canal in 1982. A severe multiyear drought, beginning in 1987, the reduction of water exports to maintain minimum environmental flows in 1991, and the listing of the Chinook Salmon and the Delta Smelt as threatened species forced water users to work with environmental authorities to come up with a new way to manage the Delta. This resulted in the formation of CALFED in 1994, which sought to involve Delta stakeholders along with State and federal authorities to come up with long term solutions to both environmental and water supply problems. However, such events as the sudden Jones Tract levee failure of 2004 (see Fig. 1.4) and the disastrous breaches of New Orleans levees in 2005 made levee concerns more

urgent than previous years. These issues, along with funding problems and the continued environmental and water supply issues mentioned earlier, put severe strains on CALFED and its idea that consensus between the various stakeholders in the Delta would help fix its problems.

The Sacramento-San Joaquin Delta has changed significantly, from a seasonal freshwater tidal marsh to a major hub of California's water supply and agriculture, in a relatively brief period of time. Much of California's current use of the Delta has relied on the stability and performance of levees constructed around the time European settlers first entered the Delta during the Gold Rush era. This chapter has focused mainly on the historical background of the Delta and its levees, in order to give context for the research being performed on the levees and peaty organic soils that lie underneath them. The next chapter will focus on much of the technical background regarding the flooding and seismic hazards of Delta levees, the peaty organic soils that support the levees, and previous studies to assess the risk of flooding, in order to demonstrate the motivation for research.

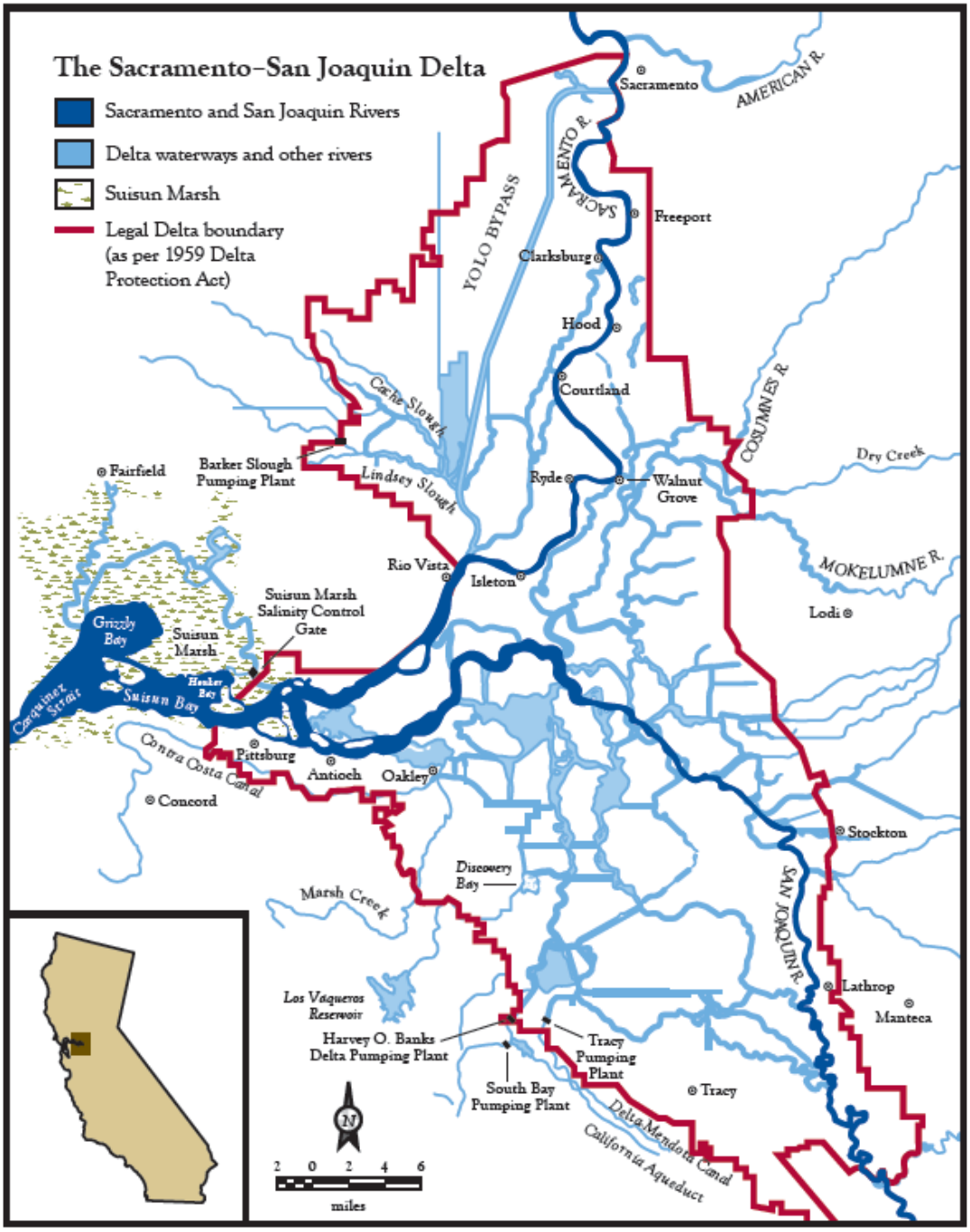

Figure 1.1: Boundary of Sacramento-San Joaquin Delta. (Lund et al. 2007)

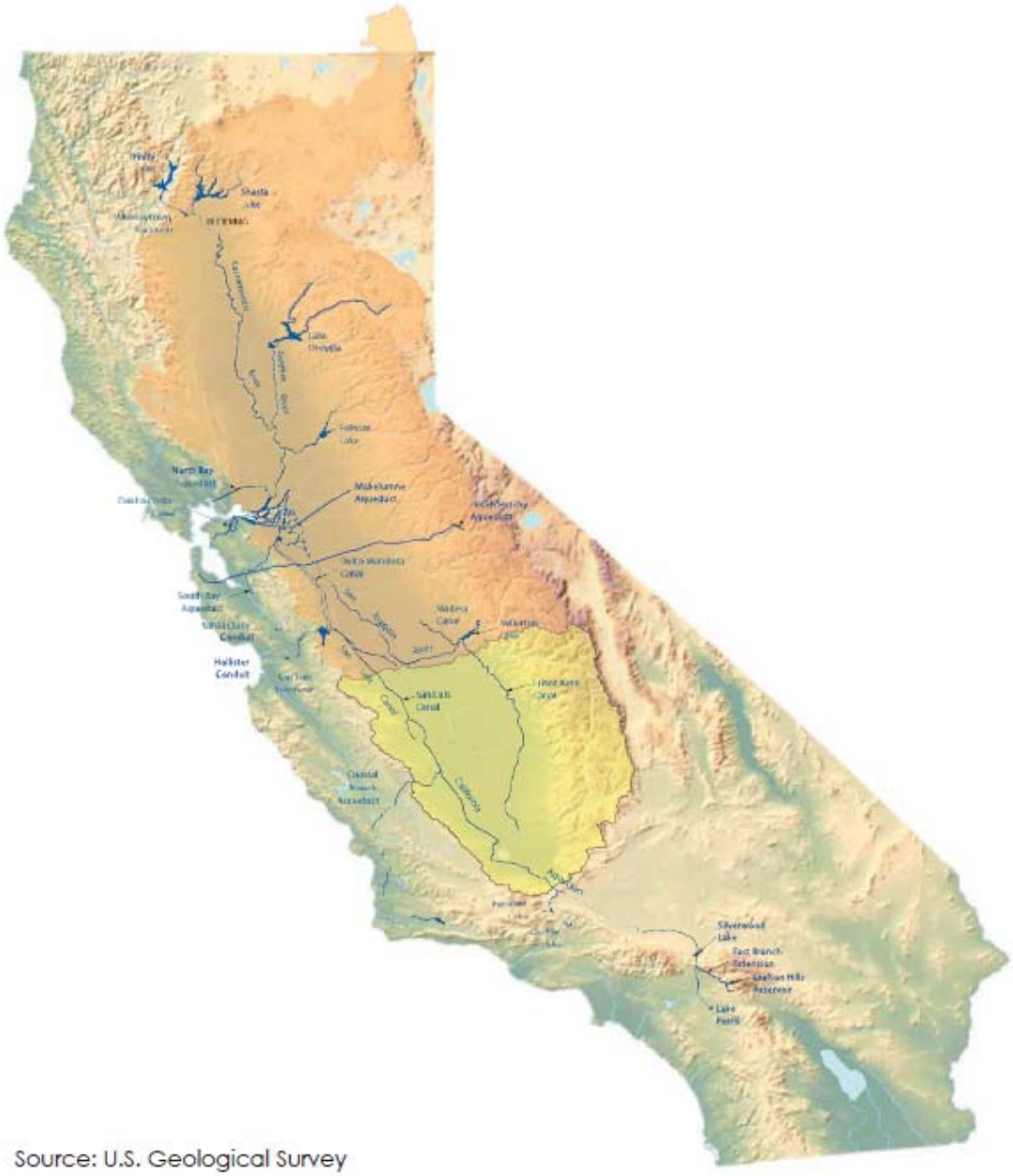

Figure 1.2: Boundary of Delta watershed. (Eisenberg et al. 2008)

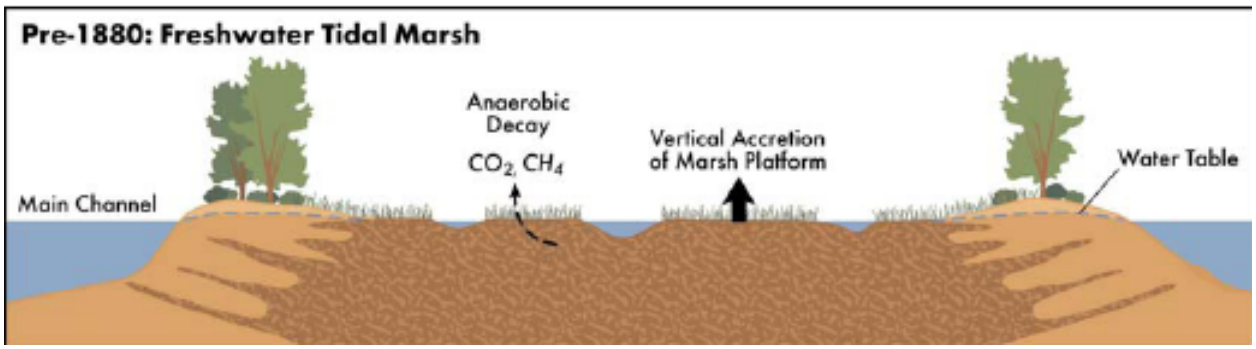

Figure 1.3: Formation of organic peaty soils in the Delta (from Mount and Twiss 2005)

Figure 1.4: Aerial photo of the 2004 Jones Tract failure. (Lund et al. 2007)

1.3. Dissertation Organization

This dissertation focuses on the dynamic field test of a model levee founded on peaty organic soil on Sherman Island in the Sacramento-San Joaquin Delta. It consists of the following six chapters.

Chapter 1

The Sacramento-San Joaquin Delta Levees are introduced, the historical background of the Delta is described, and the organization of the dissertation is presented.

Chapter 2

This chapter explains the technical background of delta levee failures and motivation for the field testing portion of this project. The chapter will first introduce the flooding hazards in the Delta and why it is an especially vulnerable area, then move on to explain some of the research that has been done to estimate the risks of seismic levee failure in the Delta, then finally summarize the unique properties of peaty organic soils that the levees are founded upon. The motivation for this project will then be addressed following the information presented.

Chapter 3

This chapter explains how the Sherman Island test site was selected and the work done as well as the geotechnical and geophysical investigations performed at the site. The investigative work performed at the site included soil sampling, CPT soundings, field strength tests, and a geophysical investigation to determine attenuation of seismic waves from the levee. The data

gathered from these investigations were used to come up with a soil profile for the site that includes both static and dynamic properties.

Chapter 4

This chapter will explain the design, construction, and testing of the model test levee on Sherman Island. The design of the model levee included finite element modeling that was used to come up with levee dimensions and estimate passive pressures developed from a base that the NEES@UCLA MK-15 shaker. Construction of the model levee, including placement of sensors, compaction specifications of the levee fill, specifications of reinforcement material for the levee fill, and long-term remote monitoring are specified. Finally, the instrumentation and test sequence of the model levee will be explained. Sample test results will be presented, along with the method used to calculate the force input into the embankment from the MK-15 shaker. Special emphasis will be taken to describe the data archiving process on NEEShub.

Chapter 5

This chapter will focus on the interpretation of results from the dynamic shake testing. Calculation of SSI quantities, such as base shear, base moment, base displacement, and base rotation will be described, and dynamic impedance functions will be presented and compared to analytical impedance functions in the literature. Shear strains in the peat soil developed during shaking will be presented. Residual pore pressure response from the shake tests are calculated and the shear strain – pore pressure response from the field testing is compared to the response generated from dynamic laboratory testing on Sherman Island peat samples. Finally, a series of dynamic finite element tests to validate the results of the field testing are presented.

Chapter 6

Conclusions from the study are summarized and several recommendations for future work are presented.

Chapter 2. Technical Background and Project Motivation

The Sacramento-San Joaquin Delta, as seen in the previous chapter's discussion, is a unique and important area for the State of California. It serves as a critical water distribution hub, a major agricultural center, and a unique ecological and recreational area. The Delta has seen rapid development in the last 160 years from its previous state as a freshwater tidal marsh to a complex network of water channels, islands, and levees. However, the future of the Delta's ability to serve all of these important functions is very uncertain, not only because of the water supply issues that were previously mentioned, but also because of the very high flooding risk of the Delta due to levee instability and seismic hazards.

This chapter will highlight the main risks to flooding in the Delta in order to demonstrate what is already known and provide motivation for this research. First, this chapter will take a look at flooding hazards in the Delta and why it is such a highly vulnerable area in the first place. Second, the seismic hazards of the area and some of the research that has been done to assess the risk of levee failure and island flooding due to earthquakes will be addressed. After that, the focus will shift to the peat soils in the Delta, which many of the levees in the area are founded upon. This information will then be used to address the gaps in knowledge engineers have in understanding the risks to levee failure and demonstrate what engineers hope to learn from this project.

2.1. Flooding Hazards in the Delta

Flooding in the Delta has historically been a major obstacle to those who have settled in the Delta, as the Delta is originally a tidal wetland and therefore susceptible to seasonal variations in water levels, thus making it naturally more flood-prone. Chapter 1 briefly mentions

the 'levee war' that many of the early settlers engaged in; building levees higher than their neighbor in order to prevent flooding of their reclaimed land. Even after the initial reclamation of land in the Delta for farming purposes, flooding has still occurred frequently. Since 1900, more than 158 Delta islands have been flooded because of levee breaches (DRMS Phase 1 2009). Fig. 2.1 shows the location and frequency of floods due to levee breaches since 1900. The frequency of floods due to levee breaches is increasing as well, with the annual frequency of floods having increased to 1.39 in the period between 1980 and 2006 from 0.80 from the period from 1950-1980 (DRMS Phase 1 2009). Even with such a high incidence of flooding, attention to this topic has only become widespread since the failures of the New Orleans levee system from Hurricane Katrina in 2005. Because flooding in the Delta due to levee breaches occurs at such a high rate, it is therefore useful to understand on a technical level why they occur and why the consequences to flooding are becoming more severe with time.

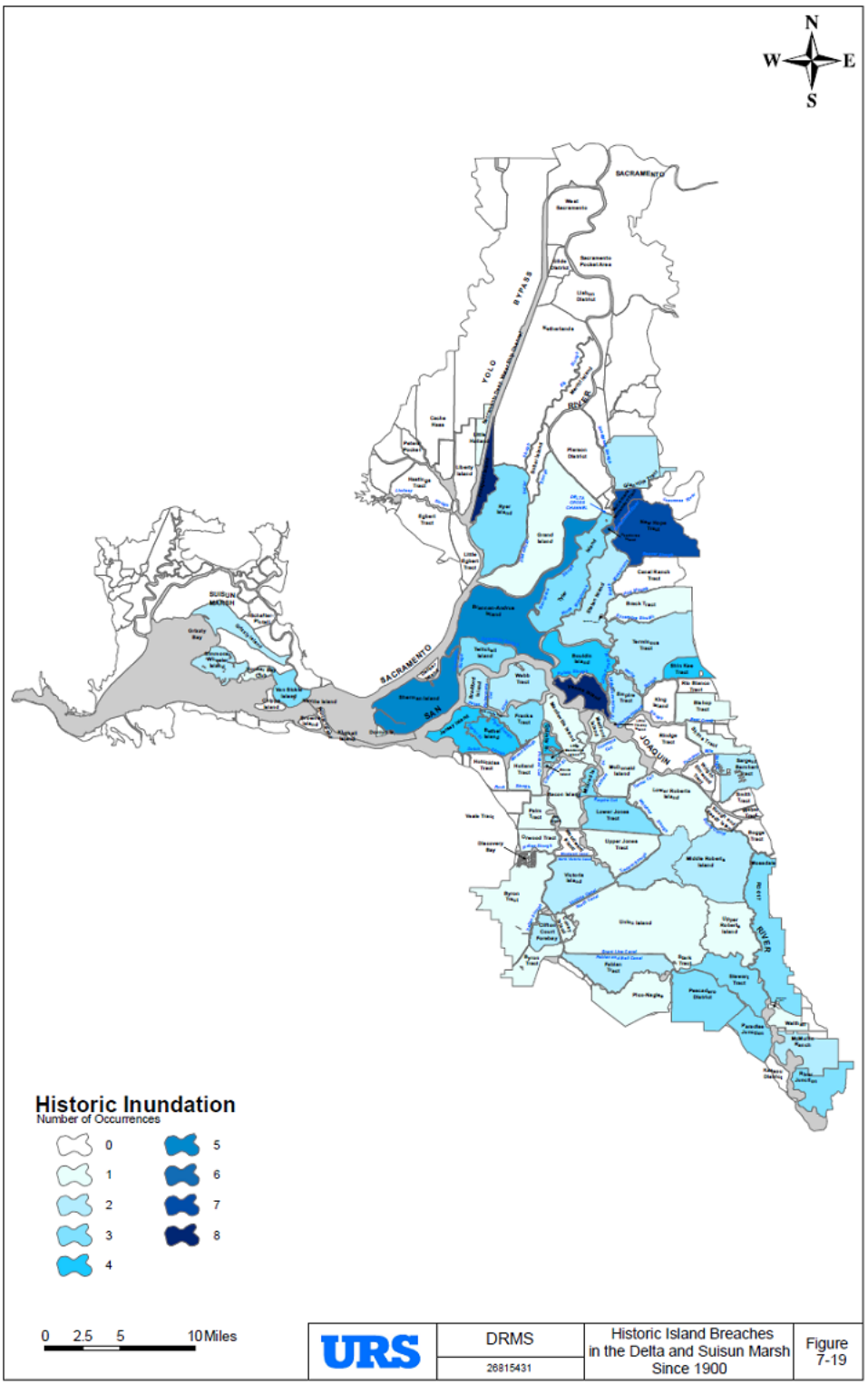

Figure 2.1: Location and number of island floods due to levee breaches (DRMS Phase 1 2009)

Two of the major threats to flooding in the Delta have been the problem of land subsidence of the islands, mainly due to microbial oxidation of the peat soils, and sea level rise. Figs. 1.3 and 2.2 (from Mount and Twiss 2005) show conceptually how this process reduces levee stability. Fig 1.3 shows how peat soil formed over the last 6,000 – 8,000 years by the gradual anaerobic decay of marsh plants and tules. Once reclamation began in the late 1800's and early 1900's, drainage ditches were constructed in order to lower the water table below crop root zones, as seen starting in Fig 2.2. Lowering the water table then initiated the microbial oxidation of the peat by removing the anaerobic conditions that had allowed the peat to accumulate. According to Mount and Twiss (2005), conversion of the soil to gaseous CO_2 accounts for roughly 75% of the elevation loss due to subsidence. Poor land management practices, such as burning peat soils and wind erosion, accelerated soil losses due to microbial oxidation. Along with oxidation of the peat soils, consolidation and compaction of the underlying peat has accounted for the remaining 25% of land subsidence that has occurred.

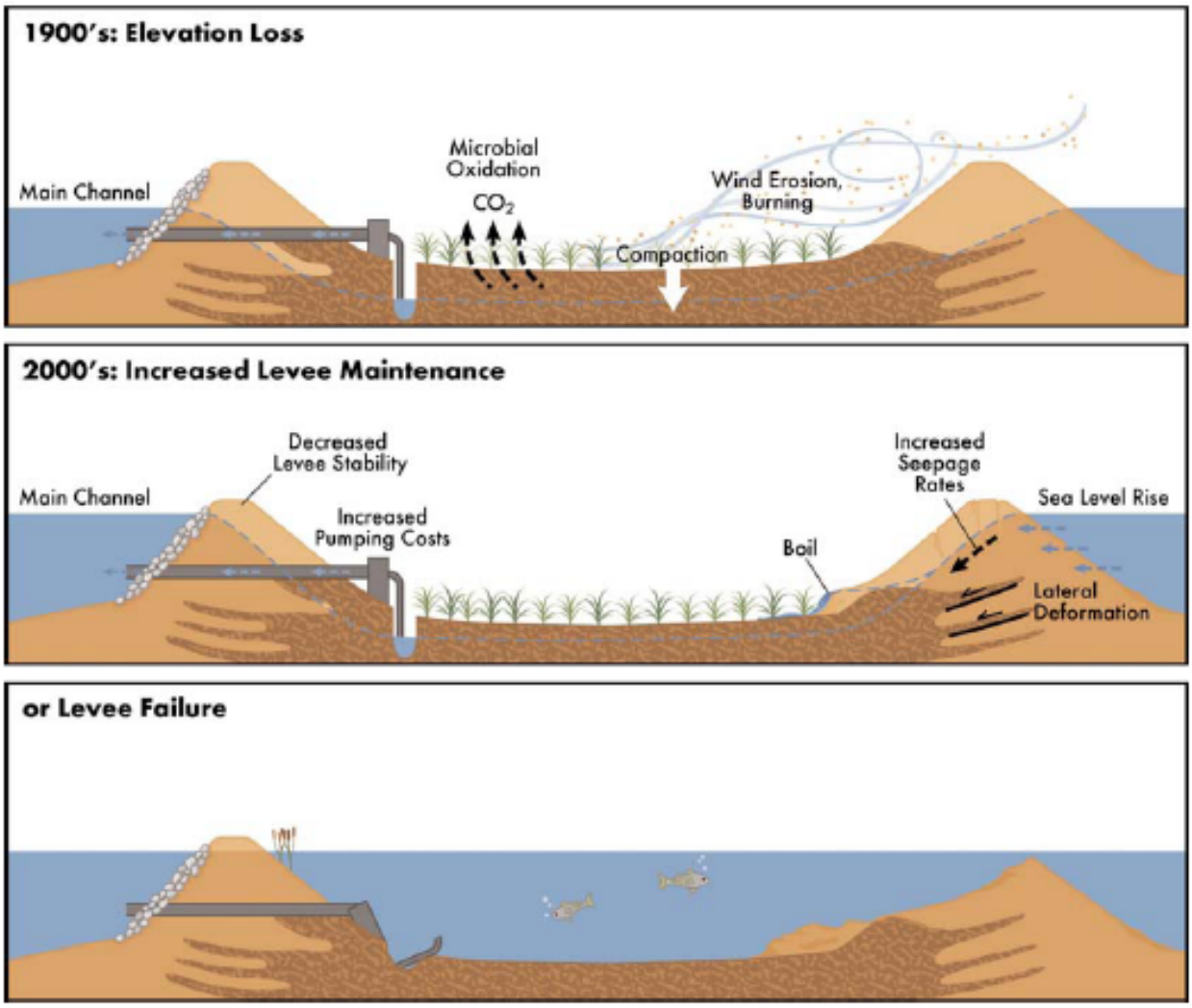

Figure 2.2: Conceptual diagram of land subsidence and levee failure. (Mount and Twiss 2005)

Land subsidence and sea level rise exacerbate the problems that lead to levee failure for a multitude of reasons, as demonstrated in Fig. 2.2. First, the rise in water level increases the hydrostatic pressure on the water-bearing side of the levee, which can then cause problems in the foundation soils such as reduced lateral support, reduced shear resistance, and the promotion of settlement or deformation of the underlying peat. Also, the decrease in island elevation decreases the factor of safety for the levees, in the same ways as explained above. The consequences of these problems include lateral spreading, cracking, and slumping of levees, which can then lead

to failure by erosion or overtopping. For example, Foott, Sisson, and Bell (1992) found in their investigation of a cracked levee on Sherman Island that the underlying peat had settled and moved laterally because of the lowered water table and subsided land on the island. Furthermore, land subsidence and sea level rise also increase the hydraulic gradient, and thus the seepage rate of water, in the levees, which can lead to piping failure or the formation of boils.

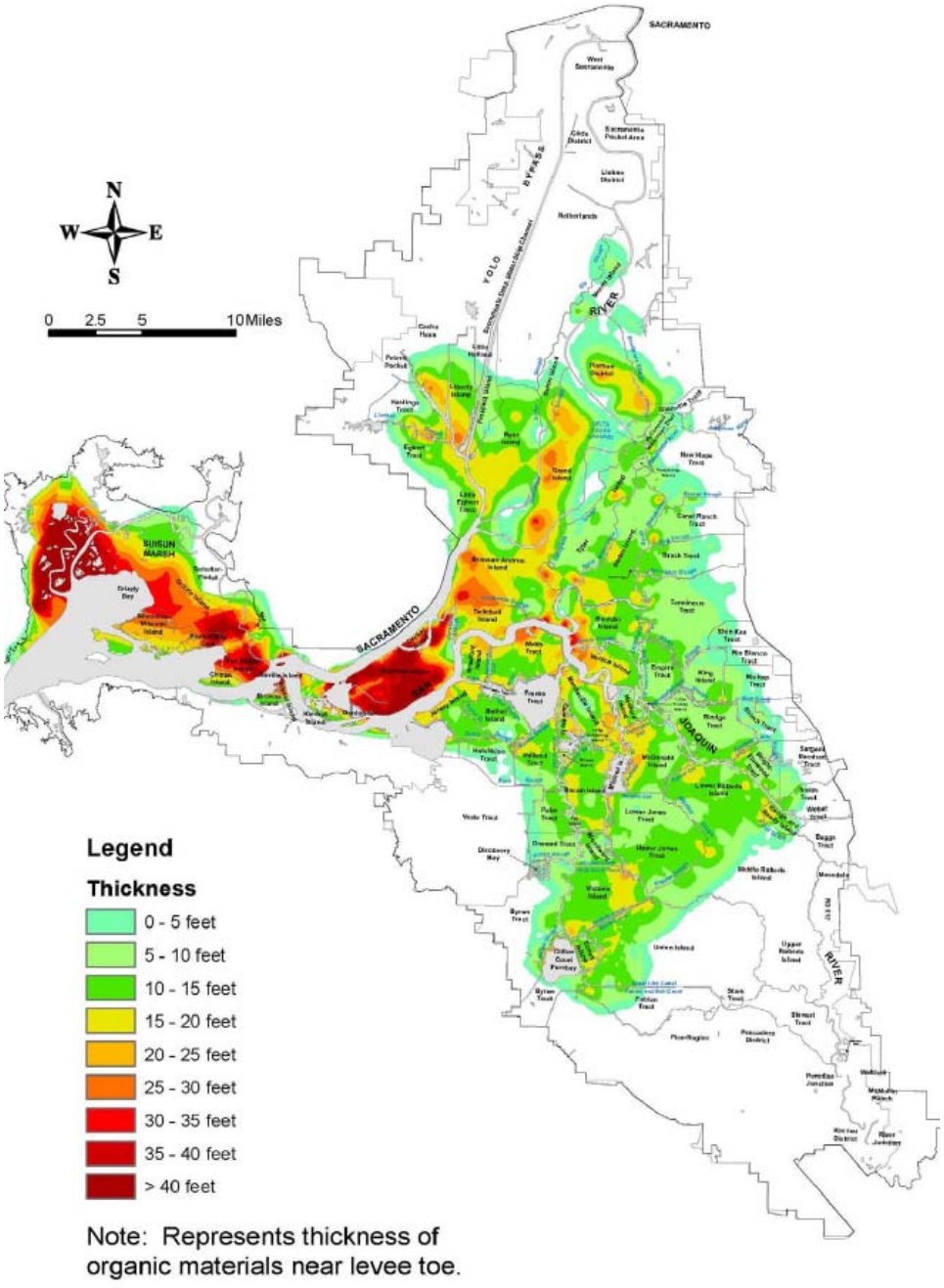

Figure 2.3: Thickness of peat deposits in the Delta. (DRMS Phase 1 2009)

Although many destructive land practices, such as the burning of peat soil, have ceased, land subsidence still continues in many parts of the Delta, especially in the central and western

parts of the Delta, which have the thickest deposits of peat (Fig. 2.3), at an average rate of 3.2 to 4.8 cm/year (Mount and Twiss 2005). Today, the elevation of many of these islands is at or below sea level, with some of the subsided islands reaching up to 25 feet below sea level. In general, the mean elevation of Delta islands (Fig. 2.4) is lowest where deposits of peat are thickest, especially in the central and western areas of the Delta. In the eastern and southern parts of the Delta, where the peat layer is not as thick, land subsidence has either stopped or slowed down considerably, especially when the organic content of the exposed soil is less than 20% (Mount and Twiss 2005).

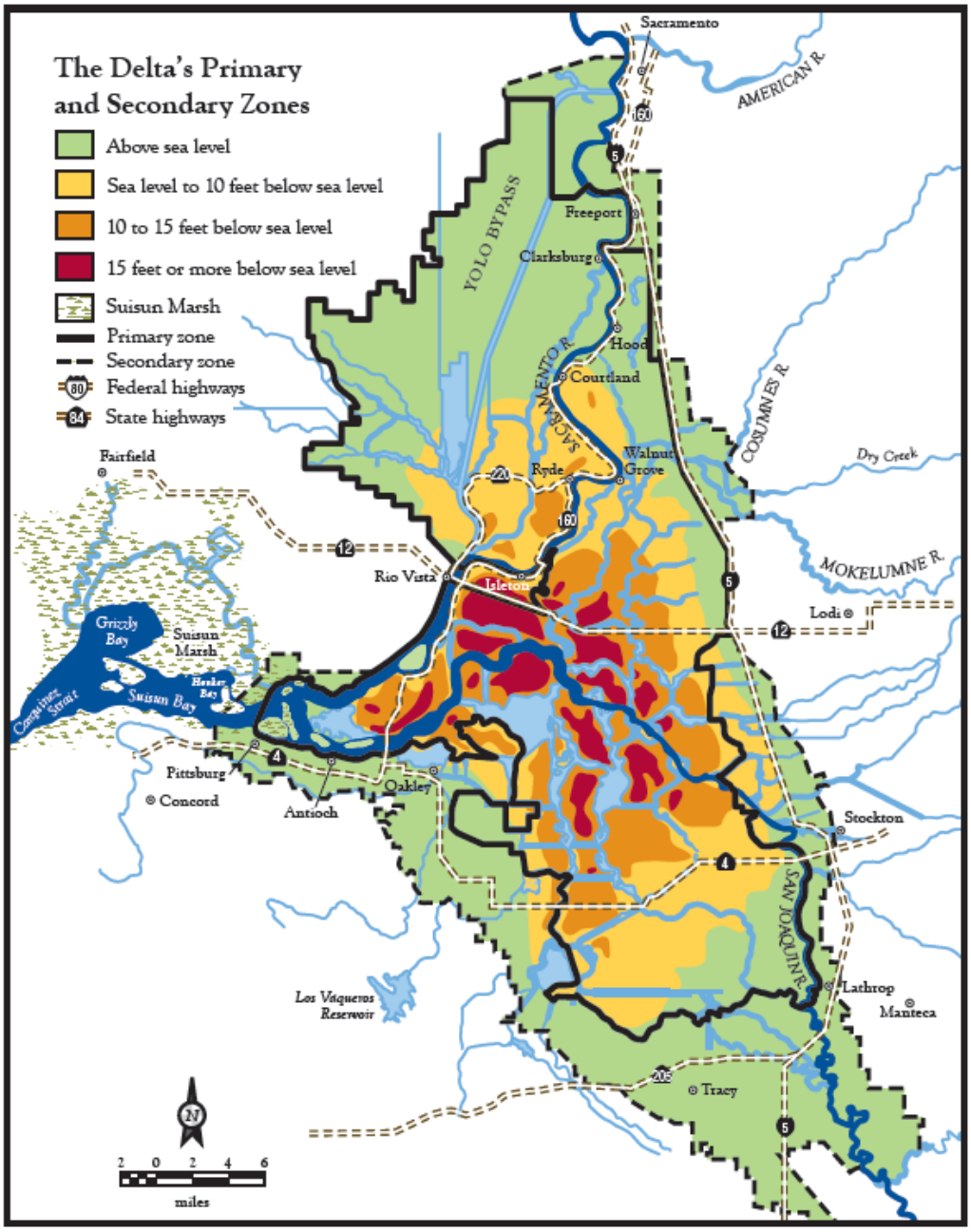

Figure 2.4: Current Elevation of Delta islands (Lund et al. 2007)

Although flooding in the Delta is a relatively common phenomenon, the consequences of a levee breach and a flooded island are pretty severe. First, the costs of repairing a levee breach can be very expensive, and repair and dewatering of a flooded island may take a long time. For example, the failure of a levee in the Jones Tract in June 2004 resulted in roughly $100 million

in repair and damage costs (DRMS Phase 1 2009). In some cases, such as the 1938 Franks tract failure and the 1983 Mildred Island failure, the flooded island is simply abandoned (Lund et al. 2007). Irreversible floods like these permanently change the landscape of the Delta. When a levee breaches, especially on a deeply-subsided island, the rapid flooding of the island can draw in saline water from the San Francisco Bay, temporarily degrading water quality. Known informally as a "big gulp," (Mount and Twiss 2005), flooding of this magnitude can have significant detrimental impacts on California's water supply, especially in the case of multiple flooded islands due to an earthquake (this will be explained in more detail in the next section).

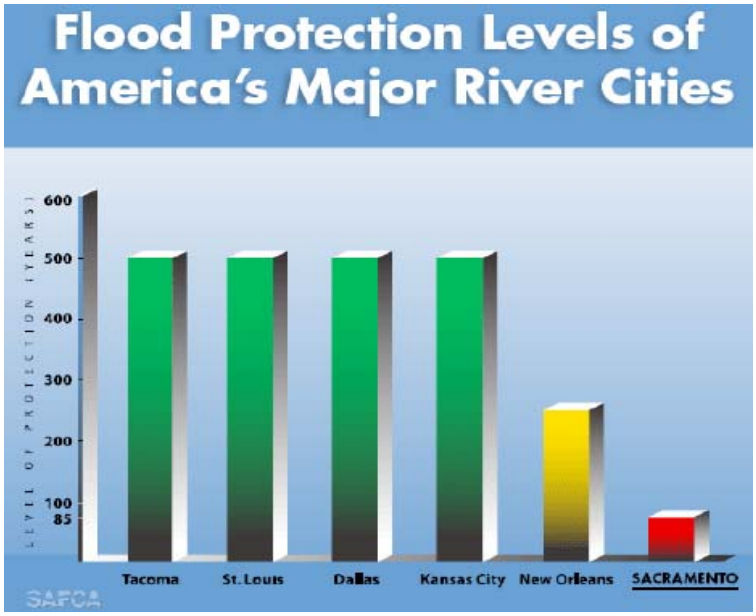

Figure 2.5: Flood protection levels of major US cities (source: safca.org)

The flooding risks in the Sacramento and the Delta are high. According to DRMS Phase 1 (2009), the levees that safeguard the city of Sacramento only offer protection for a 100-year flood event. Compared to other cities in the United States (Fig. 2.5), Sacramento levees provide the lowest level of flood protection. This is even lower than the level of flood protection for the newly rebuilt New Orleans levees, who suffered massive damage during hurricane Katrina. Even

with such a low level of flood protection, the levees in the Delta are considered to provide even less flood protection. With that in mind, one must consider the risks of levee failure in the case of a seismic event. As will be seen in the next section, the additional factors of a possible earthquake in the Delta make the risk of flooding more of a matter about how many islands will flood, as opposed to if any will flood.

2.2. Seismic Events and Flooding

The Sacramento-San Joaquin Delta is close to a large number of active faults in the nearby San Francisco Bay Area, such as the the Calaveras fault, the Hayward fault, and the Midland fault zone (Fig. 2.6). In general, there are two principal sources of seismic hazard in the Delta: small magnitude earthquakes generating from local faults such as the Midland and western Tracy Faults, and large magnitude earthquakes from more distant faults like the Calaveras and San Andreas Faults. Of the over 150 levee failures that have led to island flooding since 1900, no reports have been found that indicate the failure was earthquake induced, mostly because of a historical lack of earthquakes leading to strong ground motions in the Delta. Arguably the largest earthquake in the Bay Area's recorded history, the 1906 San Francisco earthquake caused little damage in the Delta, as the levees were still in the early stages of construction and therefore much smaller than today's configuration. The 1989 Loma Prieta earthquake, which caused much damage in the Bay Area, was centered so far from the Delta that any registered shaking did not cause any perceptible damage to the levees (DRMS Phase 1 2009). While these major earthquakes did not cause much damage, other low-magnitude and distant earthquakes have caused some damage to Delta levees. For example, Finch (1988) mentions a levee on the northern edge of the Webb Tract which almost failed during the 1983

Coalinga earthquake. In 1985, several distant, low-magnitude earthquakes damaged levee sections that were constructed from loose sand (Finch 1988). In the case of these scenarios, the damage may have been a result of liquefaction.

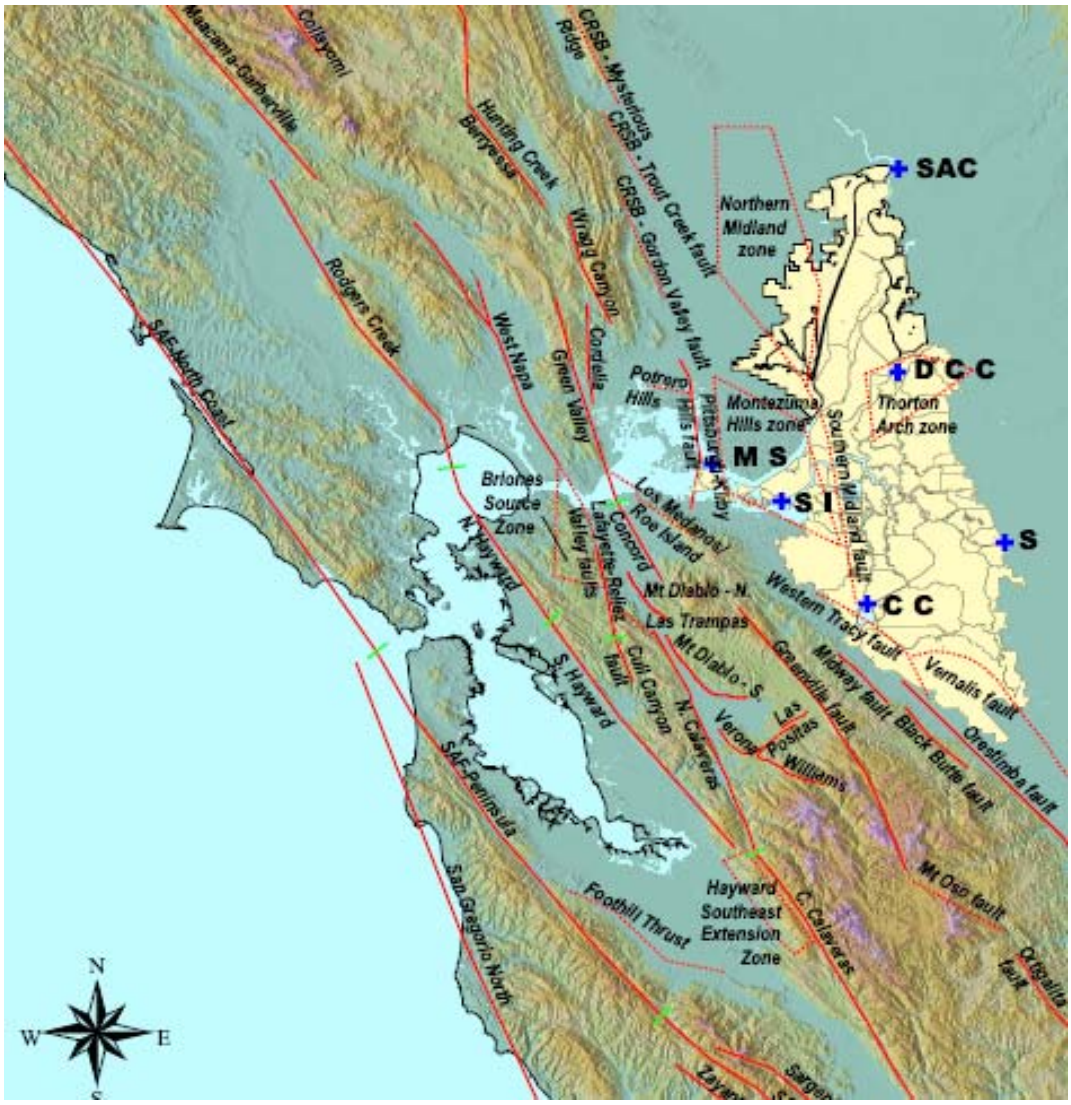

Figure 2.6: Faults near the Delta (DRMS Phase 1 2009)

The lack of any significant historical damage due to an earthquake is not a good indicator that the levees are not vulnerable to earthquake damage. Instead, it suggests that the levees have not been tested by moderate or high seismic shaking. Therefore, it is important to understand the seismic hazards in the Delta and the vulnerability of levee failure due to earthquake shaking. The

biggest concern about a seismic event hitting the Delta is multiple simultaneous levee failures, which can lead to significant loss of life, property, and water deliveries to Central and Southern California.

2.2.1. Seismic Hazards in the Delta

The first steps in understanding the risks of levee failure due to seismic events is to know the possible sources of seismicity, the likelihood that a major seismic event will occur, and the predicted intensity of ground motions that may occur. A standard practice for computing these predictions is the probabilistic seismic hazard analysis (PSHA) methodology. The PSHA methodology is useful because it considers aleatory variability in ground motions from a particular earthquake scenario and epistemic uncertainties through the use of logic trees that include the range of possible conditions in the seismic hazard model, such as ground motion predictions and possible sources of shaking (DRMS phase 1 2009). The end result of a PSHA is in the form of a hazard curve, which gives the annual probability of exceedance of a given intensity measure, such as peak horizontal acceleration, or spectral acceleration at some period. This section will summarize the current state of knowledge of seismic hazard in the Delta, including predictions of the occurrence of a strong earthquake, the expected ground motions in the Delta, and which sources are most likely to contribute to it.

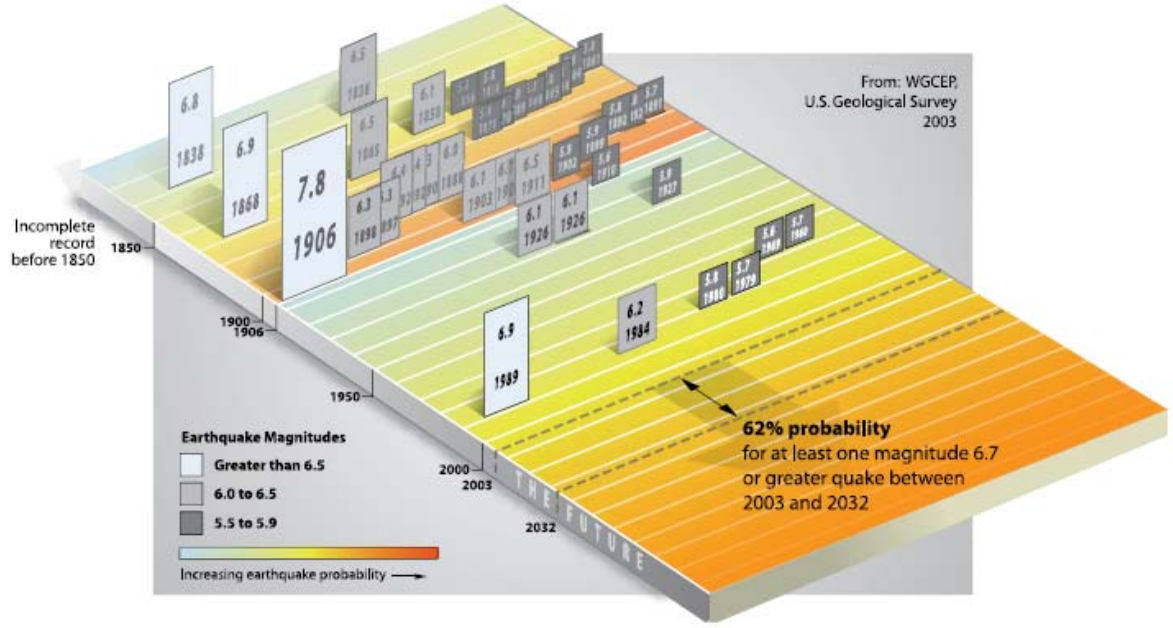

Figure 2.7: Significant seismic events in the Bay Area from 1838 – 2003, and the probability of a large earthquake (M > 6.7) occurring from 2003-2032. (DRMS Phase 1 2009)

According to a study done by the Working Group on California Earthquake Probabilities (WGCEP) in 2003, it was estimated that the probability of a large (M > 6.7) earthquake occurring in the Bay Area over a 30-year interval (2002-2032) was 62%. Fig. 2.7 shows the seismic events (M > 5.5) that have happened in the Bay Area, from 1838 – 2003, and the probability of a large event (M > 6.7) happening. It is interesting to note that since the 1906 San Francisco earthquake, only ten M > 5.5 earthquakes have occurred, while over 30 events have been recorded in the time period leading up to 1906. In 2007, the WGCEP performed a similar study, this time considering the probability of an earthquake occurring for the entire State of California, instead of the Bay Area and Delta subregion. The results of the updated study were very similar to the 2003 study, with a 63% probability of a large earthquake occurring between 2007-2036. Fig. 2.8 shows the updated probabilities of a large earthquake occurring in the Bay Area-Delta subregion for each of the significant faults in the area. The two faults that contribute

most to the earthquake threat in the Delta are the Hayward Fault and the San Andreas fault, which had large ruptures in 1868 and 1906, respectively. The high probability of a large earthquake originating on the Hayward fault is significant, because the average interval of earthquakes occurring on that fault is 140 years (Brocher et al. 2008).

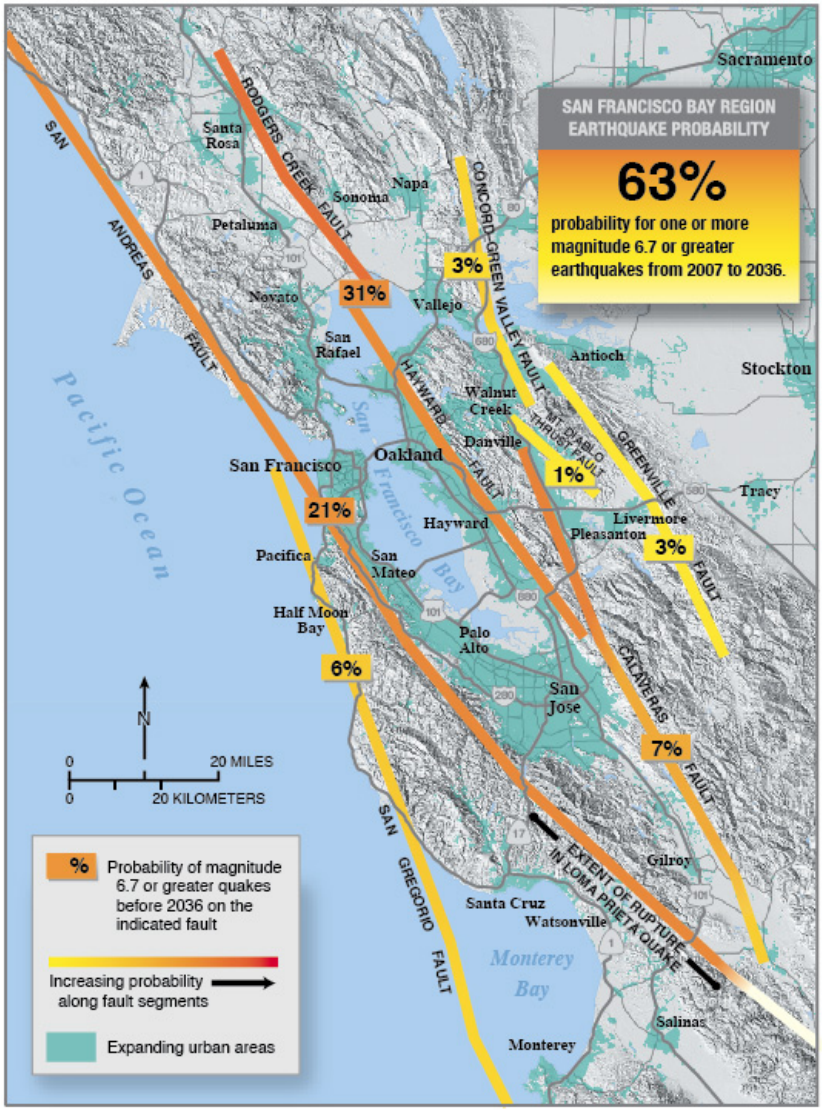

Fig. 2.8: Contribution of individual faults to large earthquake probability in the Delta. (WGCEP 2008)

In a PSHA, once the possible sources of seismic activity have been characterized and the probability of a characteristic earthquake has been evaluated, the attenuation of ground motions must then be characterized before the development of hazard curves. The 2009 DRMS study used the newly-developed Next Generation Attenuation (NGA) relationships to provide the attenuation of peak ground acceleration (PGA) and spectral accelerations (SA) at 5% damping. Fig. 2.9 shows map of PGA with an annual probability of exceedance of 0.01 (i.e., a 100-year ground motion) from the DRMS 2009 study. The PGA consistent with the Pleistocene sediments underlying the peat (not counting for amplification of waves in peat) increases from roughly 0.12g at the eastern edge of the Delta to 0.2g at the western edge, which is nearer to the Bay Area faults. The 200-year PGA from the DRMS study shows similar results to the PGA evaluated from previous studies of levee stability in the Delta (Torres et al. 2000, CDWR 1992), as seen in Fig. 2.10. The differences in results, especially in the western portion of the Delta, are mostly due to the use of new attenuation relationships and time-dependent models in the DRMS study, while the previous studies used the Poisson model for earthquake recurrence, which is time-independent.

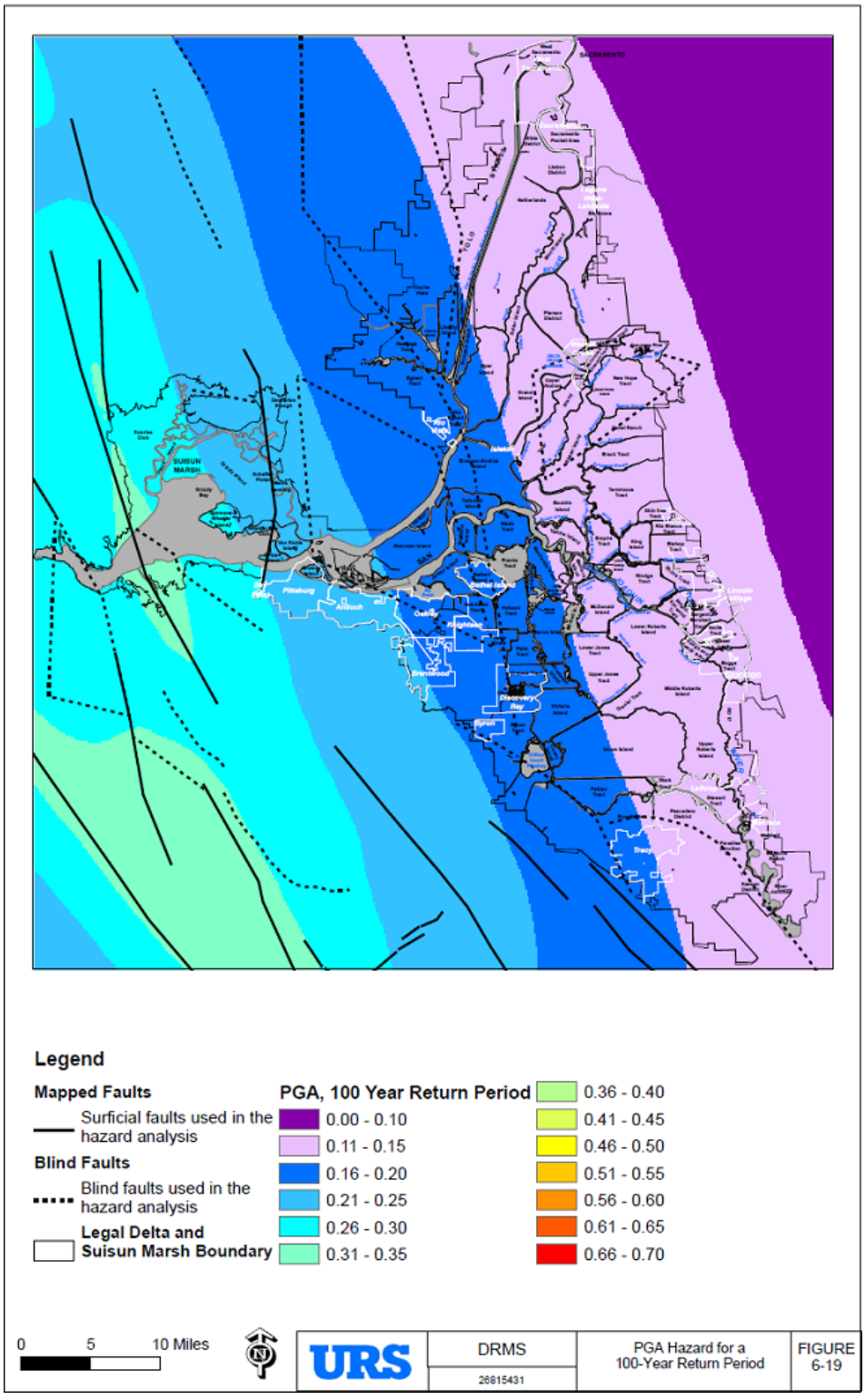

Fig. 2.9: Base rock PGA contour map of the Delta for a 100-year event. This does not account for ground motion amplification due to the peat. (DRMS phase 1 2009)

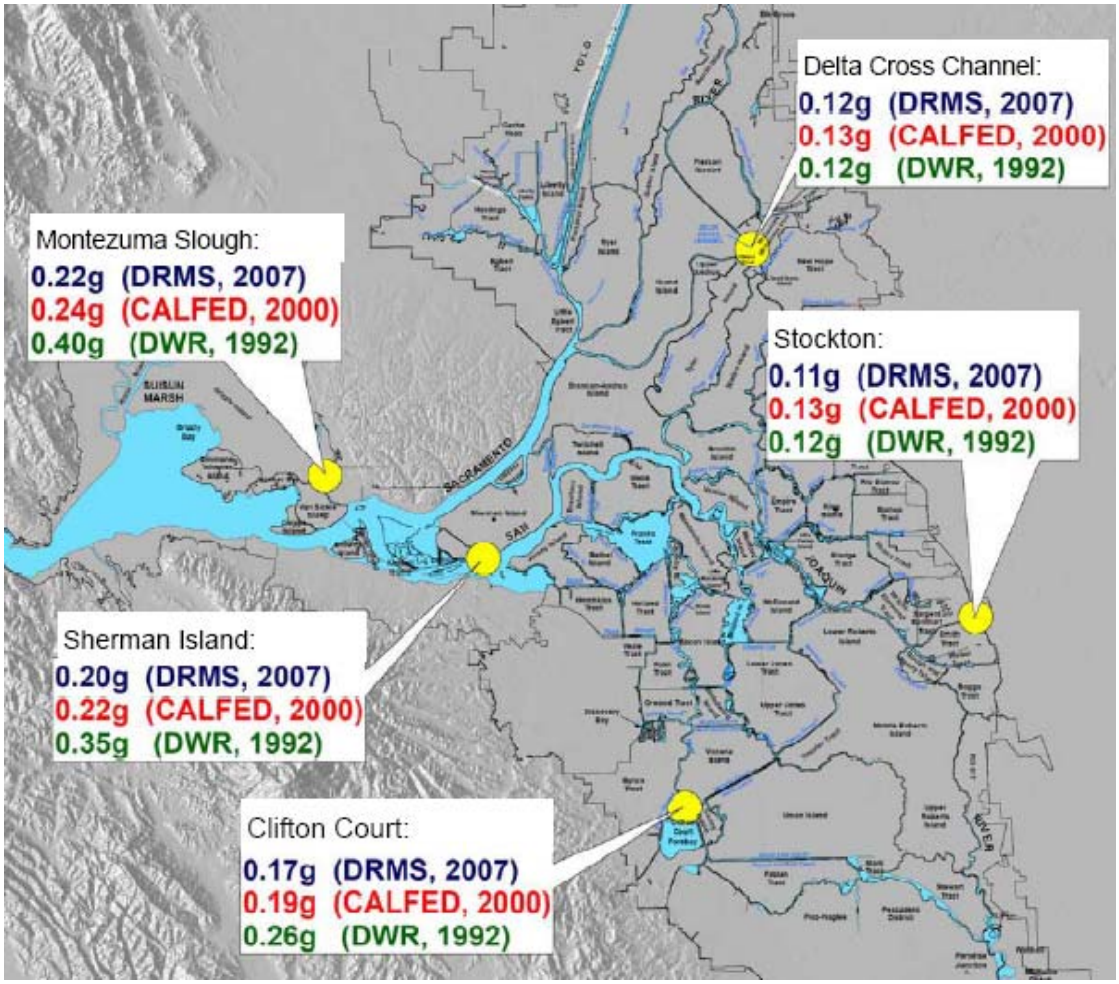

Fig. 2.10: Comparison of 200-year base rock PGA from three studies. (DRMS Phase 1 2009)

The Hazard curve for the Sherman Island site is shown in Fig. 2.11, with the mean hazard denoted as a solid line and the percentile hazard curves shown in dashed lines. For a 100-year event earthquake (annual exceedance probability of 0.01), the mean PGA hazard is 0.22 g, with a 90% confidence interval of 0.18-0.24 g. At higher return rates, the confidence intervals for the mean PGA are wider, partly due to the seismic source contributions to PGA (Fig. 2.12). At lower recurrence rates, faults like the Hayward and Calaveras fault contribute the most to PGA, while at higher recurrence rates (1000+ year events), fault zones such as the Midland and Montezuma Hills zones contribute the most. De-aggregation of the mean PGA hazard for

Sherman island is shown in Fig. 2-13 for the 100 year and 500 events. The 100-year event deaggregation shows the PGA hazard is controlled mainly by events in the M 6-7 range, with nearer events participating at lower magnitudes and farther-away events participating at higher magnitudes. As the return period increases, nearer events at around M 6 tend to dominate over the farther away events at higher magnitude. In general, this means that most seismic hazard in the Delta comes from faults in the western portion of the Central valley, which are parallel to the San Andreas plate boundary.

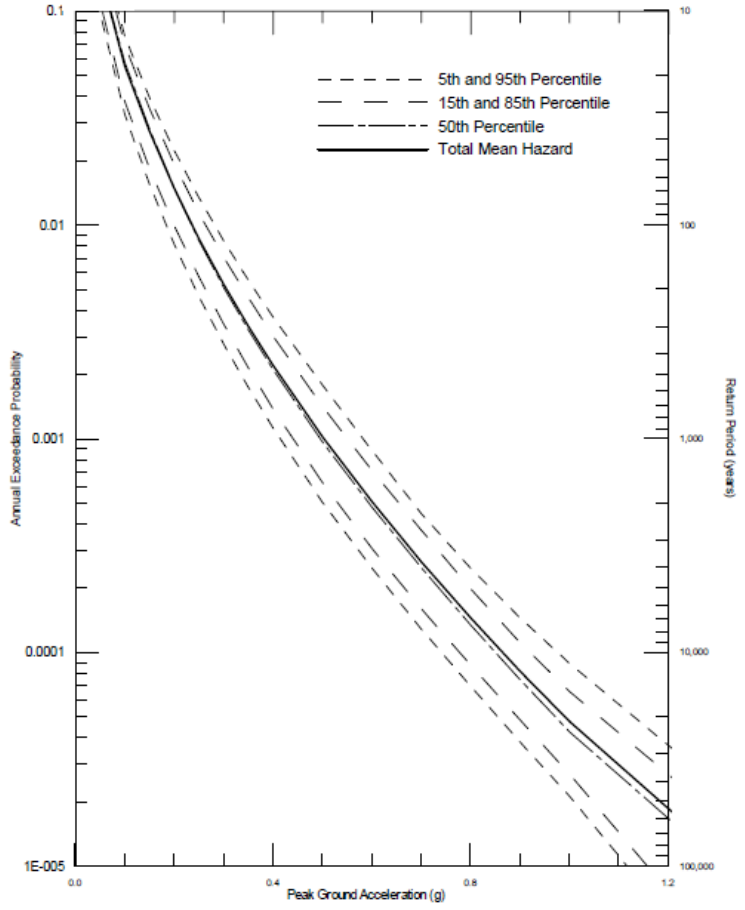

Fig. 2.11: PGA Hazard curve for Sherman Island site (DRMS Phase 1 2009)

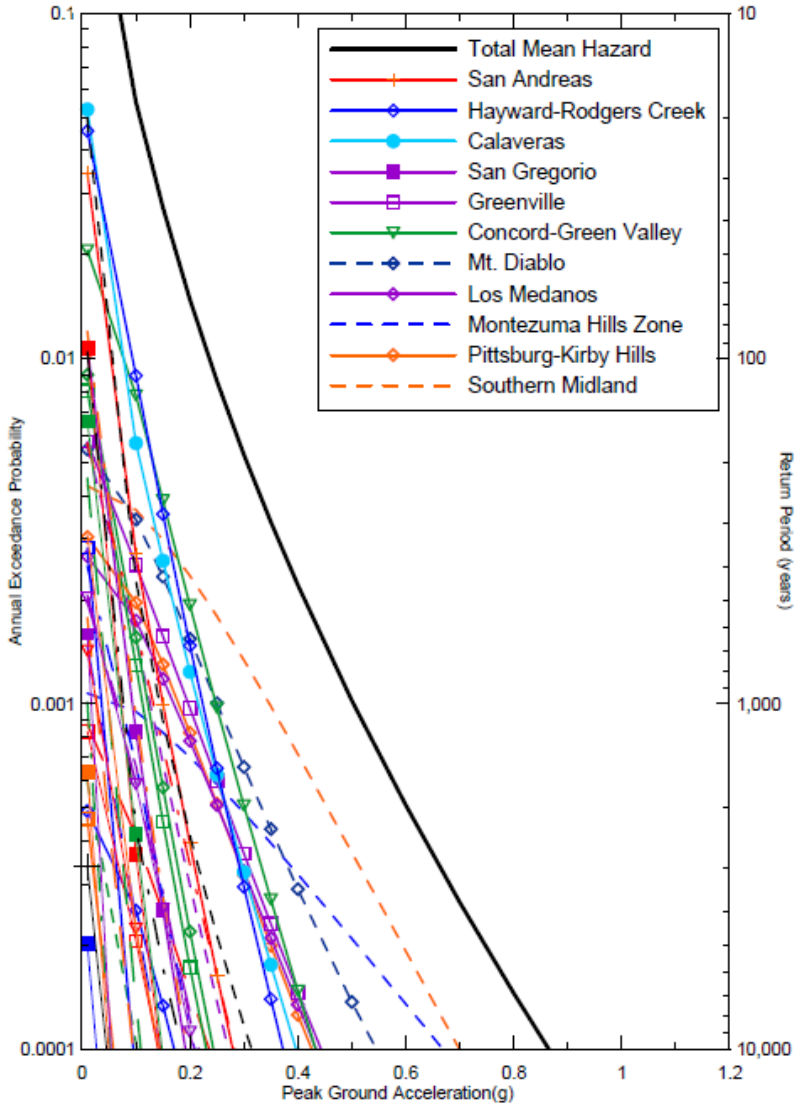

Fig. 2.12: Seismic Source contributions to PGA for Sherman Island (DRMS Phase 1 2009)

a)

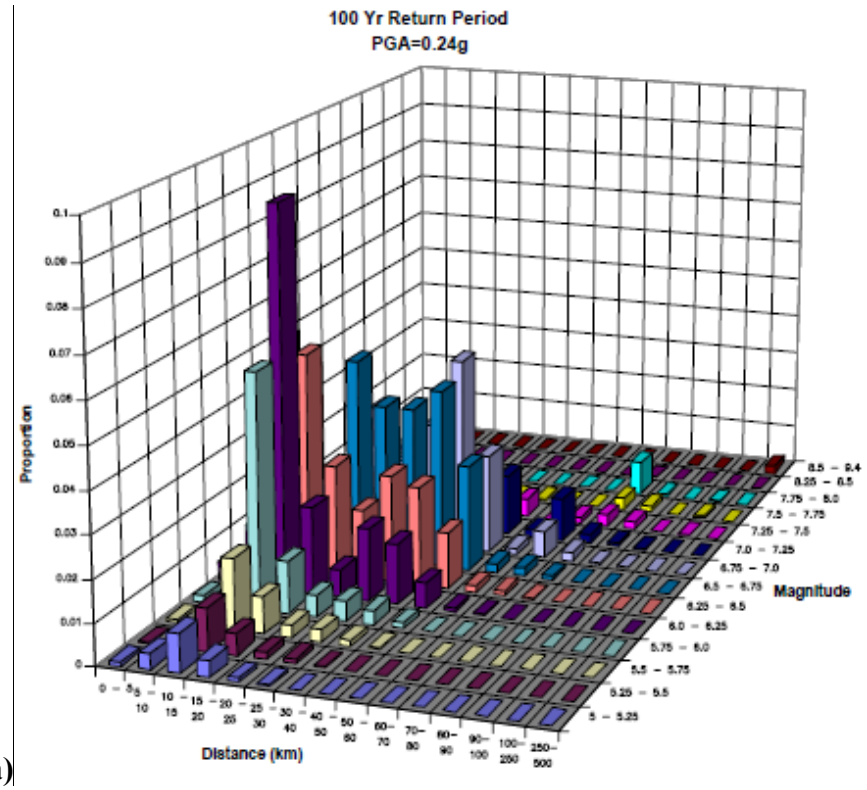

b)

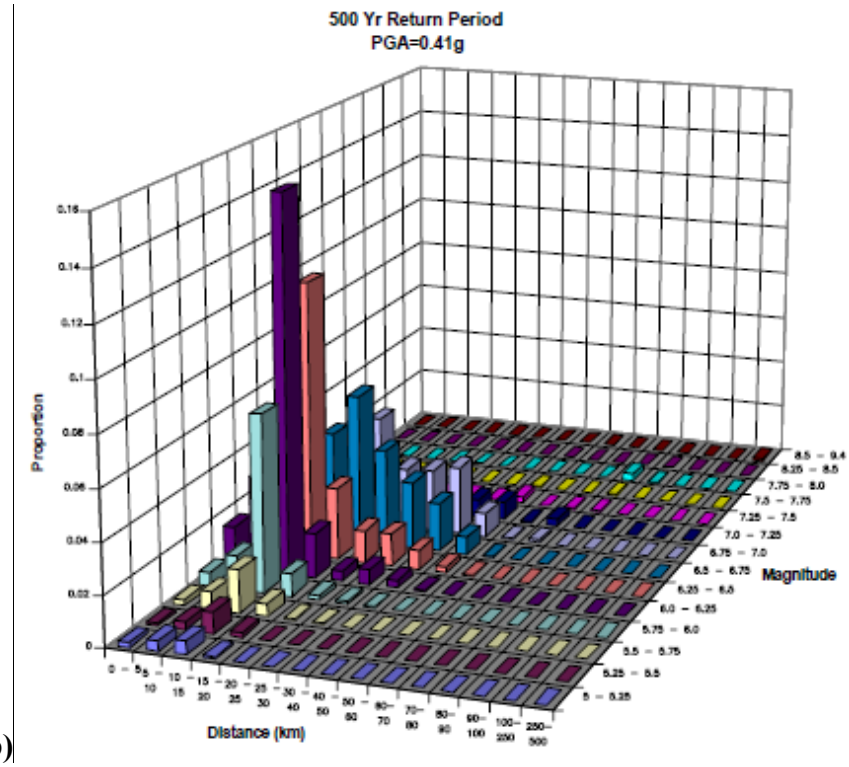

Fig. 2.13: Deaggregation of mean PGA for Sherman island for a) 100 year, b) 500 year events (DRMS Phase 1 2009)

2.2.2. Studies on Levee Vulnerability

Given the many hazards to island flooding from levee breaches in the Delta, seismic hazard is especially perilous because of the possibility of multiple simultaneous levee breaches flooding many islands in the Delta. Many studies have been performed to assess the performance of levees and the risk of levee failure due to an earthquake hitting the area. The most recent comprehensive study on levee stability due to seismic events is the Delta Risk Management Strategy (DRMS), sponsored by bond measures from the State of California, which sets out to quantify the Delta's seismic and flood risk using the best information currently available. Before summarizing the methods used and the results obtained from the DRMS study on levee stability due to seismic events, this section will discuss some previous studies' assessment of levee vulnerability, including studies from Finch (1988), the California Dept. of Water Resources (1992) and the CALFED Bay-Delta Authority (2000).

The study performed by Finch (1988) focused on the performance of Twichell Island's Three-Mile Slough levee. Specifically, it deals only with the liquefaction of dredged sand on the toe berm of the levee, which when lost, would lead to failure. The seismic hazard in this study was performed using a deterministic seismic hazard analysis to find the maximum credible earthquake of seven nearby faults, which then used a simplified relation to evaluate the factor of safety. This study found that the MCE of each of the seven faults considered would cause failure, and even a moderate earthquake of M = 6, centered at a distance of 14 miles from the site, would cause liquefaction failure. Although it did not consider the failure of peat, this was the first quantitative study to find the potential failure due to liquefaction.

The 1992 CDWR study was conducted on a much broader scope than the Finch study. This study sought to provide a preliminary assessment of the stability of Delta Levees during earthquake shaking. Seismic hazard (PGA) was calculated using both the deterministic MCE and PSHA framework. Amplification factors of waves through the peat soil were calculated after performing site response analyses that considered different site conditions, dynamic soil properties, earthquake records, and seismic hazards. Two potential modes of levee failure were considered in this study: the liquefaction of levee/foundation fill, and the cyclic yielding and deformation of non-liquefiable soils. The final results of this study consisted of maps that characterized the levees into vulnerability classes for various potential earthquake scenarios. Fig. 2.14 shows the mapped damage susceptibility for a very severe earthquake. The general trend of this figure indicates that levees on the western edge of the delta are most susceptible to damage, and the susceptibility decreases in the eastern portions of the Delta. Overall, the final results of this study characterized the vulnerability of levees in a qualitative manner, because of the many unknowns of the Delta soils, such as amplification/attenuation characteristics of shallow and deep profiles, strength loss of organic soils, and liquefaction resistance of foundation and levee soils.

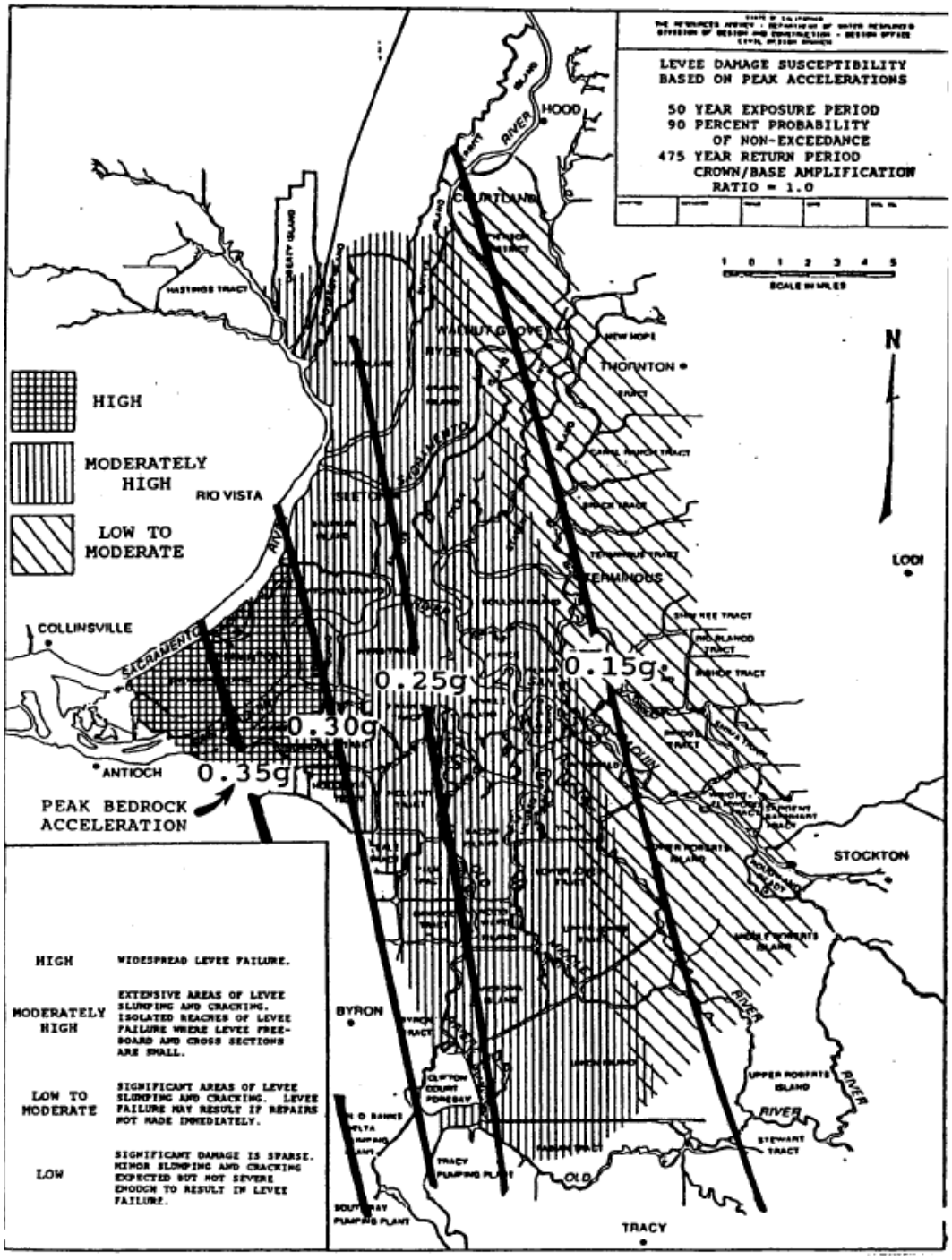

Figure 2.14: Levee damage susceptibility for a 475-year earthquake scenario. (CDWR 1992)

The 2000 CALFED study on levee vulnerability was conducted in a similar manner as the 1992 CDWR study. However, this study sought to quantify the fragility of levees and give a range of the number of levees expected to fail in an upcoming earthquake. The levees for each island were classified into four damage potential zones, based on the presence of liquefiable soils in the levees, the presence of levees on thick deposits of soft peat, and levee geometry. Much like the 1992 CDWR study, the two modes of failure considered were failures due to liquefaction of levee and foundation soils, and inertially-induced seismic deformation of levees on top of non-liquefiable soils. The fragility (in terms of levee failures per 100 miles) for each damage potential category was calculated for different PGA (0.05-0.30g) was calculated for both modes of failure, as seen in Table 2.1. Using these results, combined with the results from PSHA of the area, a probabilistic analysis of the expected number of levee failures was conducted. The hazard curve for the expected number of levee failures is shown in Fig. 2.15. For example, a 500-year event anticipates the peak bedrock acceleration to be 0.35g, with 10-70 levees expected to fail in that single event.

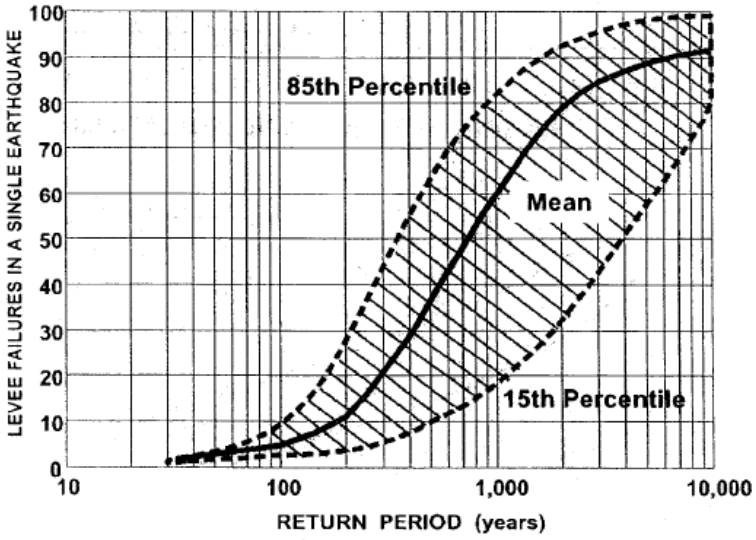

Figure 2.15: Expected number of levee failures in a single earthquake (Torres et al. 2000).

The Delta Risk Management Strategy (DRMS), as mentioned earlier, was sponsored by the State of California to quantify both seismic and flood risks using the best information currently available. For this study, several thousand borings and lab tests to classify and characterize the Delta levees. Delta levees were classified into 22 categories based on four factors: the equivalent clean sand blow count $(N_1)_{60\text{-}CS}$ of the levee fill, the $(N_1)_{60\text{-}CS}$ of the foundation sand, the thickness of the peat underlying the levee, and the waterside slope. A table of the vulnerability classes (VC) used in this study can be seen in Table 2.1. Two vulnerability classes were developed and studied for the Suisun marsh, but they will not be mentioned here. VCs 1-14 are potentially liquefiable sites, while VCs 15-22 are not considered to be liquefiable. Levees were also classified into three general vulnerability groups, according to their probability of failing under a 0.3g PGA, as seen in Fig. 2.16. According to the methodology used by the DRMS, the majority of the Delta levees show a high vulnerability to seismically induced failure. Methods to analyze the potential for liquefiable sites were performed using well-established methods. For non-liquefiable sites, hazard was evaluated by calculating pseudostatic yield acceleration (see Fig. 2.17) and then performing a Newmark sliding block analysis. This approach is well suited for problems involving sliding and shear failure, since soil is assumed to behave in a rigid plastic manner. For Delta levees, the yield acceleration was calculated to be between 0.05g, for levees founded on thick peat deposits, and 0.24g, for levees not founded on peat. Overall, the thickness of peat was found to be a significant contributor to the probability of failure of levees not founded on liquefiable soil, and in general, the probability of levee failure on thickest peat ranges from 0.3-0.5 for a 0.5g PGA. Based on this information, the DRMS calculated the number of island expected to simultaneously fail due to seismic events within the

next 25, 50, and 100 years, as seen in Fig. 2.18. For example, a 25-year event was calculated to have a 50% probability of 20 or more islands flooding. Widespread failure of the Delta levees has been forecast to cost billions of dollars in damage and disrupt water deliveries for up to two to three years. Some even think that with such sudden changes, water delivery shortages would be permanent, and much of the state would have to look elsewhere to find its water supply.

Table 2.1: Vulnerability classes used in DRMS study (DRMS Phase 1 2009)

Geographic Area	Vulnerability Class Index	Waterside Levee Slope	$(N_1)_{60\text{-}cs}$ Fill	$(N_1)_{60\text{-}cs}$ Foundation	Peat Thickness (ft)	Random Input Variables
Delta	1	Any	0-20	Any	0	$(N_1)_{60\text{-}cs}$ Fill, $(N_1)_{60\text{-}cs}$ Foundation, S_u
	2	Any	0-20	Any	0.1-10	$(N_1)_{60\text{-}cs}$ Fill, $(N_1)_{60\text{-}cs}$ Foundation, S_u, Peat Thickness
	3	Any	0-20	Any	10.1-20	$(N_1)_{60\text{-}cs}$ Fill, $(N_1)_{60\text{-}cs}$ Foundation, S_u, Peat Thickness
	4	Any	0-20	Any	>20	$(N_1)_{60\text{-}cs}$ Fill, $(N_1)_{60\text{-}cs}$ Foundation, S_u, Peat Thickness
	5	Any	>20	0-20	0	$(N_1)_{60\text{-}cs}$ Foundation
	6	Any	>20	0-5	0.1-10	$(N_1)_{60\text{-}cs}$ Foundation, Peat Thickness
	7	Any	>20	0-5	10.1-20	$(N_1)_{60\text{-}cs}$ Foundation, Peat Thickness
	8	Any	>20	0-5	>20	$(N_1)_{60\text{-}cs}$ Foundation, Peat Thickness
	9	Any	>20	5.1-10	0.1-10	$(N_1)_{60\text{-}cs}$ Foundation, Peat Thickness
	10	Any	>20	5.1-10	10.1-20	$(N_1)_{60\text{-}cs}$ Foundation, Peat Thickness
	11	Any	>20	5.1-10	>20	$(N_1)_{60\text{-}cs}$ Foundation, Peat Thickness
	12	Any	>20	10.1-20	0.1-10	$(N_1)_{60\text{-}cs}$ Foundation, Peat Thickness
	13	Any	>20	10.1-20	10.1-20	$(N_1)_{60\text{-}cs}$ Foundation, Peat Thickness
	14	Any	>20	10.1-20	>20	$(N_1)_{60\text{-}cs}$ Foundation, Peat Thickness
	15	Steep	>20	>20	0	
	16	Steep	>20	>20	0.1-10	c, ϕ, Peat Thickness
	17	Steep	>20	>20	10.1-20	c, ϕ, Peat Thickness
	18	Steep	>20	>20	>20	c, ϕ, Peat Thickness
	19	Non-Steep	>20	>20	0	
	20	Non-Steep	>20	>20	0.1-10	c, ϕ, Peat Thickness
	21	Non-Steep	>20	>20	10.1-20	c, ϕ, Peat Thickness
	22	Non-Steep	>20	>20	>20	c, ϕ, Peat Thickness

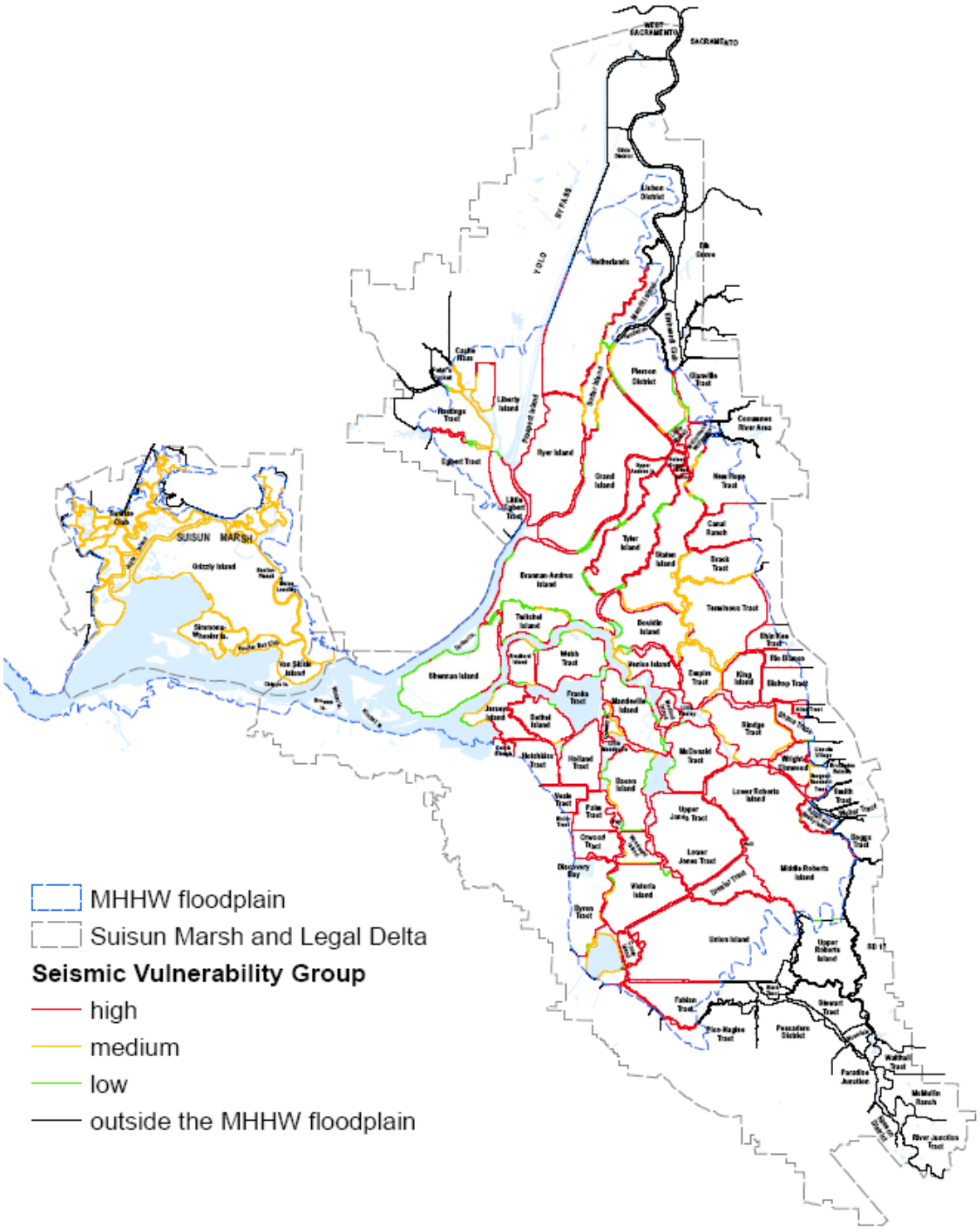

Figure 2.16: Seismic Vulnerability classification of Delta levees. (DRMS Phase 1 2009)

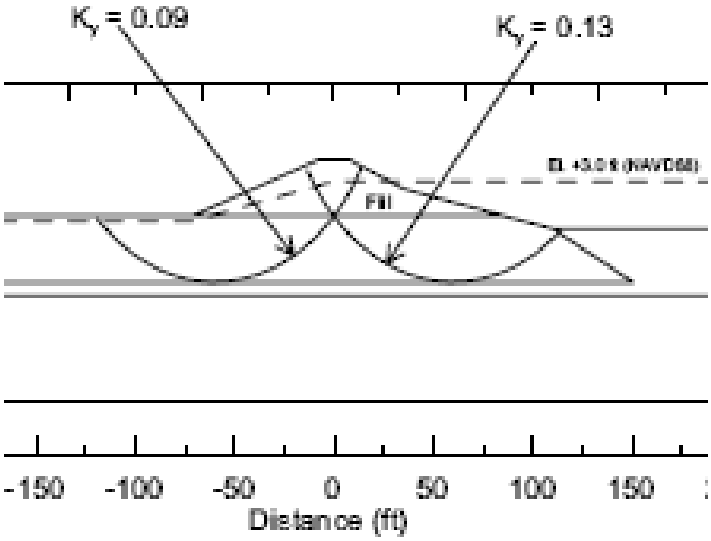

Figure 2.17: Pseudostatic yield accelerations and accompanying rotational failure modes (DRMS Phase I 2009)

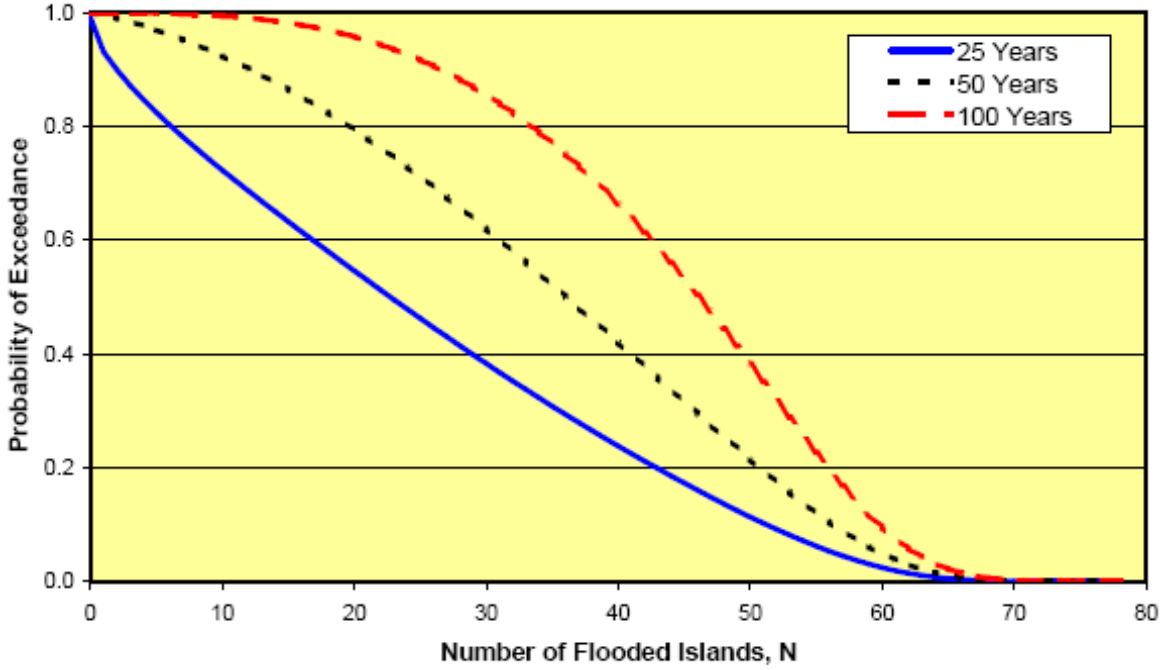

Figure 2.18: Probability of exceeding number if flooded islands for 25, 50, and 100 year exposure periods. (DRMS Phase 1 2009)

2.3. Peaty Organic Soils

Because of the high contribution of thick peat deposits to the probability of failure of non-liquefiable levees, it is therefore important that we understand the unique characteristics of peat soils, as well as their dynamic properties. This section will define what peat soils are, the defining characteristics in terms of engineering properties, and how peats behave dynamically.

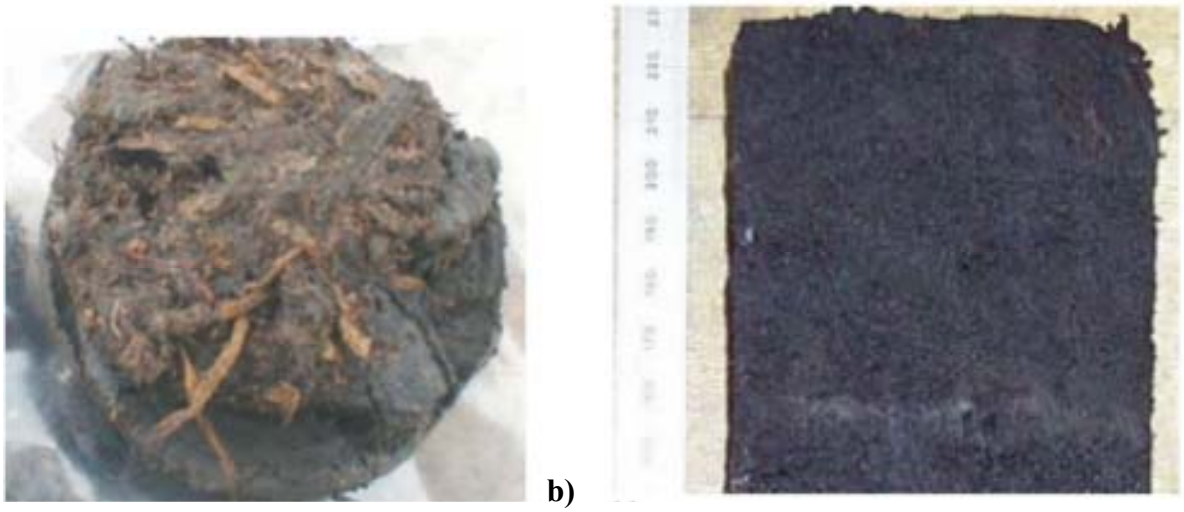

a) **b)**

Figure 2.19: Photograph of a) fibrous peat, b) amorphous peat (Kishida et al. 2009a)

Peat soils are generally categorized as soils that contain high amounts of decomposed and fragmented plant matter that has fossilized. These soils may contain inorganic matter, but in general, are characterized by their organic content. Peat soils come in two general modes, as seen in Fig. 2.19: fibrous peats (Fig. 2.19a), which are generally younger, show less decomposition, and show root networks of long-dead plants; and amorphous peats (Fig. 2.19b), which are significantly more decomposed and older than fibrous peats and may contain significant amounts of inorganic matter. A state-of-the-art paper by Mesri and Ajlouni (2007) identified seven distinctive characteristics of fibrous peats:

1. Very high initial permeability. Peats can have anywhere from 100-10,000 times the initial permeability of soft clays.
2. The permeability of peats decreases dramatically as they are compressed under embankment loads.
3. Peats are extremely compressible.
4. Peats have the highest rates of secondary compression versus compression index for all soils. (See Fig. 2.20).
5. The frictional resistance of peat (φ') can be very high when compared to soft clay and silt deposits. Shear deformation needed to bring about the maximum friction resistance can be anywhere from 5-10 times that needed for soft clays and silts.
6. The ratio of undrained shear strength to consolidation pressure (defined as $s_u(TC)/\sigma_p'$) is very high, typically twice that of soft clays and silts.
7. Very low ratios of undrained Young's modulus to undrained shear strength (defined as $E_u/s_u(TC)$).

Furthermore, peats also exhibit very high initial water contents and void ratios; it is not uncommon for peats to have natural water contents of 500-1,000%, or void ratios from 5-15. Therefore, peats can also compress very quickly, and it can be very difficult to distinguish primary from secondary consolidation, as seen in the example in Fig. 2.20. Amorphous peats, which were not covered in this study, typically exist at lower void ratios, and have lower compressibility, permeability anisotropy, and friction angles than fibrous peats. A study done by Marachi et al. (1983) on San Joaquin Delta peats shows many similarities to the characteristics of peats mentioned in Mesri and Ajlouni (2008), with lower friction angles, ranging from 28 to 35 degrees.

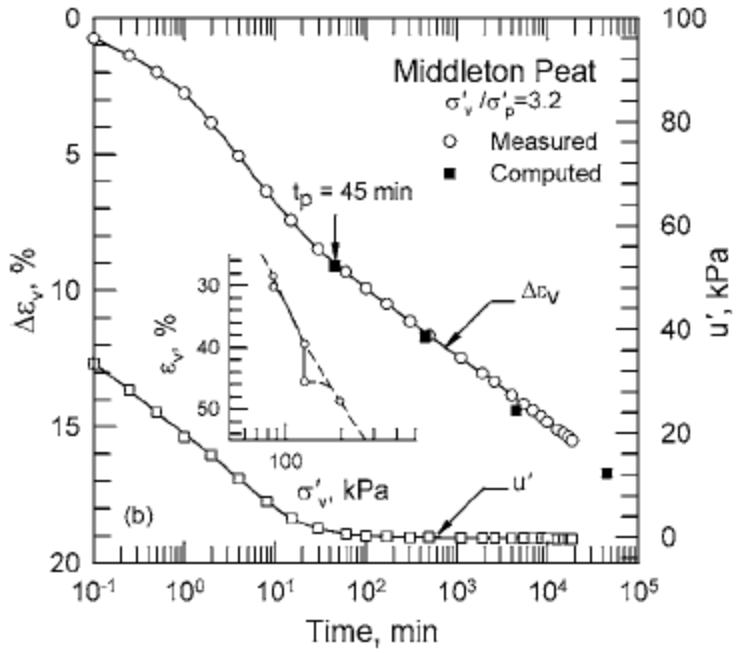

Figure 2.20: Example of primary and secondary compression rate for normally consolidated peat. (Mesri and Ajlouni 2007)

2.3.1. Dynamic Properties of Delta Peat

Peat soils also exhibit dynamic properties that are unique amongst most other soils. Multiple studies, such as Boulanger et al. (1998), Wehling et al. (2003), and Kishida et al. (2009a, b), have been performed to study the dynamic properties of peaty organic soil in the Delta. In each of these studies, peat soils were sampled either underneath a levee crest or from the free field, using thin-walled Shelby tubes to minimize sample disturbance. Most peat soils sampled consisted of highly fibrous material, and so material anisotropy was very high. Dynamic tests performed on these soils generally consist of strain-controlled cyclic triaxial tests to find modulus reduction and damping curves. Other tests performed on the peat soil include torsional shear and resonant column tests to find dynamic properties at small strains and bender element

tests to find the maximum shear modulus. In the case of the Wehling et al. (2003) study, dynamic properties of soils on Sherman Island were compared for peats underneath the levee crest, the mid-toe of the levee, and the free-field, in order to obtain an understanding of how consolidation stress affects dynamic properties. For example, Fig. 2.21 shows the results of bender element tests to find normalized G_{max} for peat beneath the three locations. We can observe that maximum shear modulus depends on the location of the peat soil in relation to the levee. Free-field peat tends to show a much greater increase in shear modulus with effective consolidation stress than peat sampled from underneath the levee crest. Shear modulus, modulus reduction, and damping curves from cyclic triaxial testing performed in the same study are shown in Fig. 2.22. The shear stress-strain curve shows higher nonlinearty for the free-field soil than for the soil from underneath the levee and the levee crest. Modulus reduction curves show much greater reduction in all strain levels for the free-field peat, as opposed to the peat from beneath the levee crest. Interestingly, the Wehling et al. (2003) study noted that peat from underneath the levee crest exhibited greater modulus reduction than peat from underneath the mid-toe of the levee. This was attributed to the effect of bedding plane characteristics, rather than consolidation pressure. Finally, the damping curve shows that free-field peat consistently exhibits higher damping at all strains than peat sampled from underneath the levee. Fig. 2-23 shows comparisons of modulus reduction and damping ratio curves for Sherman Island peat from the Boulanger et al. (1998) study to clays of varying plasticity indices from the Vucetic and Dobry (1991) study. In this case, we can observe that Sherman Island soils have much higher damping ratios at low strains than what is expected for clays. At higher cyclic strains, modulus reduction behaves similarly to clays with high plasticity (PI = 100). Similar behavior is exhibited for modulus reduction.

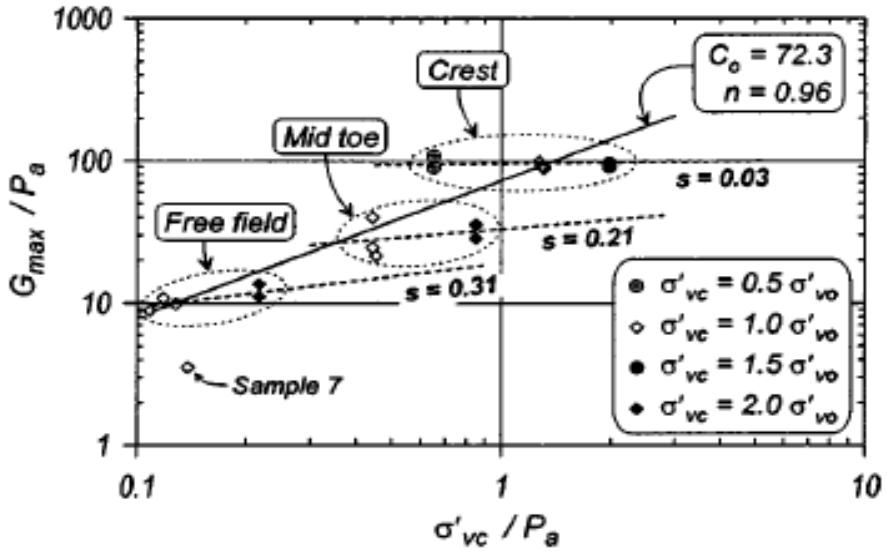

Figure 2.21: Normalized maximum shear modulus (G_{max}) for peat sampled from beneath the levee crest, mid-toe, and free field, compared to reconstituted peat. (Wehling et al. 2003)

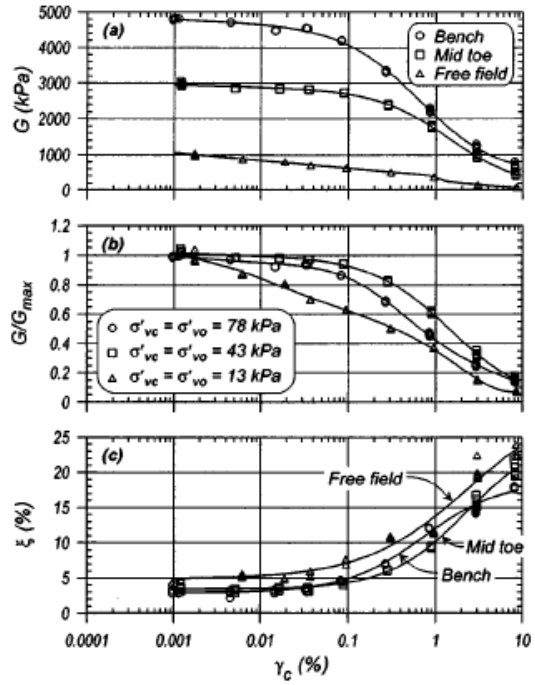

Figure 2.22: Shear modulus, modulus reduction, and damping curves for strain-controlled cyclic triaxial testing from Sherman Island (Wehling et al 2003).

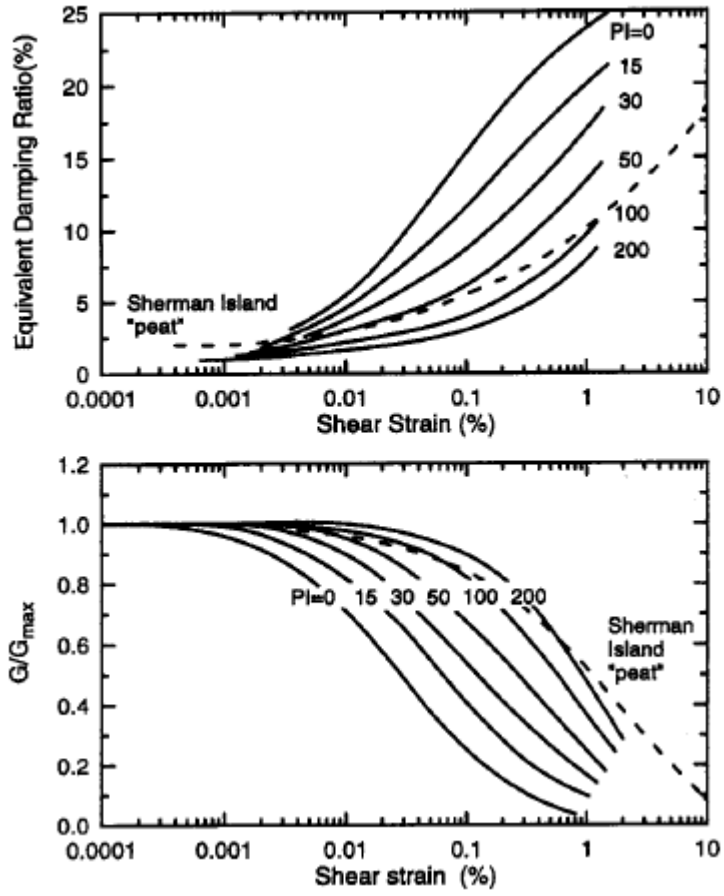

Figure 2.23: Comparison of damping and modulus reduction curves for Sherman Island peat compared to clays of varying Plasticity indices from Vucetic and Dobry (1991) (Boulanger et al. 1998).

2.4. Project Motivation

Previous studies on the vulnerability of Delta levees have tended to focus on vulnerability of levees due to liquefaction of levee foundation or fill soils, with attention only being recently paid to levees founded on peat soils. Liquefaction is clearly an important driver of seismic hazard in the Delta, but understanding all possible sources of risk is crucial for accurate hazard

evaluation. Peat soils are much more prevalent underneath Delta levees than sandy soils (Fig. 2.24), but much less is known about their seismic behavior. In general, levees founded on peat have not performed well in seismic events, and the state of knowledge of seismic performance of levees founded on peat deposits in the Delta is lacking. Levees founded on peats in Japan have not performed well, though it is unclear whether liquefiable lenses of soil in the peat contributed to their poor performance (Tokimatsu and Sekiguchi 2006). Studies such as the DRMS have only considered traditional Newmark sliding block analyses. However, these analyses consider only one potential mode of failure: limit equilibrium failure which assumes the soil behaves in a rigid plastic manner. Therefore, we do not fully understand the mechanisms that can lead to levee failure as a result of an earthquake, or the risk levels that lead to levee failure due to these mechanisms. Potential modes of failure that may be difficult or impossible to capture in a Newmark analysis include (see Fig. 2.25): spreading or slumping due to post-cyclic consolidation, sliding of the levee on cyclically-weakened peat, or bearing failure from distributed shear deformations in the peat, and better information is needed to see if these phenomena might occur. Overall, we would predict levee slumping to be the most likely form of failure to occur as it has been observed in Japanese levees founded on peat during the 1993 Kushiro-oki (Sasaki 2009) and the 2007 Niigata earthquakes.

Because our knowledge of levee behavior on peat soils is limited, the proposed method for learning about the mechanisms of failure has been to conduct a full-scale test of a levee structure or embankment to investigate the in situ deformation potential of peaty organic soils under realistic ground motions. Work to study the seismic deformation potential of levees on peaty organic soil was conducted by researchers at UCLA, Cal Poly, and the California State Department of Water Resources. A grant to study this phenomena was awarded through the

George E. Brown Network for Earthquake Engineering Simulation (NEES), and much of the NEES@UCLA staff and facilities were utilized as part of the larger project team. NEES@UCLA specializes in field testing, which includes the deployment of field shakers to impose large horizontal forces in the frequencies of earthquake motion. The proposed test embankment was well-monitored, using a combination of above and below ground accelerometers, pore pressure transducers, sand slope inclinometers to record data during shaking. In addition to the field testing, laboratory testing of the peat soils will be performed to see if levee deformation is predictable using deformation analysis procedures. However, the field testing will be the main component of this project, and the lab testing is currently being conducted as part of another project. Two tests were performed on the embankment, and this proof-of-concept study may be used to perform additional work.

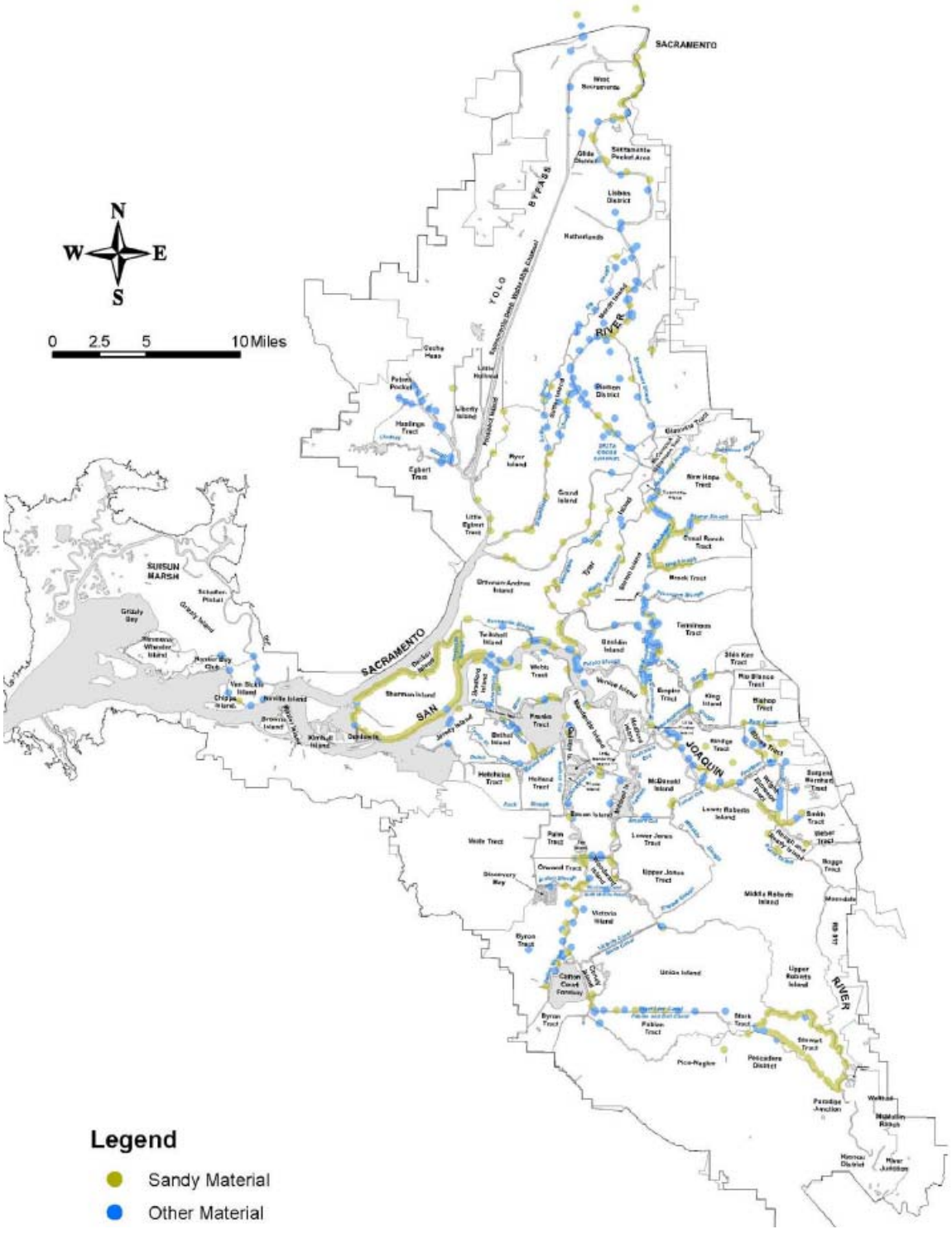

Figure 2.24: Presence of sandy soils underneath Delta levees versus other soils, which include peats (DRMS Phase 1 2009).

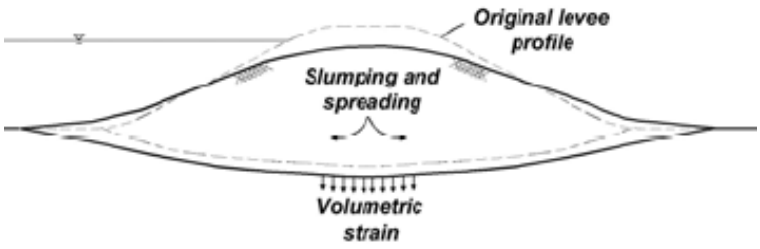

a)

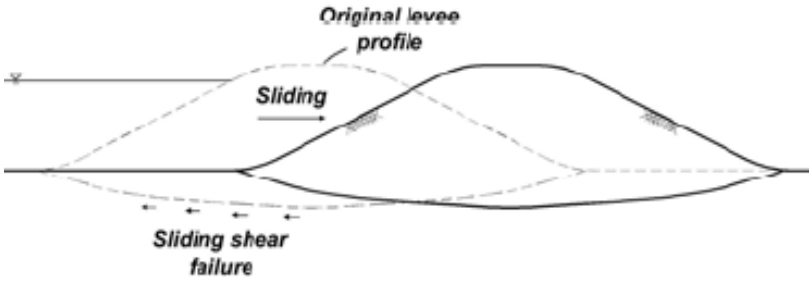

b)

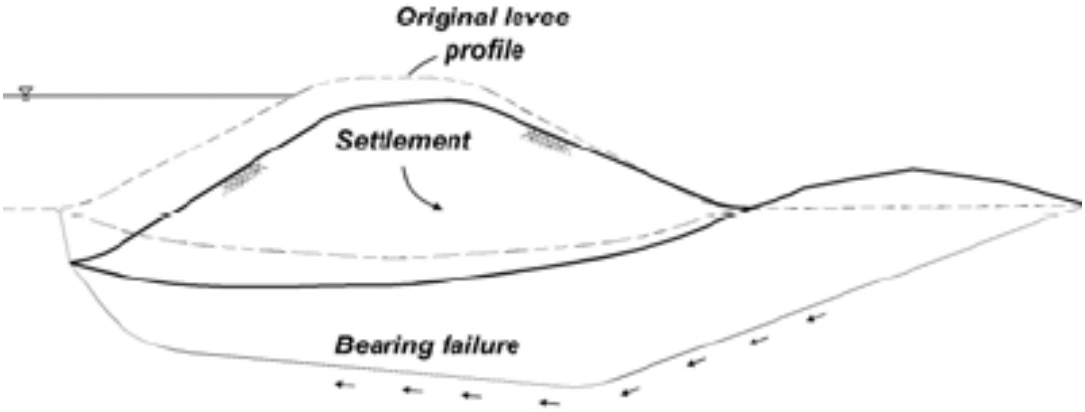

c)

Figure 2.25: Potential levee failure mechanisms: a) post-cyclic consolidation and/or volumetric strain, b) sliding failure, c) bearing failure.

Chapter 3. Site Identification and Investigation

This chapter explains site selection and geotechnical/geophysical investigations performed at the site. The first section describes process of how the project team selected and received permission to use the Sherman Island site. The next sections then explain both the geophysical and geotechnical investigations performed to assess the material properties of the peaty organic soil underlying the test specimen. A total of six separate visits, one to a prospective site and five to the test site, were performed, and are summarized in Table 3.1. Investigative activities were often coordinated with other activities, as seen in the project schedule shown in Fig. 3.1. The last section of this chapter discusses the interpretation of the site stratigraphy based on the various investigations performed.

Table 3.1. Summary of geotechnical and geophysical studies performed at site.

Date	Description
March 26, 2009	Investigation of prospective site at Blackrock
March 24, 2010	Sherman Island geophyiscal investigation measuring ambient vibrations, and SASW using hammer striking ground surface, and people jumping up and down.
June 15, 2011	Geotechnical site investigation using hand augers, tube samplers, and vane shear device
August 2, 2011	Cone penetration testing. Measure embankment density.
August 24-27, 2011	Geotechnical site investigation using hand augers and tube samplers. SASW Geophysical Investigation.
September 12-13, 2012	Cone penetration testing.

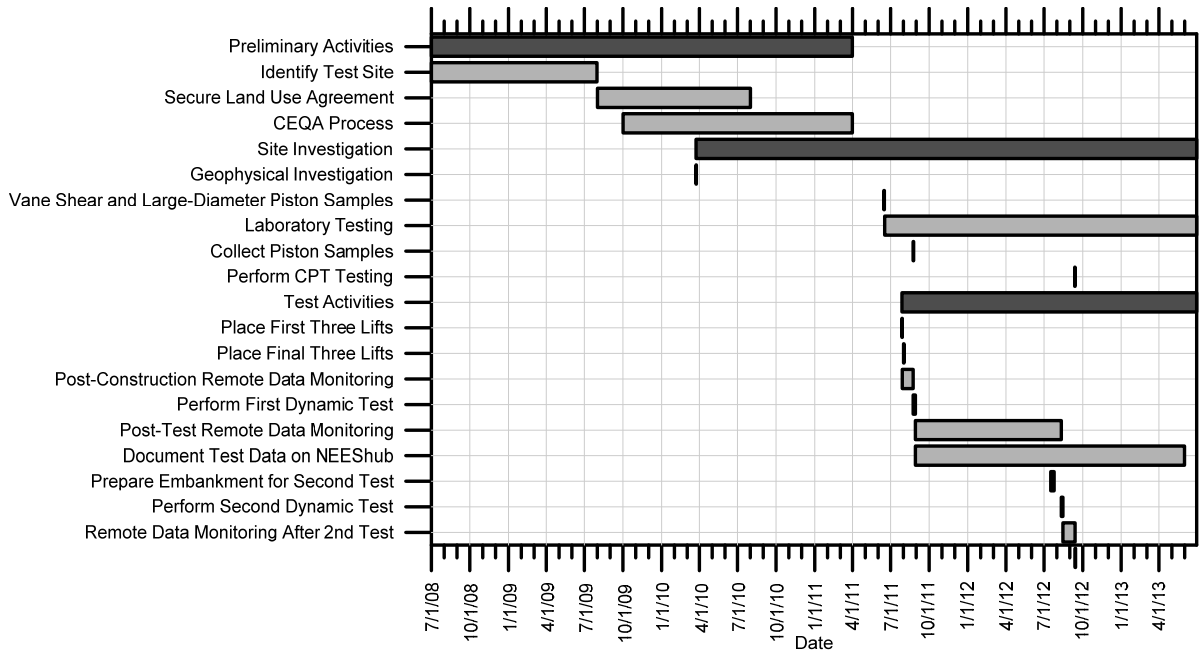

Figure 3.1: Project schedule.

3.1. Site Identification and Selection

The project schedule, shown in Fig. 3-1, has the project activities broken up into three broad categories: “Preliminary Activities,” “Site Investigation,” and “Test Activities.” Of the Preliminary Activities, one of the very first tasks of this project was to select an appropriate site for destructive cyclic field testing and obtain permission from the State of California to use the site for research purposes. Michael Driller, a Senior Engineer at the California Department of Water Resources (DWR), was a collaborator in this project and was involved in the coordination between the UCLA project team and the State of California in finding a site appropriate for destructive testing. Other DWR employees that assisted in the coordination of a site included Bryan Brock and Frank Glick, CEG.

Initially, one of the goals of this project was to perform the shake testing on an unused levee founded on peaty organic soil in the Sacramento Delta or nearby Suisun Marsh that the project team could potentially damage and subsequently repair. With that in mind, a site investigation of the unused levee at the Blacklock site in Little Honker Bay, located in the Suisun Marsh, commenced in March 2009. Levees at the Blacklock site had been deliberately breached to create tidal wetlands, and therefore was ideal from a land use perspective because damage to the levees would not have adverse consequences. The purpose of this site investigation was to determine if the levees were founded on top of peaty organic soils. One hand auger boring was advanced from the top of the levee crest into the underlying foundation soils. By visual inspection of the hand auger tailings, the foundation soils of the Blackrock levees were determined to be mostly soft clays resembling Bay Mud with a small amount of fibrous organic material (Fig. 3.2). Ash content testing (ASTM D2974) performed at Cal Poly further confirmed that this soil was not peaty organic soil (Fig. 3.3).

Figure 3.2: Foundation soils from 12' depth below levee crest at Blacklock site.

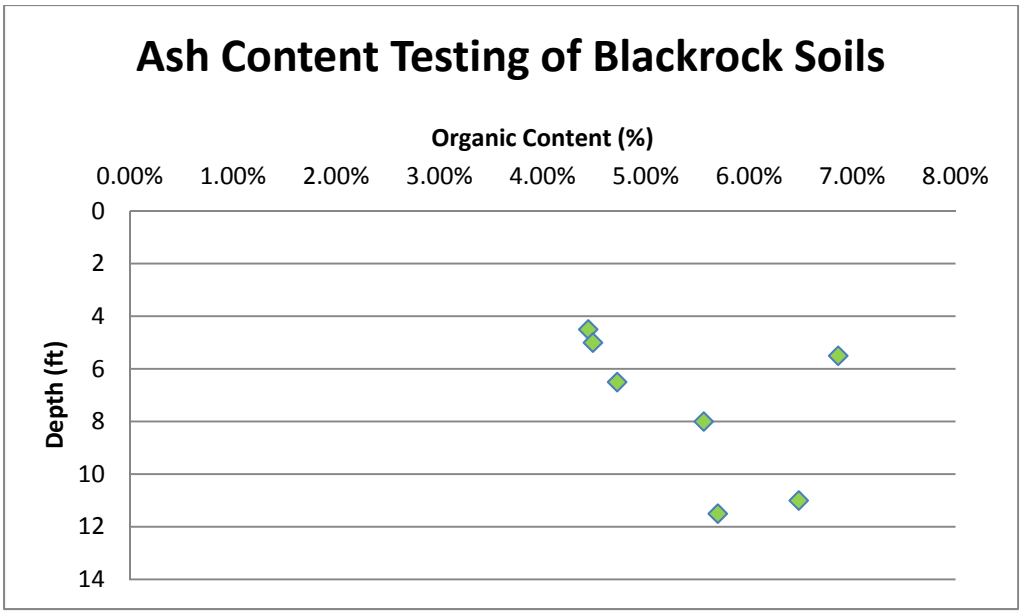

Figure 3.3: Ash content testing of Blackrock site soils.

After the Blackrock site investigation, the project team focused its efforts on finding a new site to perform the shake testing. After a period of a few months, the project team decided that a suitable existing levee site did not exist. A meeting with the California Department of Water Resources (DWR) was held, where the new plan of constructing a model levee on the peaty organic soil on one of the Delta Islands was proposed. Likely candidates included Sherman Island, Twichell Island, Prospect Island, and Dutch Slough. The project team and the DWR personnel decided to focus their attention on constructing a model levee on the interior of Sherman Island, on land which is owned by DWR. After identifying the site, a three-way land use agreement was initiated by the project team among UCLA, DWR, and the Sherman Island Reclamation District 341. Furthermore, the process of compliance with the California Environmental Quality Act (CEQA) could begin. Overall, these preliminary activities required a significant amount of time in the project schedule because of the difficulties in identifying a suitable test site, and because the site selected by the project team was determined to be a

jurisdictional wetland by the US Army Corps of Engineers. The site is also a habitat to several endangered species, such as the California Garter Snake and the Burrowing Owl, and the presence of these species at the test site initiated a complex permitting process. Because of these reasons, site investigation and testing activities did not start for roughly two years after the project's start date.

3.2. Sherman Island Geophysical and Site Investigations

Once the project team had identified and selected a site to begin investigation and testing, work could begin. As seen in Table 3.1 and the project schedule in Fig. 3.1, the project team conducted five geophysical and/or site investigations at the Sherman island site. Initially, the team conducted a site visit and geophysical investigation on Sherman Island to measure geophysical properties required to estimate impacts of the proposed testing activities on nearby levees. As the project progressed, additional site investigations were performed to obtain tube samples suitable for laboratory testing, and measure cone penetration resistance. This section summarizes the findings from each of these site investigations.

3.2.1. March 2010 Geophysical Investigation

The results presented in this section were adapted from Brandnberg et al (2010). for use in this dissertation.

On March 24, 2010, the project team made geophysical measurements on Sherman Island to identify tolerable vibration amplitudes and spatial attenuation of vibrations for the upcoming study. The vibrations recorded during the geophysical investigation had very small amplitude resulting either from ambient sources (i.e., sources already at the site such as traffic, wind, waves

crashing on levees in the adjacent waterways), or from active sources such as a person jumping up and down or striking a plate with a sledgehammer. Adequate metadata were not recorded to archive the data on NEEShub, but the key results are nevertheless presented here.

Measurements were made at two different sites: Site A is on the interior of the island on land currently used as a cow pasture, and site B is on the levee beneath the Antioch Bridge (Fig. 3.4). The goals of the geophysical study were to (1) measure the shear wave velocity of the peat, (2) quantify attenuation of seismic waves with distance from a source, and (3) quantify ambient vibrations (e.g., due to traffic, waves, wind, etc.) on the levees to identify a lower bound for safe levels of shaking.

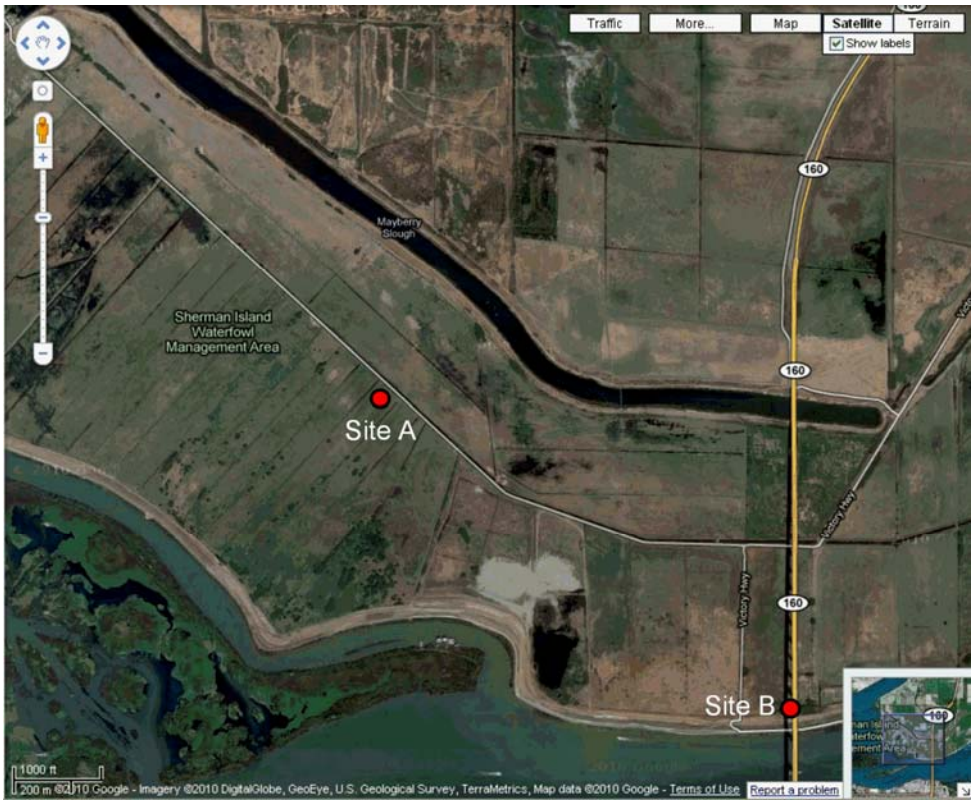

Figure 3.4: Sites on Sherman Island where geophysical measurements were made on March 24th, 2010.

Two different experimental setups were utilized to make the geophysical measurements (Fig. 3.5). At Site A, four accelerometers were aligned in a linear array spaced at 7.6m (25ft*)* intervals. The accelerometers were shallowly embedded in the peat soil to provide coupling between the soil and the sensors. Active vibrations were generated by either striking a steel plate with a sledgehammer, or by a person jumping on the surface of the peat. Active vibration is useful for measuring travel time of waves between adjacent sensors and attenuation of wave amplitude with distance from the source. Multiple measurements were made for each experimental configuration to develop a sense for the repeatability and quality of the recorded data. Following active vibration, ambient vibrations were recorded for a period of 5 minutes during which time none of the researchers walked near the sensors. Ambient vibration measurements quantify the steady vibrations that are constantly propagating through the peat due to waves, wind, and other ambient sources.

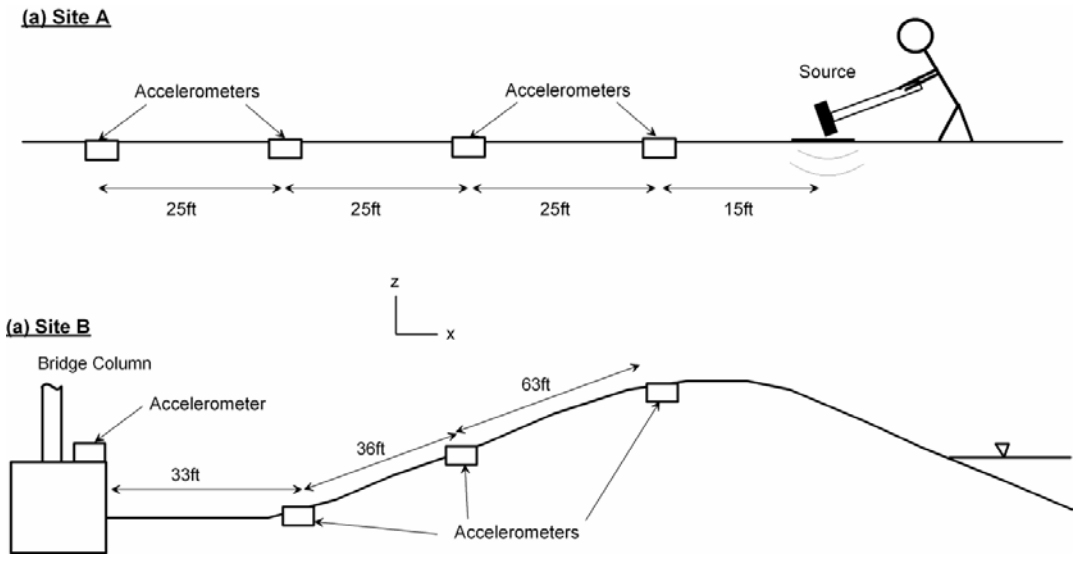

Figure 3.5: Experimental setups utilized at the two sites (sensors drawn much larger than actual size for clarity).

At Site B, the accelerometers were aligned in a linear array with one accelerometer placed on the foundation for the Antioch Bridge column, and three accelerometers placed on the levee slope. One of the accelerometers was placed at the top of the levee, just off the levee road. Ambient vibration measurements were made for a period of 10 minutes. Site B was selected because of the potential for ambient vibrations induced by the bridge due to cars and trucks driving past and propagating waves downward through the bridge columns. Presumably, these ambient vibration levels are safe since they are constantly present at this section of levee, and the ambient vibrations were therefore useful for us to determine tolerable levels of vibration from the experimental study. Following measurement of ambient vibrations, the project team drove a car on the levee road and recorded typical traffic vibrations. Furthermore, a person jumped up and down repeatedly on the crest of the levee within a few feet of the sensor to record those vibrations.

The recorded acceleration records were integrated in time to obtain velocity records for the purpose of determining arrival times of the generated waves. It is thought that velocity is a more relevant parameter than acceleration because it is the most commonly utilized ground motion measure for monitoring construction vibrations and their effects on adjacent structures (e.g., Dowding 1996). The source produces a mix of different wave types, with the predominant types being downward propagating p-waves and horizontally-propagating Rayleigh waves. Measurements of Rayleigh wave velocity, which is slightly lower than shear wave velocity (Kramer 1996), were desired. Prior to integrating the recorded acceleration records, the mean acceleration value was subtracted from each record, and the records were band-pass filtered to remove low-frequency drift and high-frequency noise. Another benefit of utilizing velocity records instead of acceleration records is that the undesired high-frequency p-wave arrivals have

much lower velocity amplitude than the desired Rayleigh wave arrivals, but the acceleration amplitudes can be quite similar for the p- and Rayleigh waves. It is often difficult to make an accurate travel time pick when p-wave arrivals and Rayleigh wave arrivals both have significant amplitude, hence velocity is better-suited to making travel time picks than acceleration for this data. Fig. 3.6 shows the velocity records obtained from a person jumping on the ground surface at a distance of 15 ft from the first accelerometer in the linear array at site A. The same data is plotted in two different ways; the left column shows the velocity traces scaled such that the waveforms appear to have the same amplitude, which is useful for making travel time picks, and the right column shows the velocity traces plotted at the same scale, which is useful for visualizing attenuation of wave amplitude with distance. The time at which the person's feet hit the ground is not known because the sensors were triggered manually, but the source timing is not required to measure Rayleigh wave velocity since we are examining differences in travel times from one receiver to the next.

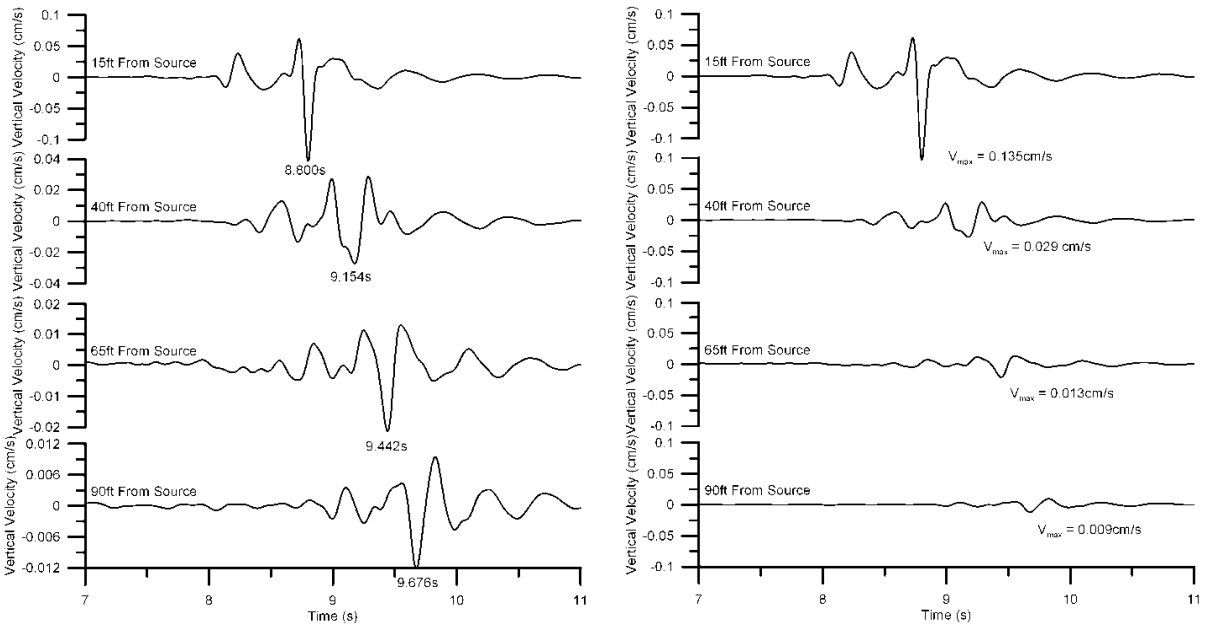

Figure 3.6: Recorded velocity records and travel time picks for Rayleigh wave velocity determination.

The waves produced a signature downward spike in the vertical velocity records that was used for travel time determination. The downward spike arrived at the first sensor at a time of 8.800 seconds, and the last sensor at a time of 9.676 seconds. The travel time of the Rayleigh wave from the first sensor to the last sensor is 9.676s - 8.800s = 0.876s, and the distance between these sensors is 75ft. Therefore, the Rayleigh wave velocity is 75ft / 0.876s = 85.6 ft/s = 26 m/s. This wave velocity value is extremely low compared with typical soils such as sands or even soft clays, but is reasonably consistent with the observation that the peat soils are very soft and compressible, and is close to suspension logging measurements made in free-field peat on Sherman Island (GeoVision 2000). Repeating this process for each combination of travel times between sensors, and for multiple records of different source excitations produces Rayleigh wave velocity estimates in the range of 21 m/s to 33 m/s. Shear wave velocity is slightly higher than

Rayleigh wave velocity for typical Poisson ratios for soil. Therefore, a reasonable rough estimate of average shear wave velocity for the peat at Site A is about 30 m/s.

The soil at Site A is dispersive, which can be seen by observing that the frequency content of the high-amplitude spike decreases with distance from the source faster than the low frequency content. At small strain levels, soil is often considered to be a visco-elastic material, and any material that exhibits viscous damping is dispersive and attenuates high-frequency waves more quickly with distance than low frequency waves. Frequency content must therefore be considered when using geophysical measurements to predict attenuation for the field test. Ideally the geophysical measurements would have the same frequency as the large-scale vibrations during testing to minimize assumptions that must be made to estimate attenuation. Fig. 3.7 shows the Fourier amplitude spectrum for the closest velocity record in Fig. 3.6 (i.e. 15 ft. from the source). The predominant frequency of the motion is about 2.6*Hz*, which coincides very well with the range of frequencies used in the MK-15 shaking of the test specimen. Therefore, the geophysical measurements are appropriate for estimating attenuation that occur during the shaking program because the frequencies are so similar.

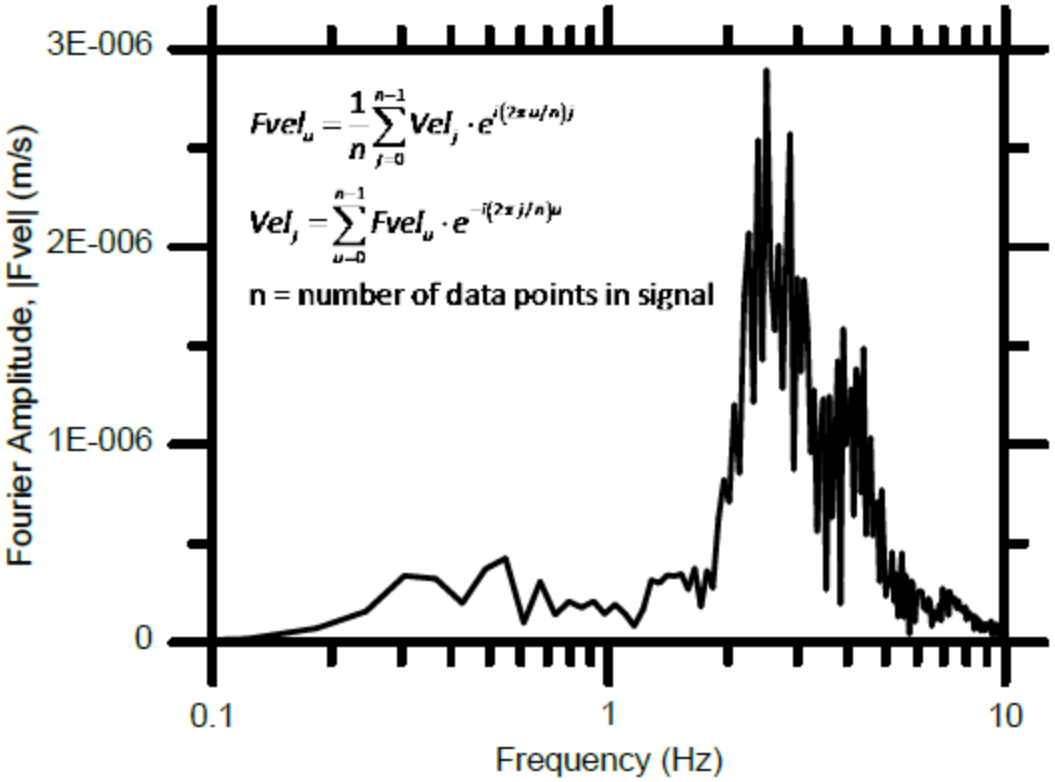

Figure 3.7: Fourier amplitude spectrum for the velocity measurement 15ft from the source in Fig. 2.3.

Attenuation of wave amplitude with distance from the source is clearly evident in the velocity records in Fig. 3.6. Attenuation is caused by two factors for this data: (1) geometric spreading of the wavefronts as they propagate away from the source, and (2) material damping. In this case, the wave propagation mode is best characterized as Rayleigh waves propagating along a cylindrical wavefront, and material damping is the small-strain value since wave amplitudes were in the linear (small strain) range of the soil behavior. Wave amplitude as a function of distance can be expressed using the form shown in Eq. 3-1

$$\frac{A_1}{A_2} = \left(\frac{r_2}{r_1}\right)^{\zeta} e^{\alpha(r_2 - r_1)} \qquad \text{… Eq. 3-1}$$

where A_1 is the wave amplitude at distance r_1 from the source, A_2 is the wave amplitude at distance r_2 from the source, ξ is a geometric damping term (ξ=0.5 for cylindrical wavefronts), and α is a material damping parameter.

The material damping parameter, α, was determined experimentally from the data recorded at site A using linear regression. Fig. 3.8 shows the recorded peak velocity values from waves generated by a person jumping and also from the sledgehammer striking the steel plate. A total of 10 waves were excited by jumping and 5 by striking with a sledgehammer to get a sense for the repeatability of the attenuation measurements. Each accelerometer recorded three components of ground motion. Only the vertical, z, and horizontal, x, components are discussed here. The other horizontal component, y, perpendicular to the direction of wave passage exhibited very small vibration levels, which was anticipated.

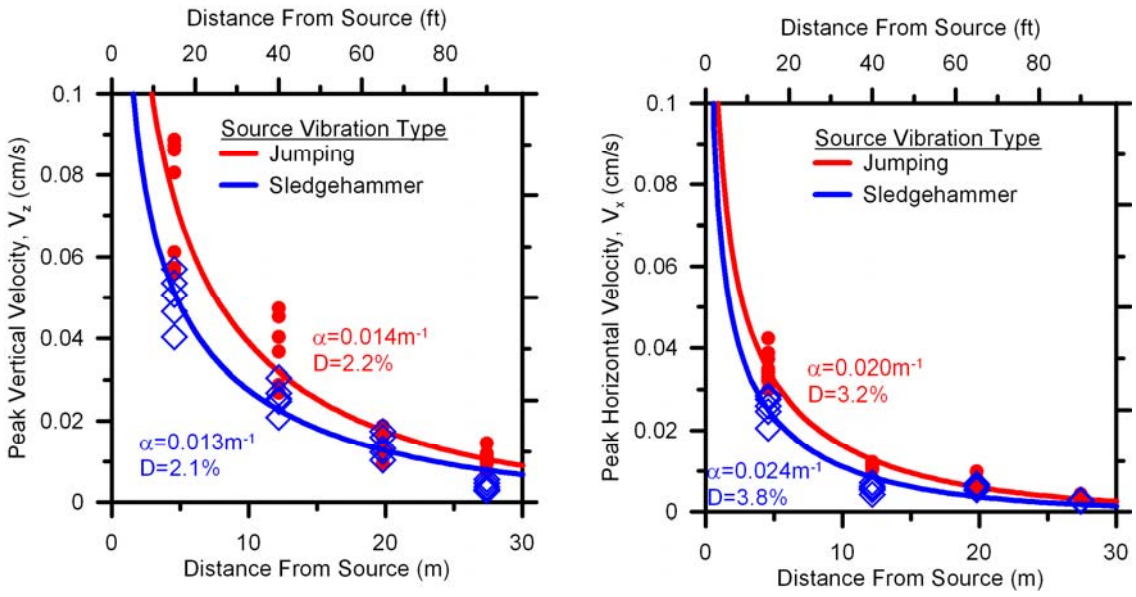

Figure 3.8: Attenuation of vertical and horizontal velocity values from Site A.

The peak velocity for each source excitation was recorded and plotted versus distance from the source (Fig. 3.8). The material damping coefficient, α, was selected to provide a least-squares fit with the recorded data. The sledgehammer strikes produced data with consistently lower peak velocity amplitude, and α values were regressed separately for different source types. For a given α, wave velocity, V, and excitation frequency, f, the percent material damping, D, can be calculated as $D = V\alpha/2\pi f$. For V = 30m/s and f = 2.6 Hz, damping values are in the range of about 2% to 4%, which agrees well with values measured from laboratory experiments on peat specimens from Sherman Island (Fig. 3.9).

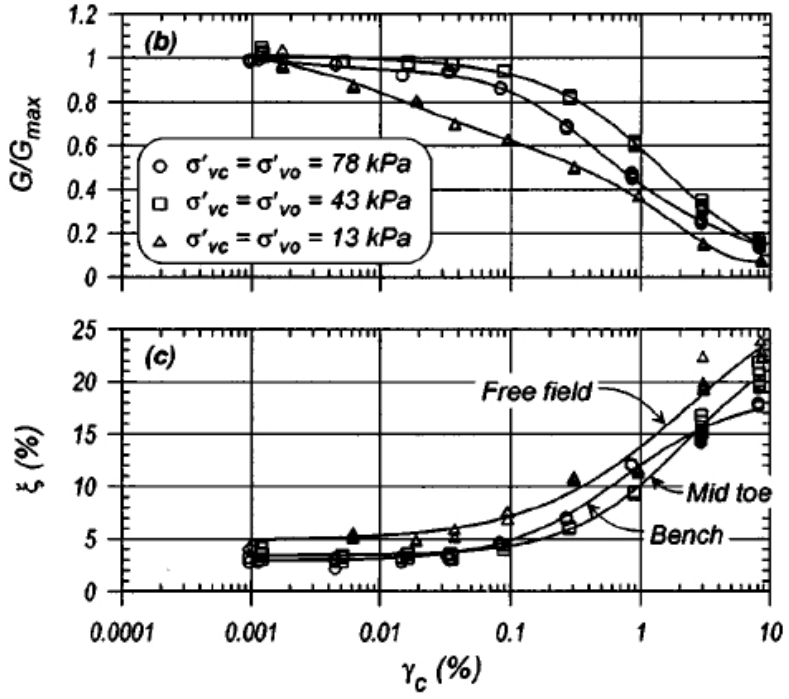

Figure 3.9: Modulus reduction and damping curves for Sherman Island peat (Wehling et al. 2003).

Ambient vibrations were measured during quiet time (i.e. with nobody walking or cars driving near the sensors) to understand the vibration levels that are constantly occurring at Sites A and B. Fig. 3-10 shows the vertical velocity records recorded at Site A, and on the crest of the levee at Site B. A few spikes of velocity are present in the record from Site A, and it is unclear what caused these spikes. On average, the levee crest at Site B exhibits slightly larger ambient vibration than the interior of the island at Site A. Peak ambient vibrations approach about $2x10^{-5}$ m/s, which corresponds to extremely small imperceptible levels of shaking based on the Caltrans vibrations manual (Jones and Stokes, 2004).

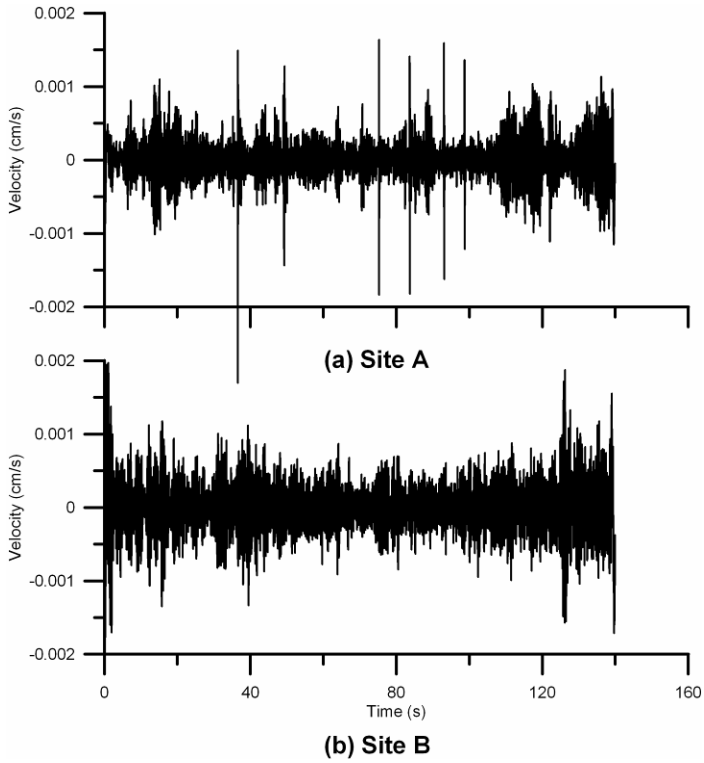

Figure 3.10: Ambient vibrations during quiet time.

Fourier amplitude spectra for the ambient vibrations are presented in Fig. 3.11. At Site A, peaks in the spectra tend to occur in the frequency range between 1 and 4 Hz, whereas at Site B some lower-frequency content is apparent. It is believed that this lower frequency content arises from the Antioch Bridge. The long columns of the bridge would be anticipated to produce relatively low-frequency vibrations.

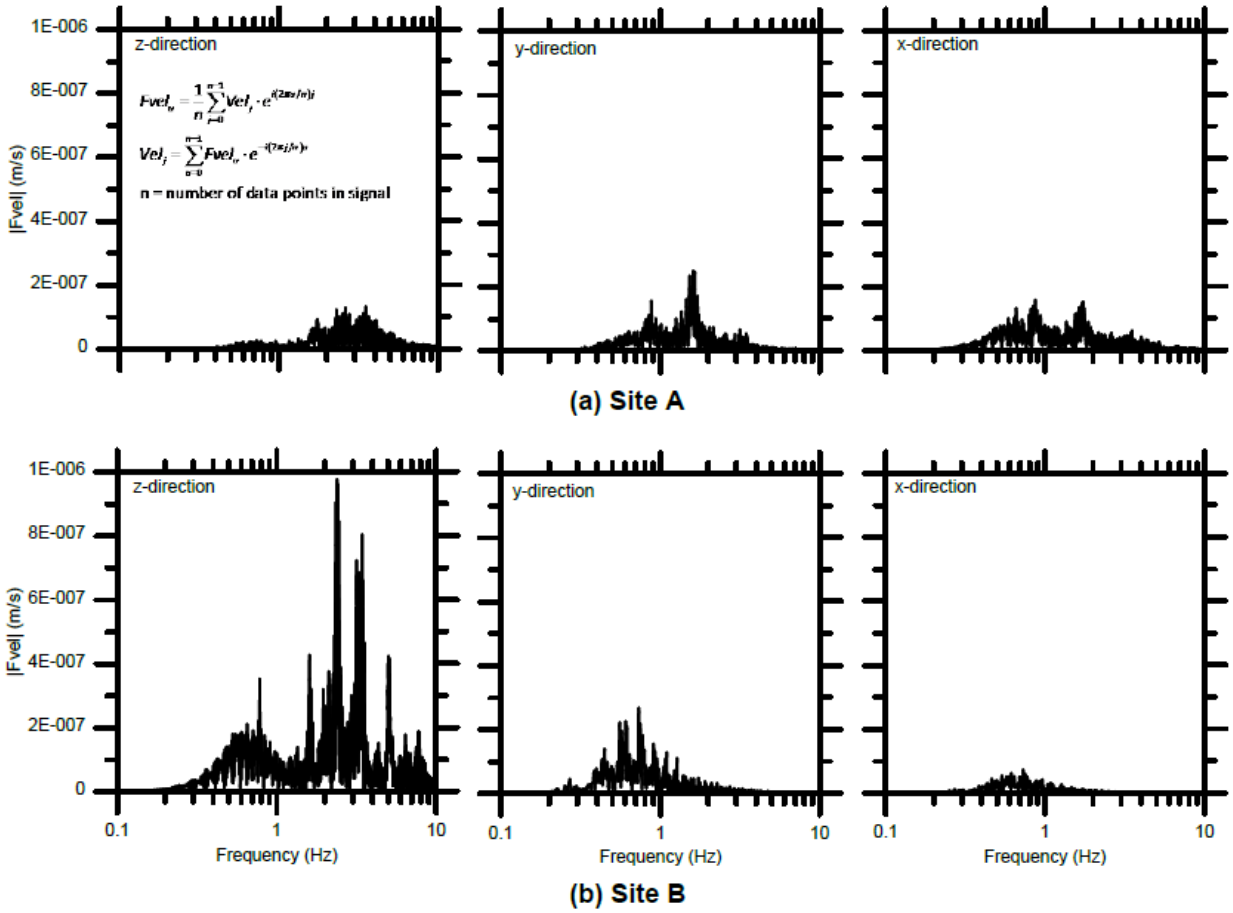

Figure 3.11: Fourier spectra of ambient vibrations during quiet time.

At Site B, vibrations were measured as a person jumped 10 times on the levee road within a few feet of the sensor, and also as we drove a car on the levee road. These vibrations are intended as ambient vibrations corresponding to common events such as typical traffic on the levee road, or construction operations. The person jumping induced vertical vibrations a bit higher than $5x10^{-3}$ m/s, while car induced vibrations at the levee crest a bit higher than $5x10^{-4}$ m/s. These levels are significantly higher than the ambient vibrations during quiet time. Vibration levels in Fig. 3.12 are believed to be well within the safe limits for the levee because

the vibration sources correspond to typical day-to-day occurrences on the levee. Hence, these measurements provide a reasonable estimate of vibration levels that are safe.

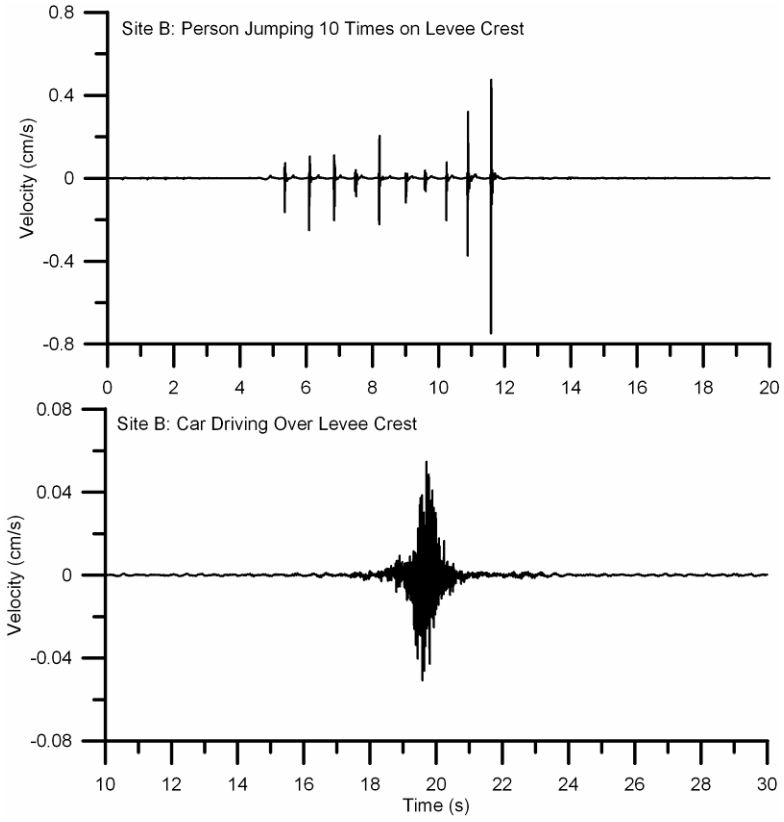

Figure 3.12: Vertical velocity on levee crest due to person jumping and a passing car.

The primary outcome of the March 24th, 2010 geophysical study was development of a safety plan for the shaking tests of the specimen. Engineers with the Department of Water Resources were concerned that shake testing could propagate waves through the peat that would reach the levees, and shake them with intolerable levels of vibration. Assuming that material damping is D=3%, excitation frequency of the shaker is 3Hz, and peak acceleration is A_{max} 0.5*g*, the source excitation function is $A(t) = A_{max}\sin(2\pi ft)$, where t is time. Velocity is the integral of acceleration in time, so the source velocity function is $V(t) = -(A_{max}/2\pi f)\cos(2\pi ft)$. Therefore,

the source velocity amplitude is $A_{max}/2\pi f = [(0.5g)*(9.81m/s^2)] / [2\pi(3Hz)] = 0.26m/s$. The shaker and test levee are not a point source, hence a reasonable reference distance, r_0 must be selected to represent the test configuration. In this case, it is assumed that $r_0 = 6m$, which is roughly half of the width of the test specimen. This selection of r_o makes sense based on the observation that waves will begin attenuating in the peat when they leave the test specimen, whereas they will be relatively constant within the specimen. The resulting velocity amplitude attenuation function is plotted in Fig. 3-13.

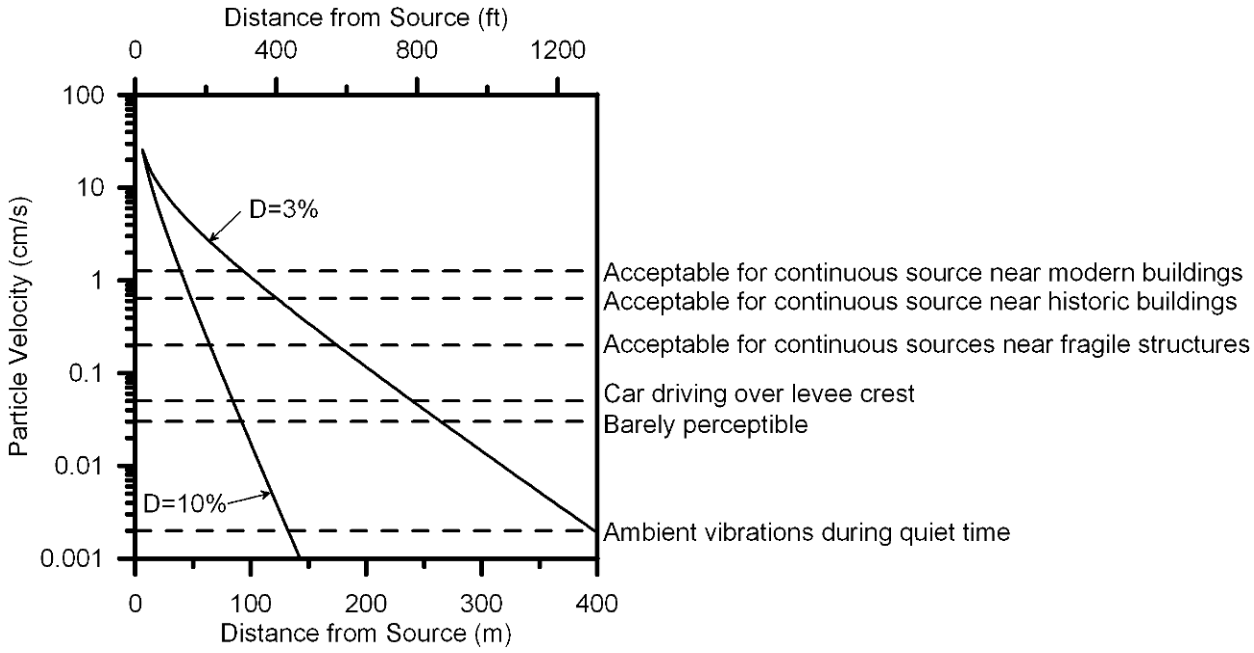

Figure 3.13: Predicted attenuation of peak ground velocity with distance from test specimen, and several measured limits for tolerable vibrations.

Superimposed in dashed lines on the on the attenuation curve in Fig. 3.13 are various vibration levels measured during the geophysical investigation, or specified in the Caltrans vibrations manual (Jones and Stokes 2004). For example, vibrations at a distance of 400ft from the test specimen are expected to be lower than those that are acceptable for historic structures, at a distance of 800ft from the test specimen the vibrations will be barely perceptible and similar to

vibrations generated by a car driving on the levee road. The Caltrans vibration manual specifies that a vibration level of 0.2*cm/s* is acceptable for continuous sources (e.g., pile driving) near fragile structures. It is thought that this measure is a reasonable tolerable level of vibration that can be induced on the nearest levee, and one can predict this level of vibration will be exceeded only at within 600 ft from the test specimen.

It is believed that the estimates in Fig. 3.13 are conservative because of the assumption that the soil behavior will exhibit its small-strain elastic response, without any decrease in shear modulus or increase in damping. In reality, the testing will induce shear strains in the soil that are larger than the small-strain elastic range. For example, if the test mobilizes shear strains approaching 1% in the near field, the equivalent material damping ratio would be expected to increase to 10% (see Fig. 3.9). Hence, a second plot is included in Fig. 3.10 showing attenuation with distance for 10% material damping. Of course, the large strains would be mobilized only in a limited region beneath the test specimen, hence equivalent material damping would vary with distance away from the source, eventually reaching the small-strain levels. Therefore, the true attenuation curve would be expected to lie between the D=3% and D=10% curves in Fig. 3.13.

The predicted attenuation results from Fig. 3.13 are plotted as a contour map on Fig. 3.14 to graphically display the anticipated vibrations caused by the test. The contour map is plotted for D=3%. Outside of the green shaded region, vibration levels induced by the test program are anticipated to be smaller than ambient vibration levels, and therefore will not be discernible above the "noise". Note that the two nearest levees lie outside of the region where discernible measurements can be made. Hence, it was anticipated that even under the strongest anticipated shaking levels imposed during our test, there would not be an increase in vibration amplitude at

the levees above the ambient levels to which they are constantly subjected. Furthermore, the infrastructure nearer to the test site would also not be affected by our test. For example, anticipated shaking levels at the cross-road would be between smaller than those that are acceptable for historic buildings. This level of shaking would not be anticipated to cause any impact to a road. Permanent ground deformations were anticipated to be roughly limited to the region immediately beneath the test specimen, and this region was re-graded following the test.

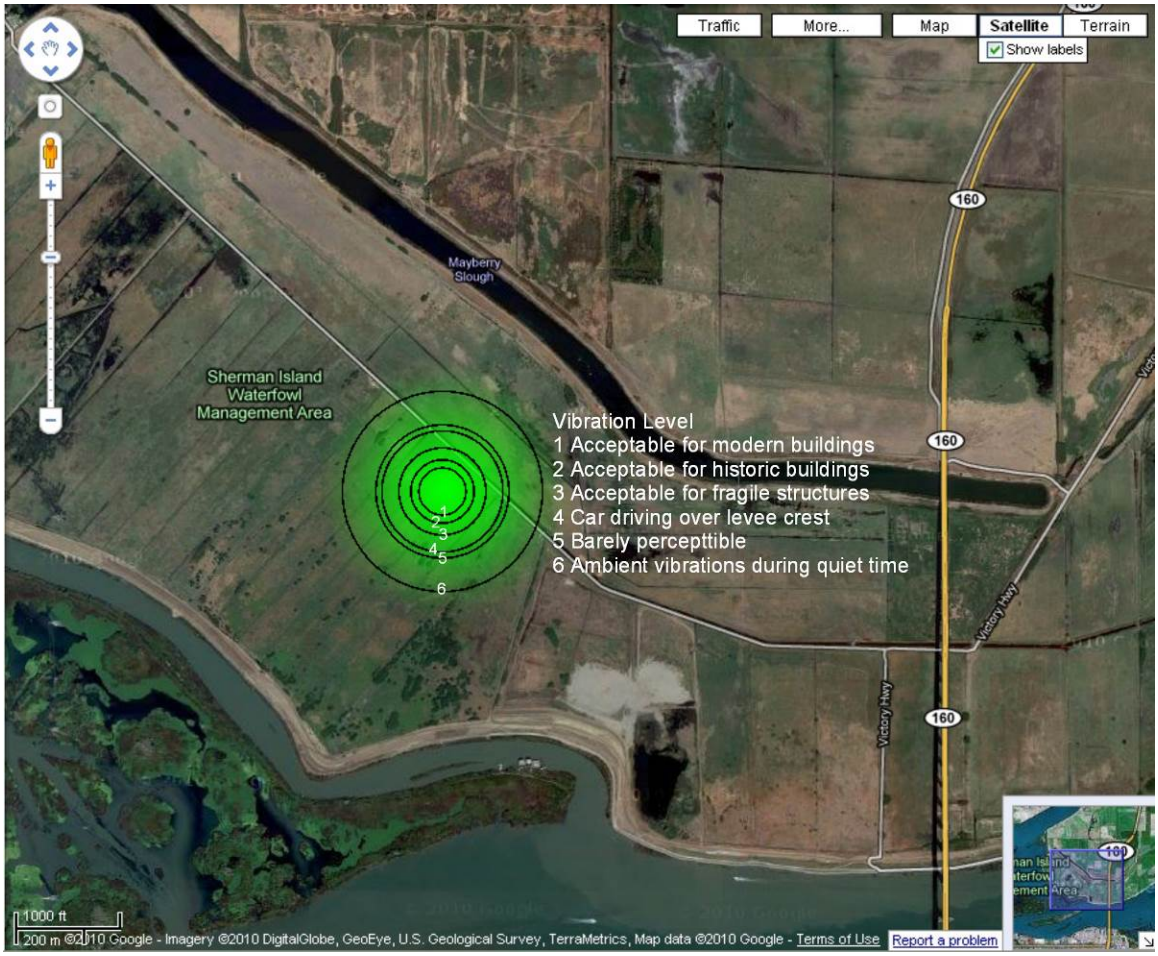

Figure 3.14: Attenuation map showing a sample test site and attenuation of velocity with distance.

3.2.2. June 2011 Geotechnical Site Investigation

On June 15th, 2011, the project team visited the site to hand auger vertical boreholes, retrieve samples, and measure vane shear strength. Hand auger borings identified the site profile to consist of dessicated peaty organic soil in the upper 1.5m over very soft, saturated fibrous peaty organic soil. The deepest boring was advanced to a depth of 3.5m, and soft fibrous peat existed to this depth. Two different hand augers were used to advance the boreholes. One was a 6 inch diameter hand auger used to collect 5 inch diameter tube samples. This equipment was borrowed from the UC Berkeley geotechnical laboratory. The second hand auger was a 3 inch diameter auger used to collect vane shear data, and construct a profile of site stratigraphy. The vane shear data utilized a small diameter Geonor H60 handheld device borrowed from Professor Daniel Pradel. The vane shear data are suspected to be an inaccurate measure of undrained shear strength because the peat is highly permeable, and water could easily be squeezed out of the peat soil. Nevertheless, the vane data in Fig. 3.15 is presented because it provides some measure of site stratigraphy. When the hand auger advanced deeper than about 3m, the borehole would squeeze shut, thereby preventing vane shear measurements. The softness of the peat soil was clearly indicated when Prof. Brandenberg was able to advance the hand auger vertically from a depth of 3m to about 4m without turning the auger to cut through the peat. He was able to simply push the auger vertically by hand. This would be inconceivable in virtually any other type of soil, including the softest clays. Laboratory tests performed on the collected tube samples included ash content and consolidation. Results of these laboratory tests are beyond the scope of this dissertation.

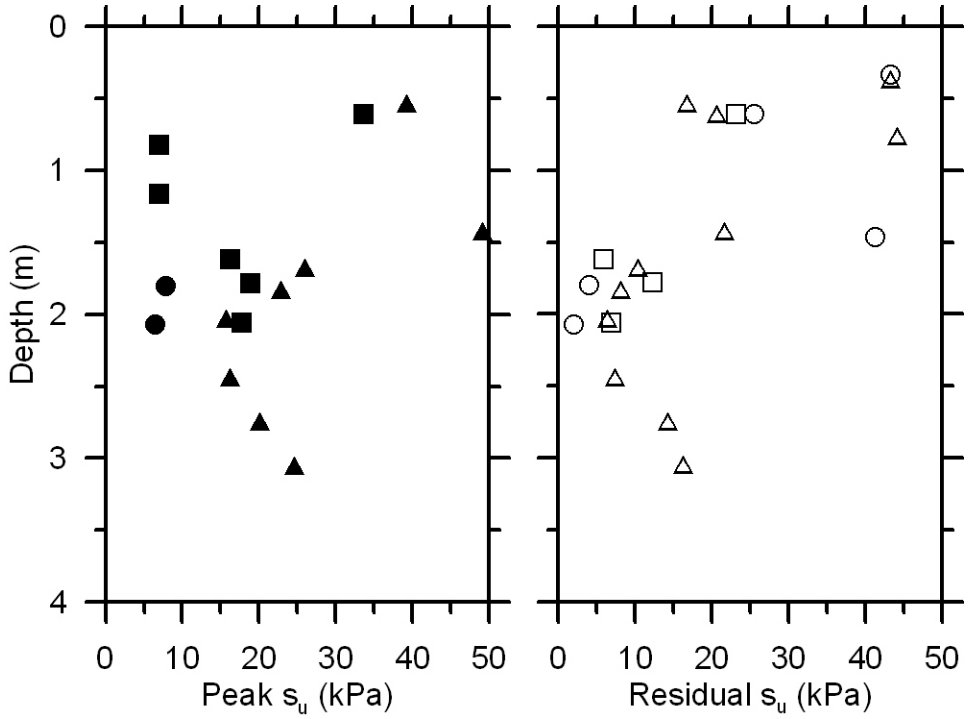

Figure 3.15: Vane shear test results. These results are likely an erroneous measure of undrained strength because of the high permeability and fibrous nature of the peat.

3.2.3. August 2nd, 2011 Investigation

The project team returned to the site in late July 2011 to construct the embankment, and coordinated with Doug Wahl, a UC Davis graduate student at the time, to perform cone penetration testing using the NEES@UCLA CPT rig. The rig was being used in Prof. DeJong's research group at UC Davis for the purpose of variable rate cone penetration testing at the time, hence researchers from his group helped with the testing. Results from this CPT sounding are presented in Fig. 3.16. The soil profile from the CPT sounding consists of organic soil to a depth of approximately 11m overlying sand. The results of the CPT sounding exhibit errors associated with a grounding problem in the data acquisition system for the load cells in the cone tip and sleeve. The grounding error resulted in erroneous measurement of negative tip resistance and sleeve friction in the peat layer. The magnitude of the errors in the data is believed to be fairly

small, but the peat is so weak that even small errors result in physically meaningless results. The data from the underlying sand layer are believed to be reasonably accurate, but it is suggested that the CPT data recorded on September 12-13 be used instead (presented in section 3.2.5).

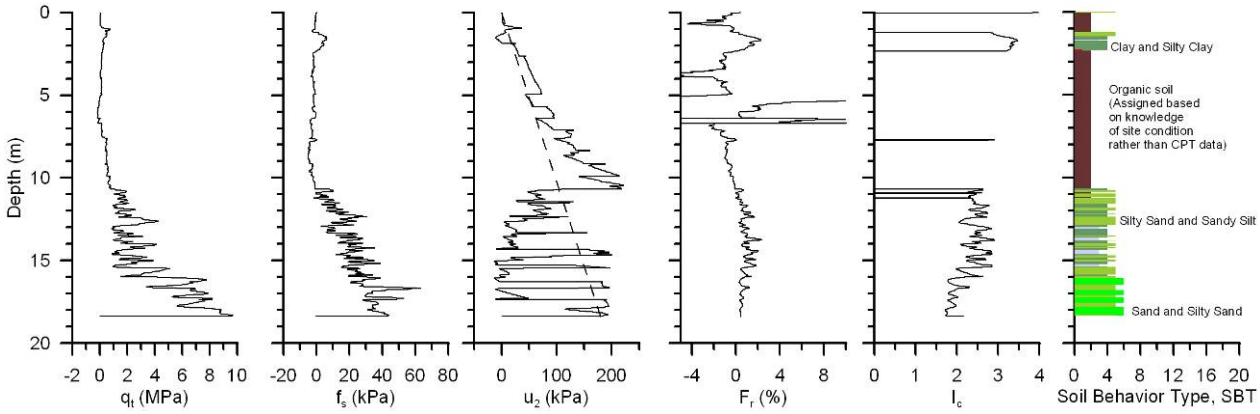

Figure 3.16: Cone penetration test sounding performed on August 2nd, 2011.

3.2.4: August 24th Site and Geophysical investigation

In late August, 2011, the project team returned to the site to perform the dynamic field test and while on site, another geotechnical site investigation was performed to collect piston samples in Shelby tubes for the purpose of cyclic laboratory testing. The piston sampler was made specifically for collecting these samples, and consists of a Shelby tube drive head manufactured by Humboldt (part number H-4202.7A), with the threaded connection modified to accept a 1" threaded steel rod. Teflon pistons, approximately ¼" to ½"thick were machined to fit inside the Shelby tubes, and were attached to a threaded rod. The threaded rod fit inside the steel pipe, and could be locked at the top of the steel pipe to prevent the piston from moving. The sampling procedure consisted of hand-augering a hole through the upper approximately 3m of peat to the depth where the peat became very soft and the borehole would squeeze shut (Fig. 3.17). The piston sampler was then lowered to the bottom of the borehole and pushed by hand

through the peat with the piston locked at the end of the Shelby tube until the sampler had reached the desired depth (Fig. 3.18). A single person could push the sampler by themselves, but typically at least two people were present to help guide the sampler to minimize disturbance. The piston was then unlocked, and the sampler was advanced by the length of the Shelby tube. Water was poured down the steel pipe on top of the piston to form a seal to provide suction to the sample, and the sampler was pulled out of the ground by hand. The Shelby tubes were kept upright at all times, and a plastic cap was affixed to the bottom and sealed with duct tape (Fig. 3.19). Molten wax was poured into the top of the Shelby tube and the tubes were stored in a bucket of water (Fig. 3.20). This sampling procedure worked extremely well, and full recovery was achieved for every sample.

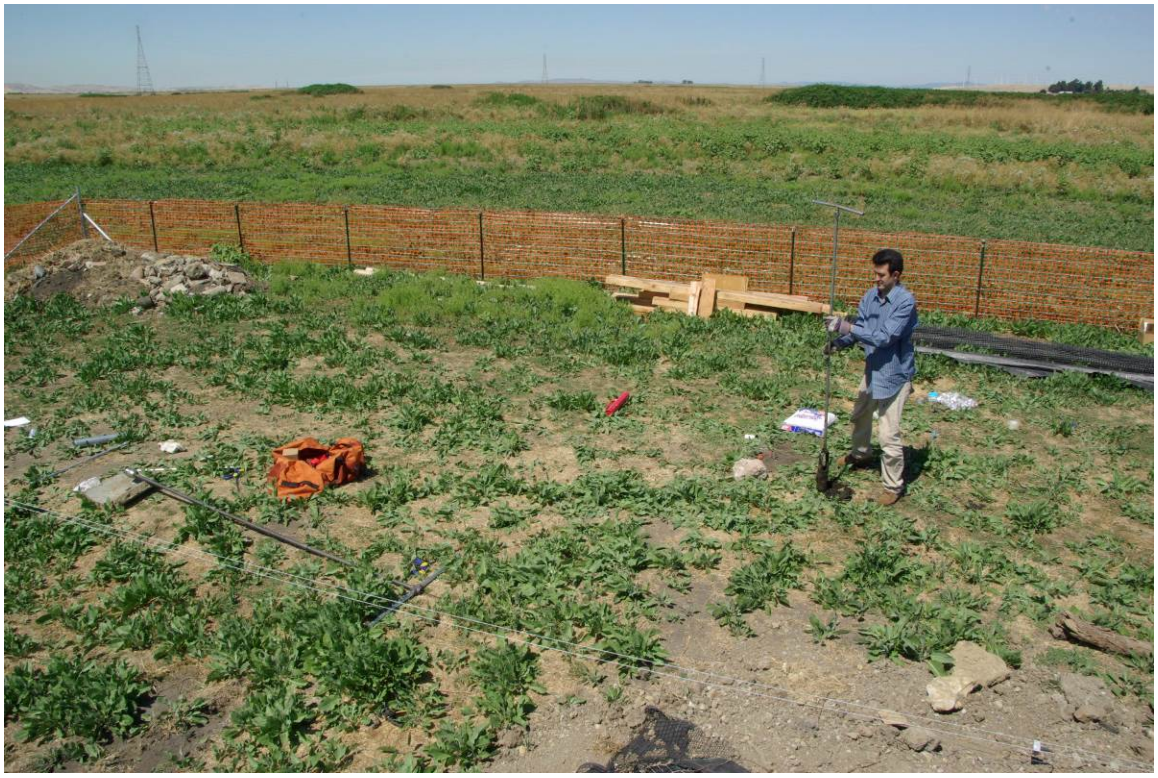

Figure 3.17: Hand augering.

Figure 3.18: Hand piston sampling.

Figure 3.19: Sample inside Shelby tube after removing piston.

Figure 3.20: Shelby tube samples stored in bucket of water with wax placed on top of specimen.

After bringing the samples back to the laboratory, consolidation testing and cyclic triaxial testing commenced, and is still ongoing. This work is beyond the scope of this dissertation. Shafiee et al. (2013) summarizes some findings from these laboratory tests.

As part of the August 24th investigation, spectral analysis of surface waves (SASW) was performed using a vertical shaker and triaxial Episensor accelerometers. Figure 3.21 shows the experimental configuration and the resulting phase velocity dispersion curve. Dispersion curves were computed using two different input signals to the shaker: (i) a fast sweep that could easily be processed in the frequency domain, and (ii) a step sweep in which the frequency was increased in 1Hz increments, and left at each frequency for 10 s to reach a steady state. The benefit of the fast sweep is that a fast Fourier transform can be computed for the entire signal, and phase lag can be computed in the frequency domain. The down side is that noise in the

signals at low frequency translates to significant measurement noise in the computed phase velocity. The step sweep signals, on the other hand, were analyzed in the time domain by fitting harmonic functions in a least-squares sense to the measured data, and computing phase lag between the curve fit signals. This approach attenuates noise by averaging, and produces a better dispersion curve at low frequency. The two dispersion curves agree very well at frequencies higher than 15 Hz, but the fast sweep dispersion curve exhibits more noise at lower frequencies. The phase velocity at low frequency under 30 m/s, which agrees well with the March 24th, 2010 study in which a sledgehammer was used as the active source. Furthermore, the phase velocity at higher frequency approaches 60 m/s, which corresponds to waves trapped inside the desiccated crust. An inversion of the dispersion curve to obtain a shear wave velocity profile was not performed, but one can infer that the upper 2m of desiccated peat has a shear wave velocity near 60 m/s, while the soft saturated peat below has a shear wave velocity near 25 to 30 m/s.

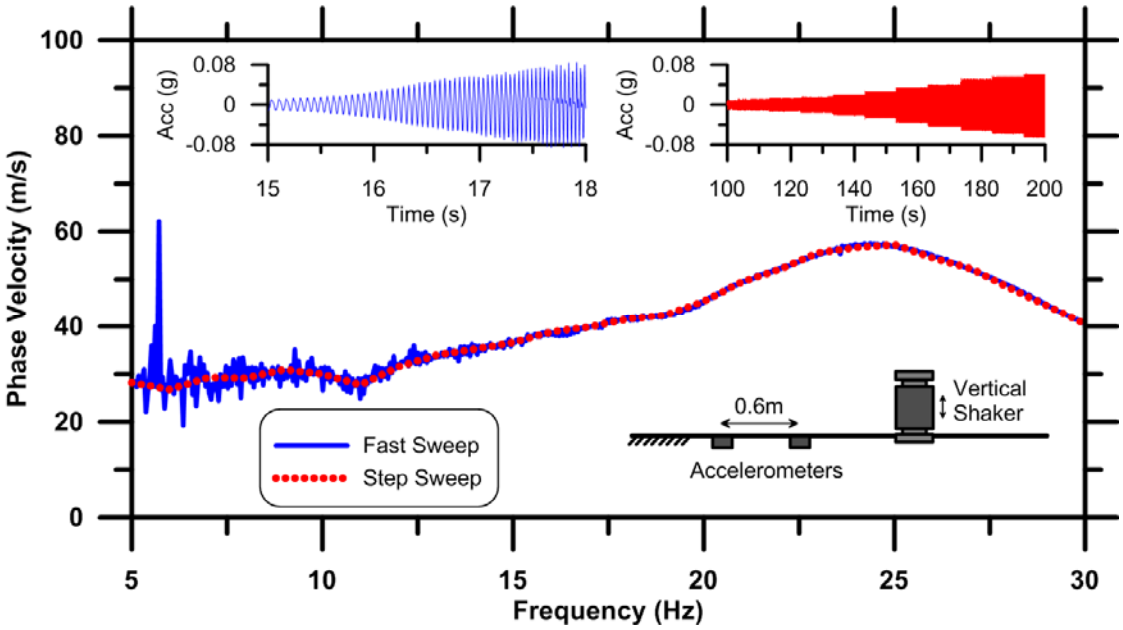

Figure 3.21: Phase velocity versus frequency from SASW analysis.

3.2.5. September 2012 Site Investigation

The cone penetration testing conducted on August 2nd, 2011 did not produce reliable data due to the grounding problem in the data acquisition system. Therefore, on September 12-13, 2012, cone penetration testing was repeated at the site. Again the UC Davis CPT rig was utilized, but this time the data acquisition system had been fixed. Chris Krage and Andrew Makdisi, both UC Davis students, operated the CPT rig. Three CPT soundings were performed during this investigation, and the results are shown in Fig. 3.22. The location where these tests were performed is shown in Fig. 3.23. The data confirm that the peat is extremely soft (the CPT rod had to be held up with pipe wrenches to prevent it from penetrating into the peat under its own weight when the grip was released to raise the hydraulic press). The soil behavior type (SBT) for the peat below a depth of 2m was generally in the "Sensitive fine-grained", "Clay – organic soil", and "Clays: clay to silty clay" regions based on the Robertson (1992) normalized SBT chart. These SBT values are not required to classify the soil as peat, but are nevertheless interesting. Furthermore, the sand beneath the peat had SBT primarily in the "Sand mixtures: silty sand to sandy silt", Sands: clean sands to silty sands", and "Silt mixtures: clayey silt & silty clay". Dissipation tests performed in the peat indicated that the time required for dissipation of 50% of the excess pore pressure (i.e., t_{50}) ranged from about 1 to 2 minutes, indicating the range of hydraulic conductivity of the peat is about 10^{-7} to 10^{-5} cm/s following the procedure given in Robertson et al. (1992). These measurements reflect horizontal hydraulic conductivity, which is expected to be much higher than vertical (e.g., Mesri and Ajlouni 2007).

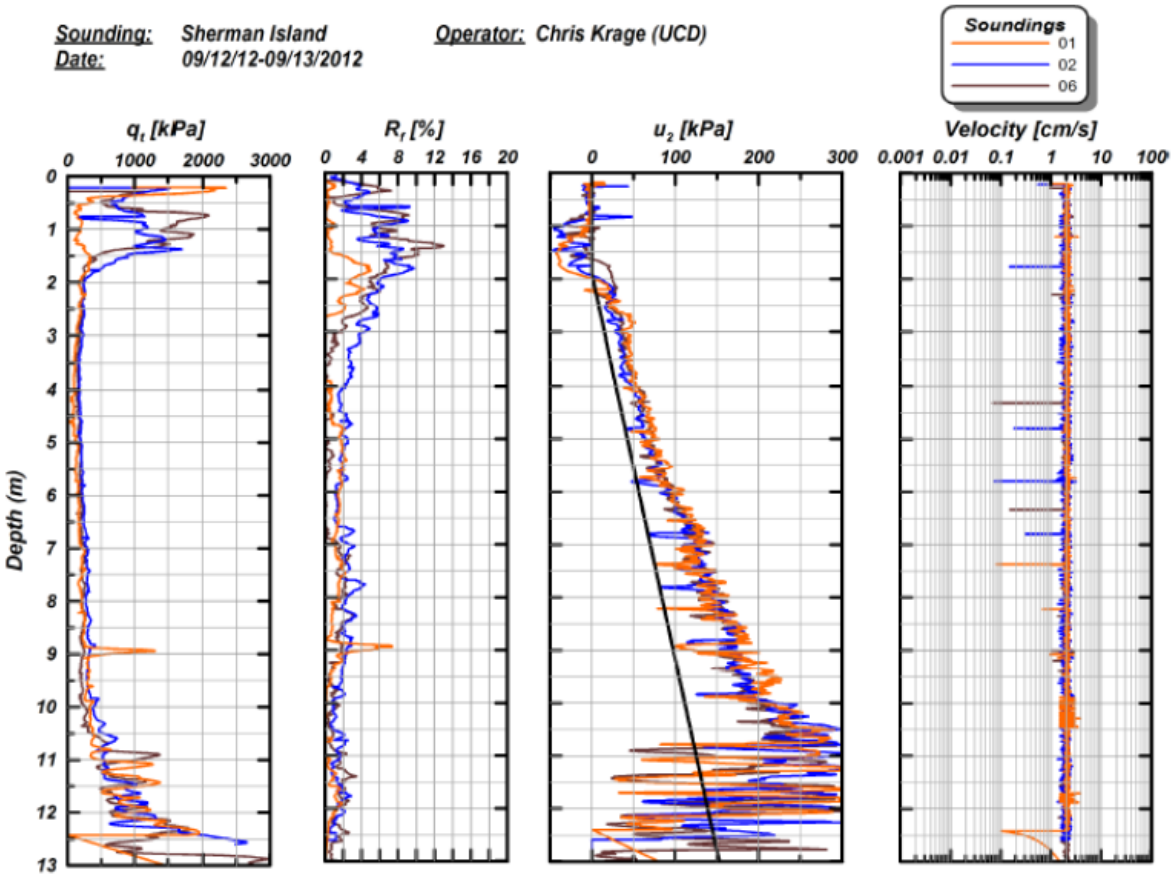

Figure 3.22: Cone penetration test results from CPT testing on September 12 to 13, 2012. Velocity refers to the speed at which the shear wave travelled from the sledgehammer to the CPT cone.

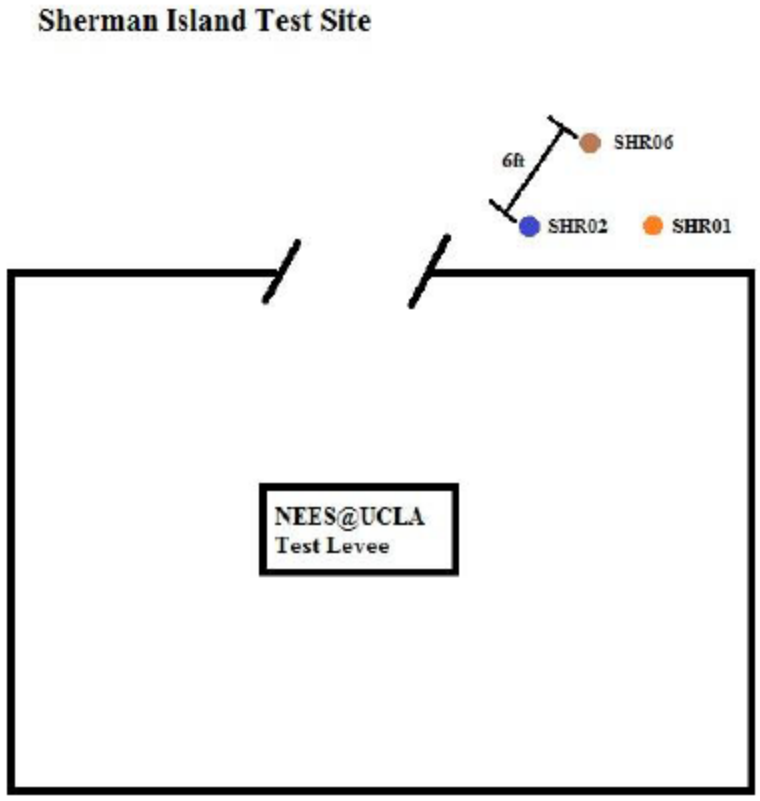

Figure 3.23: Location of CPT soundings performed on September 12th and 13th, 2012.

As part of the test, pore pressure dissipation tests were performed in the sand layer to verify existence of artesian head, which was measured in the pressure transducers embedded in the peat beneath the embankment. At a depth of 14m, approximately 12m below the ground water table, the measured pore pressure at the end of the dissipation test was 168 kPa. At a depth below the water table of 12m, hydrostatic pressure would be 120 kPa. Therefore, one can conclude that approximately 50 kPa of excess pore pressure exists in the sand beneath the peat. Furthermore, the dissipation test indicates that the soil beneath the peat has much higher permeability than the peat as excess pore pressures dissipated in a matter of seconds during the dissipation tests.

The geology at the site consists of Pleistocene sand deposits overlain by peat. The river elevation is about 7m higher than the phreatic surface at the test site, which explains the artesian head. Artesian pressures are anticipated because the sand is hydraulically connected to the adjacent river, and the surface of Sherman Island is approximately 4m below river level (sea level in this case). Artesian pressures have been observed by others, and contribute to an ever-increasing fraction of agricultural land in the Delta becoming too wet to farm (e.g., Deverel and Hart 2012). Based on the measured artesian pressures, and measured total unit weights, our interpretation is that the effective stress at the sand/peat interface is approximately zero. This is a rather startling finding that may have implications for future stability of Delta islands, but is beyond the scope of this dissertation.

3.3. Interpretation of Site Stratigraphy

Based on our site investigation and geologic history of the site, an interpretation of the stratigraphy is shown in Fig. 3-24. The site consists of Holocene peat resting atop Pleistocene sand. At the position of the model levee, the thickness of the peat is 11m, and the water table depth was 1.5-2m. Note that the groundwater level fluctuates significantly over time due to pumping from the reclamation district. The elevation of the Pleistocene sand is likely variable, but it was drawn as a straight line in the absence of better information. The elevation of the surface of the peat is approximately 4 to 5 m below sea level, and the Sacramento River and water in Mayberry Slough are at approximately sea level. Furthermore, peat deposits do not lie within the river, therefore the Sacramento River is hydraulically connected to the sand deposit underlying the peat, resulting in artesian conditions. The groundwater elevation is maintained at

a depth of 2m by pumping water through the drainage ditch, though seasonal variations are present due to alterations in pumping for agricultural reasons.

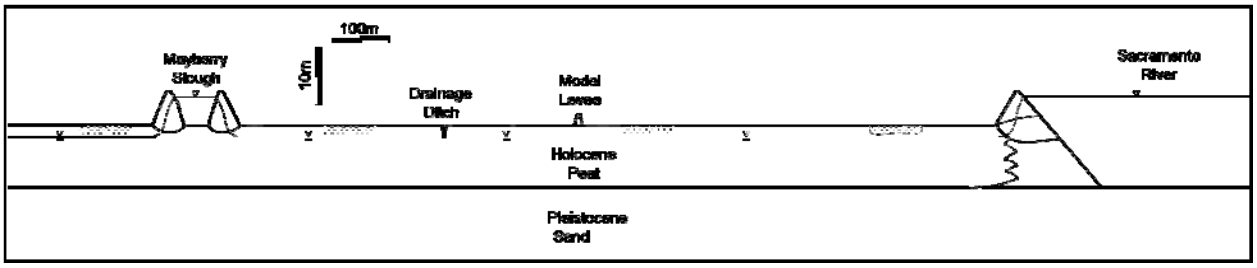

Figure 3.24: Interpreted geologic cross-section of Sherman Island location where test was performed (vertical scale exaggerated x10).

Lab testing performed on the peat samples is ongoing, but some preliminary test results were presented by Shafiee et al. (2013). Combining these preliminary lab test results with measurements of shear wave velocity and our interpreted stratigraphy, one may arrive at the interpreted geotechnical profile in Fig. 3.25:

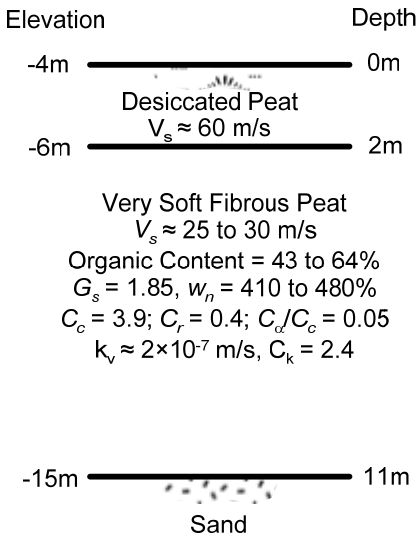

Figure 3.25. Interpreted geotechnical profile. Lab test values from Shafiee et al. (2013)

Chapter 4. Model Levee Design, Construction, and Testing

This chapter explains the design, construction, monitoring, and shake testing of the Model levee on Sherman Island, as well as the collection and archiving of data from the tests. The first section will go over how the model levee was designed: which criteria were chosen for the design, how the shaker base was designed, as well as what materials were to be used in the levee. The next section will describe how the model levee was constructed, repaired in preparations for the 2011 shake tests, and how the project team was able to monitor long-term settlement and pore pressure dissipation. Next, I will describe the shake testing of the model embankment: how it was instrumented, which data acquisition systems were used, what types of motions were imposed, and how the forces input into the test levee were calculated. Finally, this chapter will cover how the data was processed and archived on NEEShub, a major component of this project.

4.1. Model Levee Design

The first set of tasks for the field testing of the model levee involved designing the model levee and shaker base to achieve certain design objectives. A significant portion of this project's work was the design and construction of the test embankment on Sherman Island. Since the purpose of this experiment was to simulate a fairly large earthquake on a Delta levee founded on peat soil, much of the design needed to consider the stresses that would be imposed on the peat from the MK-15 shaker. Additionally, since the test embankment needed to include a shaker base to mount the MK-15 shaker, much of the design also focused on determining the horizontal force that the embankment could sustain from the cyclic loading as well as any reinforcement that

would be needed to make sure the model levee could transmit the imposed forces into the underlying peat.

4.1.1. Design of Model Levee and Shaker Platform Dimensions

Design of the model levee and shaker frame consisted of an analysis of the cyclic stress ratios (CSR) that would be developed in the peat during shaking given an assumed levee geometry and force amplitude, and analysis of the maximum passive pressure that would develop on the embedded shaker base. From these analyses, the project team could then provide specifications of the levee geometry and shaker base dimensions for construction and estimate the maximum force that could be imposed on the levee.

The first step in designing the model levee consisted of developing initial dimensions of the levee to be tested, as well as dimensions of the platform with which to mount the MK-15 shaker upon. Once these dimensions were developed, analyses were performed to estimate the capacity of the levee and the shaker frame to withstand horizontal loading. Figure 4.1 shows the initial schematic used to design the dimensions of the levee and the shaker frame. This figure shows a section of the proposed model levee, with 2:1 side-slopes. In this instance, the goal was to determine the height H of the shaker base (indicated in gray) and the length of the bench (given as nH) to develop maximum passive pressure during the horizontal loading.

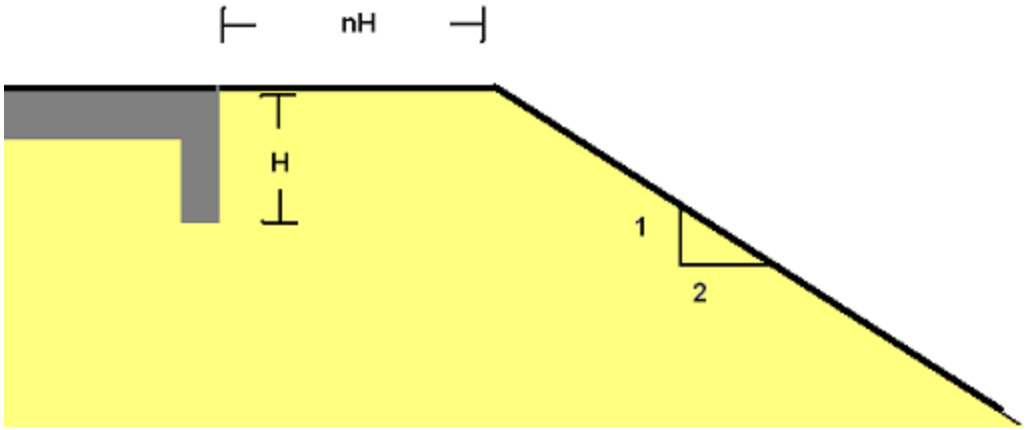

Figure 4.1: Initial embankment configuration for passive pressure design.

In order to estimate the capacity of the embankment's passive pressure, the levee and shaker frame were modeled using the PHASE2 finite element program. Figure 4-2 shows a close-up of the mesh used in the analyses. In this figure, one can see three materials used: the yellow material indicates the backfill, which was assumed to be clean sand with a friction angle of 40^{o} and a density of 1900 kg/m^3 (120 pcf). The gray material was initially assumed to be concrete, with a density of 2400 kg/m^3 (150 pcf). The green material was also modeled to be the clean sand, but at a friction angle that represented the interface friction angle between the shaker base and the soil. The passive pressure was then computed by imposing a static displacement on the outer edge of the shaker base and then measuring the normal stresses along the wall-soil interface. Figure 4.3a shows a deformed mesh with displacement contours for a 0.91m (3 ft) deep shaker base, while figure 4.3b shows the undeformed mesh with stress contours. Note in Fig. 4.3b the high normal stresses at the toe of the shaker base. This high stress concentration is due to the sharp corner at the base of the stiff material, and this was corrected in later analyses. In order to verify these results were adequate, the passive pressure of the deformed wall was compared to the passive pressure computed using the log-spiral passive pressure formulation, as

seen in Fig. 4.4 for the 0.91m deep shaker base. Despite the high stress concentration at the bottom edge of the shaker base, the results from the FEM shows good agreement with the log-spiral solution for a flat backfill.

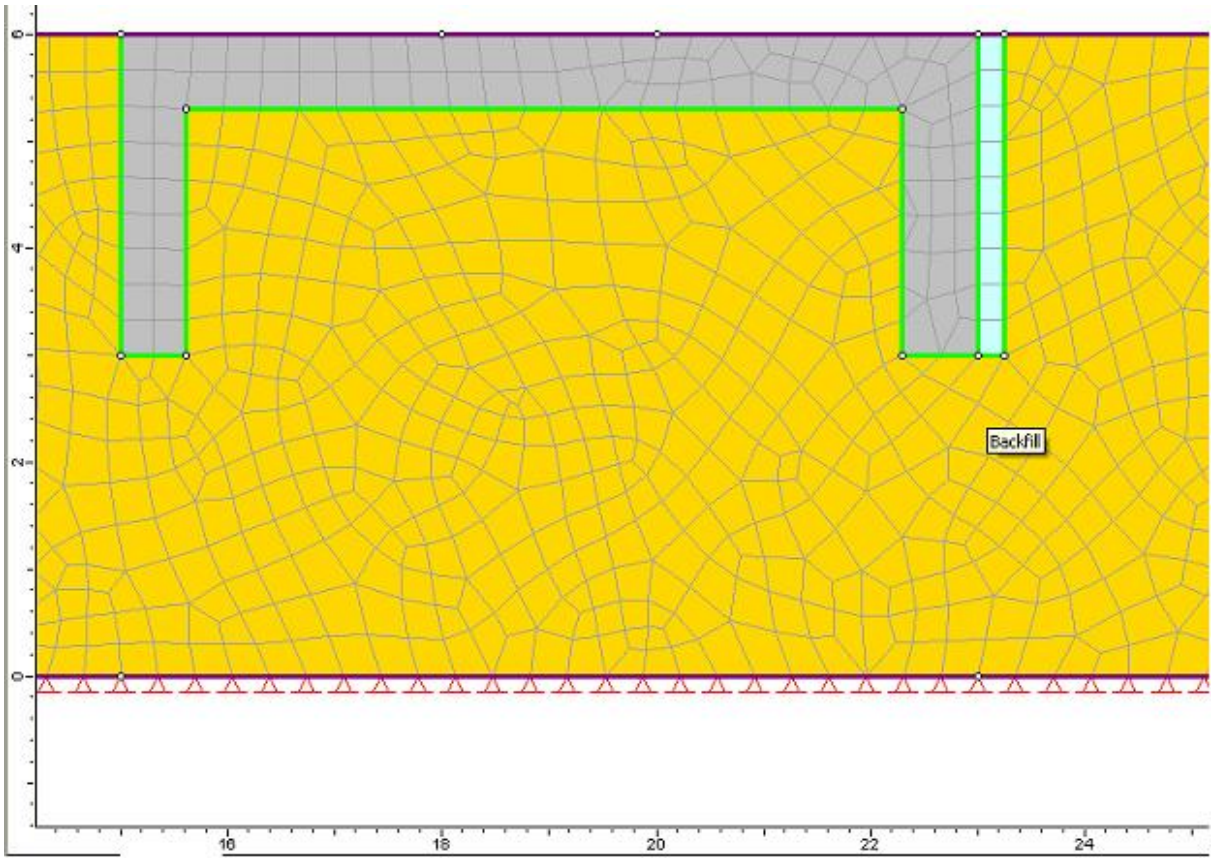

Figure 4.2: Close-up of PHASE2 mesh to model passive pressure development.

a)

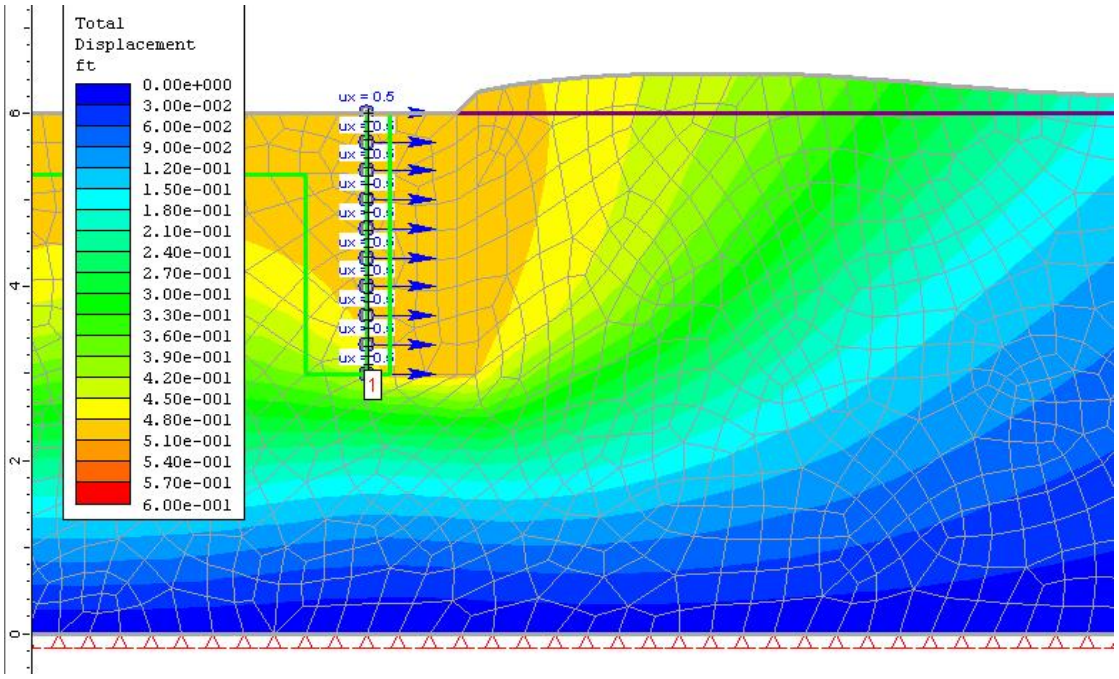

b)

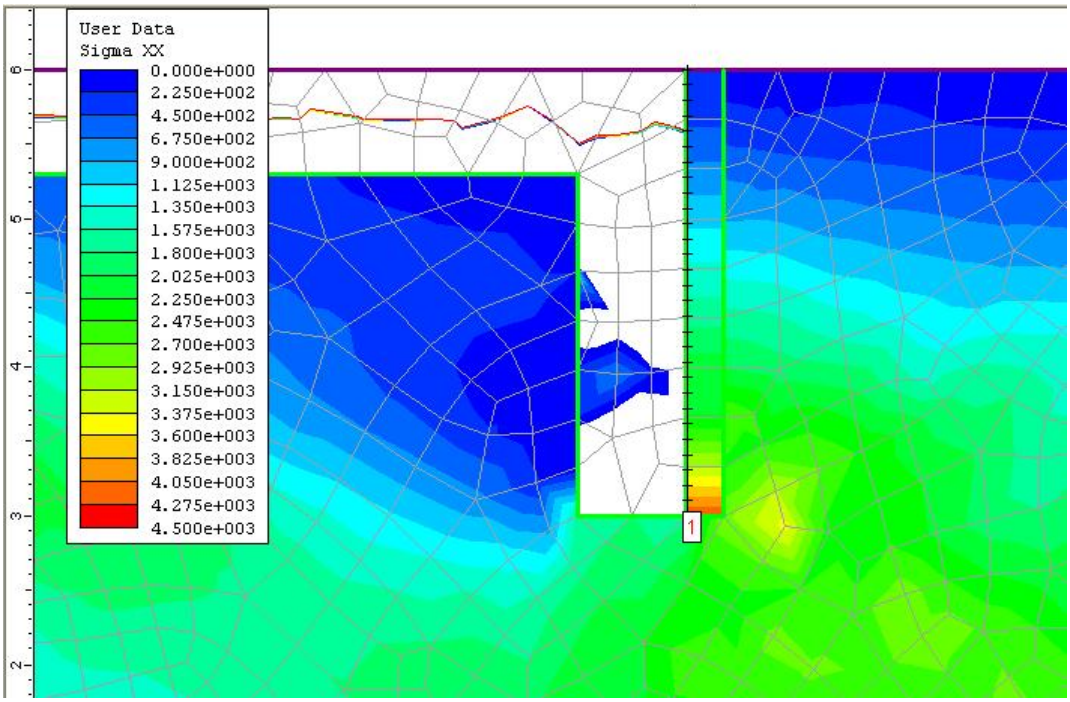

Figure 4.3: a: Deformed mesh contour to find passive pressure b: Stress contours from imposed displacement

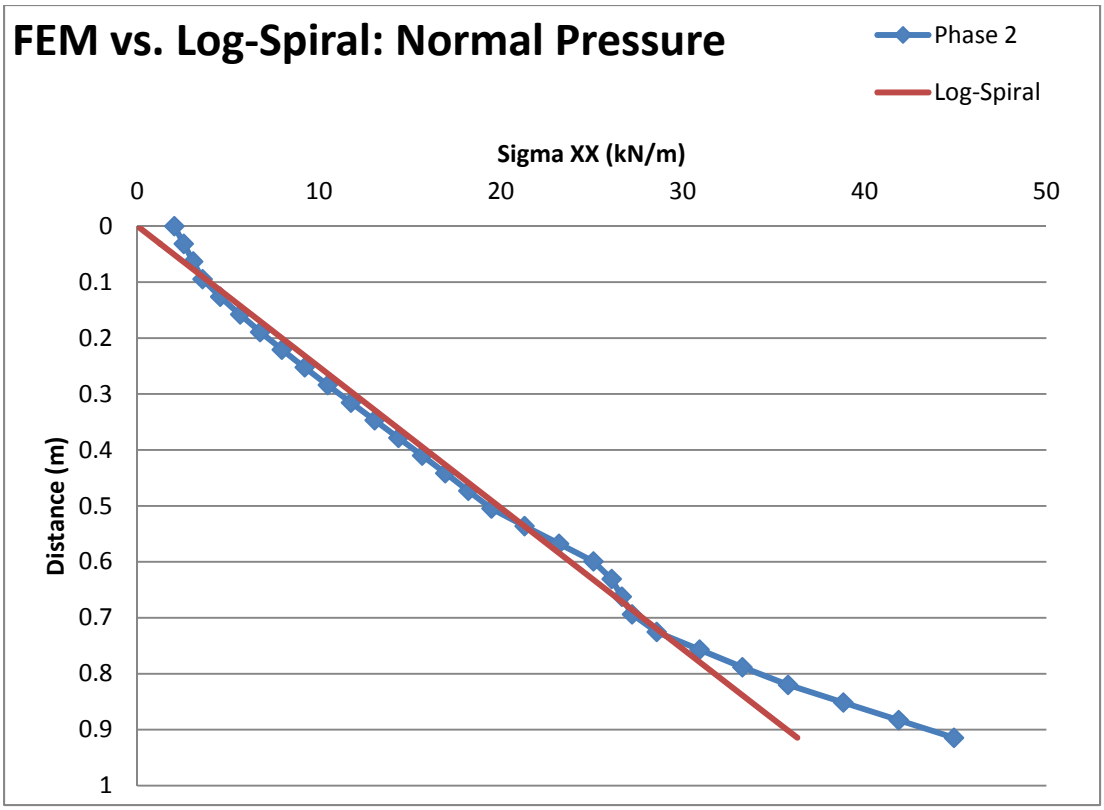

Figure 4.4: Comparison of passive pressure from Phase 2 modeling with log-spiral passive pressure.

Once the results from the FEM analyses were verified with the established log-spiral solution, the dimensions of the model levee could be developed and the passive pressure capacity could be estimated. Figure 4.5 shows the side and plan view of the initial embankment dimensions. In this case, the model levee has a base width of 12.19 m (40 ft) and a crest height of 1.83 m (6 ft) with 2:1 sideslopes and a crest width of 4.88 m (16 ft). Initially, the project team designed the model levee to have a width of 3.05 m (10 feet), but that was increased to 3.66 m (12 feet) in order to fit the MK-15 shaker. Further analyses to find the passive pressure coefficient when compared to the bench length were performed, and Fig. 4.6 shows the results for 0.61 m (2 ft) deep shaker base with an interface friction angle (δ) of 20 degrees. Assuming an

η of 2 (a 1.22 m bench length), this gives a coefficient of passive pressure K_p of roughly 5.5. Using Eq. 4.1, one can find the resultant passive force (per unit length of shaker base) to be:

$$P_p = K_p \gamma H^2/2 \quad \text{.. Eq. 4.1}$$

Where:

K_p = Passive pressure coefficient

γ = Unit weight of backfill (assumed to be 1900 kg/m^3)

H = 0.61 m

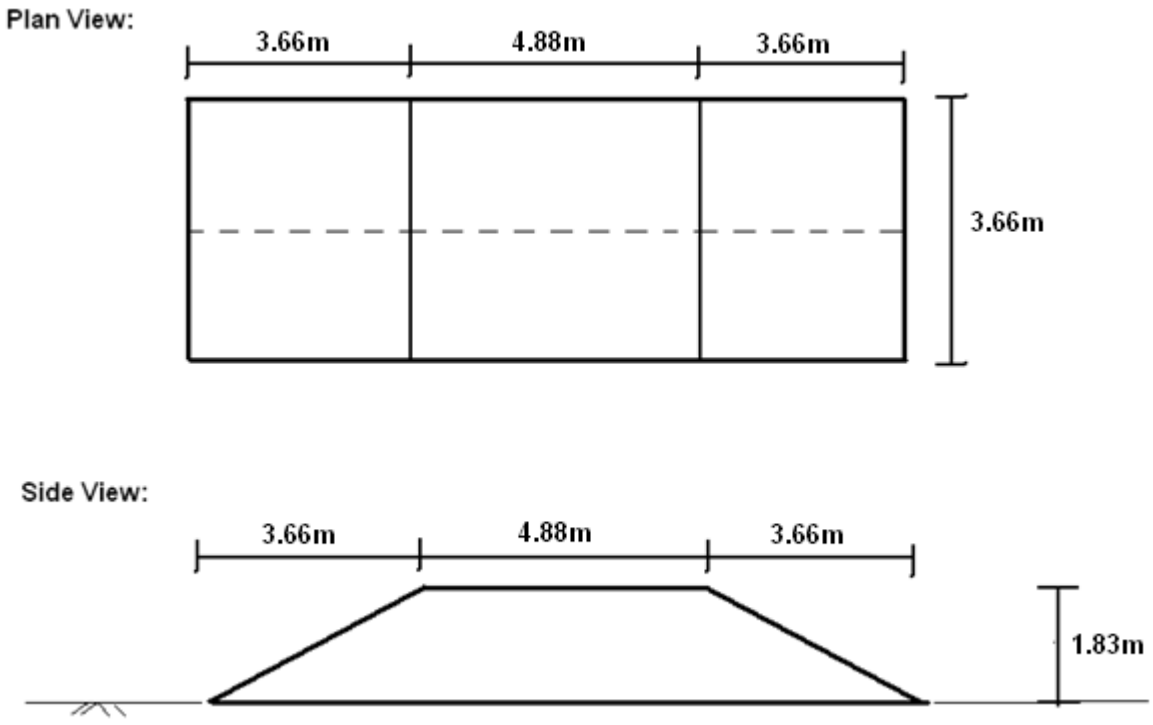

Figure 4.5: Proposed embankment dimensions

The calculation gave a resultant passive force of 19.26 kN/m, giving a total passive force of 65.65 kN for a 3.05m (10 ft) wide shaker base. In order to increase capacity, the shaker base was extended to be three feet deep. Repeating the same calculation, using a bench length of 1.22 m, the total passive force was calculated to be roughly 120 kN. Furthermore, under the consensus of Drs. Stewart and Brandenberg, and myself, it was decided that the model levee would be reinforced using geogrids, thus increasing the static capacity. Furthermore, since the loading on the levee from the shaker would be cyclic and not static, it was estimated that the embankment could take up to roughly 133 kN of shaking.

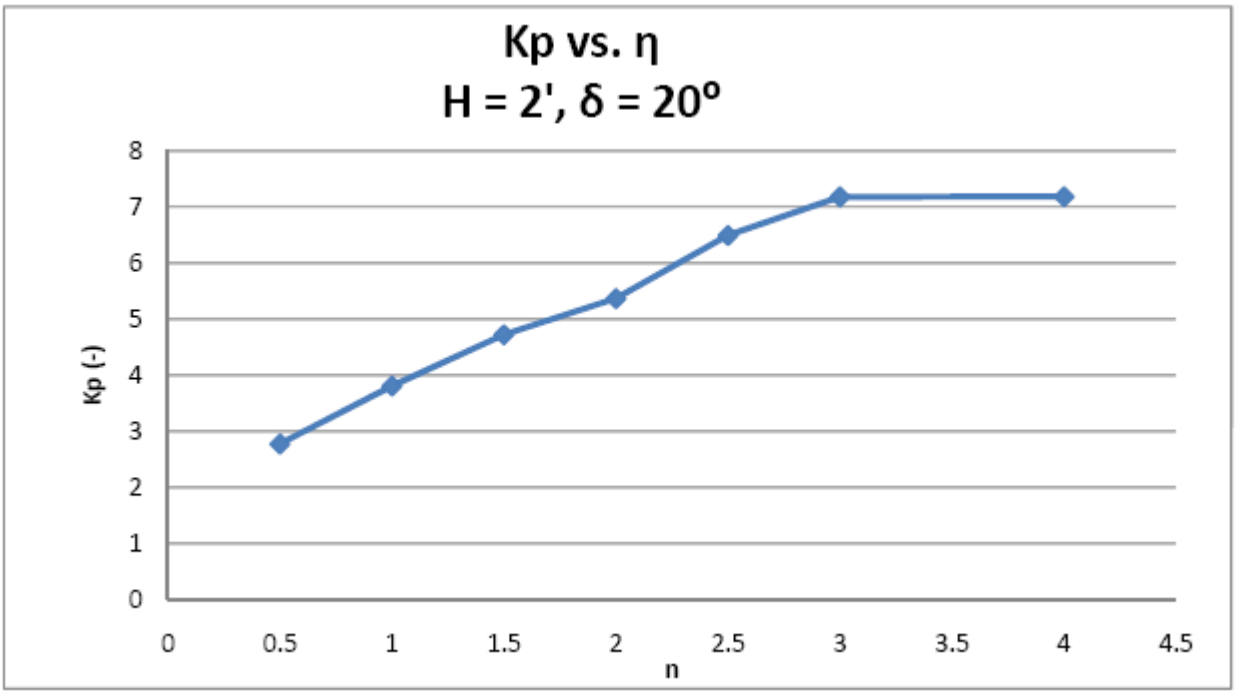

Figure 4.6: Coefficient of passive pressure versus bench length (as a function of shaker base height)

4.1.2. Modeling and Development of Dynamic Stresses During Shaking

In order to estimate the dynamic stresses imposed on the peat during shake testing, the levee on the soft peat was modeled using the open source OPENSEES software. The goal of this modeling was to estimate how large the stresses in the soil would be from the levee shaking. In this case, the project team wanted to see how large the cyclic stress ratios (CSR) of the peat soil would be during shaking. The CSR is defined as the ratio of the cyclic shear stress to the initial effective stress, or as seen in Eq. 4.2:

$$CSR = \tau_{cyc}/\sigma'_{v0} \quad \text{.. Eq. 4.2}$$

Where τ_{cyc} defined as one-half the difference in principal stresses, or:

$$\tau_{cyc} = \frac{1}{2} (\sigma_1 - \sigma_3) \quad \text{.. Eq. 4.3}$$

In these analyses, the team wished to see if the CSR developed in the peat would exceed 0.35, which is indicative of a large earthquake with strong ground motions.

The first task in performing these dynamic analyses was to come up with the mesh, material properties, and boundary conditions of the model. The mesh was generated using GiD, a pre and post-processing program used to generate the mesh and view data for OPENSEES simulations. Figure 4.7 shows the mesh that was generated for use in these analyses. This two-dimensional mesh consisted of 876 unstructured quadratic elements connected by 931 nodes. One important thing to note is the base of the levee is not flat on the peat, but follows a settlement profile determined from a simple consolidation analysis. Figure 4.8 shows the soil properties used in the consolidation analysis. Consolidation properties of the peat were determined from laboratory testing using reconstituted peat obtained from the March 2010

geophysical investigation. Ultimate settlement calculations indicated that the center of the model levee would settle roughly 30 cm (1 ft) on the soft peat soil, and a settlement profile was developed based off of these calculations.

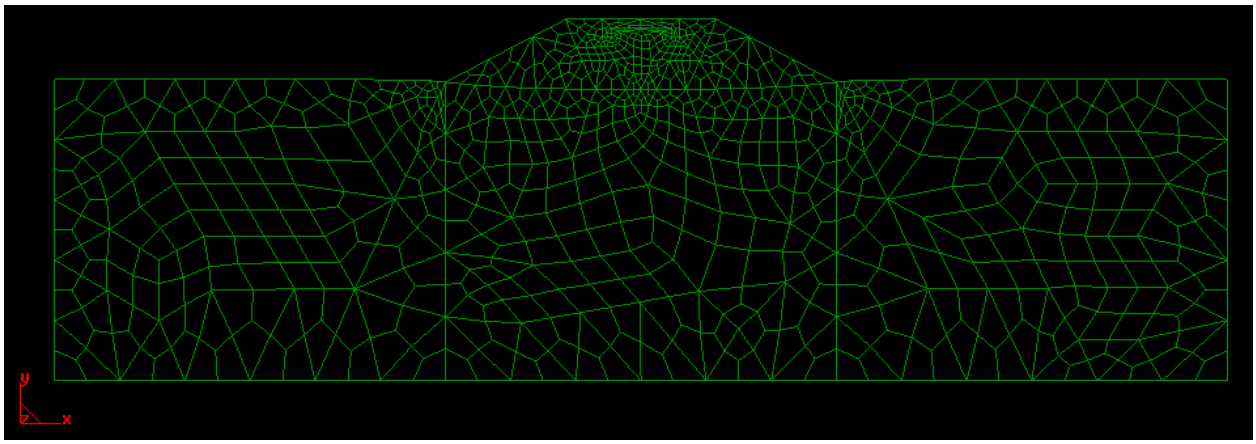

Figure 4.7: Mesh generated using GiD.

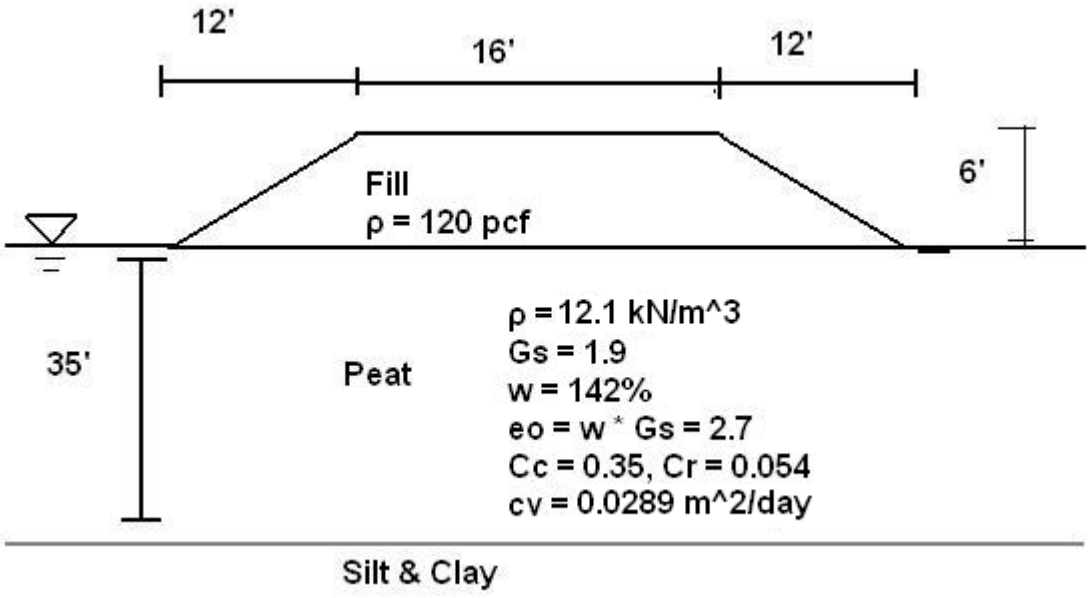

Figure 4.8: Soil properties used in consolidation analysis

Material properties of the levee and peat were modeled as elastic isotropic materials, for simplicity of calculation. Therefore, the only information that was needed for each of these materials was their Poisson ratio, the Young's modulus, and the density. For all materials, the Poisson ratio (ν) was assumed to be 0.3. The densities of the peat, backfill, and concrete used in these analyses were 1,120, 1,920, and 2,400 kg/m^3, respectively. The Young's modulus of the peat was calculated using Eq. 4-4:

$$E_{peat} = 2G(1+\nu) = 2\rho V_s^2(1+\nu) \quad \text{.. Eq. 4.4}$$

Using V_s = 30 m/s. The Young's Modulus for the backfill was assumed to be based off the maximum shear modulus for sand, as mentioned in Kramer (1996), and was calculated using Eq. 4.5:

$$E_{sand} = 2G_{max}(1+\nu) = 1000K_{2,max}(\sigma_m')^{1/2} \quad \text{..Eq. 4.5}$$

Where:

$K_{2,max}$ = 40 (value at 40% relative density)

σ_m' = effective stress at three feet depth from the top of the levee crest (in lb/ft^2).

Finally, the Young's modulus of the concrete was computed using Eq. 4-6:

$$E_{conc} = 57{,}000(f'_c)^{1/2} \quad \text{..Eq. 4.6}$$

Where:

f'_c = the assumed compressive strength of concrete = 4,000 psi

The units for the Young's modulus were then converted to SI for this set of analyses. Rayleigh damping was considered for this model, with a nominal damping ratio of 5%.

Once the material properties were established, the boundary conditions of the model could be constructed. In order to prevent reflection of ground motions that may arise from fixed boundary conditions along the vertical sides of the model, horizontal and vertical foundation dashpots were assigned to the nodes along the edge of the peat layer in the model following the procedure by Lysmer and Kuhlemeyer (1969). The formulae used for these dashpots are given in Eq. 4.7a and 4.7b:

$C_{horiz} = \rho V_p HW$ .. Eq. 4.7a

$C_{vert} = \rho V_s HW$ .. Eq. 4.7b

Where:

H = tributary height of the node (normally element height)

W = width of soil considered in model (3.65 m)

V_p = Primary wave velocity of peat = $\sqrt{\frac{G_{peat}(2-2\nu)}{\rho_{peat}(1-2\nu)}}$ … (Eq. 4.7c, from Kramer (1996)).

Before running the dynamic analysis, a gravity analysis with fixed vertical boundaries was performed and the horizontal reaction forces were recorded. Once the displacement constraints were removed from the boundaries, the horizontal reaction forces were imposed at the nodes to simulate normal horizontal pressure from the soil.

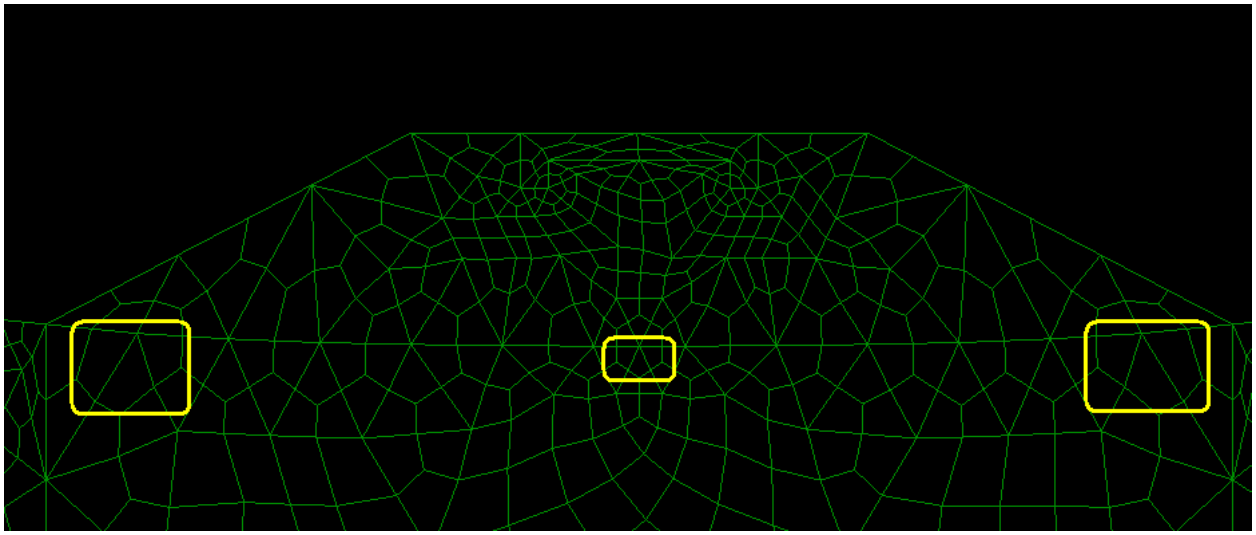

Figure 4.9: Location of elements used to calculate CSR.

Dynamic loads from the MK-15 shaker were modeled as harmonic horizontal forces at fixed frequencies. Loads were imposed along five nodes at the top of the levee crest, representing the input force into the shaker base from the shaker. Harmonic loading occurred until the model levee system achieved a steady state response, usually after 15 seconds of shaking. The simulation program consisted of shakes at force amplitudes of 89 kN (20,000 lbs) and 178 kN (40,000 lbs), with frequency ranges in between 0.5 to 5.0 Hz. CSR's were calculated for three locations in the peat just underneath the model levee: underneath the left and right toes of the levee as well as underneath the center. For each location, the calculated CSR consisted of the average CSR generated from three quadratic elements just underneath the model embankment, as indicated in Fig. 4.9. For each element, the point of reference with which to calculate the effective stress consisted of finding the average depth of the four Gauss points. The water table was assumed to be at the top of the peat layer, which is consistent with the conditions of many of the Delta levees. Fig. 4.10 shows CSR versus frequency of loading for 89 kN (20,000 lbs) harmonic shaking. Two distinct sets of peaks appear in this figure: one underneath the center

at 0.6, 2.2, and 3.2 Hz, and one underneath the levee toe for 0.6, 1.3, and 3.2 Hz. The highest CSR generated for this loading was roughly 0.22 at 1.3 Hz underneath the left toe. Further analyses at 178 kN (40,000 lbs) show a similar form of CSR vs. frequency, with a maximum CSR of 0.45 at the same frequency and location as the 89 kN simulations, which is sufficient for a large earthquake. Eigen-analyses were also performed on the levee to see what mode shapes the CSR peaks would correspond to. For example, the peak CSR underneath the left toe of the levee corresponds to the mode seen in Fig. 4.11b, which appears to be a rocking mode, at a frequency of 1.32 Hz. This kind of mode shows high shear deformation in the peat close to the levee toe, while there seems to be significantly less shear deformation underneath the center of the levee. Another mode, as seen in Fig. 4.11a, more closely resembles a sliding mode, and has a frequency of 0.65 Hz. This mode also shows similar high CSR under the levee toe.

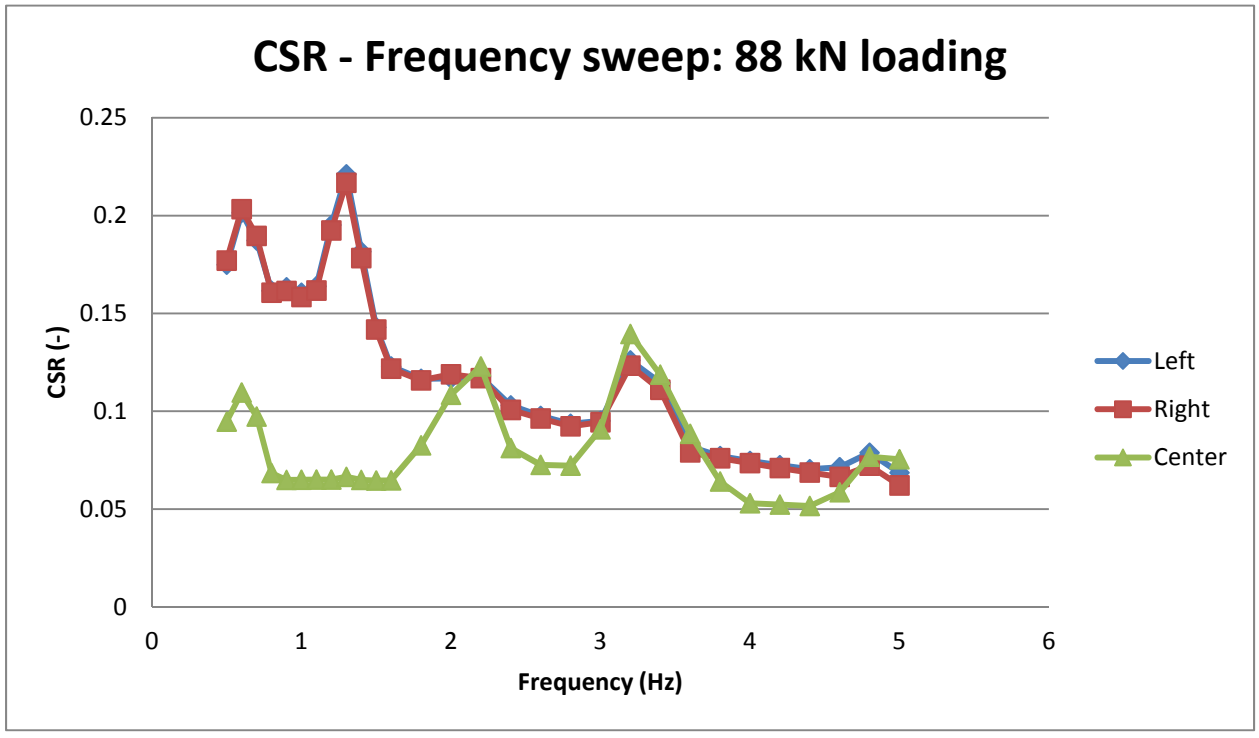

Fig. 4.10: CSR vs. loading frequency for 89 kN loading.

a)

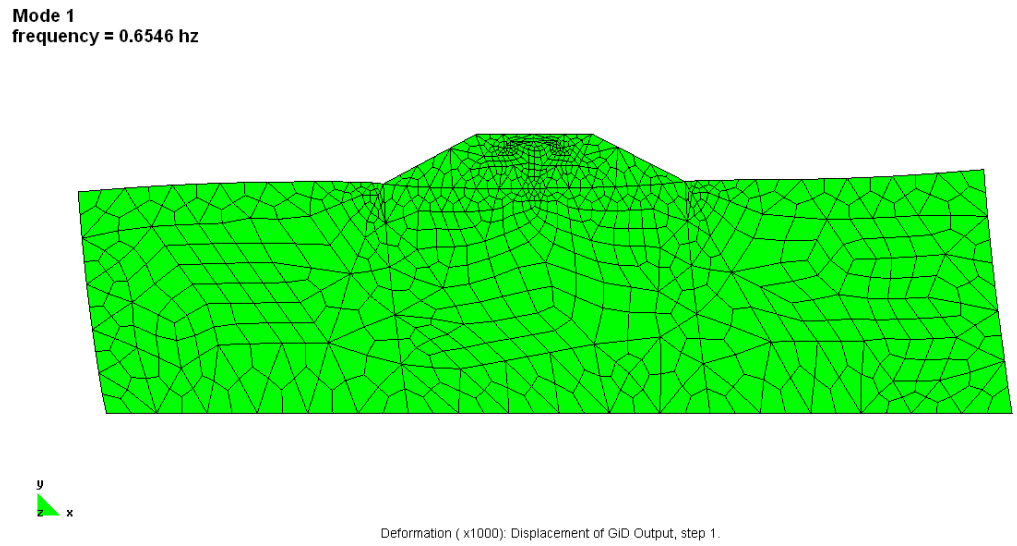

b)

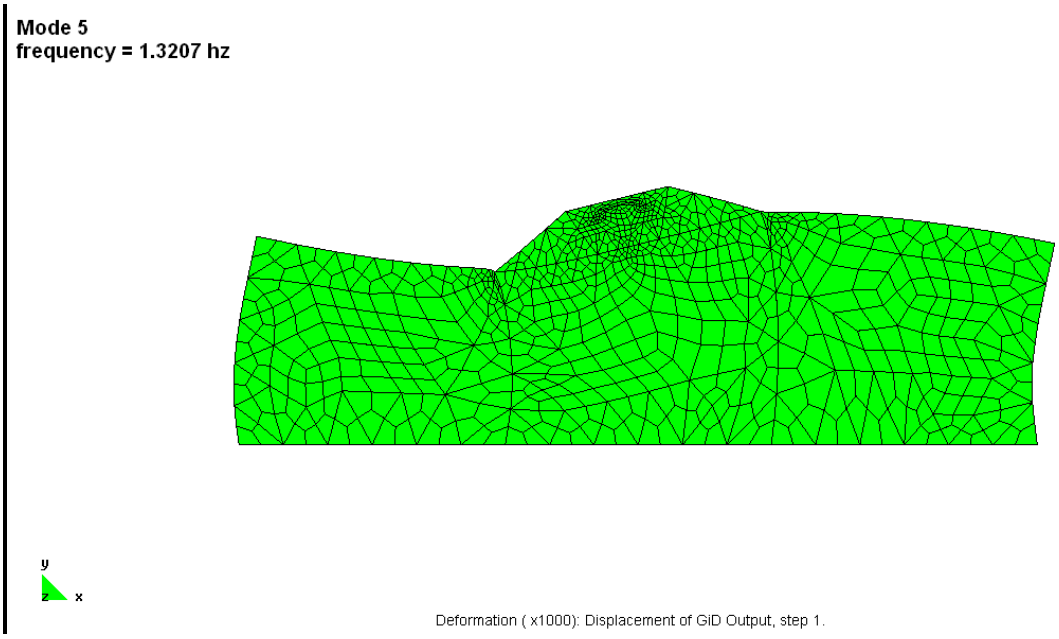

Figure 4.11: Mode shapes from Eigen-analysis for a) 0.65 Hz, b) 1.32 Hz

4.1.3. Fill selection, compaction specifications, and geosynthetic selection

During the June 2011 site investigation, the project team set out to find a source of fill to be used to construct the embankment. After meeting with DWR officials, a nearby site on Sherman Island containing stockpiled material for levee repairs was identified for use in the model levee and samples were brought back to UCLA to classify the fill and obtain compaction specifications and classify the fill. Modified Proctor tests were performed on the fill, and the resulting compaction curve can be seen in Fig. 4.12. Maximum dry density using the Modified Proctor test was 19.4 kN/m^3 (123.5 pcf) at a water content of 11%. For the test levee, the relative compaction was to be within 90% of optimum, at water contents above optimum to keep the fill from drying out too much. This corresponds to a compacted density of 17.3 kN/m^3 (115 pcf), with water contents above 11%. Wet wash sieve testing was performed on the fill to classify it, and the corresponding grain size distribution can be seen in Fig. 4.13. The fines content (percentage of soil passing the #200 sieve) was 45%. Atterberg index tests performed on these fines gave a plastic limit of 17% and a liquid limit of 40%. Using the U.S. Soil Classification system, the embankment fill was classified as a sandy clay (SC) according to the Unified Soil Classification System (USCS), although material behavior is likely controlled by the fine fraction.

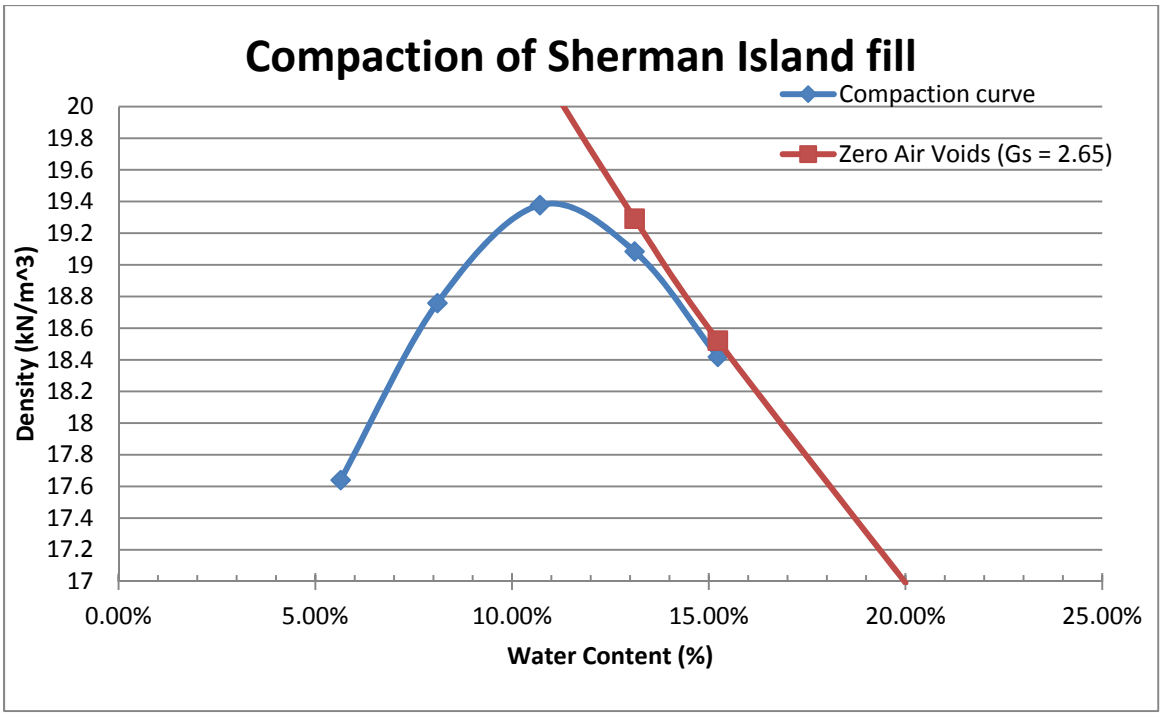

Figure 4.12: Compaction curve of Sherman Island fill.

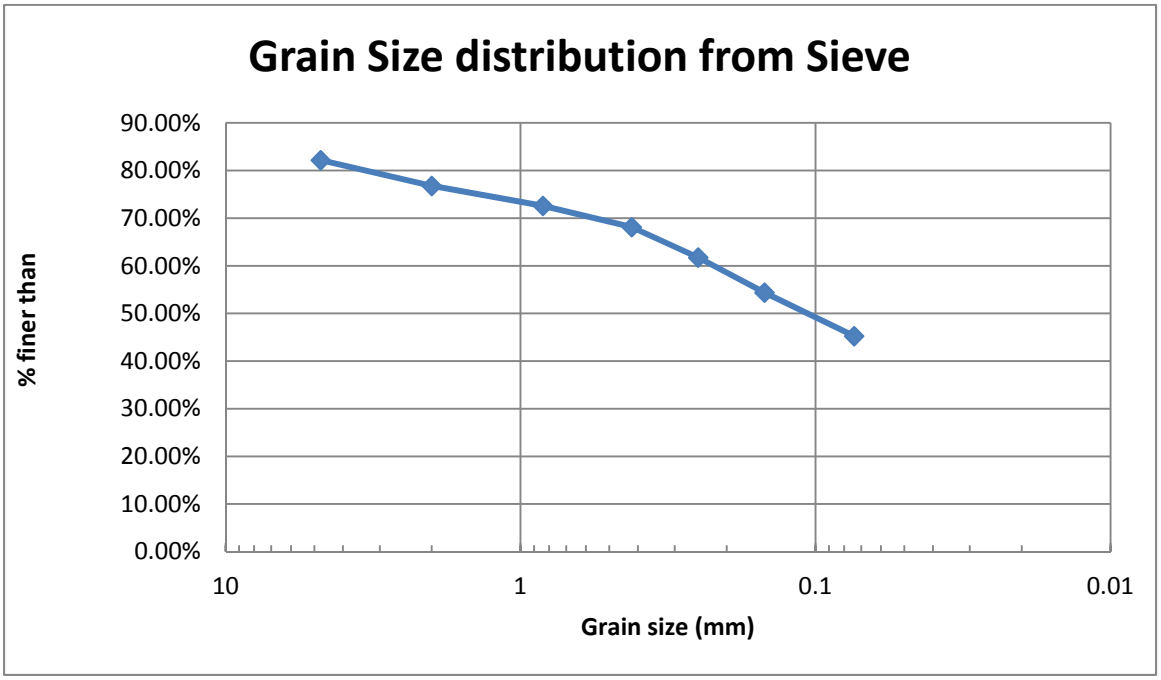

Figure 4.13: Grain size distribution of embankment fill.

One important issue that arose during the design of the model levee was the selection and placement of geosynthetics to reinforce the embankment during shaking. For this levee, the geosynthetics used consisted of two materials: a biaxial geogrid to reinforce the levee, and a geofabric to prevent migration of fines. The geogrid selected was Mirafi BXG10 biaxial geogrid, and the geosynthetic selected was Mirafi N-series geotextile. Details on how the model levee was constructed will be explained in the next section.

4.2. Model Levee Construction, Repair, and Long-Term Remote Monitoring

This section will describe construction and repair of the model test levee on Sherman Island, as well as the set up and use of a remote data acquisition system and corresponding sensors to monitor consolidation settlement and pore water pressure dissipation. Placement of below-grade sensors and construction of the model embankment took place during July 2011, and long-term monitoring of the embankment occurred between July 2011 and September 2012. Repair of the embankment and the construction of a berm around the embankment were performed in July 2012, prior to the second suite of shake tests.

4.2.1. Model Levee Construction and Repair

Table 4.1 shows the timeline of model levee (embankment) construction, monitoring, and testing. The first task in preparing the site for testing was to establish where the test levee would be placed within the site, clear the ground vegetation, and place the underground sensors needed for long-term consolidation settlement and pore water pressure dissipation. The sensors used in the long-term remote monitoring consisted of an in-place inclinometer and four piezometers. The inclinometer was oriented horizontally and placed at the contact between the embankment and

the peat and was used to measure embankment settlement. Piezometers were used to measure pore water pressure. Prior to the placement of any sensors, eight PVC tubes were inserted into boreholes excavated with a hand auger to act as guides for the later placement of subsurface MEMS accelerometers. These accelerometers were not used in the long-term monitoring of the embankment, so they will be discussed in Section 4.3. The in-place inclinometer, manufactured by Geodaq, Inc., consists of five model INC500 modules connected end-to-end forming a continuous displacement measurement system with a total length of 13m (42.5 ft). The in-place inclinometer does not require passage of a traditional inclinometer sensor through the casing, as do many other inclinometers. Rather, each INC500 module includes 8 Micro-Electro-Mechanical Systems (MEMS) accelerometer sensors spaced 0.30m (1 ft) apart for a total of 40 bi-axial MEMS distributed over the full length of the model levee. MEMS sensor readings were recorded at 10 minute time intervals during the period from July 2011 to September 2012, and displacement profiles were calculated by spatially integrating the measured rotations along the inclinometer axis. Fig. 4-14 shows the placement of the PVC pipes as well as the in-place inclinometer just prior to embankment construction. Fig. 4-15 shows the inclinometer and INC500 module in greater detail.

Table 4.1: Timeline of construction and testing of model embankment.

Date	Tasks Performed
July 28-29, 2011	Install: piezometers, PVC pipes for MEMS accelerometers, horizontal inclinometer casing, remote DAQ system. First 3 lifts constructed. Remote data acquisition started
August 1, 2011	Timber shaker frame installed. Final 3 lifts constructed.
August 24-29, 2011	MEMS accelerometers installed. Surface accelerometers installed. MK-15 shaker installed. MK-15, SASW, and Atom Ant shake testing performed.
July 17-18, 2012	Repair embankment frame and re-construct final 3 lifts.
July 24, 2012	Re-install MEMS accelerometers, MK-15 shaker installed. Berm constructed around embankment with pump and level switch. Inundation begins.
August 11-15, 2012	Inundation ends. Install surface accelerometers. MK-15 and SASW shake testing performed.
Sept. 13, 2012	Embankment deconstructed. Remote DAQ uninstalled. All underground sensors removed.

Figure 4.14: In-place inclinometer casing (blue) and PVC guide pipes (white) installed just prior to construction.

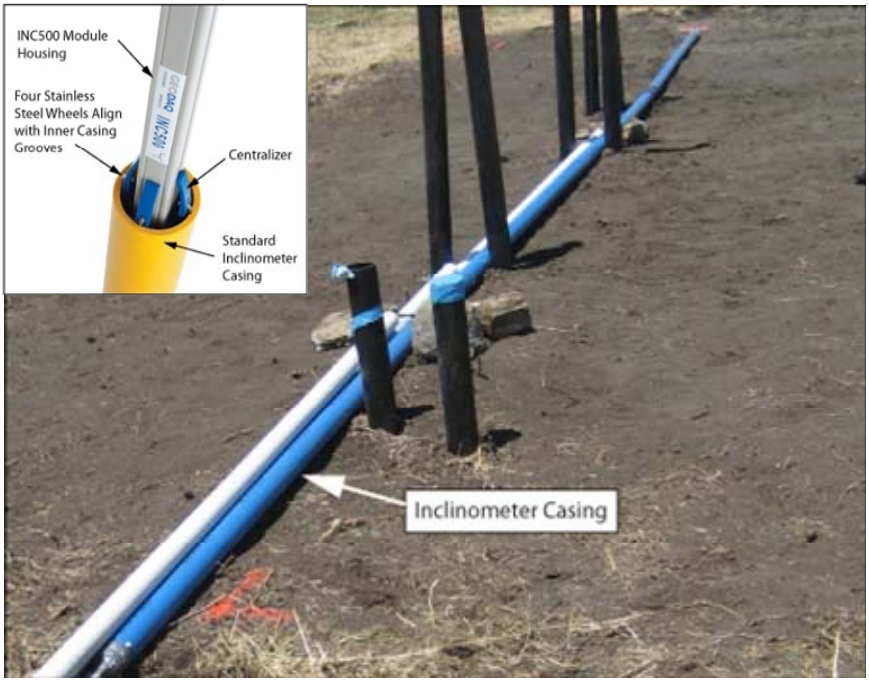

Figure 4.15: Inclinometer casing on ground surface prior to levee construction, and INC500 instrumentation detail.

Pore water pressure beneath the levee embankment was monitored at four positions using KPSI 330 piezometers manufactured by Measurement Specialties. The piezometers were installed beneath the levee at depths of 1.95m (P1), 2.33m (P3), and 3.17m (P2 and P4) to monitor changes in pore pressure during construction of the levee embankment and during long-term consolidation of the peat. Since the peat at the site was very soft, installation of the piezometers was done manually using a mandrel to push the piezometer to the desired depth. Cloth was tied around the ends of the piezometers to prevent migration of fines into the sensors. The piezometers consist of electrical resistance strain gauges mounted to a diaphragm, one side of which is in contact with the pore fluid and the other side is in contact with air inside the sealed housing of the transducer. The inside of the transducer is not vented to the atmosphere, so the piezometers are sensitive to changes in atmospheric pressure. Therefore one piezometer (P5) was left on the ground surface to monitor atmospheric pressure changes. The location of each piezometer is shown in Figure 4.16. Each piezometer was connected to a GST module that operates on the same digital network as the INC500 modules. Each GST network module includes a microprocessor, signal conditioning circuitry, a 16-bit analog-to-digital conversion circuit, and Controller Area Network (CAN) communication controller.

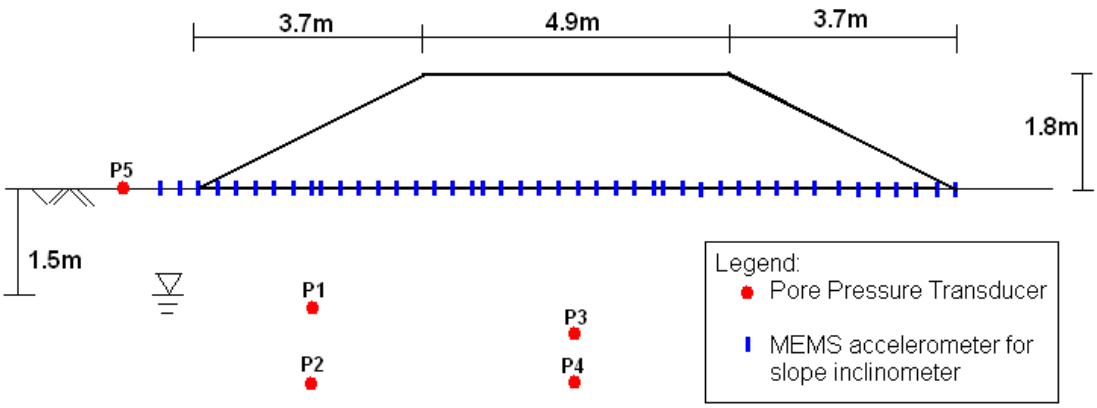

Figure 4.16: Location of piezometers and in-place inclinometer used in long-term remote monitoring.

Once the piezometers, PVC pipes, and in-place inclinometer were placed in their desired locations, we began constructing the model embankment. Sandy clay fill, sourced from a local borrow pit on Sherman Island, was compacted in six lifts, each 0.3 m (1 ft) thick, and reinforced with a combination of Tencate 2XT biaxial geogrid and Mirafi 500x woven geofabric. The clay was compacted to a dry unit weight of 17.3 kN/m^3 (110 pcf) at an average water content of 11%. Prior to construction, modified Proctor compaction testing was performed on fill from the borrow pit, and the details are in Section 4.1.3. The average dry density was about 90% of the modified Proctor maximum dry density, and average water content was near optimum. The somewhat low maximum dry density was achieved because large equipment could not drive atop the embankment, and small hand equipment was used for compaction. The geogrids were wrapped in the out-of-plane direction in order to form two vertical faces on the edge of the embankment, using pre-fabricated falsework, as seen in the schematic presented in Fig. 4.17. A sturdy timber frame was embedded into the upper 3 lifts of the embankment to support an eccentric mass shaker (MK-15), as seen in Fig. 4.18. The geogrid and geofabric were stapled to the timber frame in order to promote better coupling between the frame and the soil. A photo of the constructed embankment, with the shaker attached is shown in Fig. 4.19.

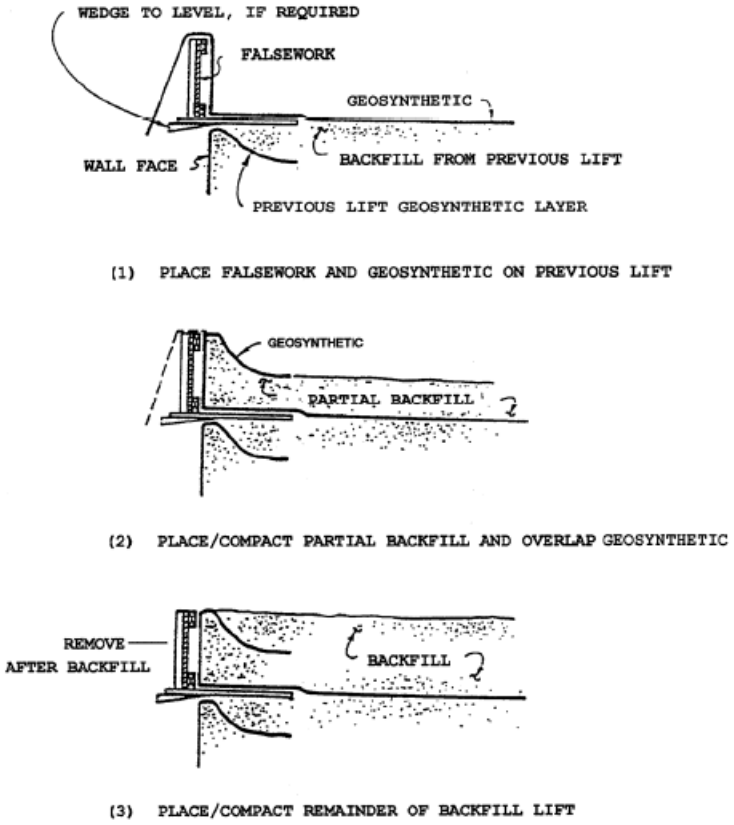

Figure 4.17: Placement of geosynthetics and embankment fill using falsework (FHWA 2001)

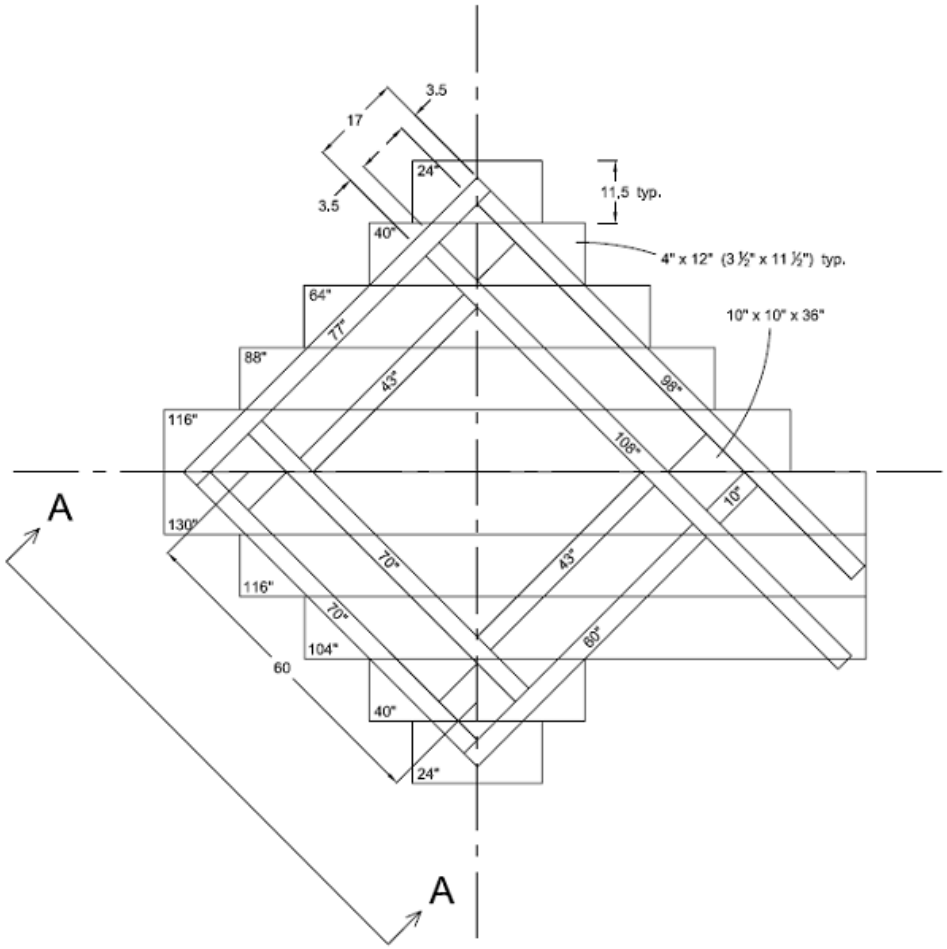

Figure 4.18 (a): Plan view sketch of timber shaker base.

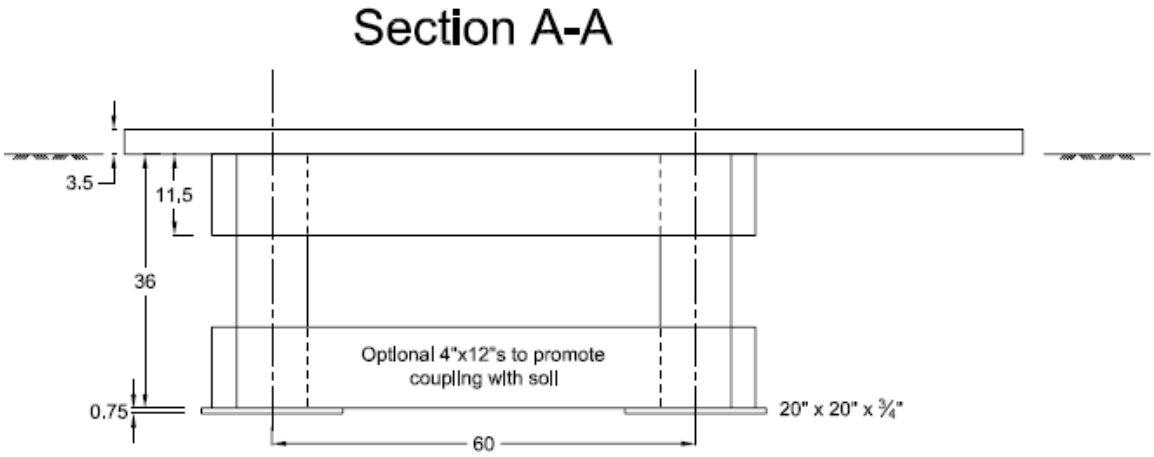

Figure 4.18 (b): Side view of timber shaker base.

Figure 4.19: Constructed model embankment with NEES@UCLA MK-15 shaker.

The embankment was shaken in August 2011, and left in place for post-test monitoring. Details of the shake testing are provided in section 4.3, and the post-test construction activities are presented here to keep all construction activities in the same section of the dissertation. During shaking in 2011, gaps formed between the shaker frame and fill, as seen in Fig. 4.20. A second test was planned for August 2012, so the project team returned to the test site to repair the embankment. The upper three lifts were removed with a small scraper, and 4x12 boards were bolted along the outside of the base of the shaker frame to anchor the base of the shaker to the embankment. The fill was then re-compacted in the same manner as the original construction, involving hand operated compaction equipment, geogrids, and geotextile fabric. In addition to repairing the frame, a berm was constructed around the embankment to permit the peat to be flooded prior to the 2012 shaking activities. The groundwater level during the August 2011 shake testing was 1.5m below ground level, and the project team wanted to raise the water level underneath the embankment until it was close to ground level during the second suite of tests

because saturated peat is softer than desiccated dry peat. A submersible pump was installed near the closest drainage ditch and water was pumped continuously through a 3-inch diameter pipe into the berm. A level switch was used to regulate how much water was coming in, and to keep the rest of the site from accidentally flooding, although the level switch never triggered a shutoff of the pump because water infiltrated into the peat so quickly.

a)  b) 

c) 

Figure 4.20: Damage to the model levee after August 2011 tests: a)Gap formation between timber shaker base and soil, b) 1m long crack on left side of embankment crest, c) 0.3 long cracks on right side of embankment crest

4.2.2. Long-Term Remote Monitoring of Model Test Levee

Readings from the in-place inclinometer and piezometers sampled at 1-minute intervals during and immediately after construction of the embankment in 2011, and subsequently at 10 minute intervals for long-term remote monitoring. Signals from these sensors were digitized at the various network nodes comprising the remote DAQ (five INC500 modules and two GST modules). Results were transmitted to a controller module (GCM) using a two wire Controller Area Network (CAN) communication system. The GCM module collects readings from the entire network and transmits the data to a web server computer via a wireless Internet modem. A monitoring station at the ground surface includes one controller module (GCM), one Internet modem, one battery and a solar panel to charge the battery. The remote monitoring station used for this project is shown in Figure 4.21 (Reinert et al. 2013(a)). A steel frame with locking lid was mounted to the ground with anchors to provide protection from vandalism and cattle. All data acquisition equipment was housed in a plastic field enclosure, so the only external components visible were the sensor cables running from the DAQ to a PVC conduit at the bottom of the model levee. The monitoring instrumentation therefore maintained a low profile.

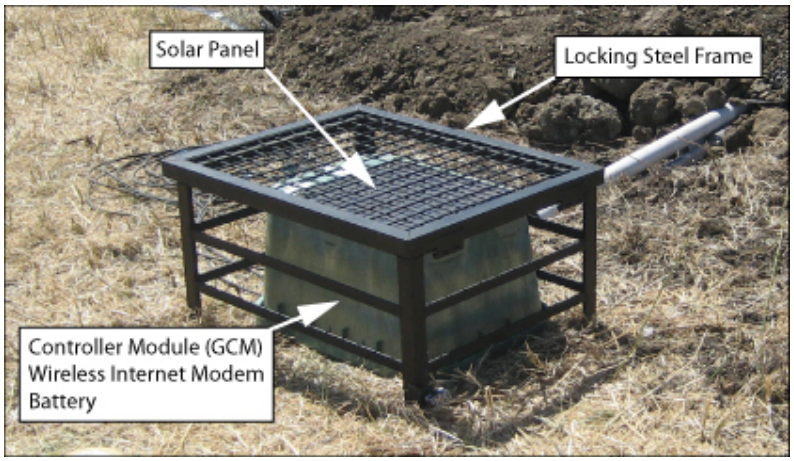

Figure 4.21: Remote monitoring station.

The test data is presented over two different time intervals of engineering interest. First the data is presented for 40 days beginning with construction of the embankment and ending a few days after dynamic testing. The reasons for presenting data for this time interval are to document the consolidation behavior of the peat following construction of the embankment, and to document any post-cyclic settlement following dynamic testing. The second time interval covers the entire lifesapan of the model levee, beginning with embankment construction and ending with levee removal, a time period which lasted just over 400 days. The purpose of presenting data from this time interval is to show changes in the groundwater level associated with pumping operations on Sherman Island, and the influence of these fluctuations on the embankment settlement.

Figure 4.22 shows settlement beneath the crest of the levee and pore pressure from the four subsurface piezometers for 40 days following construction of the embankment. Atmospheric pressure was subtracted from the four subsurface piezometer records. The recordings begin at Day 0 (Thursday, July 28, 2011), when the first of six lifts was constructed. The following day, July 29, two additional lifts were constructed. Finally, following a weekend break, the final three lifts were constructed on Monday, August 1. Piezometers P2 and P4 exhibit pronounced increases each time a lift of fill is placed, and a subsequent decrease due to consolidation. Piezometers P1 and P3 exhibit much smaller increases, likely because they are close to the drainage boundary at the ground water table. Placement of the sensors close to the drainage boundary permitted dissipation of pore pressures on the same time scale at which construction progressed. The piezometers indicate that the peat consolidates rather quickly because excess pore pressures generated by constructing lifts 2 and 3 on July 29, 2011 had essentially dissipated prior to construction of lifts 4, 5 and 6 on August 1. Following construction of lifts 4, 5 and 6,

pore pressures continue to decrease slowly throughout the 40 day period, returning to pre-construction levels after 10 days, and subsequently continuing to decrease. Pumping operations on Sherman Island drew down the groundwater table, which explains why pore pressures reduced below pre-construction levels. It is difficult to separate the fraction of pore pressure change caused by consolidation from that caused by groundwater pumping because a free-field piezometer was not installed.

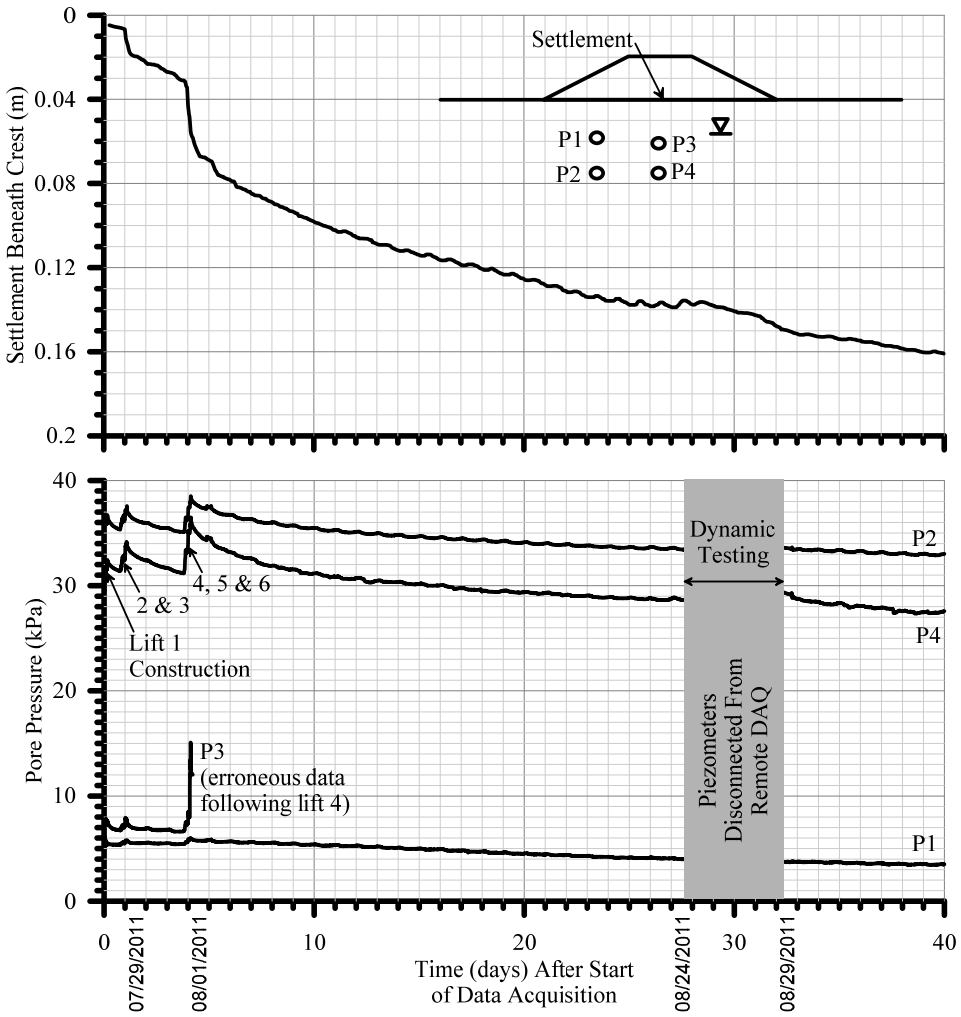

Figure 4.22. Settlement beneath levee crest and pore pressure at various positions beneath the embankment versus time for 40 days following embankment construction, including the period following dynamic testing.

The settlement data exhibit sharp increases during placement of the fill due to shear-induced immediate settlement of the embankment and perhaps some immediate volume change in the unsaturated desiccated peat. The immediate settlement obtained by summing the abrupt increases in settlement was approximately 0.06m. The settlement also exhibits a slower increase over time due to the combined effects of primary consolidation and secondary compression. High secondary compression is inferred from the rapid settlement rate following dissipation of pore pressures to pre-construction levels after 10 days. High secondary compression is a common feature of peat soil that is well documented in the literature (e.g., Mesri and Ajlouni 2007), and is usually attributed to high void ratio, high ratios of the index of secondary compression to the compression index (C_α/C_c), and high initial permeability of the peat (Mesri et al. 1997) . In laboratory oedometer tests performed on piston samples retrieved from the site (Shafiee et al., 2013), distinguishing primary consolidation from secondary compression using Casagrande's (1938) procedure was difficult due to the high c_α.

The piezometers were disconnected from the remote data acquisition system on August 24th 2011, connected to a different data acquisition system utilized during dynamic testing of the embankment, and subsequently reconnected after dynamic testing on August 29th 2011. The inclinometer remained connected to the remote DAQ during this time because these sensors could not be sampled at high frequency using the other DAQ. Dynamic testing of the embankment was intended to induce shear strain into the peat over a range of shaking intensities to observe the response. No significant increase in pore pressure or settlement was observed following dynamic testing.

An interesting observation is that the change in pore pressure induced by the surface loading is less than the change in vertical total stress at the piezometer position. For example, lifts 4, 5 and 6 combined to induce a vertical stress change of approximately 16 kPa at the surface. Elastic solutions that include the three-dimensional loading imposed by the model levee predict that the vertical stress change at a depth of 3.0m (i.e., the depth of P2 and P4) is 8.8 kPa at the position of P4 and 6.7 kPa at the position of P2. The sum of the immediate changes in pore pressure during construction of each lift, on the other hand, were only 5.5 kPa and 3.7 kPa for P4 and P2, respectively. The difference between the change in vertical stress and the change in pore pressure is likely caused by (i) three-dimensional loading conditions inducing some shear-induced pore pressure (i.e., Skempton and Bjerrum 1957), (ii) lack of saturation in the peat resulting in a B-value lower than unity, (iii) dissipation of excess pore pressure during the short time during which fill was added to the model levee, and (iv) the lateral distribution of stress through the stiffer unsaturated peat layer above the water table compared with the uniform isotropic conditions assumed in the elastic solution.

Steady-state pore pressure at the depth of P2 and P4 was more than 30 kPa at the time of dynamic testing, which is quite a bit higher than would occur for hydrostatic conditions. The transducers were approximately 1.6m below the water table, hence hydrostatic water pressures would be expected to be approximately 16 kPa. This condition can be explained by the site geology. The peat is underlain by a permeable sand layer that is continuous and connected to the San Joaquin River. Therefore, the pore pressure at the bottom of the peat layer is controlled by the river elevation rather than the depth below the water surface in the peat. The continuous pumping of water from Sherman Island maintains the water elevation below the peat surface, inducing an upward hydraulic gradient (artesian condition) and larger-than-hydrostatic pore

pressures. Artesian conditions were subsequently confirmed by CPTu tests, which indicate that the pore pressure in the sand underlying the peat is approximately 50 kPa higher than hydrostatic, resulting in a condition of essentially zero effective stress in the sand below the peat. The artesian conditions combined with continued subsidence of the peat due to biodegradation and wind erosion contribute to portions of the Delta becoming too wet to farm; a trend that is projected to continue. The geotechnical implications of the artesian conditions has not been adequately explored, though the fact that the sand below the peat has essentially zero effective stress is a bit alarming.

Figure 4.23 shows pore pressures and settlements beneath the center of the embankment over a longer time period of about 13 months, which matches the entire duration during which remote monitoring was performed. Data begin at embankment construction, during which pore pressures and settlements rapidly increase as lifts of fill are placed. Excess pore pressures dissipated quickly, and decreased to pre-construction levels after a few days. The pore pressure changes are attributed to dissipation caused by consolidation and fluctuations in groundwater depths (which can change daily from pumping related to regional agricultural operations). Approximately 50 days after the data acquisition began, pore pressures suddenly increased and fluctuated in time. This change was believed to be caused by seasonal reduction in pumping operations, which are controlled by agricultural use requirements, and is unrelated to our test activities. The levee settlement continued to occur at a significant rate even after excess pore pressures had been dissipated. This is attributed to secondary compression of the peat. The settlement rate increased upon local flooding of the peat beneath the levee. The remote monitoring data indicate that no significant changes in settlement rate or pore pressures were induced by shaking.

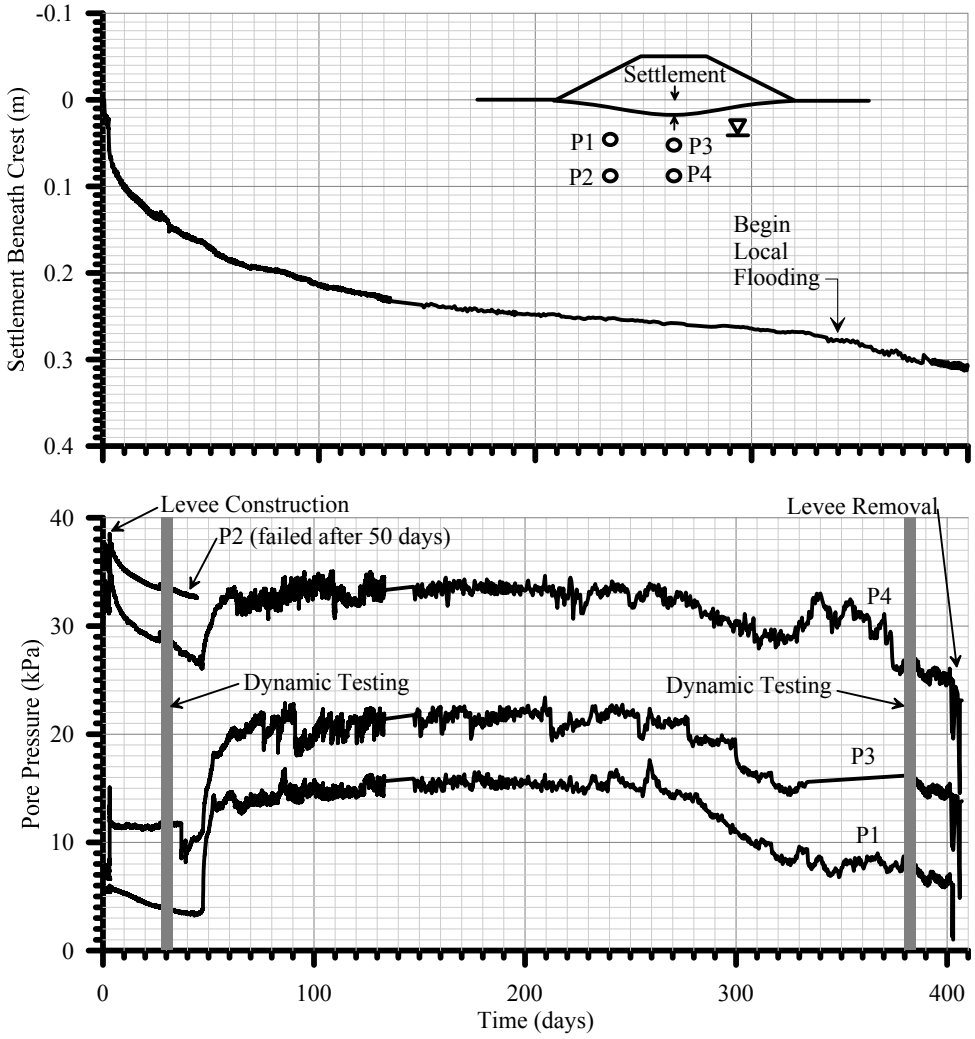

Figure 4.23. Remote monitoring data on pore pressures and embankment settlement for 403 days in between levee construction and removal, including both sets of tests from 2011 and 2012.

Settlement profiles at various times are shown in Fig. 4.24. The settlement is largest beneath the crest of the embankment and increases with time, as anticipated. These profiles are computed by integrating the measured rotation data along the inclinometer axis, resulting in a measurement of relative displacement with respect to one end of the inclinometer casing. Rigid body translation of the inclinometer casing is not measured by the MEMS sensors, but could conceivably be measured by an independent sensor. An attempt to measure the settlement of the

ends of the inclinometer casing using string potentiometers suspended from taut cable lines failed because the string potentiometers became entangled in vegetation. The assumption of zero settlement at horizontal position = 0m as shown on Fig. 4.23 is considered to be reasonable based on field observations.

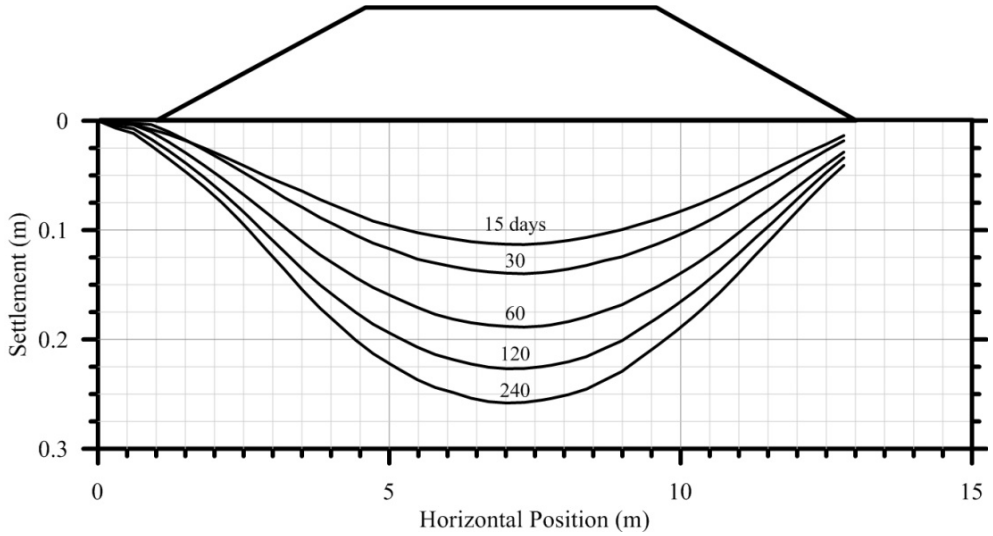

Fig. 4.24: Settlement profiles at various times following construction of the model levee.

4.3. Shake Testing of Model Test Levee

This section will describe the work done in testing the model levee, including instrumentation of the embankment and underlying peat, the types of motions imposed on the levee, the collection and processing of dynamic test data for engineering analysis, the categorization and archiving of experimental data on NEEShub, and the calculation of shaker force imposed on the levee from the NEES@UCLA MK-15 eccentric mass shaker. As mentioned earlier, shake testing of the model levee was performed over two separate periods: between August 27th-29th 2011, and August 14th-15th 2012.

4.3.1. Instrumentation of Model Levee for Dynamic Testing

Figures 4.25 (a), (b), and 4.27 show the elevation and plan views of the test embankment sensor setups for the shake tests during the August 2011 shake sequence, and Table 4.2 presents the sensor list. Sensors used for this suite of tests include: 25 triaxial accelerometers (either Episensor Triaxial Accelerometers (ES-T) or mounted sets of three Episensor Uniaxial Accelerometers (ES-U) that acted as a single triaxial accelerometer), 1 additional Episensor Uniaxial accelerometer mounted on the shaker frame in the direction of shaking, 8 underground MEMS accelerometers, 4 piezometers embedded into the peat directly underneath the embankment and 1 piezometer above the ground surface measuring atmospheric pressure, and two string potentiometers measuring vertical displacement at each levee toe. Eighteen of the triaxial accelerometers (ES1 – ES18) and the single uniaxial accelerometer (ES25) were placed on the model levee to characterize its three dimensional motion and eventually compute base shear, translation/rocking, etc. The other seven triaxial accelerometers (ES19-24, ES26) were placed in a surface array in both the x and y directions to measure propagation of surface waves in the peat. The in-peat MEMS accelerometers (M1-M8) were sealed in PVC tubes with epoxy and embedded into the soil just prior to placement of the MK-15 eccentric mass shaker. A mandrel was used to push these sensors into the peat prior to shaking. Vertical PVC pipes were used as casing for hand auger boreholes, and extended above the ground surface where levee fill was compacted around them. These pipes acted as a conduit enabling access to push the sensors into the underlying soft peat. These sensors were used to measure ground motion beneath the levee and eventually compute mobilized shear strains. M1-M4 were placed underneath the toe of

the model levee, while M5-M8 were placed directly underneath the levee crest. Four in-ground piezometers were used to monitor both consolidation of the model embankment during and after construction, transient pore pressure changes during shaking, and post-cyclic consolidation after shaking. Fig. 4.27 shows the surface array of accelerometers, and is identical for both years (with the exception of accelerometer ES19A, which was co-located along with ES19 for the 2012 shake testing due to suspicion that ES19 was faulty). ES26 was placed as far away from the model levee as our longest sensor cable would permit (approximately 100m) and is not shown in Fig. 4.27, as it is too far away from the embankment and all the other sensors. The purpose of this sensor was to quantify attenuation of shaking amplitude with distance from the model levee to document the lack of impact our testing exerted on the Sherman Island levees.

Table 4.2 (a):List of accelerometers ES1Z to ES14X used in the 2011 MK-15 shake tests

Sensor ID	Sensor Type	Coordinates			Serial #	Calibration	Units	DAQ Channel ID	Offset	Units
		x(m)	y(m)	z(m)						
ES1Z	ES-T	1.8	0	0	1442	0.2	G/V	Q330 1	Average	g
ES1Y	ES-T	1.8	0	0	1442	0.2	G/V	Q330 2	Average	g
ES1X	ES-T	1.8	0	0	1442	0.2	G/V	Q330 3	Average	g
ES2Z	ES-T	3.7	0	0	1192	0.2	G/V	Q330 4	Average	g
ES2Y	ES-T	3.7	0	0	1192	0.2	G/V	Q330 5	Average	g
ES2X	ES-T	3.7	0	0	1192	0.2	G/V	Q330 6	Average	g
ES3Z	ES-T	8.5	0	0	1445	0.2	G/V	Q330 7	Average	g
ES3Y	ES-T	8.5	0	0	1445	0.2	G/V	Q330 8	Average	g
ES3X	ES-T	8.5	0	0	1445	0.2	G/V	Q330 9	Average	g
ES4Z	ES-T	10.4	0	0	1443	0.2	G/V	Q330 10	Average	g
ES4Y	ES-T	10.4	0	0	1443	0.2	G/V	Q330 11	Average	g
ES4X	ES-T	10.4	0	0	1443	0.2	G/V	Q330 12	Average	g
ES5Z	ES-T	2.1	3.7	0	1702	0.2	G/V	Q330 13	Average	g
ES5Y	ES-T	2.1	3.7	0	1702	0.2	G/V	Q330 14	Average	g
ES5X	ES-T	2.1	3.7	0	1702	0.2	G/V	Q330 15	Average	g
ES6Z	ES-T	3.7	3.7	0	1444	0.2	G/V	Q330 16	Average	g
ES6Y	ES-T	3.7	3.7	0	1444	0.2	G/V	Q330 17	Average	g
ES6X	ES-T	3.7	3.7	0	1444	0.2	G/V	Q330 18	Average	g
ES7Z	ES-T	8.5	3.7	0	3849	0.2	G/V	Q330 19	Average	g
ES7Y	ES-T	8.5	3.7	0	3849	0.2	G/V	Q330 20	Average	g
ES7X	ES-T	8.5	3.7	0	3849	0.2	G/V	Q330 21	Average	g
ES8Z	ES-T	10.4	3.7	0	3813	0.2	G/V	Q330 22	Average	g
ES8Y	ES-T	10.4	3.7	0	3813	0.2	G/V	Q330 23	Average	g
ES8X	ES-T	10.4	3.7	0	3813	0.2	G/V	Q330 24	Average	g
ES9Z	ES-U	3.7	0	1.8	550	0.2	G/V	Q330 25	Average	g
ES9Y	ES-U	3.7	0	1.8	553	0.2	G/V	Q330 26	Average	g
ES9X	ES-U	3.7	0	1.8	552	0.2	G/V	Q330 27	Average	g
ES10Z	ES-U	8.5	3.7	1.8	530	0.2	G/V	Q330 28	Average	g
ES10Y	ES-U	8.5	3.7	1.8	546	0.2	G/V	Q330 29	Average	g
ES10X	ES-U	8.5	3.7	1.8	532	0.2	G/V	Q330 30	Average	g
ES11Z	ES-T	4.7	1.8	1.8	2446	0.2	G/V	Q330 31	Average	g
ES11Y	ES-T	4.7	1.8	1.8	2446	0.2	G/V	Q330 32	Average	g
ES11X	ES-T	4.7	1.8	1.8	2446	0.2	G/V	Q330 33	Average	g
ES12Z	ES-T	7.5	1.8	1.8	1886	0.2	G/V	Q330 34	Average	g
ES12Y	ES-T	7.5	1.8	1.8	1886	0.2	G/V	Q330 35	Average	g
ES12X	ES-T	7.5	1.8	1.8	1886	0.2	G/V	Q330 36	Average	g
ES13Z	ES-T	3.8	0	0.9	1190	0.2	G/V	Q330 37	Average	g
ES13Y	ES-T	3.8	0	0.9	1190	0.2	G/V	Q330 38	Average	g
ES13X	ES-T	3.8	0	0.9	1190	0.2	G/V	Q330 39	Average	g
ES14Z	ES-U	8.5	0	1.8	539	0.2	G/V	Q330 40	Average	g
ES14Y	ES-U	8.5	0	1.8	524	0.2	G/V	Q330 41	Average	g
ES14X	ES-U	8.5	0	1.8	1036	0.2	G/V	Q330 42	Average	g

Table 4.2 (b):List of accelerometers ES15Z to ES26X used in the 2011 MK-15 shake tests

Sensor ID	Sensor Type	Coordinates			Serial #	Calibration	Units	DAQ Channel ID	Offset	Units
		x(m)	y(m)	z(m)						
ES15Z	ES-T	8.5	0	0.9	1883	0.2	G/V	Q330 43	Average	g
ES15Y	ES-T	8.5	0	0.9	1883	0.2	G/V	Q330 44	Average	g
ES15X	ES-T	8.5	0	0.9	1883	0.2	G/V	Q330 45	Average	g
ES16Z	ES-T	3.7	3.7	0.9	1700	0.2	G/V	Q330 46	Average	g
ES16Y	ES-T	3.7	3.7	0.9	1700	0.2	G/V	Q330 47	Average	g
ES16X	ES-T	3.7	3.7	0.9	1700	0.2	G/V	Q330 48	Average	g
ES17Z	ES-U	3.7	3.7	1.8	526	0.2	G/V	Q330 49	Average	g
ES17Y	ES-U	3.7	3.7	1.8	557	0.2	G/V	Q330 50	Average	g
ES17X	ES-U	3.7	3.7	1.8	1043	0.2	G/V	Q330 51	Average	g
ES18Z	ES-T	8.5	3.7	0.9	1550	0.2	G/V	Q330 52	Average	g
ES18Y	ES-T	8.5	3.7	0.9	1550	0.2	G/V	Q330 53	Average	g
ES18X	ES-T	8.5	3.7	0.9	1550	0.2	G/V	Q330 54	Average	g
ES19Z	ES-U	19.8	1.8	0	563	0.2	G/V	Q330 55	Average	g
ES19Y	ES-U	19.8	1.8	0	566	0.2	G/V	Q330 56	Average	g
ES19X	ES-U	19.8	1.8	0	541	0.2	G/V	Q330 57	Average	g
ES20X	ES-U	27.4	1.8	0	562	0.2	G/V	Q330 58	Average	g
ES20Y	ES-U	27.4	1.8	0	564	0.2	G/V	Q330 59	Average	g
ES20X	ES-U	27.4	1.8	0	527	0.2	G/V	Q330 60	Average	g
ES21Z	ES-U	35.1	1.8	0	534	0.2	G/V	Q330 61	Average	g
ES21Y	ES-U	35.1	1.8	0	535	0.2	G/V	Q330 62	Average	g
ES21X	ES-U	35.1	1.8	0	548	0.2	G/V	Q330 63	Average	g
ES22Z	ES-U	6.1	11.3	0	528	0.2	G/V	Q330 64	Average	g
ES22Y	ES-U	6.1	11.3	0	1024	0.2	G/V	Q330 65	Average	g
ES22X	ES-U	6.1	11.3	0	559	0.2	G/V	Q330 66	Average	g
ES23Z	ES-U	6.1	18.9	0	540	0.2	G/V	Q330 67	Average	g
ES23Y	ES-U	6.1	18.9	0	523	0.2	G/V	Q330 68	Average	g
ES23X	ES-U	6.1	18.9	0	551	0.2	G/V	Q330 69	Average	g
ES24Z	ES-U	6.1	27.4	0	538	0.2	G/V	Q330 70	Average	g
ES24Y	ES-U	6.1	27.4	0	565	0.2	G/V	Q330 71	Average	g
ES24X	ES-U	6.1	27.4	0	567	0.2	G/V	Q330 72	Average	g
ES25X	ES-U	6.1	3.7	0.9	543	0.2	G/V	Q330 73	Average	g
ES26Z	ES-U	-80	1.8	0	544	0.2	G/V	Q330 85	Average	g
ES26Y	ES-U	-80	1.8	0	1045	0.2	G/V	Q330 86	Average	g
ES26X	ES-U	-80	1.8	0	555	0.2	G/V	Q330 87	Average	g

Table 4.2 (c):List of MEMS accelerometers, piezometers, and string potentiometers used in 2011 MK-15 shake tests.

Sensor ID	Sensor Type	Coordinates			Serial #	Calibration	Units	DAQ Channel ID	Offset	Units
		x(m)	y(m)	z(m)						
M1Z	MEMS	0.9	1.7	-0.9	C000176	1	G/V	Granite1 1	Average	g
M1Y	MEMS	0.9	1.7	-0.9	C000177	1	G/V	Granite1 2	Average	g
M1X	MEMS	0.9	1.7	-0.9	C000178	1	G/V	Granite1 3	Average	g
M2Z	MEMS	1.4	2	-2.7	C000177	1	G/V	Granite1 4	Average	g
M2Y	MEMS	1.4	2	-2.7	C000178	1	G/V	Granite1 5	Average	g
M2Z	MEMS	1.4	2	-2.7	C000179	1	G/V	Granite1 6	Average	g
M3Z	MEMS	2.7	1.7	-0.9	C000182	1	G/V	Granite1 7	Average	g
M3Y	MEMS	2.7	1.7	-0.9	C000183	1	G/V	Granite1 8	Average	g
M3X	MEMS	2.7	1.7	-0.9	C000184	1	G/V	Granite1 9	Average	g
M4Z	MEMS	2.7	2	-2.7	C000180	1	G/V	Granite1 10	Average	g
M4Y	MEMS	2.7	2	-2.7	C000181	1	G/V	Granite1 11	Average	g
M4X	MEMS	2.7	2	-2.7	C000182	1	G/V	Granite1 12	Average	g
M5Z	MEMS	5.2	1.7	-0.9	C000183	1	G/V	Granite2 1	Average	g
M5Y	MEMS	5.2	1.7	-0.9	C000184	1	G/V	Granite2 2	Average	g
M5X	MEMS	5.2	1.7	-0.9	C000185	1	G/V	Granite2 3	Average	g
M6Z	MEMS	5.2	2	-2.7	C000184	1	G/V	Granite2 4	Average	g
M6Y	MEMS	5.2	2	-2.7	C000185	1	G/V	Granite2 5	Average	g
M6X	MEMS	5.2	2	-2.7	C000186	1	G/V	Granite2 6	Average	g
M7Z	MEMS	7	1.7	-0.9	C000181	1	G/V	Granite2 7	Average	g
M7Y	MEMS	7	1.7	-0.9	C000182	1	G/V	Granite2 8	Average	g
M7X	MEMS	7	1.7	-0.9	C000183	1	G/V	Granite2 9	Average	g
M8Z	MEMS	7	2	-2.7	C000178	1	G/V	Granite2 10	Average	g
M8Y	MEMS	7	2	-2.7	C000179	1	G/V	Granite2 11	Average	g
M8X	MEMS	7	2	-2.7	C000180	1	G/V	Granite2 12	Average	g
P1	PPT	1.8	1.7	-2	1103768	82.433	kPa/V	Q330 83	-10.937	kPa
P2	PPT	1.8	2	-3.2	1103769	82.072	kPa/V	Q330 84	-9.9315	kPa
P3	PPT	6.1	1.7	-3.2	1103765	82.446	kPa/V	Q330 81	-10.195	kPa
P4	PPT	6.1	2	-2.31	1103767	82.196	kPa/V	Q330 80	-10.032	kPa
P5	PPT	0	0	0	1103766	82.19	kPa/V	Q330 79	-9.3905	kPa
Pot1	Stringpot	12.2	1.8	0	N/A	2	cm/V	Q330 89	Average	cm
Pot2	Stringpot	0	1.8	0	N/A	2	cm/V	Q330 90	Average	cm

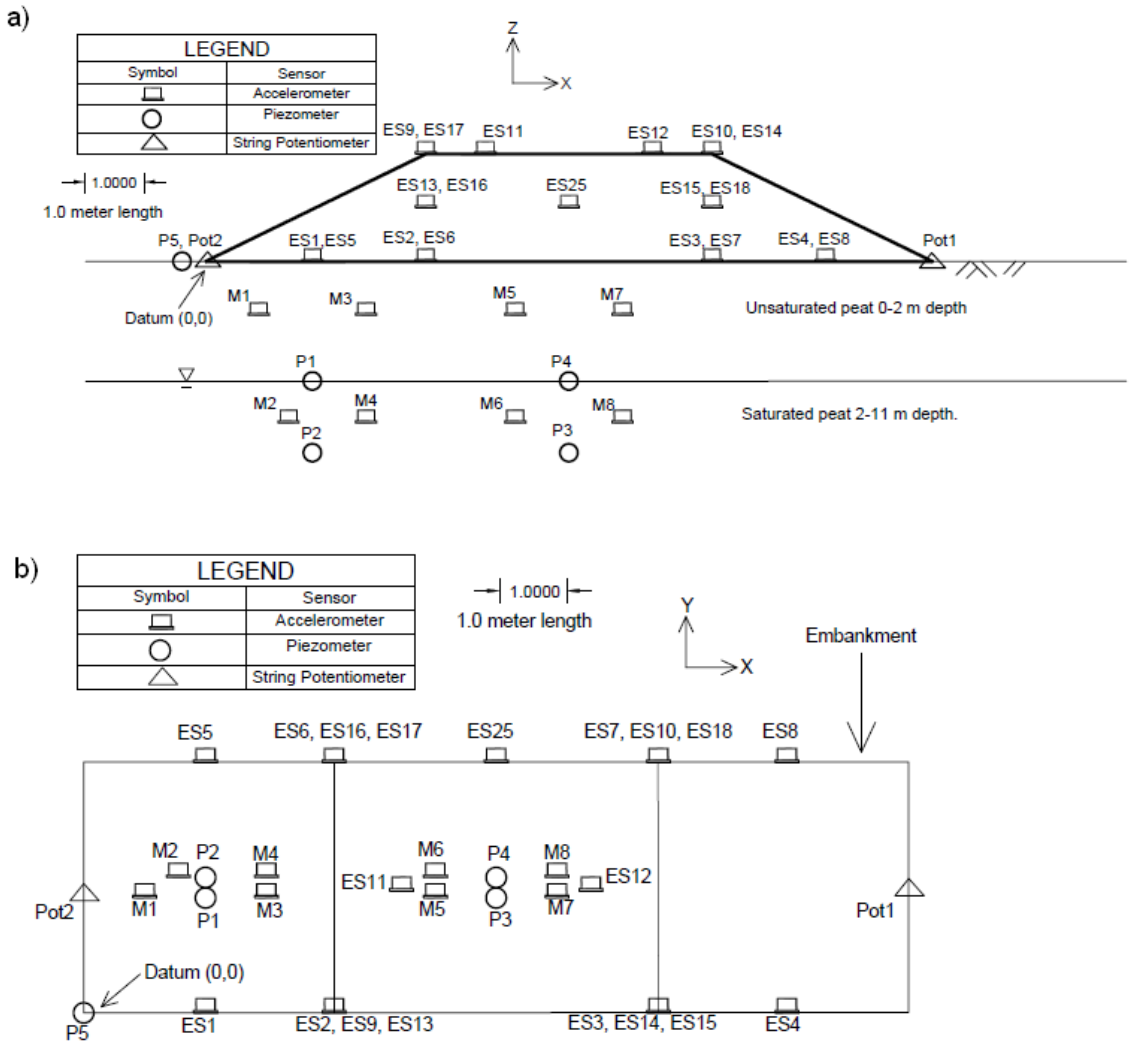

Figure 4.25: (a) Elevation and (b) plan view of the sensor layout used in the 2011 test. Shaker sketch omitted for clarity.

Figures 4.26 (a), (b), 4.27, and Table 4.3 show elevation and plan views and give properties of the sensors used during the August 2012 shake test. The sensor set up is very similar to the 2011 shake test setup, using the exact same sensors and sensor locations when possible. The above-ground accelerometers were placed in a similar array on the embankment and in the free-field, with minor adjustments in sensor location as needed. The main difference was the removal of the two string potentiometers and the addition of one co-located

accelerometer in the surface array (ES19A) due to suspicion of accelerometer ES19 being faulty. Some of the MEMS accelerometers were embedded less deeply in 2012 compared with 2011 because the project team removed the accelerometers following the 2011 test, and could not push them as deeply into the peat, which had become stiffer due to consolidation beneath the model levee. In addition, sensor M4 could not be retrieved the previous year, so one fewer MEMS accelerometer was recorded.

Table 4.3 (a):List of accelerometers ES1Z to ES14X used in the 2012 MK-15 shake tests

Sensor ID	Sensor Type	Coordinates			Serial #	Calibration	Units	DAQ Channel ID	Offset	Units
		x(m)	y(m)	z(m)						
ES1Z	ES-T	2.2	0.6	0	1442	0.2	G/V	Q330 1	Average	g
ES1Y	ES-T	2.2	0.6	0	1442	0.2	G/V	Q330 2	Average	g
ES1X	ES-T	2.2	0.6	0	1442	0.2	G/V	Q330 3	Average	g
ES2Z	ES-T	3.7	0	0	1191	0.2	G/V	Q330 4	Average	g
ES2Y	ES-T	3.7	0	0	1191	0.2	G/V	Q330 5	Average	g
ES2X	ES-T	3.7	0	0	1191	0.2	G/V	Q330 6	Average	g
ES3Z	ES-T	8.5	0	0	1445	0.2	G/V	Q330 7	Average	g
ES3Y	ES-T	8.5	0	0	1445	0.2	G/V	Q330 8	Average	g
ES3X	ES-T	8.5	0	0	1445	0.2	G/V	Q330 9	Average	g
ES4Z	ES-T	11	0	0	1446	0.2	G/V	Q330 10	Average	g
ES4Y	ES-T	11	0	0	1446	0.2	G/V	Q330 11	Average	g
ES4X	ES-T	11	0	0	1446	0.2	G/V	Q330 12	Average	g
ES5Z	ES-T	2.1	3.7	0	1702	0.2	G/V	Q330 13	Average	g
ES5Y	ES-T	2.1	3.7	0	1702	0.2	G/V	Q330 14	Average	g
ES5X	ES-T	2.1	3.7	0	1702	0.2	G/V	Q330 15	Average	g
ES6Z	ES-T	3.7	3.7	0	1444	0.2	G/V	Q330 16	Average	g
ES6Y	ES-T	3.7	3.7	0	1444	0.2	G/V	Q330 17	Average	g
ES6X	ES-T	3.7	3.7	0	1444	0.2	G/V	Q330 18	Average	g
ES7Z	ES-U	9.1	3.7	0	528	0.2	G/V	Q330 52	Average	g
ES7Y	ES-U	9.1	3.7	0	1042	0.2	G/V	Q330 53	Average	g
ES7X	ES-U	9.1	3.7	0	559	0.2	G/V	Q330 54	Average	g
ES8Z	ES-T	11.3	3.7	0.6	3813	0.2	G/V	Q330 22	Average	g
ES8Y	ES-T	11.3	3.7	0.6	3813	0.2	G/V	Q330 23	Average	g
ES8X	ES-T	11.3	3.7	0.6	3813	0.2	G/V	Q330 24	Average	g
ES9Z	ES-U	3.7	0	1.8	538	0.2	G/V	Q330 25	Average	g
ES9Y	ES-U	3.7	0	1.8	565	0.2	G/V	Q330 26	Average	g
ES9X	ES-U	3.7	0	1.8	567	0.2	G/V	Q330 27	Average	g
ES10Z	ES-U	8.5	3.7	1.8	530	0.2	G/V	Q330 49	Average	g
ES10Y	ES-U	8.5	3.7	1.8	546	0.2	G/V	Q330 50	Average	g
ES10X	ES-U	8.5	3.7	1.8	532	0.2	G/V	Q330 51	Average	g
ES11Z	ES-T	4.7	1.8	1.8	1703	0.2	G/V	Q330 37	Average	g
ES11Y	ES-T	4.7	1.8	1.8	1703	0.2	G/V	Q330 38	Average	g
ES11X	ES-T	4.7	1.8	1.8	1703	0.2	G/V	Q330 39	Average	g
ES12Z	ES-T	7.5	1.8	1.8	1886	0.2	G/V	Q330 40	Average	g
ES12Y	ES-T	7.5	1.8	1.8	1886	0.2	G/V	Q330 41	Average	g
ES12X	ES-T	7.5	1.8	1.8	1886	0.2	G/V	Q330 42	Average	g
ES13Z	ES-T	3.8	0	0.9	1190	0.2	G/V	Q330 28	Average	g
ES13Y	ES-T	3.8	0	0.9	1190	0.2	G/V	Q330 29	Average	g
ES13X	ES-T	3.8	0	0.9	1190	0.2	G/V	Q330 30	Average	g
ES14Z	ES-U	8.5	0	1.8	534	0.2	G/V	Q330 31	Average	g
ES14Y	ES-U	8.5	0	1.8	535	0.2	G/V	Q330 32	Average	g
ES14X	ES-U	8.5	0	1.8	548	0.2	G/V	Q330 33	Average	g

Table 4.3 (b):List of accelerometers ES15Z to ES26X used in the 2012 MK-15 shake tests

Sensor ID	Sensor Type	Coordinates			Serial #	Calibration	Units	DAQ Channel ID	Offset	Units
		x(m)	y(m)	z(m)						
ES15Z	ES-T	8.5	0	0.9	1883	0.2	G/V	Q330 34	Average	g
ES15Y	ES-T	8.5	0	0.9	1883	0.2	G/V	Q330 35	Average	g
ES15X	ES-T	8.5	0	0.9	1883	0.2	G/V	Q330 36	Average	g
ES16Z	ES-T	3.7	3.7	0.9	1700	0.2	G/V	Q330 43	Average	g
ES16Y	ES-T	3.7	3.7	0.9	1700	0.2	G/V	Q330 44	Average	g
ES16X	ES-T	3.7	3.7	0.9	1700	0.2	G/V	Q330 45	Average	g
ES17Z	ES-U	3.7	3.7	1.8	526	0.2	G/V	Q330 46	Average	g
ES17Y	ES-U	3.7	3.7	1.8	557	0.2	G/V	Q330 47	Average	g
ES17X	ES-U	3.7	3.7	1.8	1043	0.2	G/V	Q330 48	Average	g
ES18Z	ES-T	10.7	3.7	0.9	3849	0.2	G/V	Q330 19	Average	g
ES18Y	ES-T	10.7	3.7	0.9	3849	0.2	G/V	Q330 20	Average	g
ES18X	ES-T	10.7	3.7	0.9	3849	0.2	G/V	Q330 21	Average	g
ES19Z	ES-T	19.8	1.8	0	1193	0.2	G/V	Q330 55	Average	g
ES19Y	ES-T	19.8	1.8	0	1193	0.2	G/V	Q330 56	Average	g
ES19X	ES-T	19.8	1.8	0	1193	0.2	G/V	Q330 57	Average	g
ES19AZ	ES-T	19.8	1.8	0	1192	1.2	G/V	Q330 88	Average	g
ES19AY	ES-T	19.8	1.8	0	1192	2.2	G/V	Q330 89	Average	g
ES19AX	ES-T	19.8	1.8	0	1192	3.2	G/V	Q330 90	Average	g
ES20X	ES-U	27.4	1.8	0	562	0.2	G/V	Q330 61	Average	g
ES20Y	ES-U	27.4	1.8	0	564	0.2	G/V	Q330 62	Average	g
ES20X	ES-U	27.4	1.8	0	527	0.2	G/V	Q330 63	Average	g
ES21Z	ES-U	35.1	1.8	0	563	0.2	G/V	Q330 64	Average	g
ES21Y	ES-U	35.1	1.8	0	566	0.2	G/V	Q330 65	Average	g
ES21X	ES-U	35.1	1.8	0	541	0.2	G/V	Q330 66	Average	g
ES22Z	ES-T	6.1	11.3	0	1550	0.2	G/V	Q330 58	Average	g
ES22Y	ES-T	6.1	11.3	0	1550	0.2	G/V	Q330 59	Average	g
ES22X	ES-T	6.1	11.3	0	1550	0.2	G/V	Q330 60	Average	g
ES23Z	ES-U	6.1	18.9	0	540	0.2	G/V	Q330 67	Average	g
ES23Y	ES-U	6.1	18.9	0	523	0.2	G/V	Q330 68	Average	g
ES23X	ES-U	6.1	18.9	0	551	0.2	G/V	Q330 69	Average	g
ES24Z	ES-U	6.1	27.4	0	544	0.2	G/V	Q330 70	Average	g
ES24Y	ES-U	6.1	27.4	0	1045	0.2	G/V	Q330 71	Average	g
ES24X	ES-U	6.1	27.4	0	555	0.2	G/V	Q330 72	Average	g
ES25X	ES-U	6.1	3.7	0.9	543	0.2	G/V	Q330 73	Average	g
ES26Z	ES-T	-80.2	1.8	0	1189	0.2	G/V	Q330 85	Average	g
ES26Y	ES-T	-80.2	1.8	0	1189	0.2	G/V	Q330 86	Average	g
ES26X	ES-T	-80.2	1.8	0	1189	0.2	G/V	Q330 87	Average	g

Table 4.3 (c):List of MEMS accelerometers and piezometers used in 2011 MK-15 shake

Sensor ID	Sensor Type	Coordinates			Serial #	Calibration	Units	DAQ Channel ID	Offset	Units
		x(m)	y(m)	z(m)						
M1Z	MEMS	0.9	1.7	-1.8	C000176	1	G/V	Granite1 1	Average	g
M1Y	MEMS	0.9	1.7	-1.8	C000177	1	G/V	Granite1 2	Average	g
M1X	MEMS	0.9	1.7	-1.8	C000178	1	G/V	Granite1 3	Average	g
M2Z	MEMS	1.4	2	-0.6	C000177	1	G/V	Granite1 4	Average	g
M2Y	MEMS	1.4	2	-0.6	C000178	1	G/V	Granite1 5	Average	g
M2Z	MEMS	1.4	2	-0.6	C000179	1	G/V	Granite1 6	Average	g
M3Z	MEMS	2.7	1.7	-0.7	C000182	1	G/V	Granite1 7	Average	g
M3Y	MEMS	2.7	1.7	-0.7	C000183	1	G/V	Granite1 8	Average	g
M3X	MEMS	2.7	1.7	-0.7	C000184	1	G/V	Granite1 9	Average	g
M5Z	MEMS	5.2	1.7	-0.9	C000183	1	G/V	Granite1 10	Average	g
M5Y	MEMS	5.2	1.7	-0.9	C000184	1	G/V	Granite1 11	Average	g
M5X	MEMS	5.2	1.7	-0.9	C000185	1	G/V	Granite1 12	Average	g
M6Z	MEMS	5.2	2	-2.7	C000184	1	G/V	Granite2 1	Average	g
M6Y	MEMS	5.2	2	-2.7	C000185	1	G/V	Granite2 2	Average	g
M6X	MEMS	5.2	2	-2.7	C000186	1	G/V	Granite2 3	Average	g
M7Z	MEMS	7	1.7	-0.6	C000181	1	G/V	Granite2 5	Average	g
M7Y	MEMS	7	1.7	-0.6	C000182	1	G/V	Granite2 6	Average	g
M7X	MEMS	7	1.7	-0.6	C000183	1	G/V	Granite2 7	Average	g
M8Z	MEMS	7	2	-2.7	C000178	1	G/V	Granite2 9	Average	g
M8Y	MEMS	7	2	-2.7	C000179	1	G/V	Granite2 10	Average	g
M8X	MEMS	7	2	-2.7	C000180	1	G/V	Granite2 11	Average	g
P1	PPT	1.8	1.7	-2	1103768	82.433	kPa/V	Q330 82	-10.937	kPa
P2	PPT	1.8	2	-3.2	1103769	82.072	kPa/V	Q330 83	-9.9315	kPa
P3	PPT	6.1	1.7	-3.2	1103765	82.446	kPa/V	Q330 81	-10.195	kPa
P4	PPT	6.1	2	-2.31	1103767	82.196	kPa/V	Q330 80	-10.032	kPa
P5	PPT	0	0	0	1103766	82.19	kPa/V	Q330 79	-9.3905	kPa

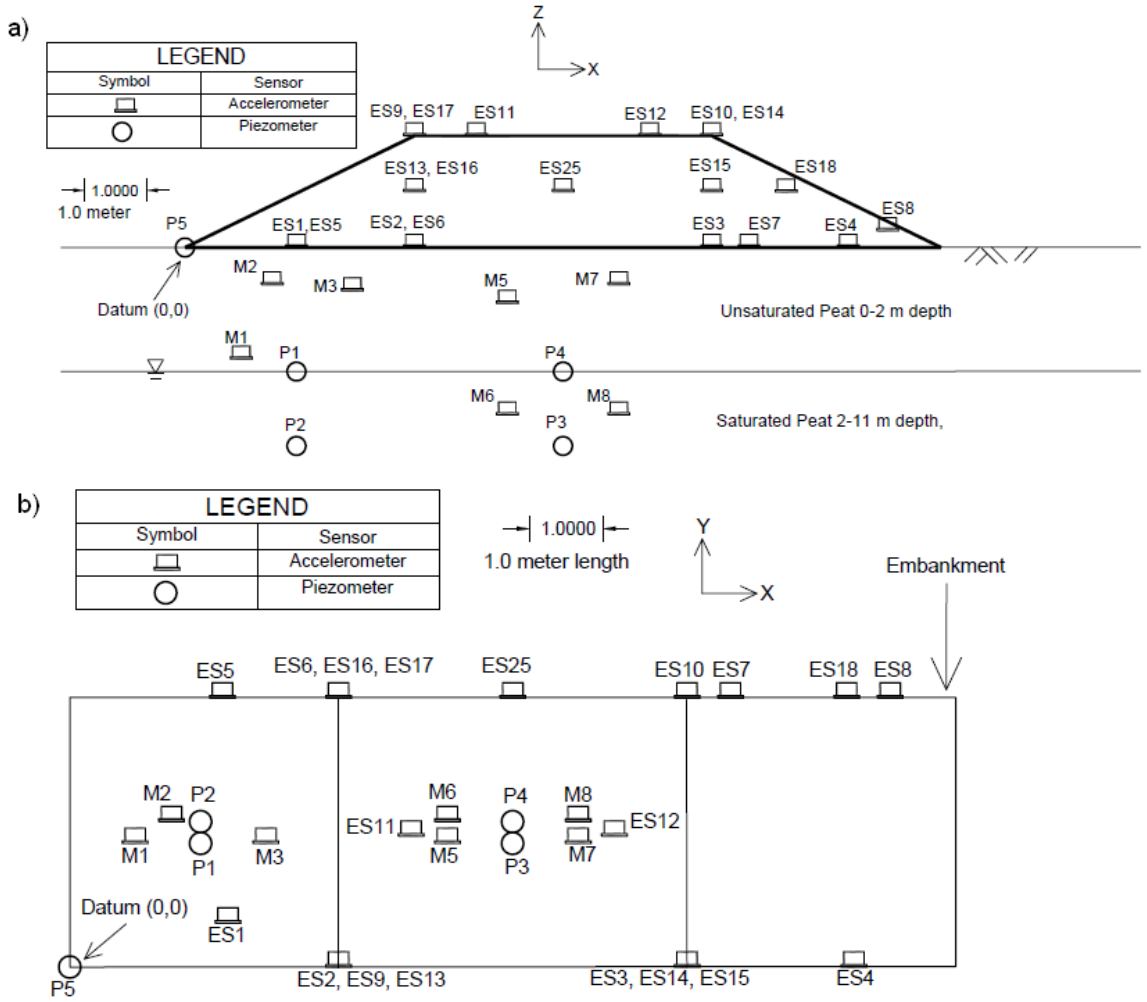

Figure 4.26: (a) Elevation and (b) plan view of the sensor layout used during the 2012 test. Shaker sketch omitted for clarity.

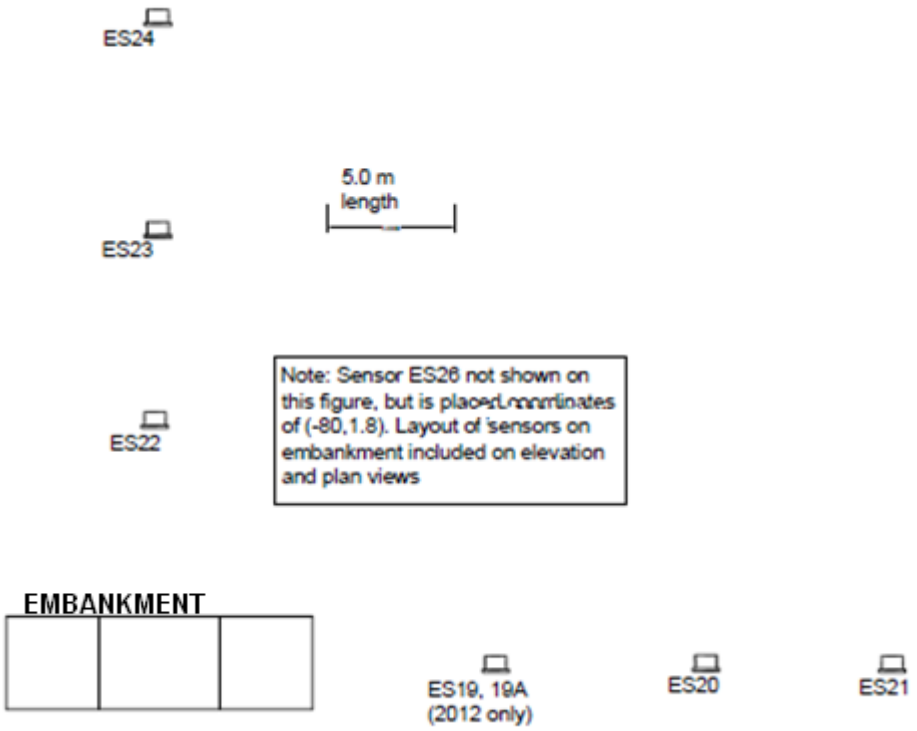

Figure 4.27: Surface array of accelerometers.

The data acquisition systems used to collect these data consisted of fifteen Kinemetrics Q330 data loggers (six channels each), which recorded all data except the MEMS accelerometer data, which were recorded on two Kinemetrics Granite data loggers. The piezometers and string potentiometers were disconnected from the remote DAQ system during dynamic testing and connected to Q330 data loggers so that data could be recorded at high frequency and synchronized with other recorded data. Test data was recorded at a sampling frequency of 200Hz. In all, 108 and 105 channels of data were recorded during the 2011 and 2012 tests, respectively.

4.3.2. Dynamic Shake Testing and Data

Shake testing on the model levee was performed with two sets of shakers: the high-

amplitude NEES@UCLA MK-15 eccentric mass shaker, capable of shaking up to 5 Hz, and the much smaller amplitude Atom Ant linear mass shaker, capable of shaking up to 100 Hz. Tables 4.4 – 4.6 summarize the sequence of motions imposed by both the MK-15 and Atom Ant shaker on the test embankment during the 2011 and 2012 shake events. In 2011, a series of 19 MK-15 motions and 8 Atom Ant motions were imposed on the embankment, while in 2012, 23 MK-15 motions were imposed. The Atom Ant shaker was broken during the 2012 test, and was therefore not used.

Table 4.4 – 2011 MK-15 Shake Sequence

Trial	Repetition	Date	Repetition Start Time PDT	Repetition Duration (s)	Frequency Function	Max. Shaker Frequency (Hz)	Shaker Eccentricity, $m_r r$ (Mg-m)
1	1	8/27/2011	14:50:00	80	Step Sweep	5.12	0.0589
1	2	8/27/2011	15:07:00	80	Step Sweep	5.13	
1	3	8/28/2011	11:49:00	360	Frequency Sweep	5.11	
1	4	8/28/2011	12:00:30	120	Frequency Sweep	5.11	
1	5	8/28/2011	12:05:30	115	Step Sweep	4.16	
1	6	8/28/2011	12:09:30	180	Dwell Sweep	3.08	
2	1	8/28/2011	12:51:30	360	Frequency Sweep	4.16	0.126
2	2	8/28/2011	13:05:30	120	Frequency Sweep	4.08	
2	3	8/28/2011	13:10:30	100	Step Sweep	3.12	
2	4	8/28/2011	13:14:30	180	Dwell Sweep	3.13	
3	1	8/29/2011	9:47:30	360	Frequency Sweep	3.13	0.251
3	2	8/29/2011	9:57:30	120	Frequency Sweep	3.12	
3	3	8/29/2011	10:04:30	125	Step Sweep	3.12	
3	4	8/29/2011	10:08:30	180	Dwell Sweep	3.13	
4	1	8/29/2011	10:57:30	120	Frequency Sweep	3.03	0.362
4	2	8/29/2011	11:32:30	360	Frequency Sweep	2.93	
5	1	8/29/2011	14:04:30	120	Frequency Sweep	2.5	0.517
5	2	8/29/2011	14:17:30	120	Frequency Sweep	2.74	
5	3	8/29/2011	14:31:30	120	Frequency Sweep	2.74	

Table 4.5 – 2012 MK-15 Shake Sequence

Trial	Repetition	Date	Repetition Start Time PDT	Repetition Duration (s)	Frequency Function	Max. Shaker Frequency (Hz)	Eccentricity Constant, $m_r r$ (Mg-m)
1	1	8/14/2012	14:10:00	360	Frequency Sweep	5.00	0.0589
1	2	8/14/2012	14:31:00	120	Frequency Sweep	3.17	
1	3	8/14/2012	14:38:00	100	Step Sweep	3.12	
1	4	8/14/2012	14:43:00	180	Dwell Sweep	3.17	
2	1	8/14/2012	15:23:00	360	Frequency Sweep	3.13	0.126
2	2	8/14/2012	15:32:00	120	Frequency Sweep	3.13	
2	3	8/14/2012	15:36:00	100	Step Sweep	3.12	
2	4	8/14/2012	15:39:00	180	Dwell Sweep	3.13	
3	1	8/15/2012	11:01:00	360	Frequency Sweep	2.22	0.251
3	2	8/15/2012	11:10:00	360	Frequency Sweep	3.08	
3	3	8/15/2012	11:18:00	120	Frequency Sweep	3.08	
3	4	8/15/2012	11:22:00	100	Step Sweep	3.08	
3	5	8/15/2012	11:25:00	180	Dwell Sweep	3.13	
4	1	8/15/2012	12:03:00	360	Frequency Sweep	0.65	0.362
4	2	8/15/2012	12:10:00	360	Frequency Sweep	2.9	
4	3	8/15/2012	12:33:00	120	Frequency Sweep	2.53	
4	4	8/15/2012	12:43:00	85	Step Sweep	2.56	
5	1	8/15/2012	13:16:00	120	Frequency Sweep	2.7	0.517
5	2	8/15/2012	13:23:00	360	Frequency Sweep	2.6	
5	3	8/15/2012	13:43:00	150	Step Sweep	2.6	
5	4	8/15/202	13:54:00	120	Frequency Sweep	2.53	
6	1	8/15/2012	15:44:00	120	Frequency Sweep	2.38	0.568
6	2	8/15/2012	15:52:00	180	Dwell Sweep	2.38	

Before proceeding with the shake sequence and dynamic test data, it is important to understand the organization of the experimental tests seen in Tables 4.4 – 4.6. First, the test data archived on NEEShub is organized into Experiments, Trials, and Repetitions in conformance with NEEShub data archiving standards, as summarized in Table 4-7. Experiments are separate components of a NEES project, which include physical experiments, simulations, and hybrid simulations. This project consists of 8 Experiments. Trials are different configurations of a sample within an experiment, and repetitions are experimental tests of the same configuration. Seven of the experiments are curated (i.e. archived according to NEEShub requirements) and have been issued digital object identifiers (DOI's). Experiments 3 through 6 were collected during the 2011 tests, and Experiments 7 through 9 were collected during the 2012 test. Each of these tests has an Experiment corresponding to the MK-15 shaker testing, an Experiment for SASW testing, and an Experiment containing continuous raw data files. The 2011 test has an additional experiment corresponding to Atom Ant testing (the Atom Ant shaker was unavailable during the 2012 test). Experiments 3 and 7, corresponding to the MK-15 shaker tests, are the most useful for potential users of the data set, and will be the main focus of this dissertation. Experiment 2 contains a report summarizing the geophysical study conducted in March 2010. Unfortunately, inadequate metadata were collected for this experiment (e.g., sensor serial numbers and precise locations), and the data are therefore not archived. Nevertheless, the geophysical report is an important component of the project, and the report is therefore available. Second, it is important to note that the $m_r r$ value given in Tables 4.4 and 4.5 correspond to an eccentricity value used to calculate the forced imposed on the model levee from the MK-15 shaker. Further details on calculation of the shaker force are given in section 4.3.3.

Table 4.6: Shake sequence for 2011 Atom Ant shake sequence.

Trial	Repetition	Date	Repetition Start Time PDT (Approx)	Repetition Duration (s)	Data File(s) for Each Event	Repetition Notes
1	1	8/28/2011	15:02:00	10	20110828220000.LVEE.txt	Fast Sweep 3 to 50 Hz.
1	2	8/28/2011	15:05:00	60	20110828220000.LVEE.txt	Slow Sweep 3 to 50 Hz
1	3	8/28/2011	15:07:00	480	20110828220000.LVEE.txt	Step 3 to 50 Hz, 10 sec. per step, 1Hz step size
1	4	8/28/2011	15:16:00	480	20110828220000.LVEE.txt	Shake at 3 Hz for 10 minutes
1	1	8/28/2011	14:47:30	10	20110829210000.LVEE.txt	Fast Sweep 3 to 50 Hz.
1	2	8/28/2011	14:49:00	60	20110829210000.LVEE.txt	Slow Sweep 3 to 50 Hz
1	3	8/28/2011	14:50:30	480	20110829210000.LVEE.txt	Step 3 to 50 Hz, 10 sec. per step, 1Hz step size

In general, three types of forcing functions were imposed on the embankment by the shakers: frequency sweeps, step sweeps, and dwell sweeps, as seen in Fig. 4.28. Frequency sweeps were intended to shake the embankment at increasing frequency until a target frequency was reached, and were either fast (100-120 seconds) or slow (300-360 seconds), as seen in Fig. 4.28 (a). Step sweeps consisted of ramping up the frequency to a specified target frequency, exciting the shaker at this frequency for a specified duration of time, usually 10 seconds, and subsequently ramping up to a new frequency and repeating this procedure until reaching a target maximum frequency, as seen in Fig. 4.28 (b). Dwell sweeps consisted of exciting the shaker at a constant frequency for an extended period of time, as seen in Fig. 4.28 (c).

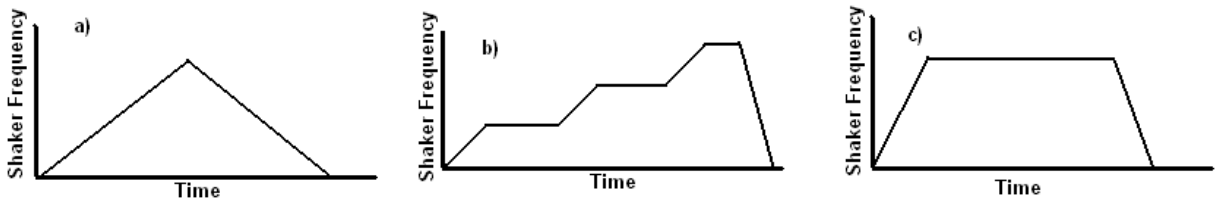

Figure 4.28: Schematic representation of shaker frequency for a) frequency sweep, b) step sweep, c) dwell sweep.

The procedure for performing each shake was: 1) the student would tell the project team which motion was desired, 2) the project team would then load the motion into the controller software, 3) the student and the project team would then decide a specific time when shaking would start, 4) the student would notify observers shortly before the shaking started using a loud airhorn beep, 5) the project team would begin recording shaker data on the NI acquisition system, 6) shaking would occur.

The raw data recorded during the shake tests consisted of hour-long blocks of data from each of the three data acquisition systems used. During a particular hour, multiple trials and repetitions could occur, which poses a logistical problem with respect to the NEEShub metadata architecture since the unprocessed raw data as it comes from the computer does not map one-to-one to a particular trial or repetition. Portions of these hour long data files corresponding to a particular repetition were extracted, and uploaded as raw data for the appropriate experiment/trial/repetition. Additionally, experiments were created for the hour-long raw data files as well (Experiment 6 for data collected during the 2011 tests, and Experiment 9 for data collected during the 2012 tests) as a complete record of all of the recorded data. Much of these hour-long blocks of data correspond to times when the shakers were not operating, but the ambient data may nevertheless be useful to potential users. However, it is expected that most users of our data will choose to work with the corrected data files. In order to extract the desired

data from the hour long blocks, a program (snippet.exe) was developed in C++ to read in the start time and duration of the shake (with 5-10 seconds extra before and after each shake), convert that time to the UNIX timestamp, and then extract the data corresponding to that timestamp and save it in a separate file. This was done separately for the Q330, Granite1, and Granite 2 data acquisition systems. Next, the files were merged together to create one single raw data file for each test. These raw data did not have a header containing data channel number and units, as became required by NEEShub after our data were processed. Rather than taking the significant time and effort to add this header to each data file, a text file containing the header information was copied into each unprocessed data folder.

The order in which the data columns were saved in the raw data files corresponded to both the amplifier channels and the data acquisition system to which each sensor was connected, but did not correspond to the logical sensor numbering scheme adopted in Tables 4.2 – 4.3. In the converted data files, the data columns were sorted by sensor label to facilitate ease of data interpretation. The 2011 tests were sorted such that the first column contained the time vector, the next 76 columns contain accelerometers ES1-ES26, the next 24 columns contain MEMS accelerometers M1-M8, the next single column contained the command frequency sent to the MK-15 shaker (not included in the sensor list, as it is not a sensor), the next 5 columns contain pore pressure transducers P1-P5, and the final two columns contain the string potentiometers. The data column scheme was slightly different for the 2012 tests, and were sorted such that the first column contains the time vector, the next 79 columns contain accelerometers ES1-ES26, the next 21 columns contain MEMS accelerometers M1-M8, the single column denoting shaker input frequency, and the last 5 columns contain piezometers P1-P5.

In order to convert the data to engineering units from their raw state as bitcounts, the sorted data first had to be converted to voltage. In this case, the conversion factor from bitcount to input voltage was $40/2^{24}$ Volts/bit to account for the 24-bit A/D conversion and the ±20V sensor output range. The next step was to apply the calibration factors as seen in tables 4.2 – 4.3 to convert from volts to engineering units. In this case, the calibration factors used for both the EpiSensor and the MEMS accelerometers came from the NEES@UCLA staff based on manufacturer specifications. The piezometers were calibrated before testing, and those values were used for conversion to engineering units. In this step, the recorded data was also adjusted from the local sensor coordinates to the global coordinate system. Looking at Fig. 4.25 and 4.26, the sign conventions in the global coordinate system were set to: horizontal (X) acceleration is positive from left to right, horizontal (Y) acceleration is positive pointing into the page, and vertical acceleration is positive upward.

Once the data was converted, offsets were then applied to the data to represent a logical starting point, as physical zero does not always correspond to zero voltage. First, the mean value was subtracted from each accelerometation record. Second method, the piezometers were offset based on the voltage associated with zero (atmospheric) pressure defined during sensor calibration. These values are summarized in Tables 4.2 – 4.3.

The extracted, sorted, converted, offset data were written to ASCII text files. A Mathcad routine was used to plot the data. Example data from one shake test can be seen in Figs. 4.29 – 4.31 for selected sensors. The purpose of showing the data is to illustrate data quality, and to provide a reference to aid users of our data who wish to verify that they are correctly plotting and interpreting the data files from NEEShub. Figure 4.29 shows horizontal acceleration in the *x*-

direction at the top and bottom of the model levee and in the underlying peat at depths of 0.9m and 2.7m. These records are for Experiment 3, Trial 2, Repetition 2, in which a sweep function was imposed by the MK.15 shaker. The maximum frequency was 3Hz, and the shaker reached this frequency at 64 s. The acceleration records exhibit a characteristic shape in which the amplitude increases as frequency increases. Accelerations are largest at the crest of the levee, with a peak of 0.11g, and amplitude decreases with depth. The lack of symmetry in the acceleration histories was caused by pounding between the shaker frame and the levee fill. The decrease in acceleration amplitude with depth is influenced by the top-down shaking condition imposed by forced vibration testing.

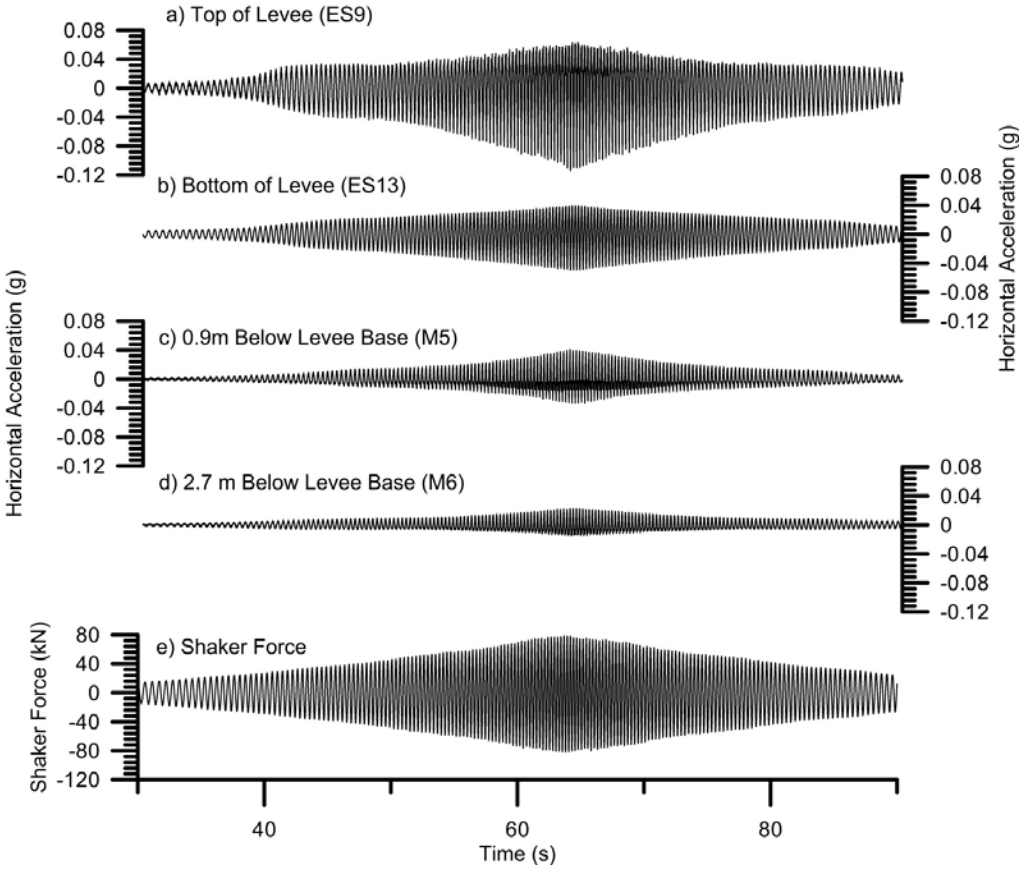

Figure 4.29: Horizontal acceleration recorded at various depths for sweep function during Experiment 3, Trial 2, Repetition 2 for the 2011 test sequence.

Fig. 4.30 shows vertical-component ground accelerations at various distances from the embankment in the *x*-direction. These records are for Experiment 3, Trial 4, Repetition 1, in which a large-amplitude sweep function was applied by the MK-15 shaker. The maximum frequency of 3Hz was reached at approximately 48 s. The largest acceleration was recorded at the embankment toe, and acceleration amplitude decreased with distance from the model levee. The ground surface motions recorded in the free-field are likely dominated by Rayleigh waves in the x-direction array and Love waves in the y-direction array. Attenuation of the waves with distance results from both geometric spreading of the wavefronts and material damping.

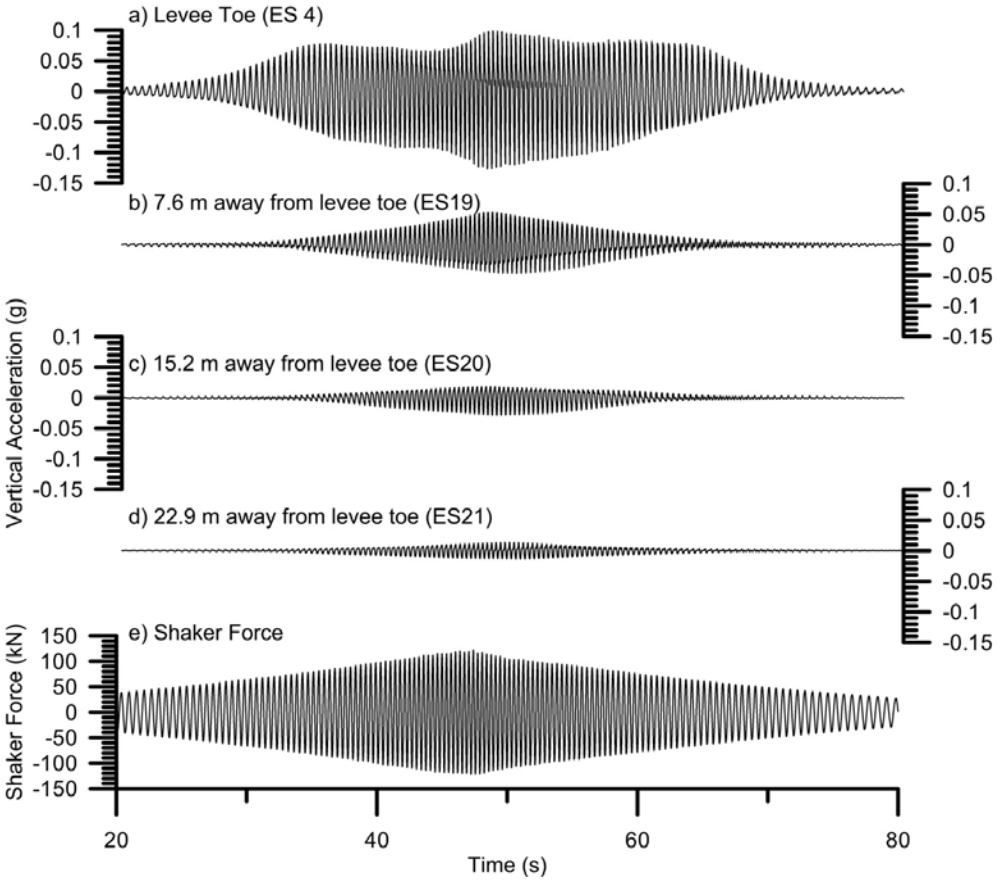

Figure 4.30: Vertical acceleration recorded on surface at various distances for sweep function during Experiment 3, Trial 4, Repetition 1 for the 2011 test sequence.

Fig. 4.31 shows a pore pressure record obtained in the peat beneath the levee at a depth of 3.2m during a sweep function from Experiment 3, Trial 4, Repetition 1. The pore pressures exhibit dynamic responses, which indicate that the sensors were responsive to the dynamic conditions during shaking, in turn suggesting the sensors were well-saturated. Unsaturated piezometers often exhibit poor response at high frequency due to the compressibility of the gas in contact with the transducer. In addition to the dynamic response, the pore pressures slowly increase during shaking by nearly 0.3 kPa from the beginning to the end of the test. Interestingly, pore pressures continue to increase after shaking ends. These small increases in pore pressure are smaller than the long-term fluctuations that are associated with pumping operations to control the groundwater level on Sherman Island. However, the shaking events occur during much shorter time scales compared with groundwater fluctuations, and pore pressure increases were repeatable for the large intensity events. These observations indicate that the pore pressures were caused by shearing induced by shaking, and not by fluctuations in ground water level.

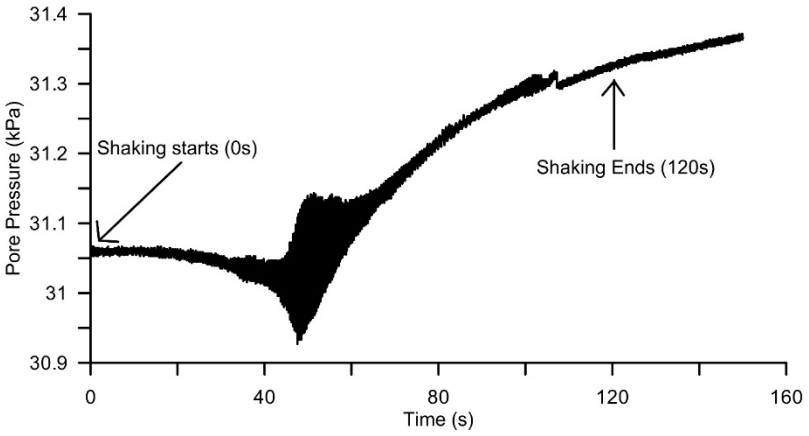

Figure 4.31: Pore pressure recorded in the peat at a depth of 3.2m from sensor P3 Experiment 3, Trial 4, Repetition 1.

4.3.3. Calculation of Shaker Force

This section has been adapted from the work presented in Reinert et al. (2012) for use in this dissertation.

The force imposed by the eccentric mass shaker is a function of the rotating mass, the angular frequency, the position of the baskets, and the acceleration of the base of the shaker in response to the imposed force. Equation 4.8 defines the shaker force in the +X direction, where m_b is the non-rotating shaker mass, m_r is the rotating mass, $a_{b,x}$ is the acceleration of the shaker base in the +X direction, r is the radius from the center of rotation to the centroid of the rotating mass, ω is the angular frequency, and θ is the angular position of the rotating mass.

$$F_{shk} = \left(m_b + m_r\right) a_{b,x} + m_r r \omega^2 \cos\theta \qquad \text{.. Eq. 4.8}$$

The position of the rotating masses is recorded using two proximity sensors that measure the passage of steel pins mounted on circular plates affixed near the pivots (Fig. 4-32). One plate contains ten pins evenly distributed around the circumference of the steel plate for the purpose of accurately measuring ω, and the other plate contains a single pin for the purpose of accurately measuring θ. As each pin passes within range of the proximity sensor, the recorded voltage jumps from 0 to 10 VDC, thereby producing a sequence of pulses. The plate with a single pin is configured such that the rotating masses are aligned in the +X direction when the pulse occurs. The plate with 10 pins is ill equipped for measuring position because the recorded pulses cannot be mapped to individual pin positions. However, this plate provides a means for accurately computing angular frequency by measuring the time that elapses between pulses.

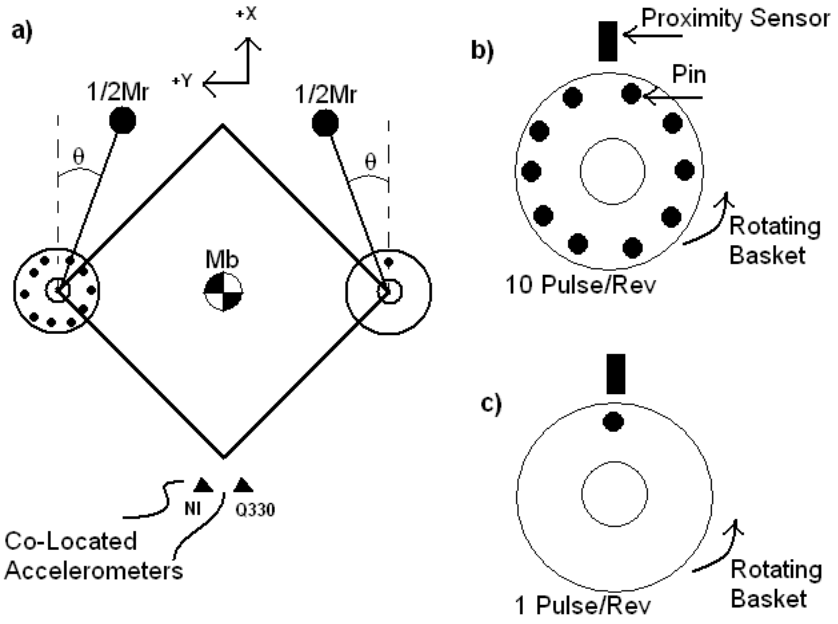

Figure 4-32: MK-15 eccentric mass shaker instrumentation detail.

The data for the proximity sensors are recorded uisng a National Instruments data acquisition system with a sampling frequency of 2000 Hz. The National Instruments system is manually triggered to begin recording a few seconds before the command is sent to commence rotation of the shaker baskets. A different data acquisition system is used to continuously record data from the accelerometers, pore pressure transducers, and string potentiometers, and the National Instruments data is therefore not time-synchronized with the other recorded quantities. Co-located accelerometers, one recorded by the National Instruments system, and the other recorded by the Q330 system, are used to synchronize the data from the two different systems. Frequency-domain cross-correlation of the records from the co-located accelerometers is used to align the shaker force function with the other recorded data.

Fig. 4.33 shows example data recorded from the proximity sensors during one of the shake tests. The voltage from the proximity sensor for the plate with 10 pins begins at 10 V,

which indicates that the shaker was initially oriented such that one of the pins was within range of the proximity sensor. The voltage subsequently drops to zero as the pin passes out of range, and then rapidly increases to ten volts again as the next pin moves into range. The duration of the pulses decreases with time as the angular frequency increases. The pulses recorded for the plate with a single pin indicate times when the baskets are oriented in the +X direction.

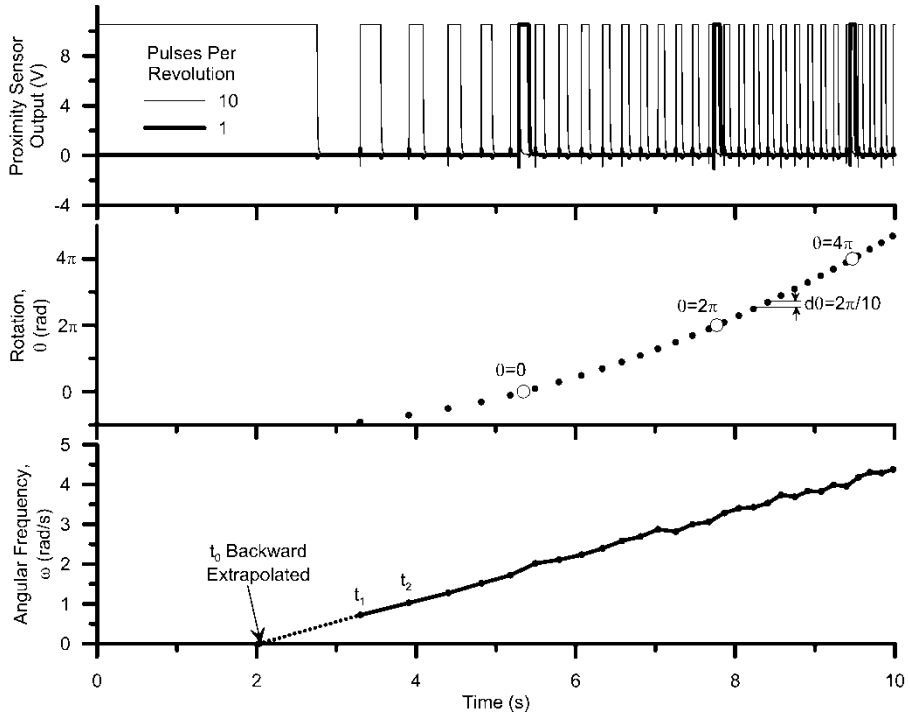

Figure 4.33: Pulses recorded from proximity sensors, and computed rotation and angular frequency.

Fig. 4.33 also shows rotation angle versus time computed from the proximity sensor data. The incremental rotation corresponding to each pulse recorded for the plate with 10 pins is equal to $2\pi/10$. A constant is subsequently subtracted from the computed rotation angle so that θ is zero at the time when the center of the first pulse is recorded for the plate with a single pin. Angular frequency is computed from the rotation angle data using numerical differentiation defined by the backward Euler equation $\omega_i=(\theta_i-\theta_{i-1})/(t_i-t_{i-1})$. Note that the time when the shaker begins

moving is not known, and is backward extrapolated by linear extension of angular frequency versus time.

The recorded proximity sensor data have now been converted into time series of θ and ω discretized into uneven time intervals corresponding to 10 data points per cycle, and the shaker force can be computed at these same unevenly sampled time intervals. However, it is desired to compute the shaker force at time intervals corresponding to the acceleration, pore pressure, and displacement data sampled at a constant frequency of 200 Hz using the Q330 data system. The simplest method involves linear interpolation of the shaker forcing function at the discrete times when samples were recorded for the other sensors. The problem with this method is that the shaker force is not anticipated to vary linearly in time; rather, it is the angular frequency that is anticipated to vary linearly in time in accordance with the command function. For this reason, a more complex cosine sweep function is utilized to interpolate the unevenly sampled shaker force data at a time t_k (Eq. 4.9), where the index i indicates the unevenly sampled rotation data, index k indicates the discrete times at which shaker forces (and related quantities) are evaluated, ω_k is linearly interpolated at t_k from the unevenly sampled ω vector, the summation indicates a cosine sweep function, and θ_0 is the initial angle of the baskets when the shaker first began rotating.

$$F_{shk} = m_r \omega_k^{\,2} \cdot \cos\left(\sum_{i=1}^{k} \left(\theta_i - \theta_{i-1} \right) + \theta_0 \right) + \left(m_r + m_b \right) a_{b,x} \qquad \text{.. Eq. 4.9}$$

Fig. 4.34 shows the shaker force data recorded from the proximity sensor system, along with interpolated shaker force using linear interpolation and the proposed cosine sweep interpolation function. The cosine sweep interpolation provides superior data quality by

preserving the smoothly varying frequency content of the command input to the shaker. Furthermore, the amplitude of the shaker force is 4% higher using the cosine interpolation method compared with the linear interpolation method because the irregularly sampled rotation data do not happen to correspond to a peak in the shaker forcing function. Although modest, this difference is not negligible and may be important for certain applications that are sensitive to the shaker force.

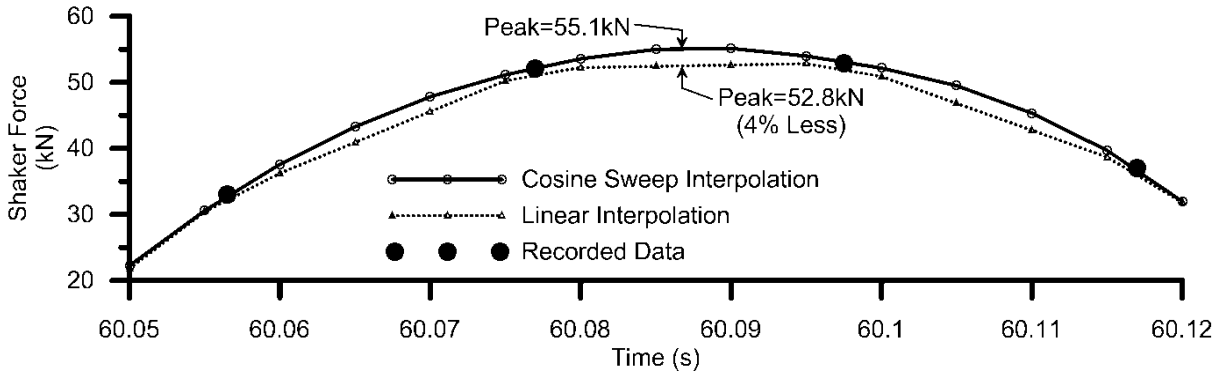

Figure 4.34: Shaker force interpolated using linear interpolation, and cosine sweep interpolation for a portion of one cycle.

Finally, acceleration of the shaker base influences the force imposed by the shaker by introducing a translational component of motion in addition to the rotational component. The influence of translation on the shaker force is a function of the displacement of the center of rotation of the rotating mass relative to the radius of the rotating mass. Fig. 4.35 shows shaker base acceleration and shaker force computed with and without the translational component for two motions; one small and one large. For the small motion, the translational component of motion has very little influence on the imposed shaker force. However, the large motion induced significant movement of the shaker base as a result of formation of a gap between the timber frame and the compacted sandy clay fill, resulting in an irregular acceleration record. Failure to account for the translational component (i.e., by computing shaker force as $m_r r\omega^2 \cos\theta$) resulted

in a 6.8% over-prediction of shaker force in this case. This case illustrates the importance of accounting for translational motion in the calculation of shaker force for cases where significant transient displacements are mobilized.

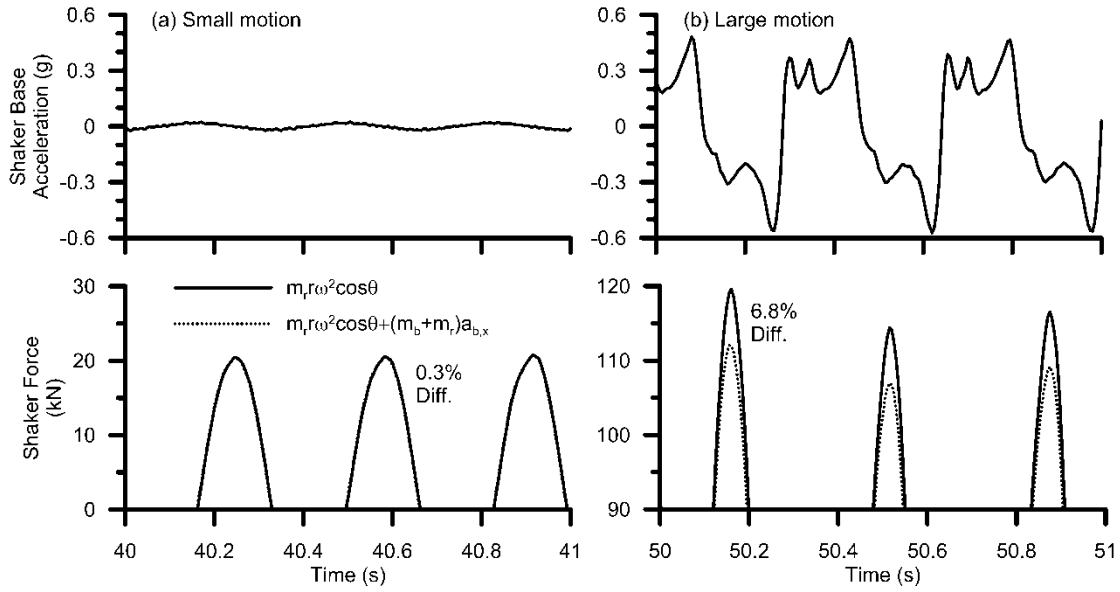

Figure 4.35: Shaker base acceleration and corrected/uncorrected shaker force functions for (a) a small motion (MK-15_1_4) and (b) a large motion (MK-15_4_1).

Chapter 5. Interpretation of Dynamic Test Data

This chapter focuses on the interpretation of data obtained from the dynamic shake testing performed on the model levee using the MK-15 shaker. The first section of this chapter focuses on measurements of translational and rotational impedance functions (i.e., dynamic stiffness and damping) of the model levee, including a description of the manner in which calculations of base displacement and rotation and horizontal force and moment about the levee base were computed from the measured data, and comparison to analytical impedance functions for rigid surface loads in the literature. The second section of this chapter focuses on the calculation of dynamic shear strains beneath the model levee during dynamic testing based on embedded accelerometer records. Shear strains are computed at different locations beneath the model levee, as well as during different test stages. The third section focuses on the residual pore pressure response of the saturated peaty organic soil underlying the model levee in relation to the shear strains developed, and are compared to results obtained from dynamic laboratory testing of peaty organic soil sampled from Sherman Island and tested by Stewart et al. (2013) The laboratory testing is beyond the scope of this PhD dissertation, and results were provided by my colleague, Ali Shafiee. The last section of this chapter focuses on a series of dynamic finite element model tests used to validate the shake testing, including comparison of shear strains with test data and rotation of principal stresses in the model levee.

5.1. Measurements of Dynamic Translational and Rotational Impedance Functions

This section explains the manner in which dynamic impedance functions were computed from the recorded data, focusing on base shear-displacement and base moment-rotation relations. First, the method used to calculate base shear, base moment, average base displacement, and

base rotation from the dynamic tests will be explained. Next, measured base shear-displacement and base moment-rotation responses will be presented and compared. Finally, the measured impedance functions are compared to published analytic impedance functions for rigid surface loads. A portion of the work presented in this section has been previously published by Reinert et al. (2013).

5.1.1. – Calculation of Impedance Functions

The procedures used to calculate the base shear, base moment, average base displacement, and average base rotation of the model test levee for the purpose of defining the stiffness and damping of levee-foundation soil interaction are explained here. A schematic of the levee and the accelerometers used to calculate these values can be seen in Fig. 5.1. The embankment was then divided into sixteen tributary wedges, and the centroid, volume, and weight of each wedge was calculated. The test data used to calculate desired quantities consisted of the x and z components of acceleration of the accelerometers on the embankment and the shaker force F_{shk}.

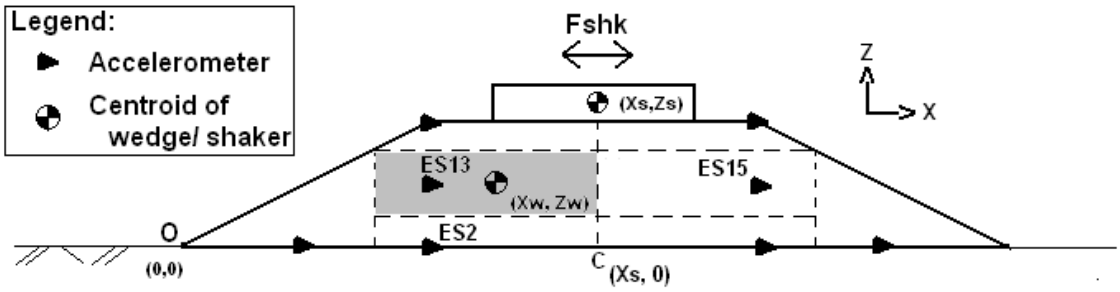

Figure 5.1: Schematic of model levee including shaker and instrumentation.

The first step was interpolating acceleration at the centroid of each wedge from the measured accelerations. For example, consider the shaded wedge in Fig. 5.1. The z-component

of acceleration at the centroid was interpolated between ES13 and ES15 since vertical acceleration is anticipated to vary horizontally due to rotation of the levee. The x-component of acceleration was taken as being equal to ES13 in this case since the elevation of the centroid is equal to the elevation of ES13. For some wedges, the elevation of the centroid is not identical to the elevation of any accelerometer, in which case the centroid acceleration is interpolated vertically between the nearest two sensors.

Once the representative accelerations for each wedge were computed, the base shear and moment of the embankment were calculated by (*i*) computing inertia force for each wedge in the horizontal and vertical directions, (*ii*) summing horizontal inertia forces plus shaker force to obtain base shear, and (*iii*) summing horizontal inertia force multiplied by vertical moment arm, vertical inertia force multiplied by horizontal moment arm, and shaker force multiplied by the height to the centroid of the shaker. Moments were computed about the center of the base [i.e., at point (x_s,0) in Fig. 5.1]. Shear is positive from left-to-right, and moment is positive clockwise. Steps (ii) and (iii) are explicitly defined in Eqs. 5.1 and 5.2 for each timestep ti.

$$V_{base,ti} = F_{shk,ti} + \sum_{i=1}^{16} -m_i a_{x,i,ti} \quad \text{.. Eq. 5.1}$$

$$M_{base,ti} = z_s \cdot F_{shk,ti} + \sum_{i=1}^{16} -m_i a_{x,i,ti} z_{w,i} + \sum_{i=1}^{16} m_i a_{z,i,ti} (x_{w,i} - x_s) \quad \text{..Eq. 5.2}$$

The final step of calculations was to compute a representative base displacement and rotation, which are combined with the shear and moment to evaluate frequency-dependent stiffness. First, displacements were computed by double-integrating the acceleration records in time. The Fourier transform of each record was computed, and the real and imaginary

components were multiplied by a Butterworth filter with an order of 5 and a corner frequency of 0.2 Hz. Note that this filter is acausal (i.e., it does not alter the phase of the signals) since the real and imaginary components are both multiplied by the same scalar. The filter was required to remove low frequency noise that would otherwise cause erroneous drift in the displacement records. The representative base displacement was then computed as the average of the x-component of displacement from the eight accelerometers along the base of the levee. Very little variation in these motions was observed, and an equally-weighted average is therefore reasonable.

The representative rotation is complicated by flexibility of the model levee. Fig. 5.2 shows undeformed and deformed positions of the accelerometers during positive and negative loading cycles. The deformed shape of the levee base is clearly nonlinear, which indicates that the rotation varies along the length of the levee. Rotations were first calculated for each of the eight wedges along the base of the levee. Next, the rotations were split up into two regions: the wedges adjacent to the center of the levee, and the wedges farther away from the center. The representative rotation in this case was computed using the outermost points of the levee. Other possible methods to calculate rotation included rotation in the center of the levee and rotations using a least-squares regression approach, since most of the mass lies near the center of the levee.

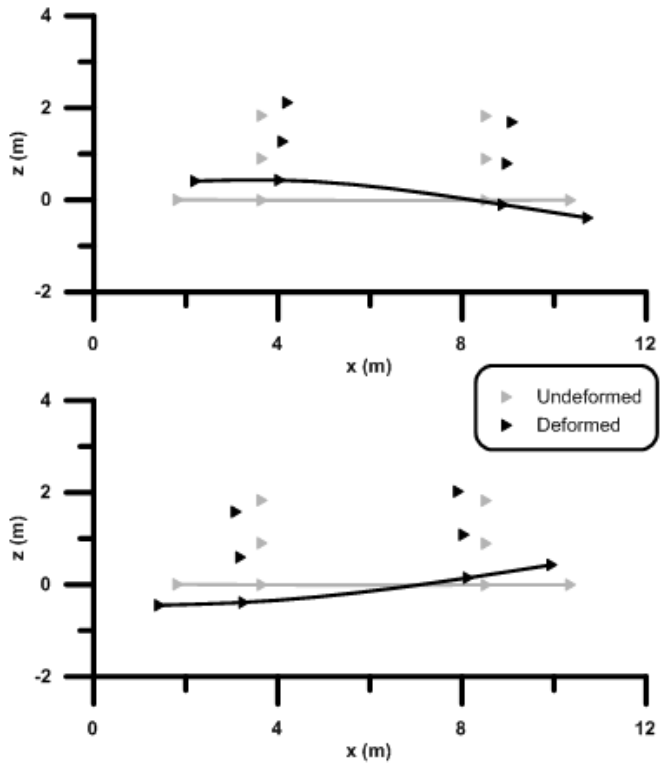

Fig. 5.2: Deformed and undeformed displaced positions of sensors during a positive and negative loading cycle (displacements amplified × 100).

5.1.2. Measured Shear-Displacement and Moment-Rotation Responses

Measured levee-foundation soil responses are presented in Figs. 5.3 and 5.4 in terms of base shear versus horizontal translation and base moment versus representative rotation. The results in Fig. 5.3 apply for the 2011 MK15_2_2 test, a low-medium intensity motion that resulted in a maximum horizontal crest acceleration of 0.11g. At 1Hz, the moment-rotation relation is obscured by noise to a sufficient extent that it is difficult to evaluate any potential hysteresis in the response. On the other hand, the horizontal force-displacement data is much less noisy and exhibits a small but clear effect of damping. Radiation damping and hysteretic damping are likely present in the measurement, though separating the relative contribution of

each is not possible from the measured data. It would be possible to measure hysteretic damping at very low frequencies where radiation damping is zero, but the field test data are too noisy at such low frequencies to measure impedance relations. As the frequency increases, the damping increases as well, and the force-displacement curves are essentially circular at 3Hz indicating that the base shear is 90° out of phase with the base translation, which is associated with first-mode resonance of the free-field site. This agrees with the geophysical study indicating the first mode resonance at the site is approximately 3 Hz. Damping also increases with frequency for moment-rotation, but not as significantly as for horizontal force-displacement. This trend was also observed by Tileylioglu et al. (2011) for a rigid concrete foundation on stiff soil.

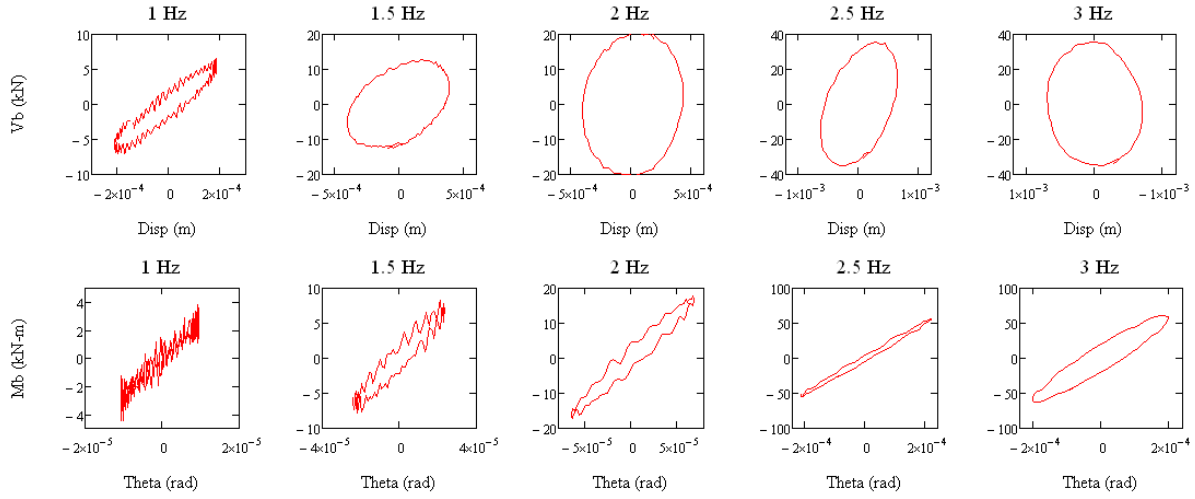

Fig. 5.3: Impedance relations for a low-medium intensity motion (2011 MK15_2_2) that resulted in peak horizontal crest acceleration of 0.06 g.

Fig. 5.4 presents the measured responses for the 2011 MK15_5_1 test, a high intensity motion that resulted in a maximum crest acceleration of 0.27g. The curves for f=3Hz are not presented because the shaker capacity was mobilized during this motion, and could not reach frequencies higher than 2.6Hz. For a given frequency, more damping is apparent in the responses

for the high intensity motion compared with the low-medium motion. This trend is likely the result of higher shear strains mobilized in the soil by the high intensity motion, which would cause (i) increased hysteretic damping, and (ii) increased radiation damping due to the reduction in shear modulus (and reduction of equivalent shear wave velocity) of the peat and associated increase in dimensionless frequency, $a_o = \omega B/V_s$, where ω = angular frequency = $2\pi f$, and B = footing half-width. The non-harmonic features in the shear-translation and moment-rotation responses for the higher frequency motions were caused by pounding between the timber frame and the model levee.

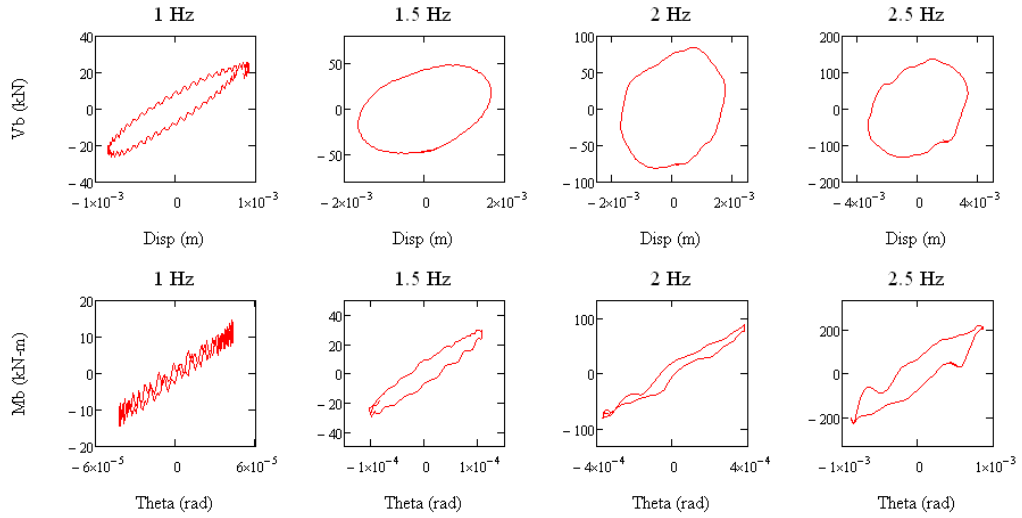

Fig. 5.4: Impedance relations for a large intensity motion (2011 MK15_5_1) that resulted in peak horizontal crest acceleration of 0.27g.

The dramatic increase in damping with frequency is consistent with analytical solutions for rigid footings on an elastic halfspace. For example, consider B = 1.85m, V_s = 25m/s, and f = 3Hz. The dimensionless frequency is $a_o = 2\pi$ (3Hz)(1.85m)/(25m/s) = 1.4. The radiation damping for a rigid rectangular footing with L/B = 12m/3.7m = 3.2 is 86% for translation and 108% for rotation using the solutions suggested by Pais and Kausel (1988). A dimensionless frequency of

1.4 is rather high for frequencies in the range of earthquake excitation, which is caused by the peat's extraordinarily low shear wave velocity.

As a basis for comparison between the 2011 and 2012 tests, Figs. 5.5 and 5.6 show measured base shear versus horizontal translation and base moment versus rotation for motions of the same intensity for the 2012 tests. The results in Fig. 5.5 apply for the 2012 MK15_2_2 test, a low-medium intensity motion that resulted in a maximum horizontal crest acceleration of 0.05g. The response from this 2012 test show little difference to the response from the 2011 test of the same intensity, with one exception being the moment-rotation response at 1Hz. This loop is not closed, and is probably that way due to the inherent from measurements at such a low amplitude.

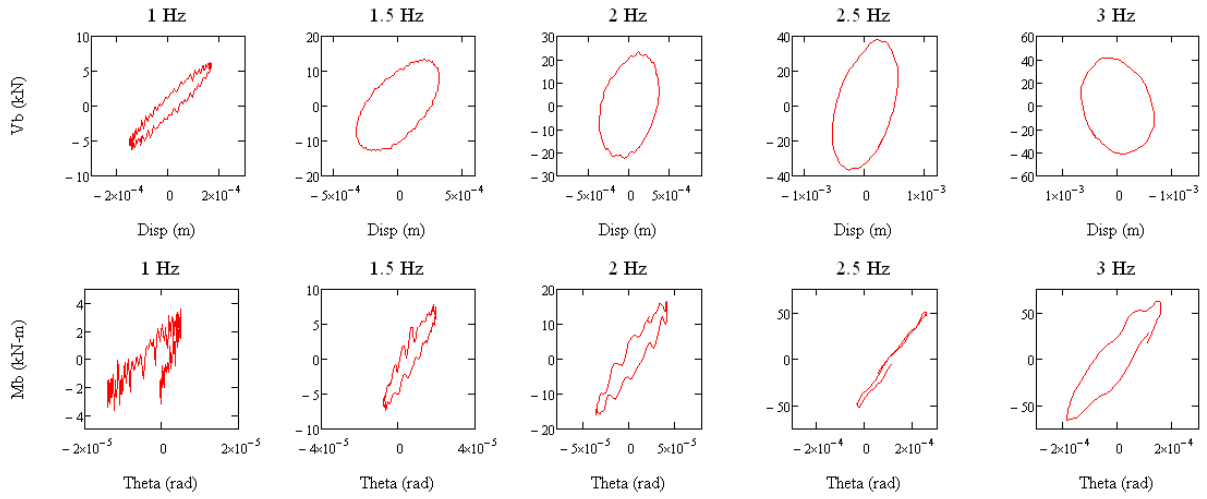

Fig. 5.5: Impedance relations for a low-medium intensity motion (2012 MK15_2_2) that resulted in peak horizontal crest acceleration of 0.05 g.

Fig. 5.6 shows the measured responses for the 2012 MK15_5_1 shake, a high intensity motion that resulted in a peak crest acceleration of 0.31g. As mentioned in Fig. 5.4, results at f=3Hz could not be presented due to the shaker not being able to reach frequencies higher than

2.6 Hz. In the case of Fig. 5.6, we see similar behavior to the responses seen in Fig. 5.4. One important feature of the data to note is that the irregularity of the loops in Fig. 5.6 is slightly less than that of the response from the 2011 test, likely due to the repairs performed on the model levee to reduce pounding of the timber base on the model levee fill. However, even the repairs could not completely eradicate pounding behavior, which is why the loops still have irregular shapes.

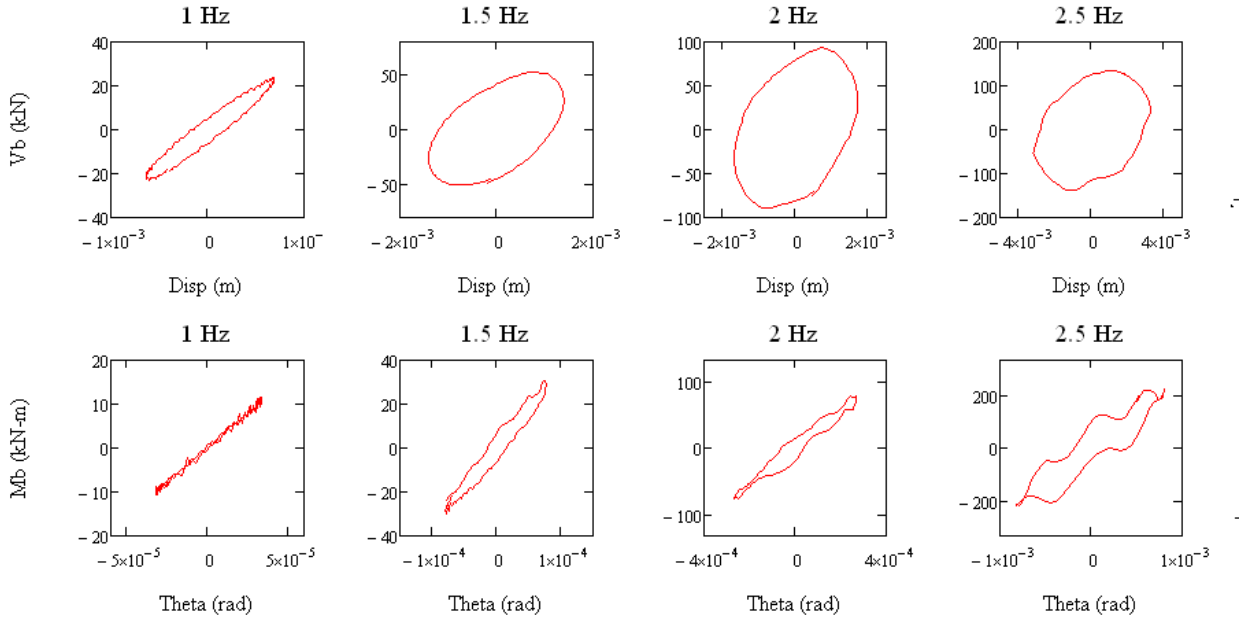

Fig. 5.6: Impedance relations for a large intensity motion (2012 MK15_5_1) that resulted in peak horizontal crest acceleration of 0.31g.

5.1.3. Impedance Functions for Frequency-dependent Stiffness

The shear-displacement and moment-rotation loops are interesting for observing the response of the levee, and this information is supplemented in this section by computation of frequency-dependent impedance functions. The impedance functions are complex-valued, and can be expressed in one of two forms, as seen below in Eq. 5.3 (NIST 2012):

$$\bar{k}_j = k_j + i\omega c_j$$
$$\bar{k}_j = k_j(1 + 2i\beta_j) \qquad \text{.. Eq. 5.3}$$

where $\bar{k}_j$ represents the complex stiffness functions, the subscript j represents the modes of translational or rotational motion, k_j and c_j represent the frequency dependent stiffness and dashpot coefficients for mode j, and ω is the circular frequency (rad/sec). Furthermore, using β_j is more advantageous because it can be interpreted as a percentage of critical damping for the soil-structure interaction (SSI) system. In any case, it is important to note that there are two components to the impedance function: a real-valued portion, k_j, which represents the dynamic stiffness, and an imaginary portion $2k_j\beta_j$. The phase difference between force and lagged displacement, which is related to damping (NIST 2012), is $\varphi_j = \tan^{-1}(2\beta_j)$.

The real and imaginary values of the impedance functions were generated for the shake tests using the following procedure. First, the portion of the V_b, M_b, Δ, and θ time series during which the frequency was increasing were extracted from the fast sweep data. The ascending branch was used instead of the entire time series because the Fourier transform of a full sweep (i.e., increase and decrease in frequency) exhibits nodes with very low frequency content that are not present if only the ascending (or descending) branch is studied. A cosine taper function was

then applied to the measured responses to eliminate spectral leakage. Next, Fourier transforms of the response quantities were taken, after padding with zeros such that the vectors were of 2^N length. The frequency-dependent stiffness quantities were then calculated using Eqs. 5.4 and 5.5:

$$F(K_{XX}) = \frac{F(V_b)}{F(\Delta)} \quad \text{.. Eq. 5.4}$$

$$F(K_{M\theta}) = \frac{F(M_b)}{F(\theta)} \quad \text{.. Eq. 5.5}$$

where F() represents the Fourier transform of the desired quantity. Once the Fourier transforms of the stiffness quantities were calculated, the real and imaginary components of the complex stiffness could be isolated and plotted versus frequency. The frequency vector is controlled by the Nyquist criterion, and therefore contains components from 0 to 100Hz since the sampling frequency was 200Hz. However, only a small portion of the data are considered physically meaningful since the frequency sweeps went only as high as 2.6 to 5Hz, depending on the particular motion. The impedance functions are therefore presented only over the frequency range corresponding to the shaker forcing function, and not for higher frequencies that are noise-dominated.

Analytical solutions for the impedance of rigid footings resting on the surface of an elastic isotropic halfspace are computed for comparison with the computed impedance functions. The rigid footing assumption is violated since the model levee was composed of flexible compacted soil. Furthermore, the elastic isotropic halfspace assumption is violated because the foundation soil conditions consist of a desiccated crust resting atop soft saturated peat. For these reasons, the analytical solutions are not expected to agree perfectly with the data, but provide a

useful context for interpreting the measured results. The analytical expressions by Pais and Kausel (1988), as presented in NIST (2012), are organized into the functional form shown in Equations 5.6, K_j is the static stiffness, where α_j is a frequency modifier, and β_j represents the radiation damping ratio (the analytical model is plotted without hysteretic damping, which simply be added to the radiation damping component for any given frequency). The values of K analyzed herein are translational in the x-direction, in which case the index j is replaced with x, or rotational about the y-axis in which case the j is replaced with yy. Static stiffnesses, frequency modifiers, and radiation damping terms are provided in Eqs. 5.7 through 12 (NIST, 2012).

$$\bar{k}_j = \alpha_j K_j \left(1 + 2i\beta_j\right) \quad \text{.. Eq. 5.6}$$

$$K_{x,\,sur} = \frac{GB}{2-\nu}\left[6.8\left(\frac{L}{B}\right)^{0.65} + 2.4\right] \quad \text{.. Eq. 5.7}$$

$$K_{yy,\,sur} = \frac{GB^3}{1-\nu}\left[3.73\left(\frac{L}{B}\right)^{2.4} + 0.27\right] \quad \text{.. Eq. 5.8}$$

$$\alpha_x = 1.0 \quad \text{.. Eq. 5.9}$$

$$\beta_x = \left[\frac{4\left(L/B\right)}{\left(K_{x,sur}/GB\right)}\right]\left[\frac{a_0}{2\alpha_x}\right] \quad \text{.. Eq. 5.10}$$

$$\alpha_{yy} = 1.0 - \left[\frac{0.55a_0^2}{\left(0.6 + \frac{1.4}{\left(L/B\right)^3}\right) + a_0^2}\right] \quad \text{.. Eq. 5.11}$$

$$\beta_{yy} = \left[\frac{(4\psi/3)(L/B)^3 a_0^2}{\left(\frac{K_{yy,sur}}{GB^3}\right)\left[\left(\frac{1.8}{1+1.75(L/B-1)}\right)+a_0^2\right]} \right] \left[\frac{a_0}{2\alpha_{yy}} \right] \quad \text{..Eq. 5.12}$$

Fig. 5.7 to 5.9 show the real and imaginary components of the complex shear-displacement and moment-rotation stiffness for a low-medium amplitude motion for the 2011 test (2011 MK15_2_2, Fig. 5,7), a large-amplitude motion for the 2011 test (2011 MK15_5_1, Fig. 5.8), and a large amplitude motion for the 2012 test (2012 MK15_5_1, Fig. 5.9). These values are plotted with the analytical solutions in Eqs. 5.8 to 5.13 with shear wave velocity V_s = 30 m/s, half width of footing B = 1.83m, Poisson's ratio ν = 0.45, and density ρ = 1120 kg/m^3. Secant stiffness is known to decrease with shear strain amplitude, thereby resulting in a lower effective V_s value. Maximum strain amplitudes mobilized during the field test are about 0.4% (see Chapter 5.2.2), which is associated with a modulus reduction value of only about 0.8 based on Wehling et al. (2003) for peat beneath levees. This corresponds to a reduction in equivalent Vs of only 11%. We consider this correction small enough to utilize Vs = 30 m/s for these calculations. As seen in Eq. 5.3, the k_j, or stiffness portion, is expressed in Eq. 5.13 for a non-embedded foundation:

$$k_j = K_j * \alpha_j \quad \text{.. Eq. 5.13}$$

Impedance functions are represented graphically as a function of the dimensionless frequency a_0, usually in the real and imaginary components. Note that in the case of Fig. 5.7, dimensionless frequency is truncated between 0.5 and 1.5, which corresponds to a frequency of 1.3 to 4 Hz, whereas the other motions are presented for a_0 = 0.5 to 1.2, which corresponds to 1.3 to 3.1 Hz.

Looking first at the translational stiffness terms, the measured real component tends to be lower than the analytical solution for the small motion, and agrees reasonably well for the larger motions. Furthermore, the real component decreases with frequency above $a_o = 0.9$, and eventually becomes negative at high frequency for the small motion. By contrast, the real component of the stiffness terms agree reasonably well with the analytical solutions for the large motions. The cause of this behavior is unclear, but levee flexibility is a likely contributor to the observed differences. The real component of stiffness is higher for the large motions than for the smaller motion. The imaginary part of the translational stiffness tends to have an upward trend as frequency increases, which agrees with the analytical solution. This indicates that radiation damping is increasing as frequency increases, which is also clear in Fig. 5.3 to 5.6. However, the measured imaginary components tend to indicate higher radiation damping in the translational mode compared with the analytical solutions.

Moving now to the rotational component, the computed impedance functions generally have trends with frequency that match the analytical solutions (i.e., the real part decreases with frequency and the imaginary part increases). However, the computed impedance functions tend to lie significantly lower than the analytical impedance functions. The cause for this behavior is expected to be the flexibility of the levee fill since significant deformations were observed along the base of the levee, resulting in a rotation profile that varied with spatial position. Rotational impedance is known to be strongly affected by foundation flexibility (NIST 2012). The negative values of the imaginary part of the rotational impedance functions may also be caused by levee flexibility, but may also be related to sensor noise as the moment-rotation loops shown in Figs. 5.3 to 5.6 show significant noise influence and don't always clearly indicate positive damping. The negative imaginary component for the moment-rotation can be seen in the way the $M_b - \theta$

loops develop. Fig. 5.10 shows a set of loops from the 2011 MK15_5_1 test. What can be seen here is that the loops for the outer accelerometers develop in a counterclockwise manner. However, loops generated from dynamic laboratory tests on soils and from the inner sensors along the levee base develop in a clockwise manner. This backward development of the loops suggests that during the shake testing, the sensors on the outer portion of the levee were out of phase with the sensors on the inner part. This is a clear indication that rigid footing solutions should not be utilized to predict the rocking impedance of levees. Additional research is required to further clarify this potentially important SSI issue, but this work is beyond the scope of my dissertation.

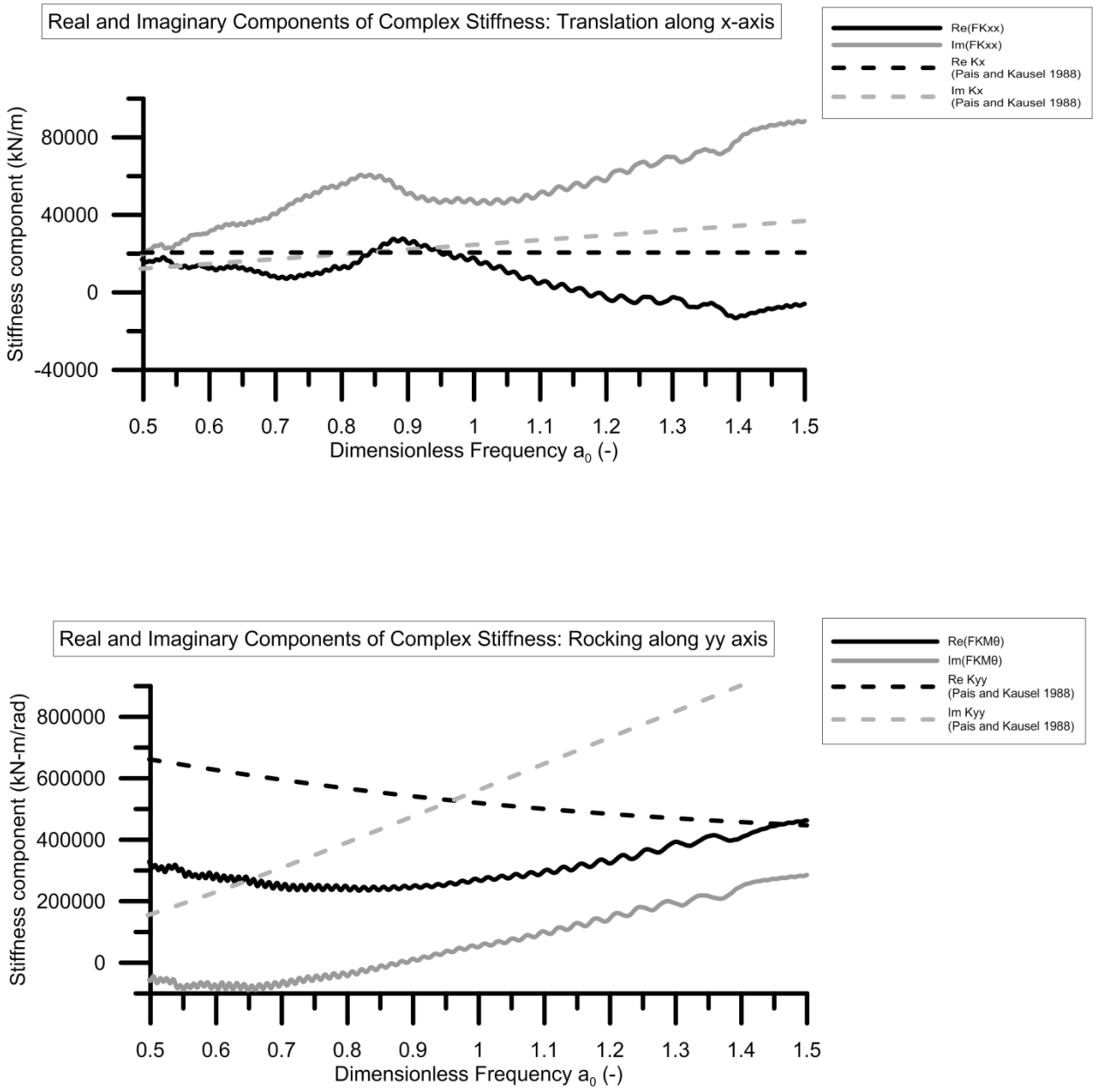

Fig. 5.7: Real and Imaginary portions of impedance functions for a) shear-displacement and b) moment-rotation for 2011 test MK15_2_2 compared with Pais and Kausel (1988).

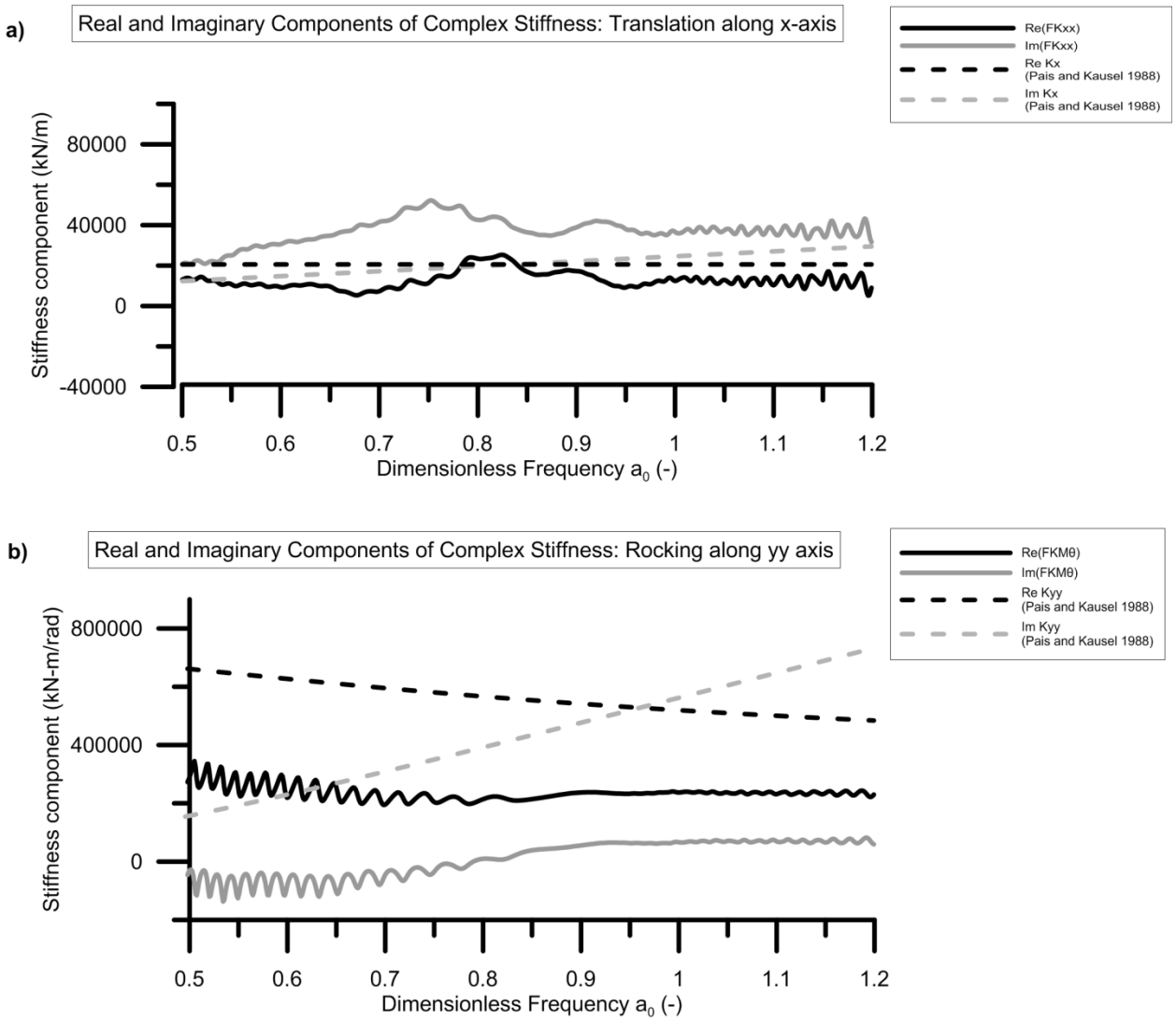

Fig. 5.8: Real and Imaginary portions of impedance functions for a) shear-displacement and b) moment-rotation for 2011 test MK15_5_1 compared with Pais and Kausel (1988).

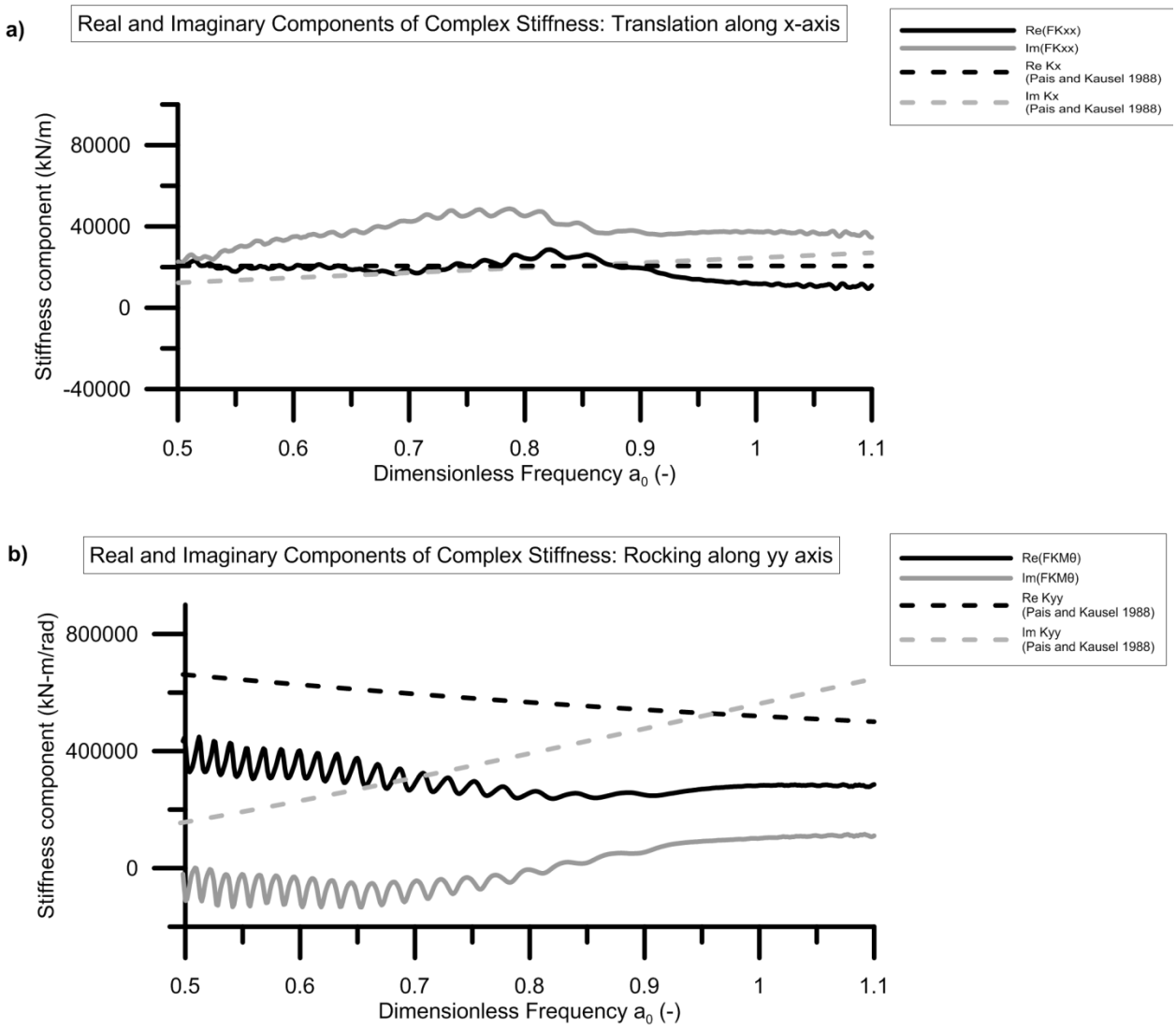

Fig. 5.9: Real and Imaginary portions of impedance functions for a) shear-displacement and b) moment-rotation for 2012 test MK15_5_1 in compared with Pais and Kausel (1988).

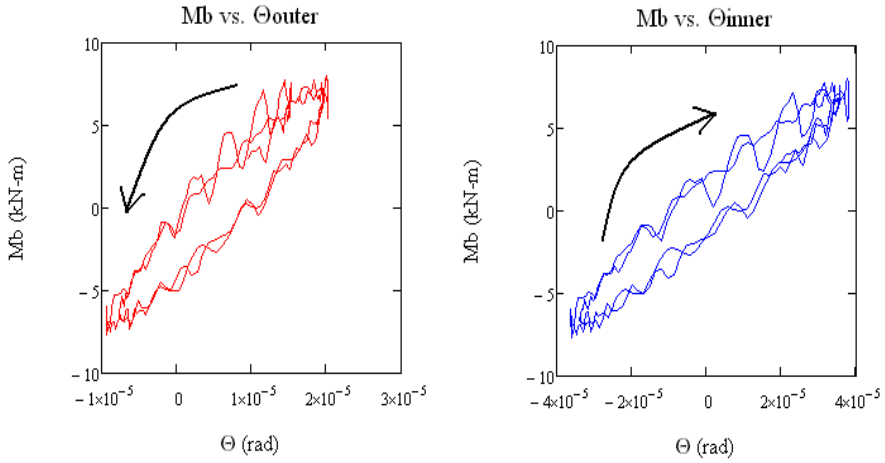

Fig. 5.10: Development of moment-rotation loops in dynamic shake testing,

5.2. Development of Shear Strains from Dynamic Testing

This section describes the calculation and interpretation of shear strains developed in the underlying peaty organic soil during shake testing. First, the process used to calculate shear strains from acceleration records inside the peaty organic soil will be explained. Next, the development of shear strains will be compared between different levee sections and different tests, with a focus on peak shear strain.

5.2.1. Calculation of Dynamic Shear Strains

The first step in calculating shear strains underneath the model levee was to ascertain which of the underground accelerometers (M1 – M8) functioned properly (See Figs. 4.26 and 4.27). In this case, for the 2011 set of tests, sensors M1 – M3 and M5 – M8 worked and sensors M4 and M8 failed, while in 2012, only sensors M1 and M5 – M8 worked while sensors M2, M3, M4, and M8 failed. With this in mind, the results from the 2011 tests will show shear strains underneath both the levee toe and levee crest, while the results obtained from the 2012 tests only show shear strains developed underneath the levee crest. Displacements of the underground accelerometers were calculated in a manner similar to the displacements of the above-ground accelerometers (explained earlier in Section 5.1.1). However, a Butterworth filter of order 5 and corner frequency of 0.5 Hz was used, instead of the corner frequency of 0.2 used for the higher resolution Episensor accelerometers.

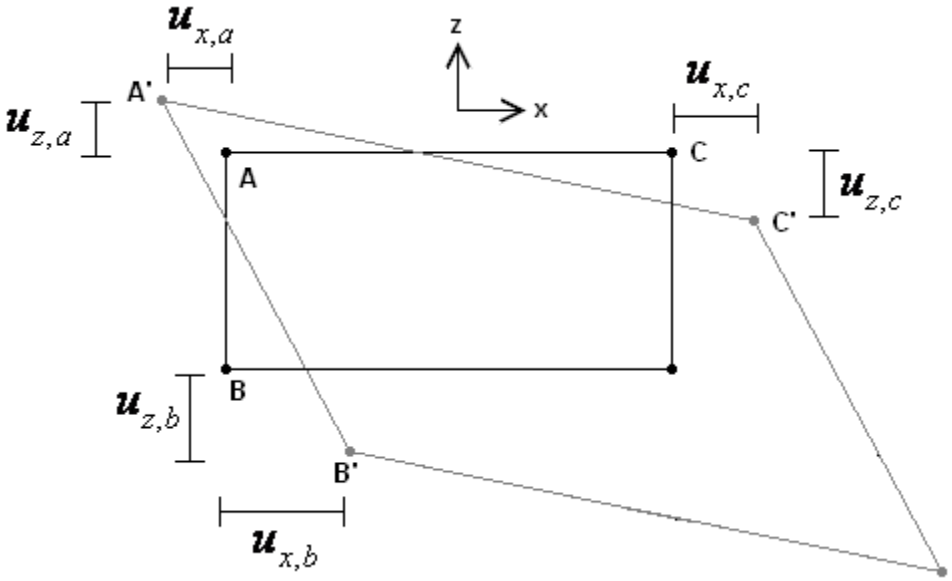

Fig. 5.11: Sensor schematic for calculation of shear strains

Fig. 5.11 shows a schematic two dimensional diagram of three points (A, B, C) in the peaty organic soil that have been deformed to new positions (A', B', C'). The three points are defined by an x-z coordinate system, similar to the way that the coordinate system for the model levee is presented in Chapter 4. The normal strains of the element defined by the three points are:

$$\varepsilon_x = \frac{\partial u_x}{\partial x} = \frac{u_{x,c} - u_{x,a}}{|x_c - x_a|} \quad \text{.. Eq. 5.14}$$

$$\varepsilon_z = \frac{\partial u_z}{\partial z} = \frac{u_{z,b} - u_{z,a}}{|z_b - z_a|} \quad \text{.. Eq. 5.15}$$

The engineering shear strain, which is the change in angle from AB to A'B' (and AC to A'C') is defined as:

$$\gamma_{xz} = \frac{\partial u_z}{\partial x} + \frac{\partial u_x}{\partial z} = \frac{u_{z,c} - u_{z,a}}{|x_c - x_a|} + \frac{u_{x,a} - u_{x,b}}{|z_b - z_a|} \quad \text{.. Eq. 5.16}$$

Having computed these strain components, and assuming that the y-direction strain components are zero, the octahedral strain can be computed as (Yang et al. (2008)):

$$\gamma_{oct} = \frac{2}{3}\sqrt{(\varepsilon_x - \varepsilon_z)^2 + 6(\frac{\gamma_{xz}}{2})^2} \quad \text{.. Eq. 5.17}$$

Octahedral strain is a reasonable representation for the peak shear strain acting at a point. One last thing to note is the sign convention for shear strain calculations. As mentioned in earlier chapters, positive is defined in the right x-direction, the up z-direction, and clockwise in rotation.

5.2.2. Dynamic Shear Strains During Shake Testing

Using the equations in the previous section, maximum shear strains were computed for each test. Figs. 5.12 – 5.14 show sets of time series for a sequence of tests at low, medium, and high shaking intensity for the 2011 test. These stacked time series show the octahedral shear strain underneath the levee crest and levee toe, along with the horizontal crest accelerations (from sensor ES9) and the shaker force. The shear strains represent the average shear strain developed between 1 and 3 m within the peat. Hence, it is an average value of the shear strains developed in the bottom 1 meter of the stiff crust and the top 1 meter of the sift peat. First, Fig. 5.12 shows the data for a low intensity shake (2011 MK15_2_2). In this case, the maximum shaker force is roughly 80 kN at 4 Hz, the maximum shear strain underneath the toe and crest of the levee are 0.06% and 0.016%, respectively. Fig. 5.13 shows a medium intensity event (2011 MK15_3_2) with peak shaker force of 95 kN at 3 Hz. For this shake, the maximum shear strains

underneath the toe and crest are 0.05% and 0.018%, respectively. Note that in between these two shakes, the shear strain underneath the toe for the higher intensity shake is slightly lower than the lower intensity shake. However, the maximum shear strain underneath the crest increases with shake intensity. The cause of this behavior is unclear, but may be related to formation of gaps between the shaker frame and levee generating more energy beneath the crest and less energy beneath the toes. Fig. 5.14 shows the time series near peak shaking intensity for a high intensity shake (2011 MK15_5_2). In this case, the maximum shaker force is roughly 175 kN at 2.6 Hz shaking, and the maximum shear strain underneath the levee toe and crest are 0.15% and 0.4%, respectively. In this case, the pounding behavior of the timber shaker base against the levee fill is readily seen in the time series. The downward spikes in the crest acceleration record indicate that the pounding behavior is in the negative x-direction.

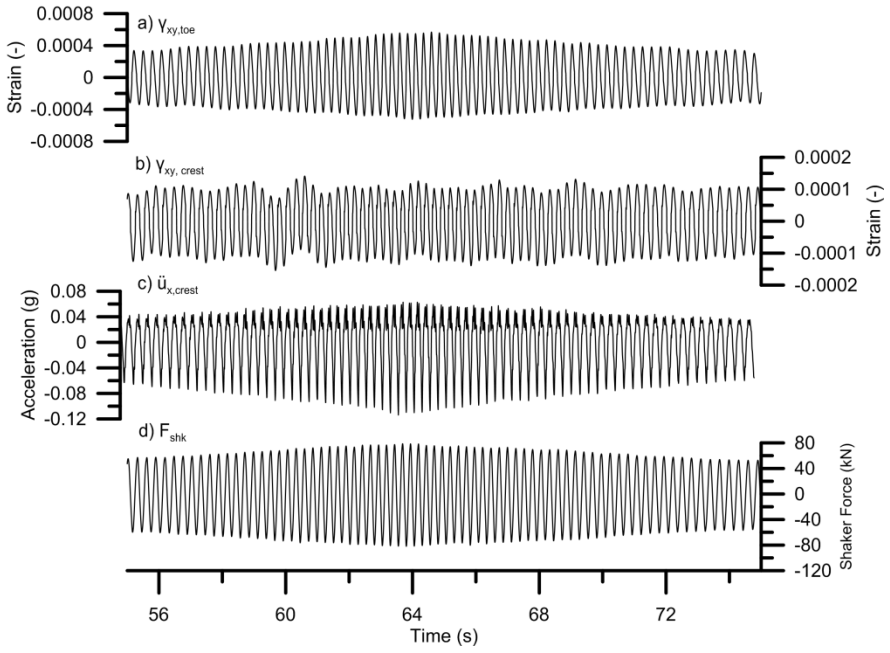

Fig. 5.12: Time series of shear strain, crest acceleration, and shaker force for low intensity shake 2011 MK15_2_2

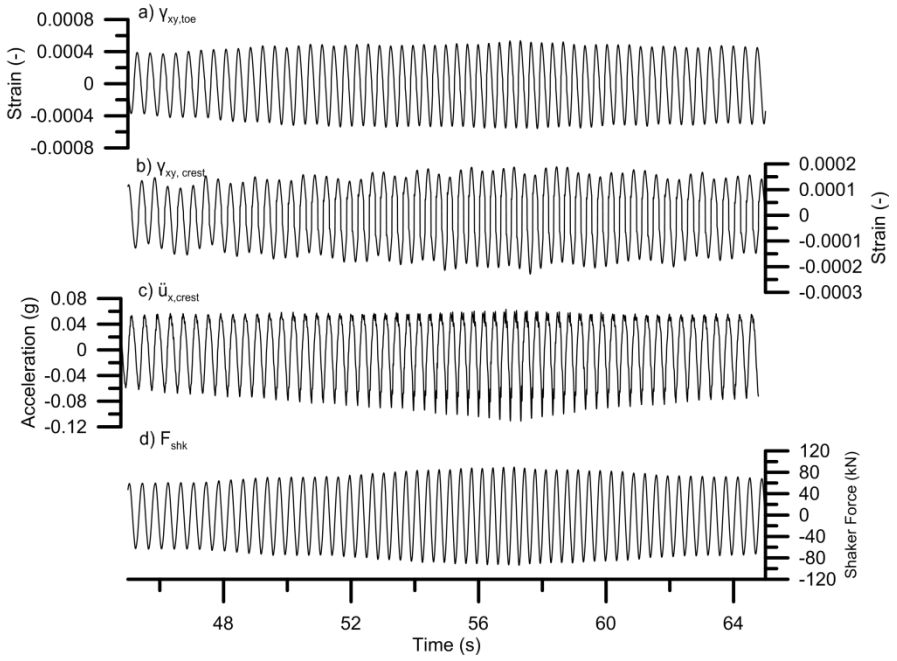

Fig. 5.13: Time series of shear strain, crest acceleration, and shaker force for moderate intensity shake 2011 MK15_3_2

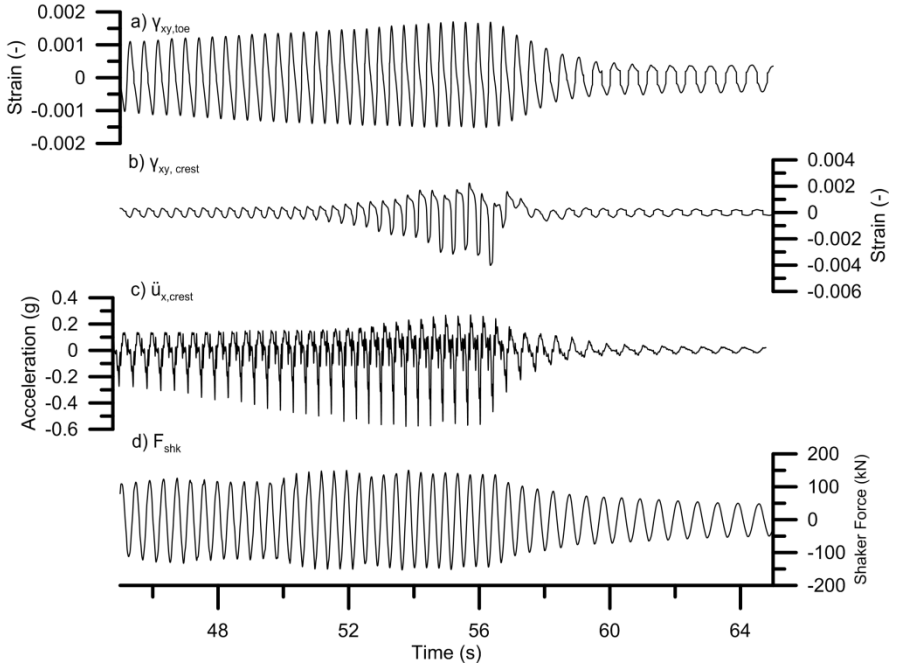

Fig. 5.14: Time series of shear strain, crest acceleration, and shaker force for high intensity shake 2011 MK15_5_2

Figs. 5.15 and 5.16, for basis of comparison, show the time series for levee crest shear strain, crest acceleration, and shaker force for a series of shakes from the 2012 shake tests. Fig. 5.16 shows the data for a moderate intensity shake (2012 MK15_3_3) with peak shaker force of 90 kN at 3 Hz. The peak shear strain is 0.05% underneath the levee crest, compared to only 0.018% for a similar forcing function for the 2011 test. In this case, the peak shear strain underneath the levee crest is much higher than the equivalent peak shear strain for the 2011 test MK15_3_2. Fig. 5.15 shows data for a low intensity shake (2012 MK15_2_2). The peak shaker force is roughly 45 kN at 4 Hz, and the peak shear strain underneath the levee crest is roughly 0.023%, which is slightly larger than the strain mobilized during the 2011 test with nearly twice as much shaker force. Although both 2011 Mk15_2_2 and 2012 MK15_2_2 had the same shaker eccentricities and shaking frequencies, the measured shaker force is significantly smaller for the 2012 MK15_2_2 test than it is for the 2011 MK15_2_2 test, with peak horizontal crest acceleration for the 2012 test being 0.05g and 0.11g for the 2011MK15_2_2 test.. It appears that the mobilized shear strains beneath the levee crest in the 2012 test were approximately double those mobilized during the 2011 test. This suggests that the stiff crust may have gotten softer due to saturation of the peat. Another interesting thing to note is that the peak shear strain occurs before the peak shaker force has been mobilized. This could indicate that resonance had been reached before the peak shaker acceleration of 4 Hz. This is in agreement with the site period of roughly 3 Hz obtained from the various geophysical and site investigations mentioned in Chapter 3.

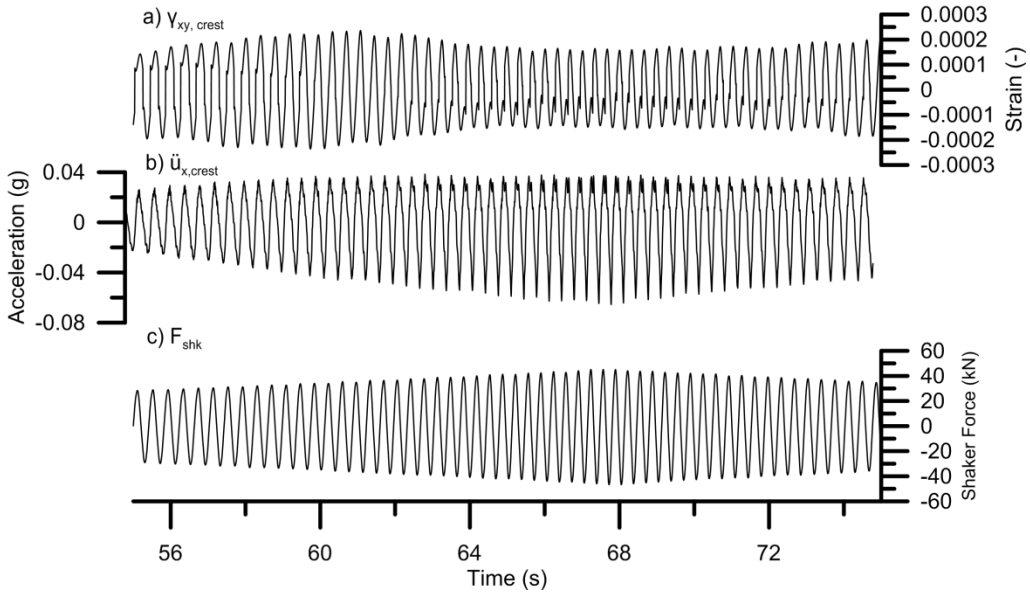

Fig. 5.15: Time series of shear strain, crest acceleration, and shaker force for high intensity shake 2012 MK15_2_2

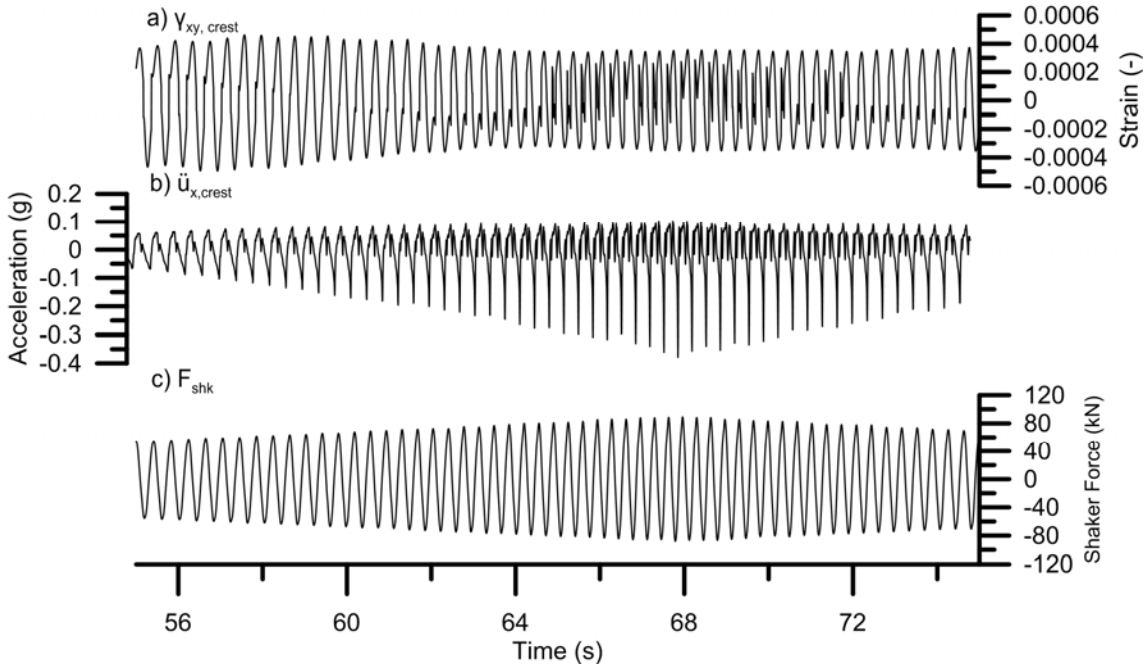

Fig. 5.16: Time series of shear strain, crest acceleration, and shaker force for high intensity shake 2012 MK15_3_3

In order to better understand the mobilization of shear strains underneath the levee, Fig. 5.16 shows two bar charts that illustrate the maximum shear strains underneath the model levee for both the 2011 and 2012 series of tests. Fig. 5.17a shows the maximum mobilized shear strains for the 2011 tests. The general trend is that the maximum shear strain underneath the levee toe is higher than the maximum shear strain underneath the crest, which is likely due to rocking on the levee and the influence of vertical strains beneath the levee toe compared with more of a simple shear mechanism beneath the crest. Once the shaking for the fourth trial started, a noticeable increase in shear strain is apparent underneath both the levee crest and the levee toe. This is likely due to both the increase in shaking intensity as well as the pounding of the shaker base on the levee fill. Fig. 5.17b shows a similar bar chart of maximum shear strains for the 2012 series of tests underneath the model levee crest. In this case, an overall increase in shear strain underneath the levee crest is observed for the 2012 tests from the 2011 tests, with the exception of a couple of tests that were terminated prematurely.

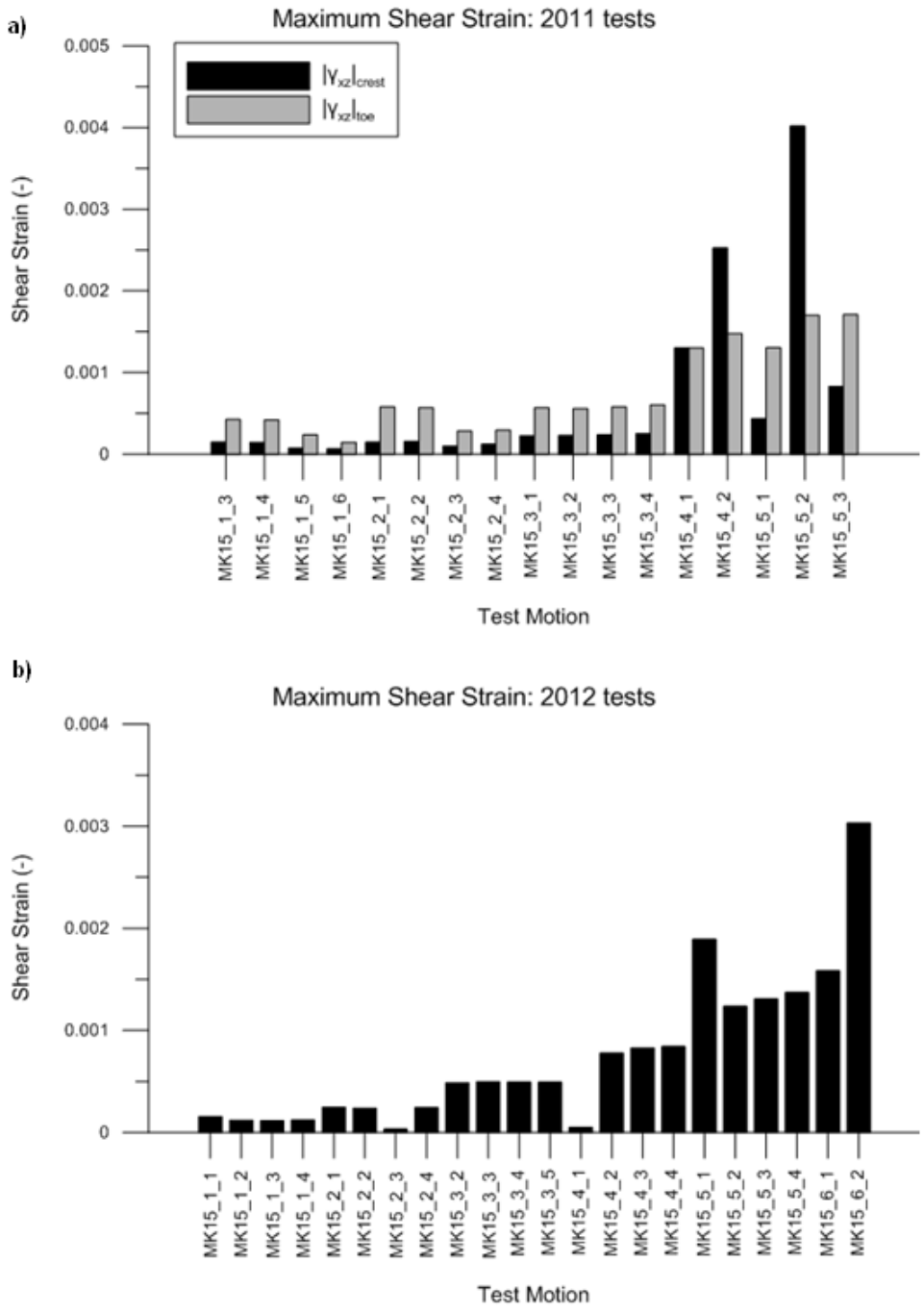

Fig. 5.17: Bar chart showing maximum shear strain underneath the model levee during dynamic tests for the a) 201 and b) 2012 series of shake tests.

5.3. Residual Pore Pressure Response and Dynamic Shear Strains

This section focuses on the pore pressure response of the peat beneath the model levee as a function of mobilized shear strains. First, the calculation of residual pore pressure ratio, r_{ur}, is presented and demonstrated by a set of sample calculations from one test. After that, the r_{ur} vs. γ_{max} response for shake tests underneath the levee toe and crest will be presented, along with comparisons of r_{ur} vs. γ_{max} to a series of cyclic triaxial and cyclic simple shear tests performed on the peaty organic soil from Stewart et al. (2013)

5.3.1. Calculation of Residual Pore Pressure Ratio

One of the main goals of the testing program is to determine whether pore pressures develop in the saturated portion of the foundation peat as a result of shear strains imposed by the shaking levee could lead to levee settlement. The residual pore pressure ratio, r_{ur}, is defined as (Kramer 1996):

$$r_{ur} = \frac{u_{res}}{\sigma_{vo}'} \qquad \text{.. Eq. 5.18}$$

Where u_{res} is the residual pore pressure (i.e., the difference between the pore pressure at the end of shaking and that before shaking; this does not include transient pore pressures generated by total stress changes during testing) and σ_{vo}' is the in-situ vertical effective stress determined from three-dimensional elastic solutions of the post construction model configuration.

Before determining the u_{res} for each test, it's important to establish the in-situ vertical effective stress. Earth pressures were not measured as part of this study, but they were computed based on the following: i) the peat layer is 11 m thick total, with a 2 m thick crust of unit weight

15 kN/m^3 overlying 9 m of soft peat with unit weight 13 kN/m^3, ii) the unit weight of the levee fill is 17.3 kN/m^3 (see Chapter 4), iii) the water table is at 2 meters depth, reaching to the top of the soft peat layer, iv) the pore water in the soft peat is not hydrostatic with excess pore pressure of 50 kPa at the bottom of the peat layer (as measured during the CPTu dissipation test in the underlying sand, see Chapter 3.2.5), and the pore pressure was assumed to vary linearly from the ground water table elevation to the bottom of the peat layer. The unit weights of the peat deeper than about 6m were not known. The unit weight of 13 kN/m^3 for the soft peat is an average value that results in zero effective stress at the peat/sand interface.

Vertical total stresses underneath the levee were modeled using Settle3D, a program that implements elastic solutions with a graphical interface. Vertical effective stress was then computed as the difference between the vertical total stress and the pore pressure. Two effective stress profiles are shown in Fig. 5.18, one at the location of sensors P1 and P2 underneath the center of the levee toe and one for sensors P3 and P4 underneath the center of the levee crest.

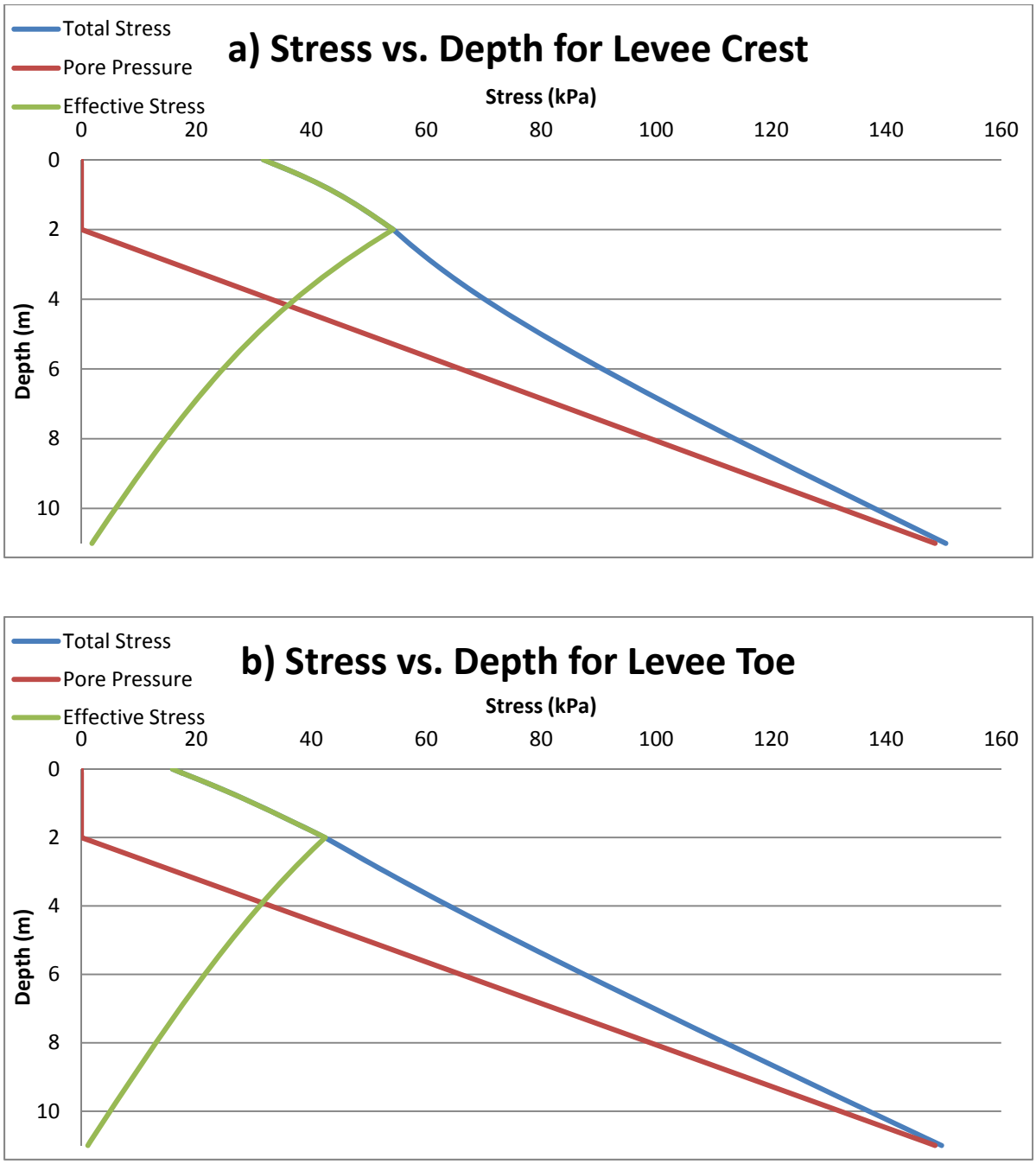

Fig. 5.18: Total stresses underneath the levee crest and toe from Settle3D

Residual pore pressures were calculated for all four piezometers for each shake test as:

$$u_{res} = u_{final} - u_{init} \quad \text{.. Eq. 5.19}$$

where u_{init} and u_{final} are the initial and final pore pressures for a given shake test. Essentially, residual pore pressure represents the change in pore pressure from before and after a shake test, but not during the shaking itself. For example, Fig. 5.19 shows dynamic pore pressure vs. time of sensor P3 for a high intensity motion (2011 MK15_5_1). Since there is inherent noise in the record, both the u_{init} and u_{final} values are taken as the mean value of the first and last 2 seconds of pore pressure data. For this example, u_{init} = 31.440 kPa and u_{final} = 31.544 kPa, giving a u_{res} value of 0.104 kPa. Hence, r_{ur} = 0.104 kPa/44.1 kPa = 2.36×10^{-3}. Note that the pore pressure was still increasing at the end of this test for this sensor. Pore pressure u_{res} was only calculated in between the beginning and end of the test window extracted from the hour-long block of data by the Snippet program.

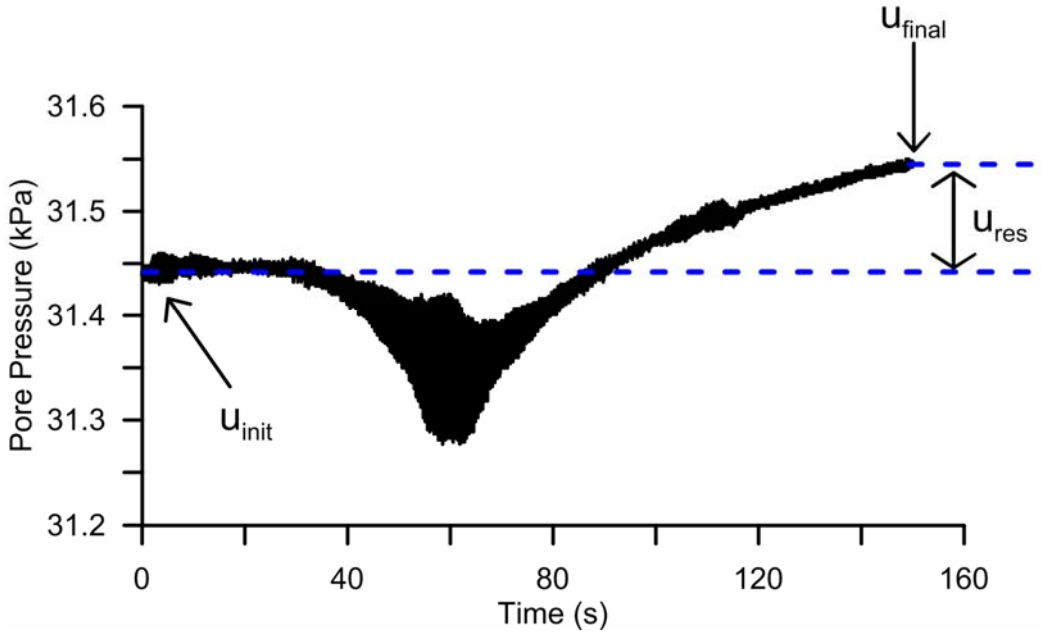

Fig. 5.18: Dynamic pore pressure response for sensor P3 during a high intensity shake test (2011 MK15_5_1)

5.3.2. Shear Strain and Pore Pressure Response

Figs. 5.20 – 5.22 show the comparison of residual pore pressure ratio vs. maximum shear strain for the 2011 and 2012 tests. Note that only the results underneath the levee crest were presented for the 2012 tests, as shear strain could not be computed underneath the levee toe for that sequence of shake tests due to failure of several MEMS accelerometers, as seen in Chapter 5.2.1. Fig. 5.20 shows a clear trend in r_{ur} with increasing shear strain for sensor P2, which is well beneath the water table, while the same trend is not present for sensor P1, which is embedded barely below the water table. The mobilized residual pore pressure ratios, although measurable and clear, are very small, which helps explain why no measurable post-cyclic settlement was measured. Higher residual pore pressure ratios were measured beneath the crest than beneath the toe. This may reflect a longer drainage path length beneath the crest limiting rapid pore pressure dissipation, whereas pore pressures may have dissipated rapidly by drainage near the toe.

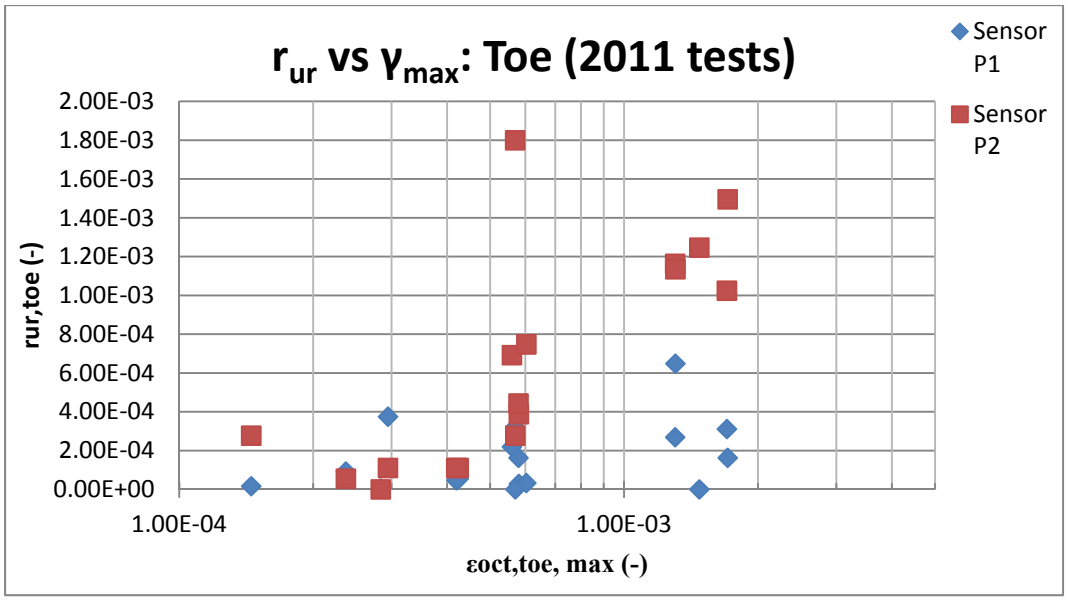

Fig. 5.20: Residual pore pressure ratio vs maximum shear strain underneath levee toe for 2011 test sequence.

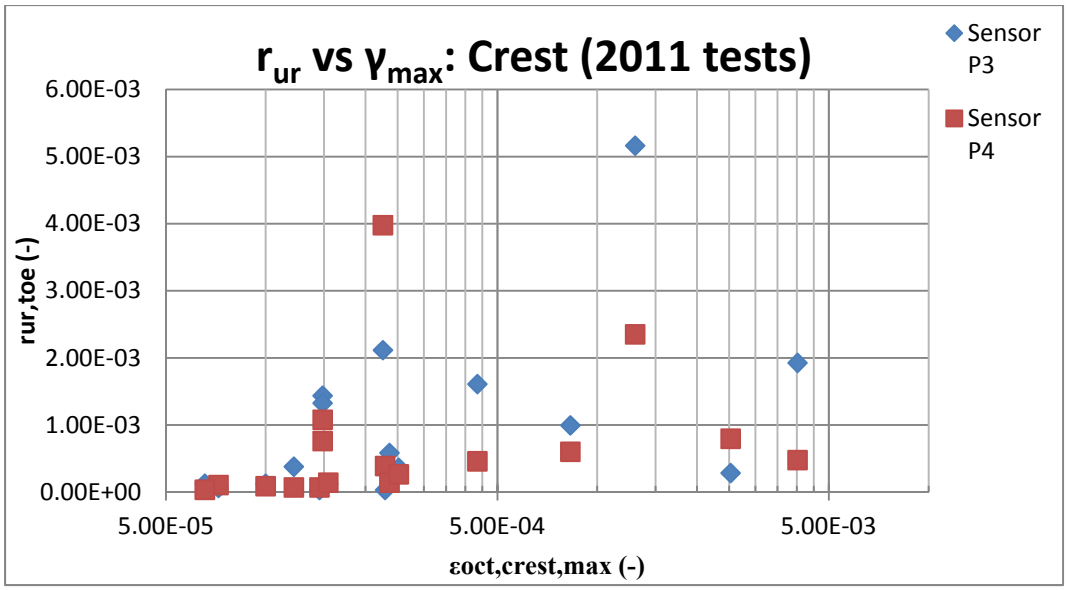

Fig. 5.21: Residual pore pressure ratio vs maximum shear strain underneath levee crest for 2011 test sequence.

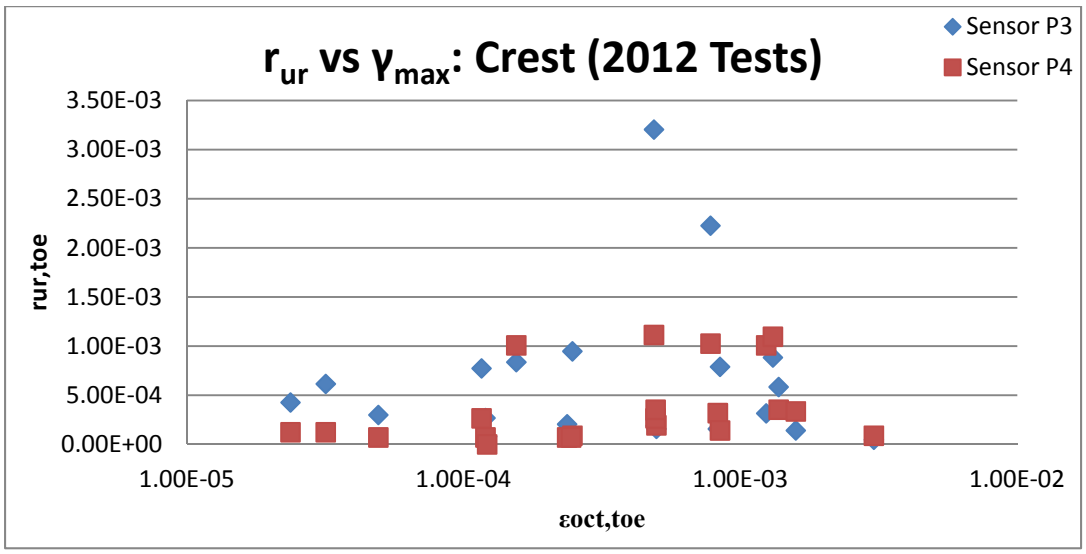

Fig. 5.22: Residual pore pressure ratio vs maximum shear strain underneath levee crest for 2012 test sequence.

Fig. 5.23 shows a comparison of the r_{ur} – maximum shear strain for the field tests along with a series of cyclic triaxial tests and cyclic direct shear tests performed on the Sherman Island peat by Stewart et al. (2013). The shear strain levels tested in the lab are comparable to those

obtained during the field testing.. For comparable strain levels, residual pore pressures in the field tests are much lower than the residual pore pressures for the lab tests. At 0.3% shear strain, for example, r_{ur} obtained from the lab testing ranged from 0.02 – 0.13, while r_{ur} from the field tests ranged from close to zero to roughly $2x10^{-3}$. A number of factors may contribute to this difference. First, pore pressure dissipation may have occurred during shaking in the field tests, whereas undrained conditions were maintained during the lab tests. Second, secondary compression results in plastic volumetric strain in drained loading, which is manifested as an increase in pore pressure during undrained loading. Hence, a portion of the residual pore pressures mobilized in the lab studies may be caused by secondary compression instead of shear, whereas this source of pore pressure generation may be less pronounced in the field tests where fully undrained conditions were likely not achieved.

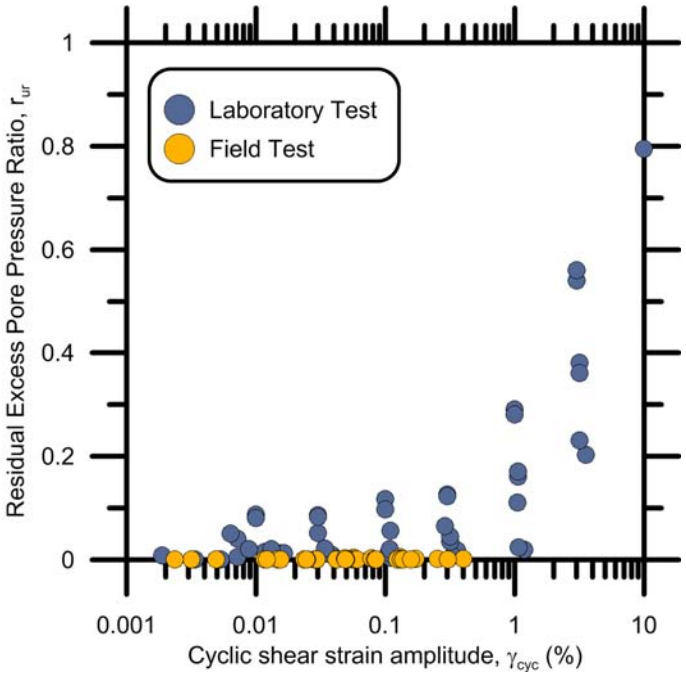

Fig. 5.23: Comparison of residual excess pore pressure vs. cyclic shear strain amplitude between field testing and laboratory testing.

5.4. Dynamic Finite Element Model Testing

This section focuses on a series of elastic 2 dimensional dynamic finite element models in OpenSees to (1) expand upon the field test measurements, (2) explore differences in stresses and strains for top-down forced vibration compared with bottom-up shaking conditions, and (3) explore how the impedance contrast between the levee and peat influences mobilization of stresses and strains. These simulations are an extension of the simulations presented in Chapter 4 as part of the design of the model levee. Construction of the finite element model (FEM) will be presented first, focusing on the mesh structure, material properties, and the various loading sequences used in the simulations. Development of shear strains beneath the levee due to top-down shaking of the model are then presented, comparing to the test results as well as among finite element scenarios with different peat stiffness. Shear strains mobilized for bottom-up shaking are then compared with the top-down forced vibration for cases with the same crest acceleration. Finally, dynamic stresses in the levee fill and beneath the levee are presented, and rotation of principal stress directions relative to a simple shear stress path are shown to increase stress demands for a given crest acceleration compared with stress demands evaluated using traditional liquefaction triggering procedures.

5.4.1. Construction of Finite Element Model

This set of finite element simulations are an extension of the simulations presented in Chapter 4, which were used for design of the model levee. Improvements include (1) development of a uniform mesh that is better suited to dynamic simulation, and (2) improvements to the geometry and soil stiffnesses based on site investigation data that was not available at the time the finite element simulations were performed to design the model levee.

This mesh is also used for different simulated loading sequences and for different material properties to explore several fundamental features of dynamic levee response. Similar to the FEM simulations seen in Chapter 4, the mesh was generated using the pre and post-processing program GiD. Fig. 5.24 shows the portion of the mesh that will be visualized herein.

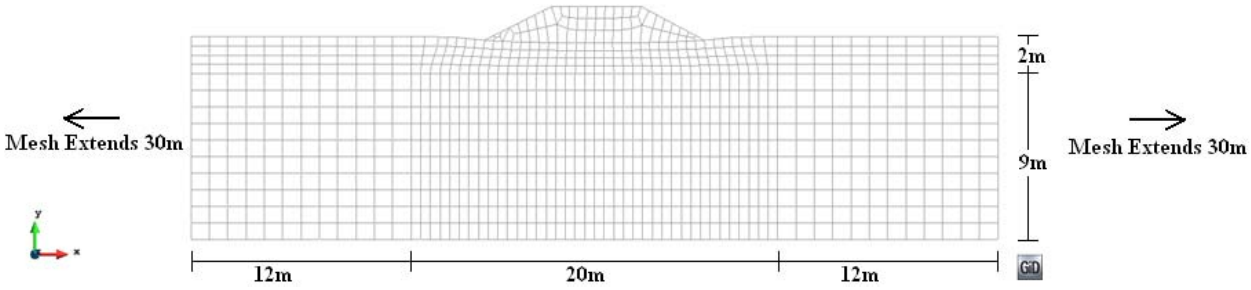

Fig. 5.24: Improved FEM Mesh for dynamic simulations.

The portion of the mesh shown in Fig. 5a contains 1,003 nodes as well as 925 quadrilateral elements. The free trial version of GiD was used to create this mesh and post-process results, and this version is limited to 1,010 nodes. A full version of GiD had originally been purchased, but the computer containing this license crashed and we could not transfer the license to another computer. The horizontal extent of the largest mesh that could be generated with the free version is too short to prevent reflection of waves from the vertical boundaries from influencing the levee response. For this reason, an additional 30m of elements were added to the left and right sides of the mesh, resulting in a total mesh size of 1,903 nodes and 1,765 quadratic elements, and total length of 104m. This mesh size was obtained by increasing the number of elements until the response of the model levee was no longer changing significantly with the horizontal mesh dimension, indicating that the influence of boundary reflections was negligible.

Despite the presence of these extra nodes and elements in the finite element simulations, visualization of the output is restricted to the region shown in Fig. 5.24.

An important aspect of the simulations to note is that they are two dimensional. However, the field loading conditions were three dimensional. It is not expected that the results from these simulations will match the field testing perfectly, but they will still provide a basis for understanding several fundamental features of peat behavior, such as reasons where high shear strains are mobilized, relative shear strains between top-down and bottom-up excitation conditions, and ratios of maximum shear strains to in-plane shear strains.

The element sizes were selected to provide at least 8 elements per wavelength based on mesh stiffness and excitation frequency. In this case, the lowest shear wave velocity was 25m/s, and the highest frequency was 3 Hz, resulting in a wavelength of about 8m. The largest mesh dimension was therefore set to be equal to 1m. This mesh may admittedly be too coarse for dynamic problems with higher frequencies (e.g., earthquake ground motions), but is well-suited to the dynamic problems for which it is utilized in this dissertation. Full Rayleigh Damping was utilized in the model, with damping set to 5% at frequencies of 0.1 Hz and 3 Hz, which is the range for which the model levee was shaken during the field tests.

All nodes along the bottom of the mesh were fixed in the x and y direction. This is considered a reasonable condition because of the large impedance contrast between the soft peat and the sand underlying it. The nodes along the sides of the extended mesh were not rigidly fixed, instead the "equalDOF" command in OpenSees applied harmonic boundary conditions to edge nodes sharing the same y-coordinate. This was done to enforce shear beam deformations at the boundaries during base excitation, and to enforce a K_0 condition.

The soil was modeled using an elastic isotropic material model that requires as input the shear wave velocity (V_s), mass density (ρ), and Poisson ratio (ν). Five different soil properties were utilized as summarized in Table 5.24. These soil properties were arranged in four different configurations as shown in Fig. 5.25. Case 1 corresponds to the measured site conditions with a desiccated crust overlying soft peat. Case 2 corresponds to a condition in which the desiccated crust is replaced with soft peat to observe the influence of the desiccated crust on mobilized shear strains (note that actual Delta levees rest atop saturated peat). Case 3 corresponds to a uniform soil condition in which the peat properties are set equal to the levee fill properties, and Case 4 corresponds to a condition in which the foundation soil is stiffer than the levee fill, which is the configuration that exists below many flood control levees outside the Delta. These cases were introduced for the purpose of observing how levee-peat interaction is influenced by the impedance contrast between the fill and the foundation soils. These four cases were picked to compare displacements, shear stresses, and shear strains over different impedance contrasts between the levee and the underlying soil. A similar study was performed by Athanasopoulos-Zekkos and Seed (2013), which focused on levees founded on peat, on clay, and on sand.

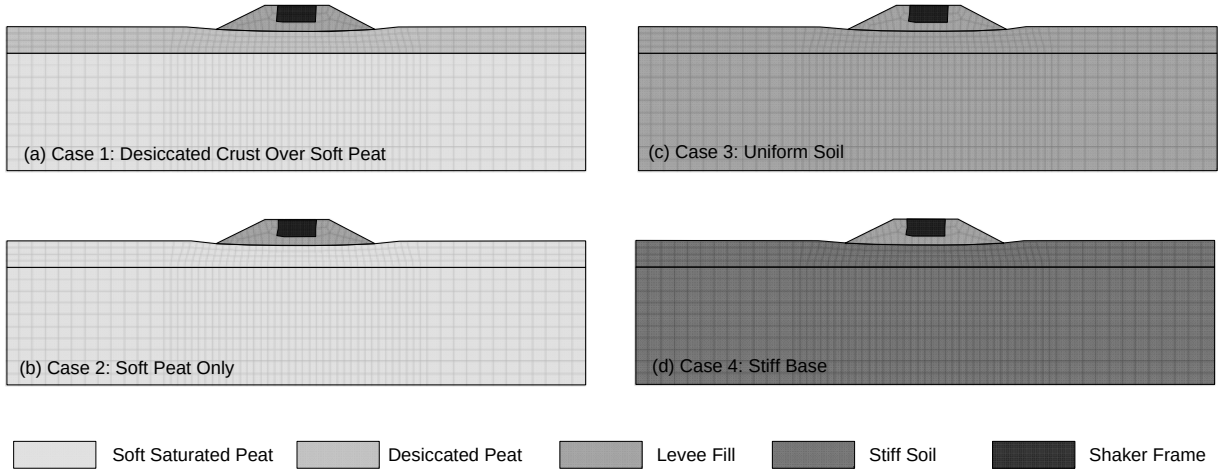

Figure 5.25: Configurations of material properties for various finite element simulations.

Table 5.1: Summary of material properties for various test configurations.

	Soil Type				
	Soft Saturated Peat	Desiccated Peat	Levee Fill	Stiff Soil	Shaker Frame
V_s [m/s] =	25	60	200	500	292
ρ [Mg/m^3] =	1.12	1.12	1.76	1.76	1.76
ν [-] =	0.45	0.30	0.30	0.30	0.30

Two loading configurations were performed for each case. The first loading configuration consisted of top-down forced vibration, as seen in the schematic of Fig. 5.26. The shaker load is represented as a force couple intended to capture the horizontal force amplitude, and the moment created by the shaker force acting at a centroid H_s above the levee crest. The horizontal shaker force, F_{shk}, is distributed between two nodes with force amplitude of $F_{shk}/2$, and the moment caused by the shaker defined as $F_{shk}*H_s$, is also distributed between two nodes as forces with

amplitude F_{shk}*H_s/2B, where B is the distance between the two nodes adjacent to the node at the center of the levee crest. For the coupled loading simulations, H_s = 0.3m, while B = 0.97m.

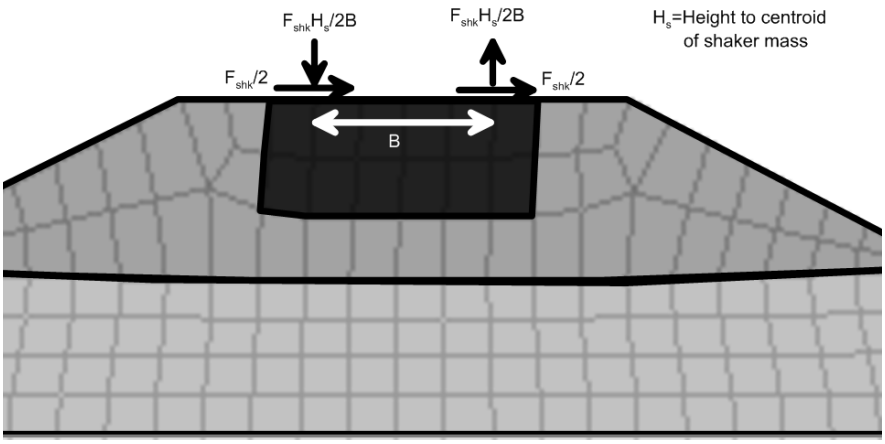

Fig. 5.26: Coupled top-down loading in finite element simulations.

The second loading configuration consists of uniform excitation applied to the fixed base nodes. This was achieved using the "pattern UniformExcitation" command in OpenSees. Using this command, all fixed nodes are excited with the same acceleration time series. Note that the side nodes were not fixed, but rather utilized harmonic boundary conditions. Hence, the sides of the domain accurately simulate the propagation of vertical shear waves.

Both sets of loading configurations were simulated using a sine sweep signal that swept from 0 – 3 Hz over a span of 10 seconds, similar to the fast sine sweeps imposed during the field tests. A cosine taper was applied to the ends of the sweep signal, which is shown in Fig. 5.27. For both the top-down and bottom-up loading configurations, the sweep is simply multiplied by the desired force magnitude (for top down loading) or the desired acceleration (for bottom up loading). Since the analysis is elastic, the principal of superposition can be used to simply scale the entire model response to a particular value. For example, the top-down and bottom-up

simulations are later scaled to the same value of crest acceleration to observe the resulting stress and strain distributions. In the case of the top-down loading, this sweep is also useful because it more accurately resembles the shaker forcing function during the field tests, where force is proportional to the square of the shaker frequency.

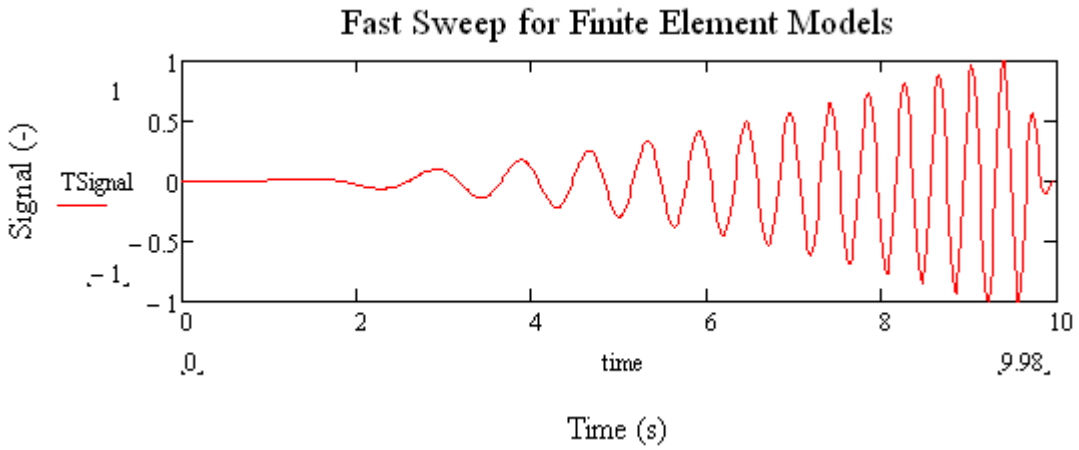

Fig. 5.27: Sweep signal used in finite element simulations.

5.4.2. Comparison of Finite Element Shear Strains with Shear Strains from Field Tests

This section focuses on the development of shear strains within the peat from the finite element simulations as a means of comparison with shear strains developed within the peat during the field tests. In this case, the finite element models will focus on the top-down coupled loading only, as this is meant to both validate the test results as well as compare between different material property configurations.

All finite element models discussed in this section were simulated with a peak shaker force of 88.8 kN. This shaker force is equivalent to the peak shaker force seen in the medium-intensity field tests, i.e. Trials 2 and 3 in the 2011 and 2012 MK-15 field tests. Therefore, the

results obtained from the simulations will be compared to the results from these field test trials. The shaker force of 88.8 kN was selected because this was roughly the maximum force exerted from the shaker before pounding between the shaker frame and levee fill became significant. Shear strains from these simulations were recorded at four Gauss points within each quad element.

Fig. 5.28 shows contours of the maximum shear strain for Case 1. These contours do not correspond to a particular time step (i.e., this is not a snapshot), but rather an envelope of the maximum shear strain for each Gauss point. The peak shear strains in the peat 1-3m below the levee toe ranges from approximately 0.04% - 0.08%, while the shear strains within the peat beneath the levee crest ranges from 0.02% - 0.06%. Rectangles are sketched in the region where subsurface accelerometers permitted calculation of peak shear strains. The peak measured shear strains for a shaking amplitude of 90 kN ranged from about 0.05% to 0.02% beneath the toe and crest of the levee for the 201 test, respectively, and were 0.05% beneath the crest for the 2012 test (strain beneath the toe couldn't be measured due to sensor malfunction). There is good agreement between the measured and predicted shear strains in this region. The peak predicted shear strains in the peat did not occur in the region where the strain measurements were made. Maximum shear strains as high as 0.1% were observed in the soft peat just below the region where measurements were made. These are approximately twice as large as the shear strains mobilized in the region where shear strains were measured during the experiments. There appear to be boundary issues along the base and corner of the model, but the effect on the area of interest is very small. Therefore, I conclude that the peak shear strains that were mobilized during the shake testing are approximately twice as large as the measured peak shear strains. However, these peaks are also at a deeper elevation compared with the positions where pore

pressures were measured. The measured shear strains tend to be more applicable to the locations of pore pressure measurements.

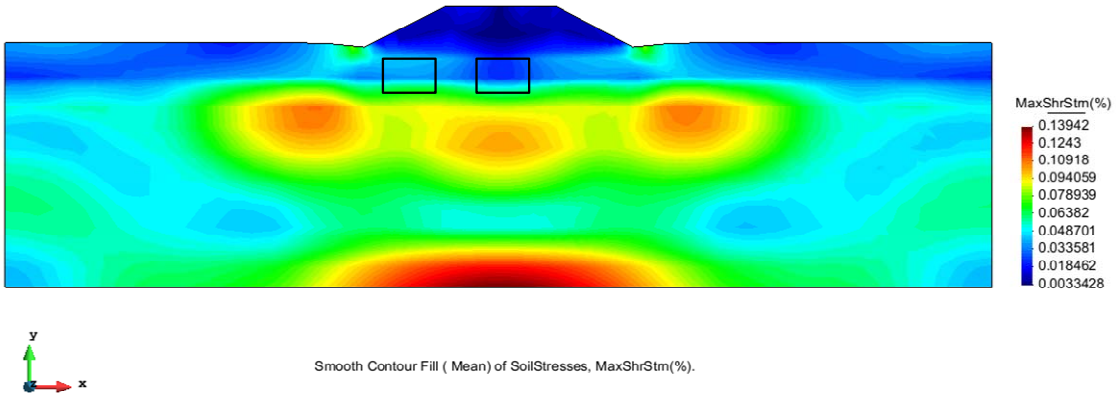

Fig. 5.28: Maximum shear strain contours for top-down for Case 1.

Figs. 5.29 shows the maximum shear strain contours for Case 2 with soft peat existing all the way to the surface. This case is a better representation of the conditions that exist beneath real levees, where a desiccated crust is not anticipated. In this case, the peak shear strains occur immediately beneath the levee, and are approximately twice as large as for Case 1. Shear strains in the region where field measurements are available range from 0.12% - 0.17%, which are more than double the strains for Case 1. This indicates that the desiccated crust influenced the response of the model levee, and resulted in smaller mobilized shear strains. Had the crust not been present, higher shear strains would have been mobilized, and some measurable settlement might have occurred as a result, though this is strictly conjecture.

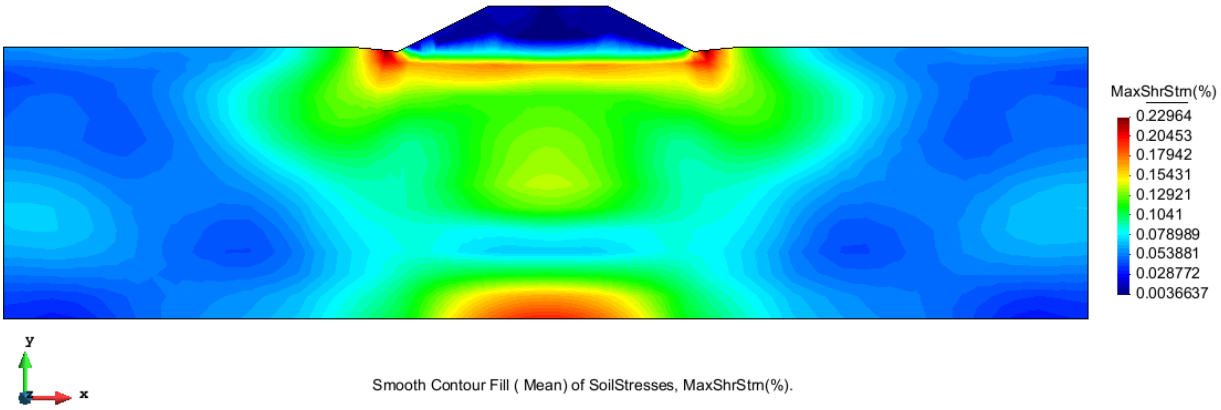

Fig. 5.29: Maximum shear strain contours of coupled top-down loading for the case of soft peat.

Figure 5.30 and 5.31 show strain contours for Case 3 (uniform soil) and Case 4 (stiff soil), respectively. For Case 3, shear strains are highest in the levee fill and immediately beneath it, and the peak mobilized strains are about an order of magnitude lower than Case 1. This is anticipated because, for a given force amplitude, much higher strains are anticipated in the soft peat than in the levee fill. For Case 4, shear strains mobilized in the levee fill increase slightly compared with Case 3, and shear strains in the stiff soil are very small. In fact, the shear strains were so small that they had to be multiplied by 100 to avoid being rounded to 0 by the GiD visualization program. The stiff impedance contrast at the levee base in Case 4 resulted in reflections of waves that increased shear strains within the levee fill compared with the uniform soil in Case 3.

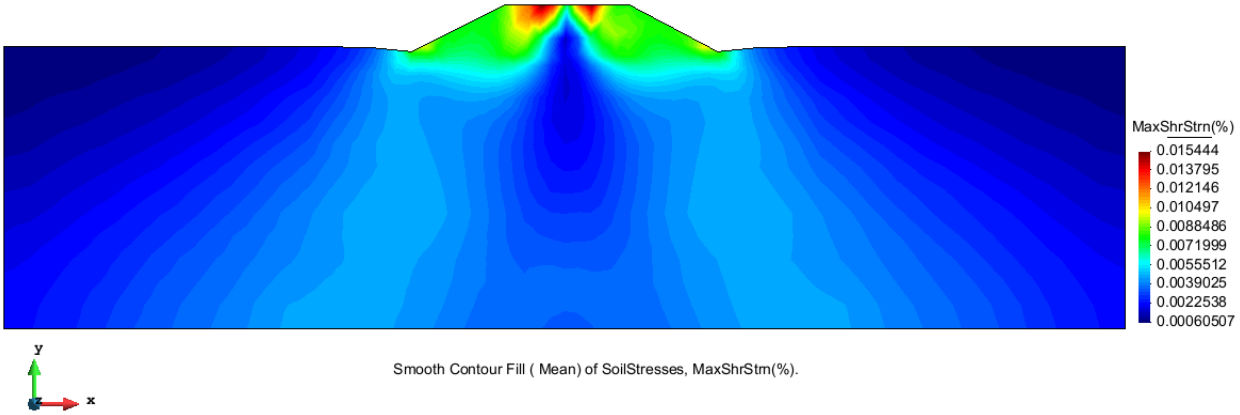

Fig. 5.30: Maximum shear strain contours of coupled top-down loading for the case of uniform soil.

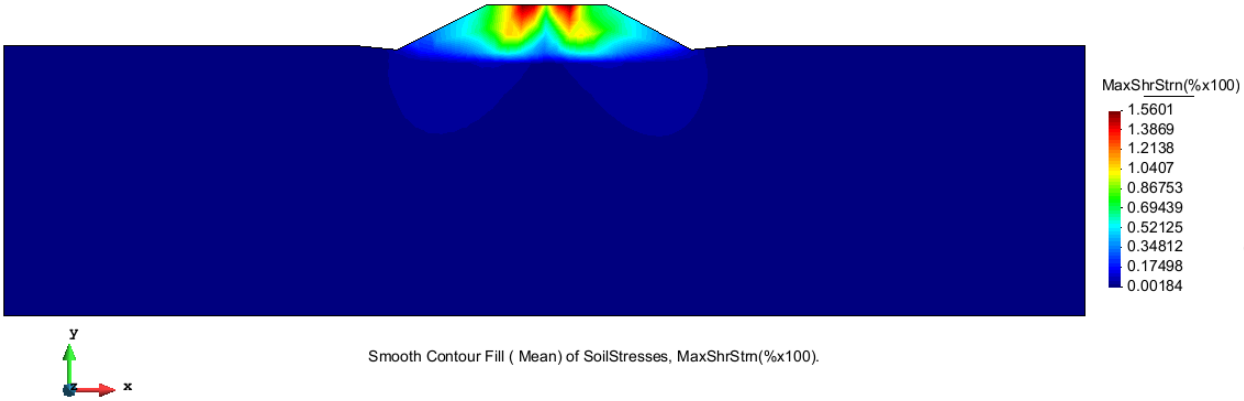

Fig. 5.31: Maximum shear strain contours (% x 100) of coupled top-down loading for the case of stiff soil.

5.4.3. Comparison of Shear Strains For Top-Down and Bottom-Up Excitation

This section focuses on assessing the shear strains that would be mobilized due to a vertically propagating shear wave (i.e., bottom-up shaking) compared with top-down forced vibration. In order to find a basis of comparison between the top-down and bottom-up excitations, the input motions are scaled so that the peak horizontal acceleration at the center of the levee crest is 0.3g (2.94 m/s^2), which is selected to be consistent with seismic hazard in the Delta. Shear strains from top-down shaking arise only from inertial interaction between the levee

and peat, whereas those from bottom-up shaking arise from a combination of site response and inertial interaction. Note that as with the previous section, the figures presented in this section show the maximum shear strain envelope for each element, rather than the time step where maximum shear strain occurs.

Figs. 5.32 and 5.33 show contours of the maximum shear strains of motions scaled to 0.3g at the levee crest for Case 1 for top shaking and base excitation cases, respectively. As with the rest of the figures presented in this section, the contour ranges are scaled to span the same range of values so comparisons can be more easily made. In the case of the top-down loading, the maximum shear strain developed is about 0.7%, which is only about half that of the maximum shear strain developed in the base excitation case (1.4%). Furthermore, shear strains in the bottom-up shaking condition are more broadly distributed spatially than for the top-down condition. Two distinct high-strain bands are present, which likely reflects a multi-modal response. Based on comparison of these strain contours, significantly higher strains would be anticipated for an earthquake ground motion compared with a top-down shake at the same crest acceleration amplitude. This could translate to measurable post-cyclic settlements based on laboratory testing performed by Shafiee et al. (2013) and presented in Section 5.3.2. The peak base acceleration needed to achieve 0.3g peak horizontal crest acceleration was 0.26g.

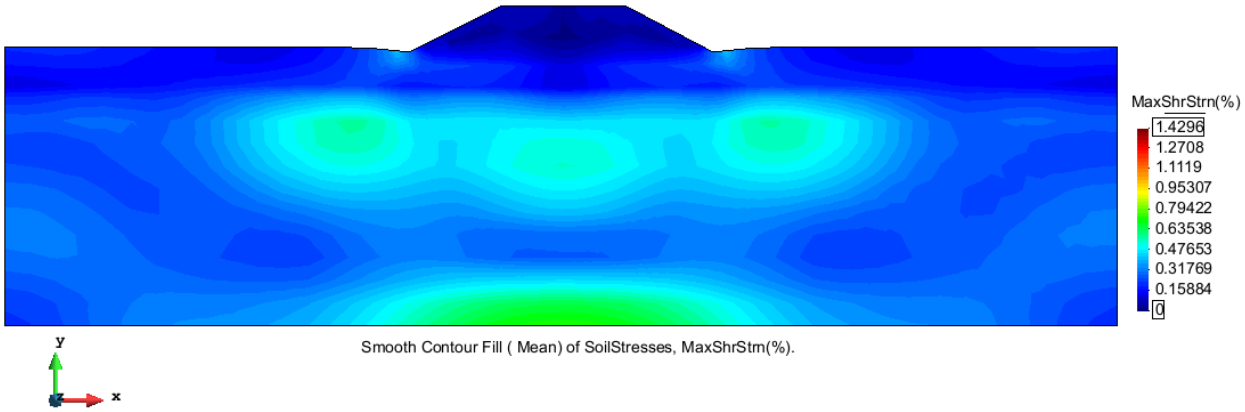

Fig. 5.32: Max shear strain contours for coupled top-down loading with 0.3g scaled motion at levee crest for the case of stiff crust over soft peat.

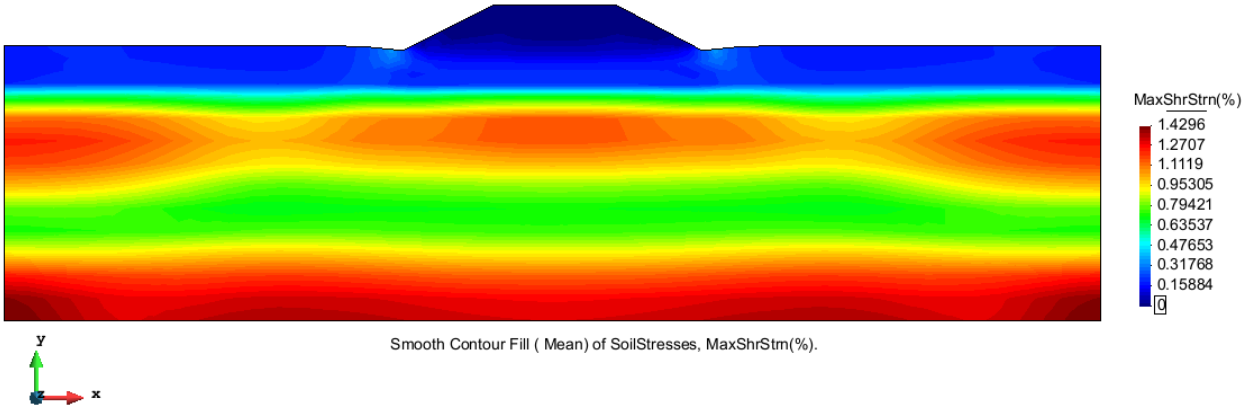

Fig. 5.33: Max shear strain contours for uniform base excitation with 0.3g scaled motion at levee crest for the case of stiff crust over soft peat.

Figs. 5.34 and 5.35 show the maximum shear strains for Case 2 with soft peat up to the surface. The results for this case follow the same trend seen in Figs. 5.32-5.33. The difference in peak maximum shear strain is less for the soft peat case when compared to the stiff crust case. Both cases show higher shear strains concentrated underneath the center of and just outside the toes of the levee. The reasons for this particular distribution of shear strains are unclear, but are related to the dynamic response of the site. Note that the sine sweep function has amplitude that varies with frequency. Therefore, sites with different modal frequencies would be expected to

have different peak strain amplitudes. The peak horizontal base acceleration needed to achieve the desired peak crest acceleration is 0.23g.

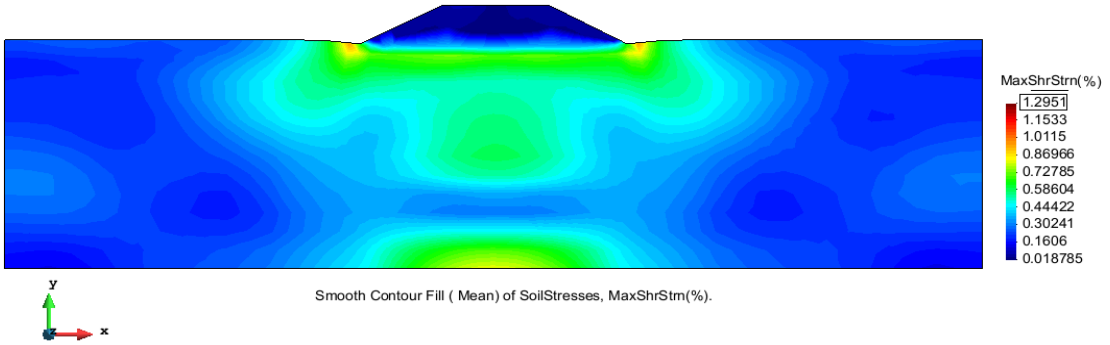

Fig. 5.34: Max shear strain contours for coupled top-down loading with 0.3g scaled motion at levee crest for the case of soft peat.

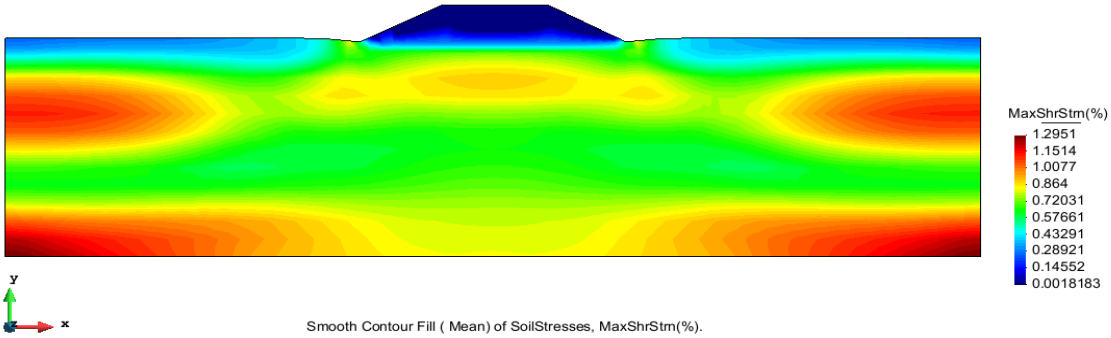

Fig. 5.35: Max shear strain contours for uniform base excitation with 0.3g scaled motion at levee crest for the case of soft peat.

The maximum shear strain for both the uniform soil cases can be seen in Fig. 5.36 and 5.37. Unlike the previous two soil property configurations, the peak shear strains occur with the top-down loading, with the highest shear strain occurring at the points where the coupled loading was applied. However, shear strains in the soil beneath the levee tend to be higher for the bottom up shaking than for the top-down. Also, the peak horizontal base excitation needed to achieve the desired horizontal crest acceleration is only 0.065g. This is the result of the first mode resonance

for Case 3 occurring at approximately (200 m/s) / (4*11m) = 4.5 Hz, which lies closer to a region of high amplitude in the input motion compared with Case 2 (25 m/s)/(4*11m) = 0.6 Hz. This further reinforces the point that shear strains are caused by both site response and inertial interaction with the levee.

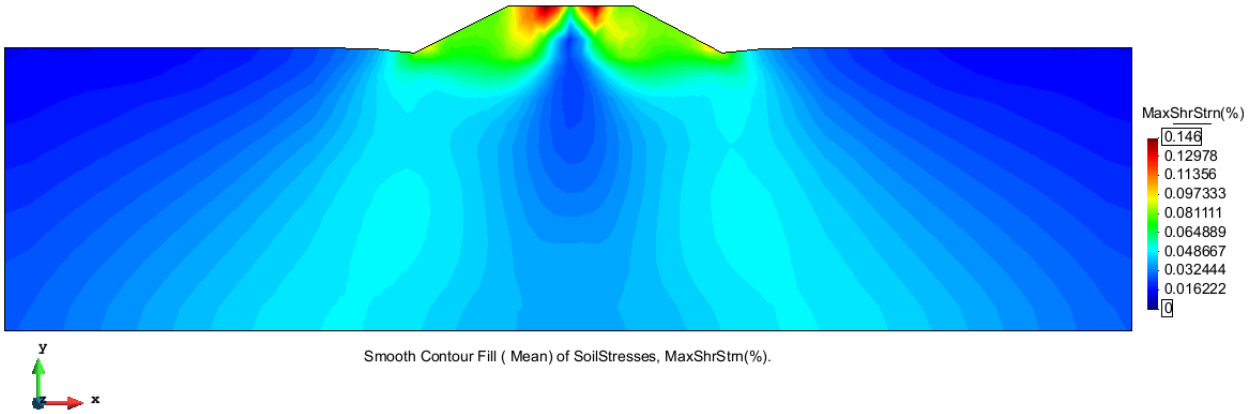

Fig. 5.36: Max shear strain contours for coupled top-down loading with 0.3g scaled motion at levee crest for the case of uniform soil.

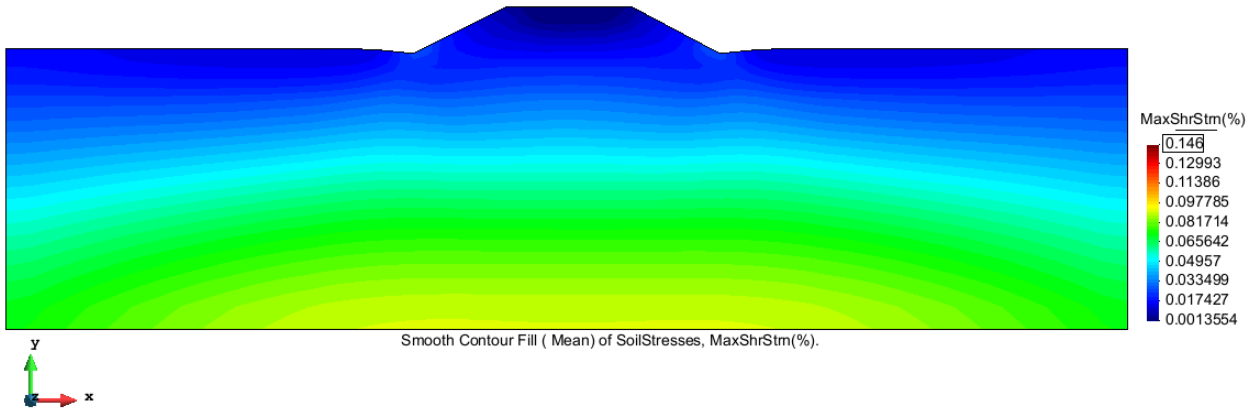

Fig. 5.37: Max shear strain contours for uniform base excitation with 0.3g scaled motion at levee crest for the case of uniform soil.

The peak shear strains for the stiff soil cases are seen in Figs. 5.38 and 5.39 for the top-down and base excitation, respectively. Similar to the uniform soil case, peak shear strains tend to be much higher in the coupled top-down shaking, with the highest shear strains occurring in the levee fill. However, underneath the levee, shear strains tend to be very close to zero for nearly the entire domain. This does not occur in the base excitation case, as seen in Fig. 5.39. Instead, higher shear strains are present both within the center of the levee fill as well as at the bottom of the stiff soil layer. Still, the maximum shear strain achieved for the base excitation case was only around 0.01% Shear strains in the stiff soil layer appear to increase uniformly with depth. Essentially, the stiff soil behaves almost like a rigid body compared to the levee fill. For the case of base excitation, a peak acceleration of 0.25g was needed to achieve a peak crest acceleration of 0.3g.

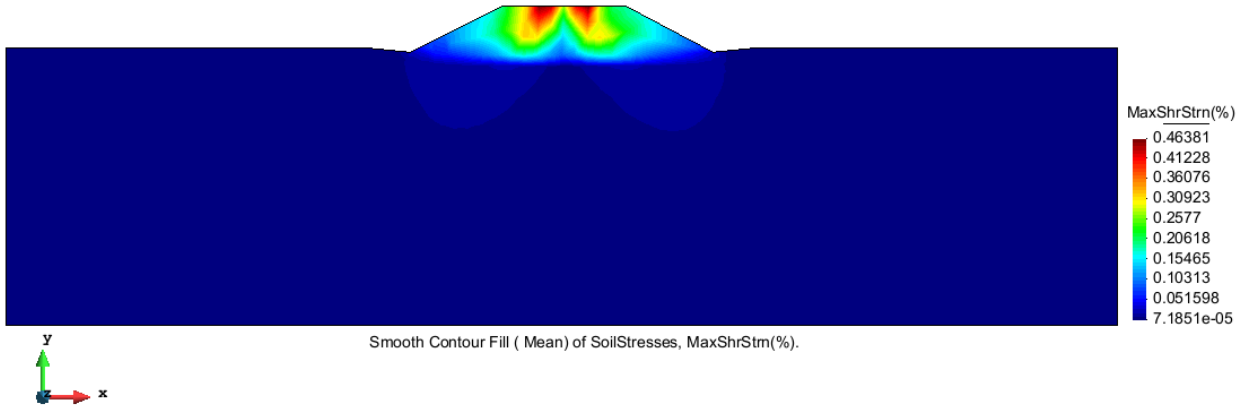

Fig. 5.38: Max shear strain contours for coupled top-down loading with 0.3g scaled motion at levee crest for the case of stiff soil.

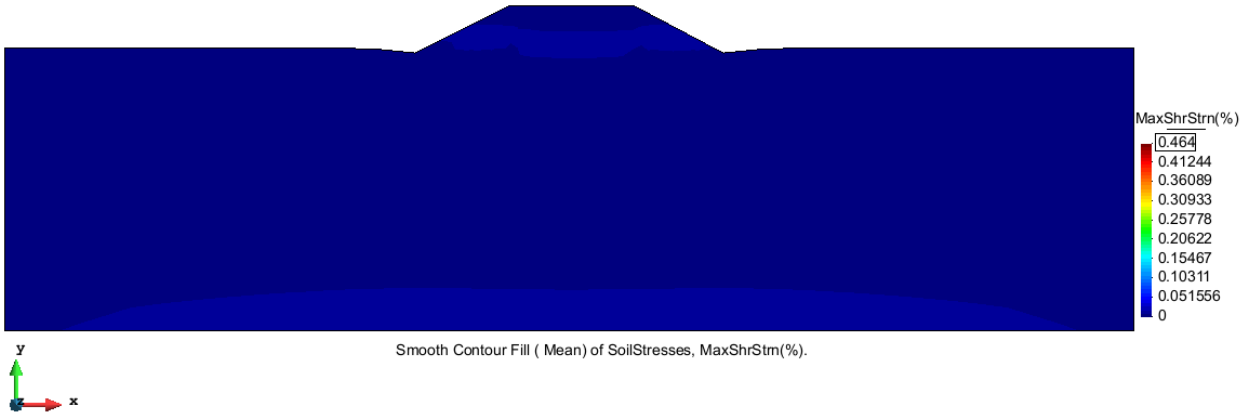

Fig. 5.39: Max shear strain contours for uniform base excitation with 0.3g scaled motion at levee crest for the case of stiff soil.

5.4.4. Dynamic Stresses Within and Beneath the Levee Fill

This section focuses on the peak stresses mobilized in the levee fill and in the underlying peat. This has implications for liquefaction triggering evaluation in cohesionless soils, and cyclic strength loss in other soils (clay, peat). Two factors are shown to alter the cyclic stress ratios for levees relative to one-dimensional wave propagation for level ground conditions. First, the shear stress component τ_{xy} is influenced by geometric anomalies associated with the two-dimensional levee geometry. This feature of behavior was also observed by Athanasopoulos-Zekkos and Seed (2013) using Quad4M simulations. Second, dynamic variations in vertical and horizontal pressures add to the τ_{xy} component, which means that the traditional definition of CSR is inadequate to characterize the shear stress demands. Consider the level ground scenario seen in Fig. 5.40, where a soil column is deformed in simple shear. An element in the soil is located at a depth D and experiences vertical and horizontal normal stresses σ_y and σ_x respectively, along with shear stress τ_{xy}. The element has a mass m and experiences a horizontal acceleration a and a cross-sectional area A that varies along the z-axis. This soil undergoes alterations in t_{xy}, but no alterations in σ_{xx} or σ_{yy}(Eq. 5.20). Therefore, using τ_{xy} to characterize shear stress makes sense,

and is in fact the assumption utilized in liquefaction triggering evaluation procedures (except that the integral in Eq. 5.20(a) is replaced by the product of total stress at the depth of interest, peak surface acceleration, and r_d (Seed and Idriss, 1971).

$$\tau_{xy} = \frac{\int_0^D m * a(z) dz}{A} \quad \text{.. Eq. 5.20(a)}$$

$$\Delta\sigma_y = 0 \quad \text{.. Eq. 5.20(b)}$$

$$\Delta\sigma_x = 0 \quad \text{.. Eq. 5.20(c)}$$

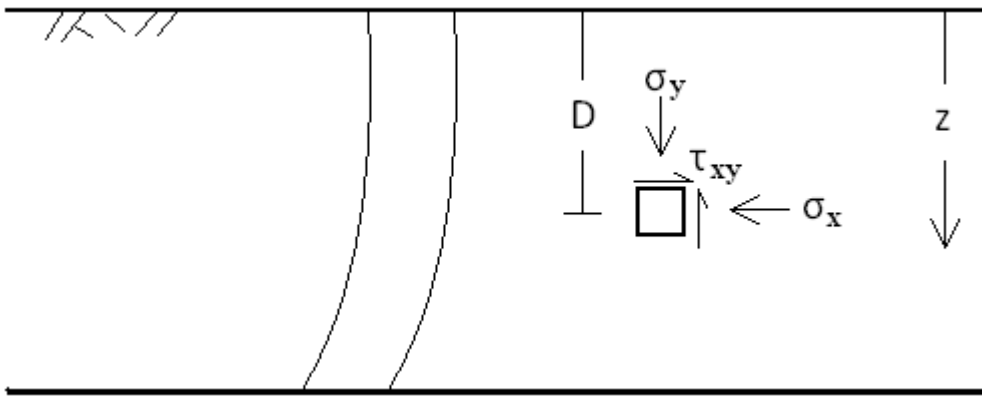

Fig. 5.40: Element in level ground in simple shear.

Now consider the same element underneath the toe of a rocking levee, as seen in Fig. 5.41. In this case, the stresses experienced are not in simple shear, but instead correspond to a wide array of different stress paths. Beneath the crest, simple shear may be a good proxy for the stress condition, but beneath the toes there are significant variations in vertical and horizontal pressures, and the shear stress τ_{xy} is also not necessarily equal to the integral of mass times acceleration of the overlying soil. These conditions can also be expressed in Eq. 5.21:

$$\tau_{xy} \neq \frac{\int_0^D m * a(z)dz}{A} \quad \text{.. Eq. 5.21(a)}$$

$$\Delta\sigma_y \neq 0 \quad \text{.. Eq. 5.21(b)}$$

$$\Delta\sigma_x \neq 0 \quad \text{.. Eq. 5.21(c)}$$

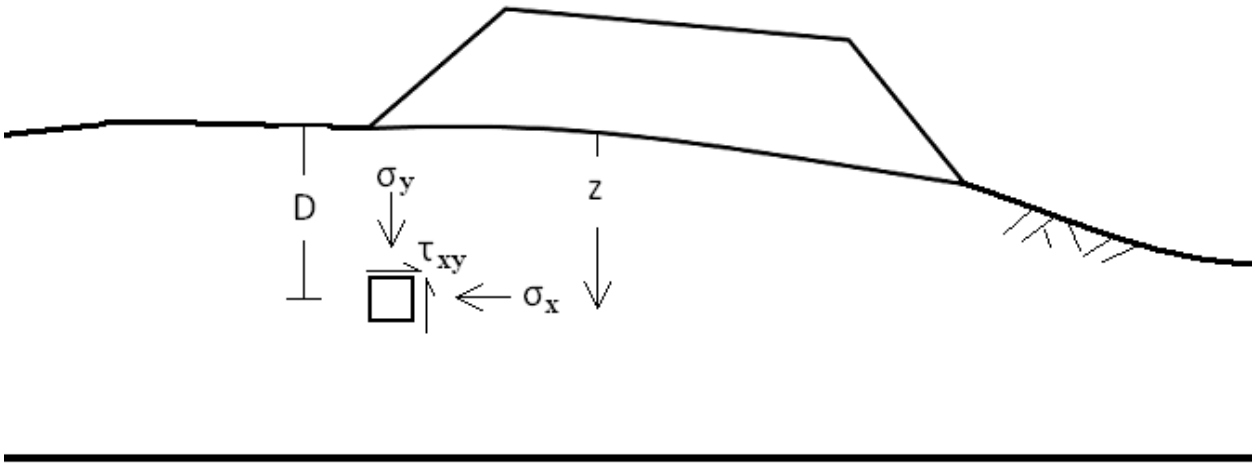

Fig. 5.41: Element in underneath the toe of a rocking levee.

In liquefaction triggering analysis, two quantities are desired in order to calculate the factor of safety against liquefaction, FS_{LF}, as seen in Eq. 5.22 (Kramer 1996):

$$FS_{LF} = \frac{CRR}{CSR} \quad \text{.. Eq. 5.22}$$

where CRR is defined as the cyclic resistance ratio, which is a function of factors such as the earthquake magnitude and vertical effective stress, and CSR is the cyclic stress ratio, which

represents seismic demand imposed on the soil, and as seen in Eq. 5.23, is defined as the cyclic shear stress divided by the vertical effective stress. Seed and Idriss (1971) proposed a method that would allow engineers to calculate CSR based on the peak horizontal acceleration (PHA) at the ground surface. This is defined as:

$$CSR = \frac{\tau_{cyc}}{\sigma_{vo}'} = 0.65 \frac{PHA}{g} \frac{\sigma_v}{\sigma_{vo}'} r_d \quad \text{.. Eq. 5.23}$$

where g is acceleration due to gravity, σ_v is the total stress, σ_{vo}' is the effective stress, and r_d is a depth-dependent stress reduction factor. This equation is frequently used by engineers to quantify seismic demand liquefaction analysis, and t_{cyc} is typically taken to be equal to t_{xy}. However, this is only valid for flat sites, similar to those seen in the simple shear condition of Fig. 5.40. Despite that, engineers still use this formulation to calculate seismic demand even in instances where this assumption does not hold. For example, the liquefaction analyses presented in Phase I of the Delta Risk Management Strategy (DRMS 2009) assumes this formulation for levee foundation sands. In other words, engineers attempt to apply this formulation for cases that more resemble Fig. 5.41, where multiple stress components interact. By neglecting the contribution of other components of shear stress, engineers may be underestimating the seismic demand in liquefaction triggering analysis.

To quantify the influence of levee-peat interaction a series of finite element analyses were performed on the simulated model levees mentioned above. The simulations consist of the same base excitations mentioned in the previous section in which the motions were scaled such that the peak horizontal acceleration at the levee crest is 0.3g. Two quantities are of interest in this case: the shear stress ratio $(\Delta\tau_{max}/\Delta\tau_{xy})_{max}$ and $(CSR)_{max}$. The shear stress ratio defines a

correction factor that should be applied to traditional liquefaction triggering procedures to better quantify the actual stress demand. As an analogy, consider a laboratory triaxial test; $\tau_{xy} = 0$ for these tests (based on the assumption of zero end-platen friction) yet the soil can still be liquefied by cyclic loading. Contours of CSR are also computed because the levee-peat interaction influences both τ_{max} and τ_{xy}, and therefore the shear stress ratio by itself is inadequate to explain whether levee-peat interaction is actually causing stress demand to increase.

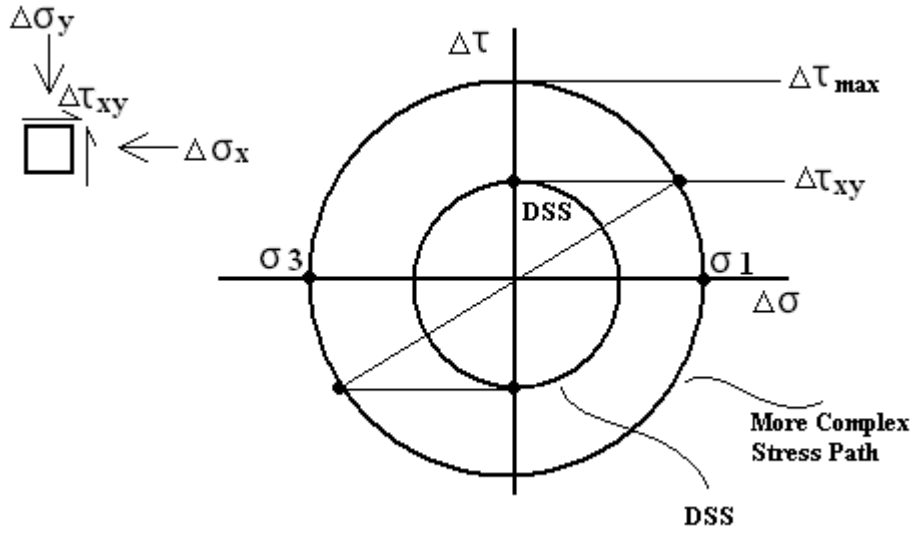

Fig. 5.42: Mohr's Circle of stress changes for $\Delta\tau_{max}$ calculation.

Fig. 5.42 shows a Mohr's circle of stress changes representing a soil element with normal stress changes $\Delta\sigma_x$ and $\Delta\sigma_y$ and shear stress change $\Delta\tau_{xy}$. This figure focuses on the development of peak shear sresses from the simple shear loading case seen in Fig. 5.40 to the more complex stress path seen in Fig. 5.41. Peak shear stress τ_{max} is the radius of the circle and can be calculated in two ways (Gere and Timoshenko 1997) :

$$\Delta\tau_{max} = \frac{\Delta\sigma_1 - \Delta\sigma_3}{2} \quad \text{.. Eq. 5.24(a)}$$

$$\Delta\tau_{max} = \sqrt{(\Delta\sigma_y - \frac{\Delta\sigma_y - \Delta\sigma_x}{2})^2 + \Delta\tau_{xy}{}^2} \quad \text{.. Eq. 5.24(b)}$$

The formulation in Eq. 5.24(b) is used because these components are output from the OpenSees analyses. As with the analyses discussed in the previous sections, the results show the maximum value across all time steps.

Fig. 5.43(a) show the maximum stress ratio for the entire model, while Fig. 5.43(b) shows a zoomed-in portion of the levee toe and the peat just beneath it, with labels noting the maximum shear stress ratio for each element. The first thing to notice in Fig. 5.43(a) is that there is a very high stress ratio along the surface of the peat outside of the levee toe. These high stress ratios are the result of Rayleigh waves propagating through the peat, which cause extensional and compressive stresses and strains, but no τ_{xy} at the surface. Upon close inspection, the stress ratio within the levee fill is significantly higher than unity in regions near the toes, ranging from approximately 1.1 to 2.5. Beneath the levee crest, the stress ratio is approximately unity, indicating that simple shear dominates the stress path in this region. Within the peat, beneath the levee toe, stress ratios can range from 1 – 1.15. Shear stress ratios deeper in the peat are essentially unity since one-dimensional site response dominates the response of the levee in this region.

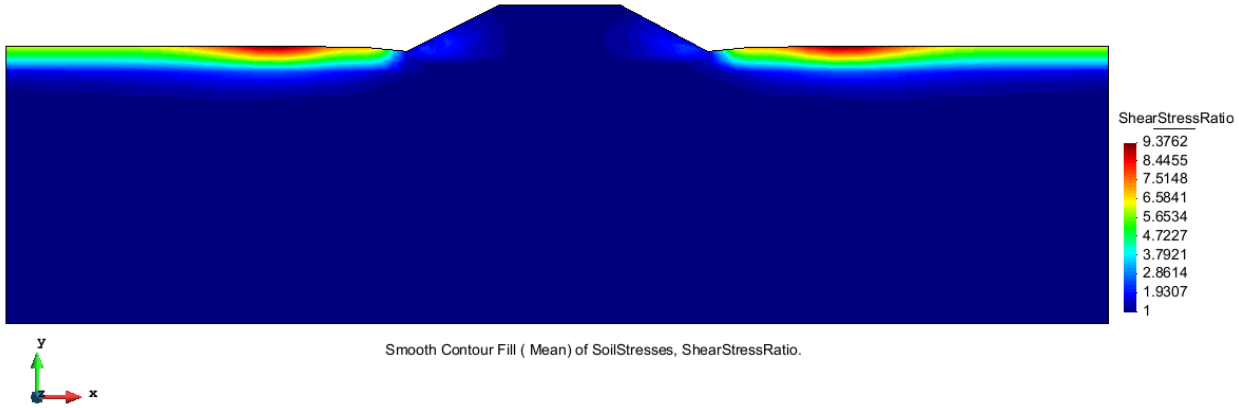

Fig. 5.43(a): Maximum shear stress ratio $(\Delta\tau_{max}/\Delta\tau_{xy})_{max}$ over the entire domain for the stiff crust case.

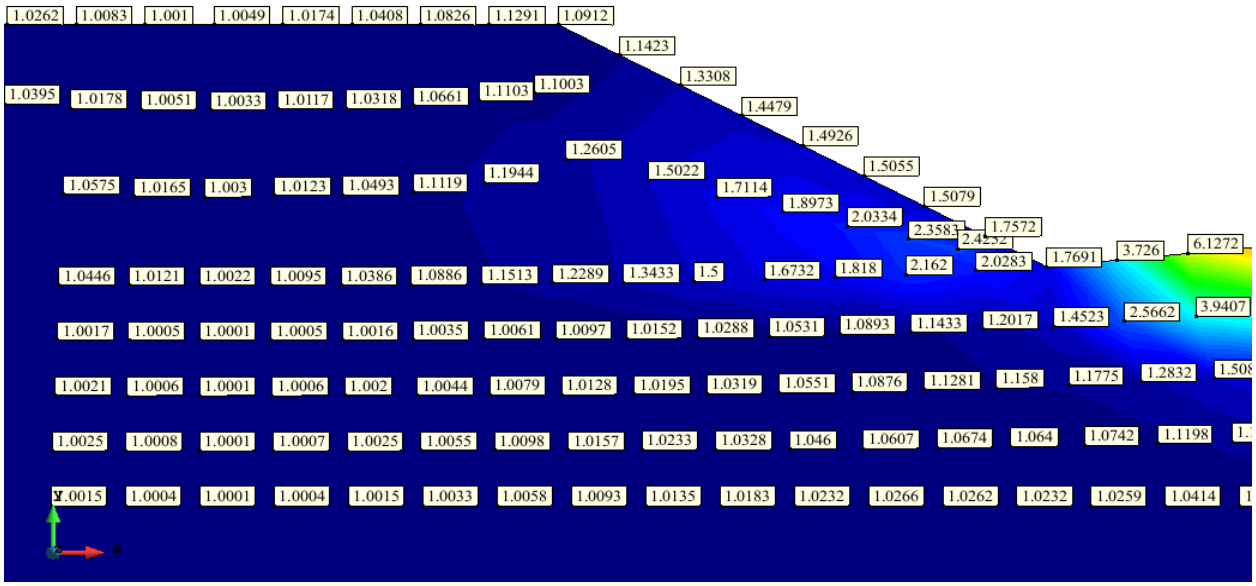

Fig. 5.43(b): Shear stress ratios at the levee toe and in the peat for the stiff crust case.

Stress ratios are shown in Fig. 5.44 for Case 2 (soft peat). Within the levee fill at the toe, stress ratios range from about 1.1 to 2.4, similar to Case 1. Once again, Rayleigh waves are responsible for the high shear stress ratios at the surface of the peat to the sides of the levee.

Fig. 5.44(a): Maximum shear stress ratio over the entire domain for the soft peat case.

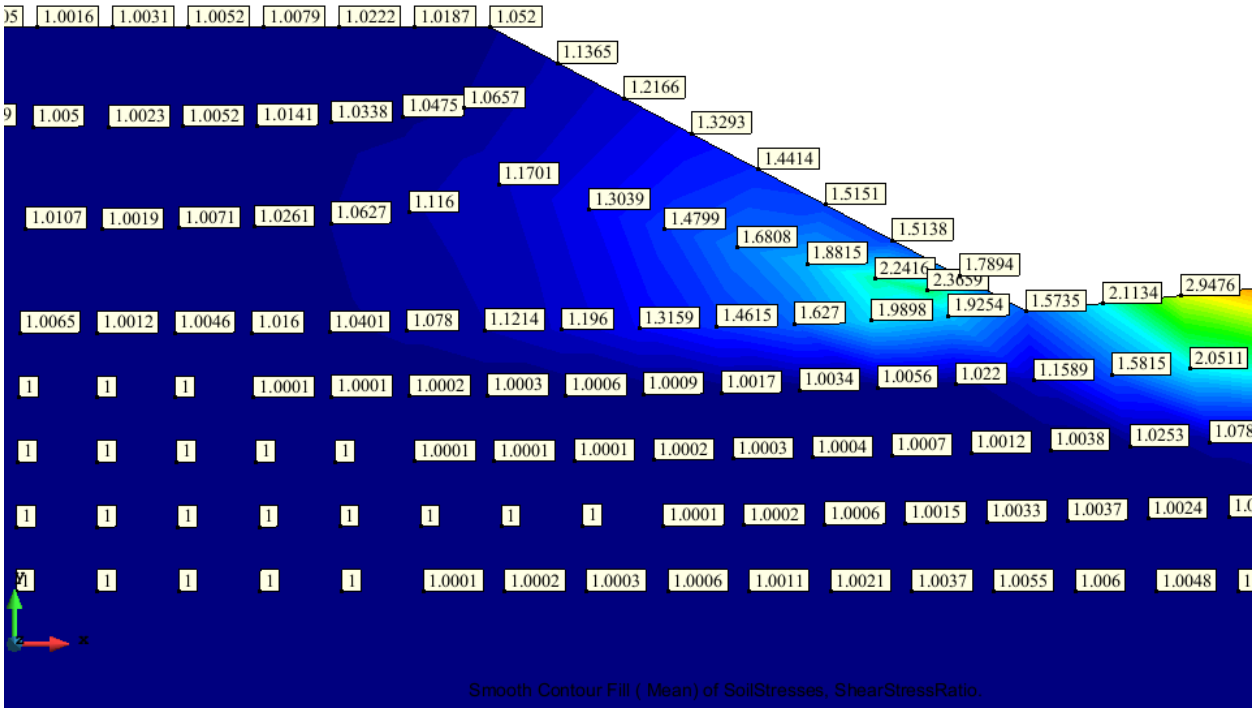

Fig. 5.44 (b): Shear stress ratios at the levee toe and in the peat for the soft peat case.

Figs. 5.45 shows the shear stress ratios for Case 3 (uniform soil). Near the levee toe, the stress ratios only go as high as 1.4, which is significantly lower than for Cases 1 and 2. This is likely attributed to vertical accelerations in the levee toe associated with rocking; a stiffer base condition permits less rocking and therefore less vertical stress change compared with a softer base case.

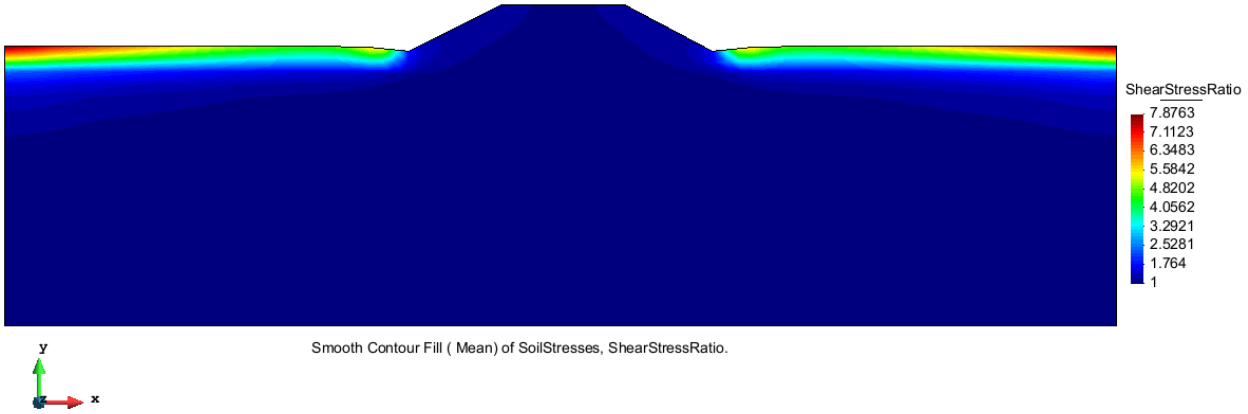

Fig. 5.45 (a): Maximum shear stress ratio over the entire domain for the uniform soil case.

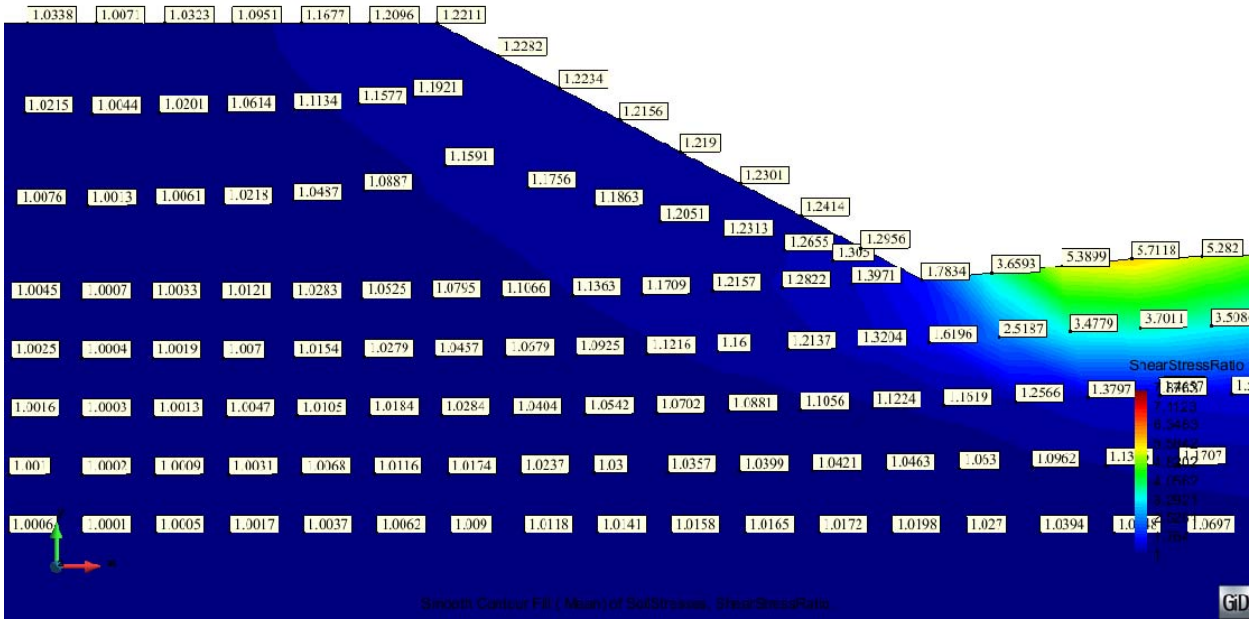

Fig. 5.45(b): Shear stress ratios at the levee toe and in the peat for the uniform soil case.

Fig. 5.46 shows the shear stress ratio contours for the stiff soil case. As with the uniform soil case, the peak shear stress ratios occur on the top of the free field soil layer. One thing to notice is that the region of high shear stress ratios moves farther away from the levee toe as soil stiffness increases. This is probably due to the increase in Rayleigh wavelength with stiffer soil.

Looking at Fig. 5.46 (b), almost no increases in shear stress ratio occurs either in the levee fill or in the underlying stiff soil, as the stiff soil essentially behaves like a rigid body compared to the simulated levee. The only area showing significant increases in shear stress ratio are right at the levee toe.

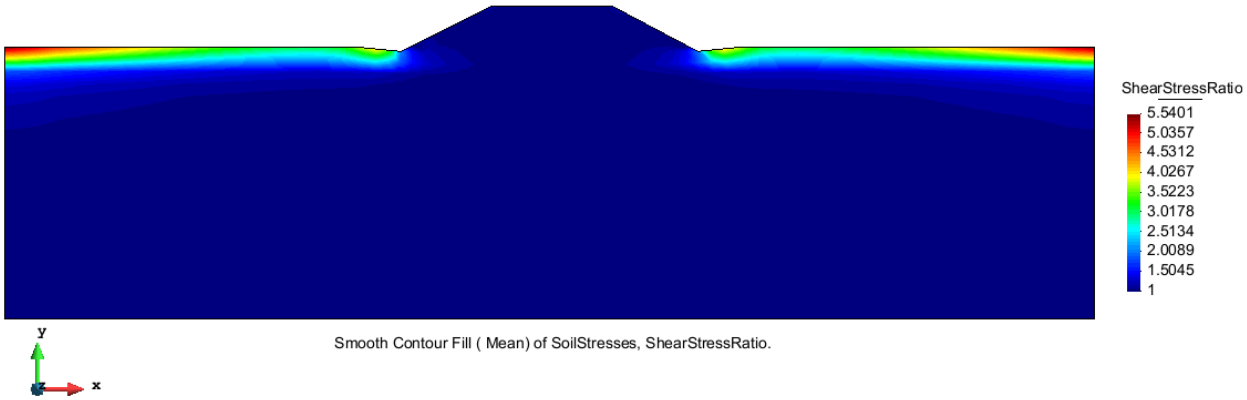

Fig. 5.46 (a): Maximum shear stress ratio over the entire domain for the stiff soil case.

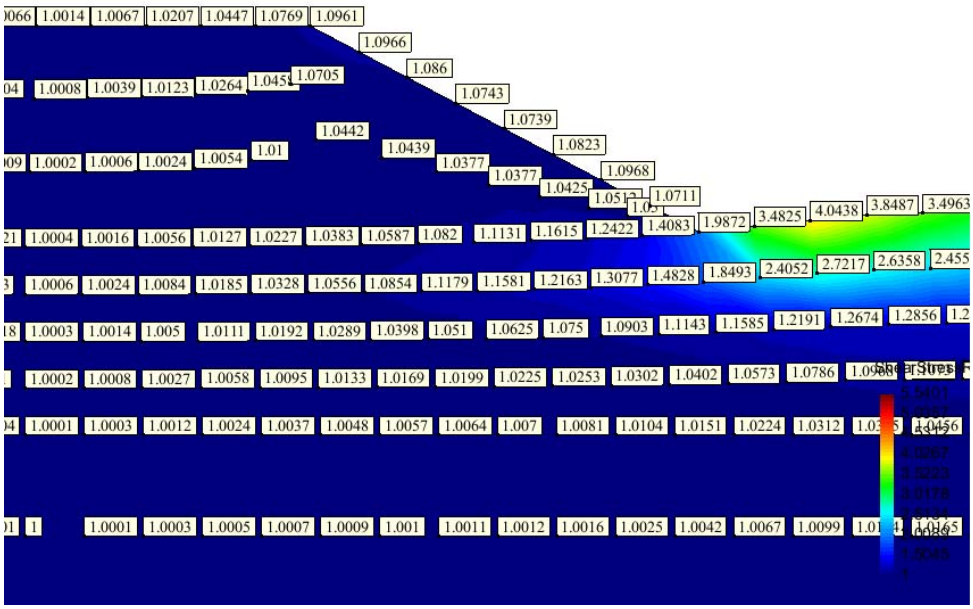

Fig. 5.46 (b): Shear stress ratios at the levee toe and in the peat for the stiff soil case.

Figs. 5.47 – 5.54 show the CSR contours for all the soil and shake configurations seen in this section. The figures are presented with the stiff crust first, the soft peat second, the uniform soil third, and the stiff soil last. Figures alternate in between the motions scaled to achieve 0.3g peak horizontal acceleration (PHA) at the levee crest and the motions where the base was excited at 0.3g peak acceleration. These figures are presented in order to understand the influence of amplification in addition to principal stress rotation. First, the highest CSRs occur in the case of the uniform soil with the base shaken to a PHA of 0.3g (Fig. 5.52). As mentioned earlier, the reason why the CSRs are so high for this case is that the first-mode site frequency for the uniform soil is roughly 4.5 Hz, while the peak excitation frequency is 3 Hz. Frequencies close to the first mode frequency generally show a high amplification. For another example, consider the case of the stiff soil. Given that H = 11m and Vs = 500 m/s, the first mode site frequency is 11 Hz. Considering a transfer function for an elastic layer, like one seen in Chopra (2007), motions with frequency content much lower than the first mode frequency show little amplification. Hence, the response is considered to be similar to a rigid body. This is further apparent in Figs. 5.53 and 5.54, where the CSR is uniform through most of the entire domain. Also, the CSR for both the stiff soil cases are fairly low, with maximum values at 1.56 and 1.35 across the entire domain for the motions scaled at the levee crest and at the levee base, respectively. However, it is also interesting to note the two cases of soft soils. For example, the first mode frequency of the soft peat case, given H = 11m and Vs = 30 m/s, is only 0.7 Hz. Looking at the sweep function in Fig. 5.26, the amplitude of the signal at that frequency is only at 5% of the peak amplitude. This explains why the first two soil behavior configurations behave so similarly, since both the peat and the stiff dessicated crust are so soft compared to the uniform and stiff soil cases.

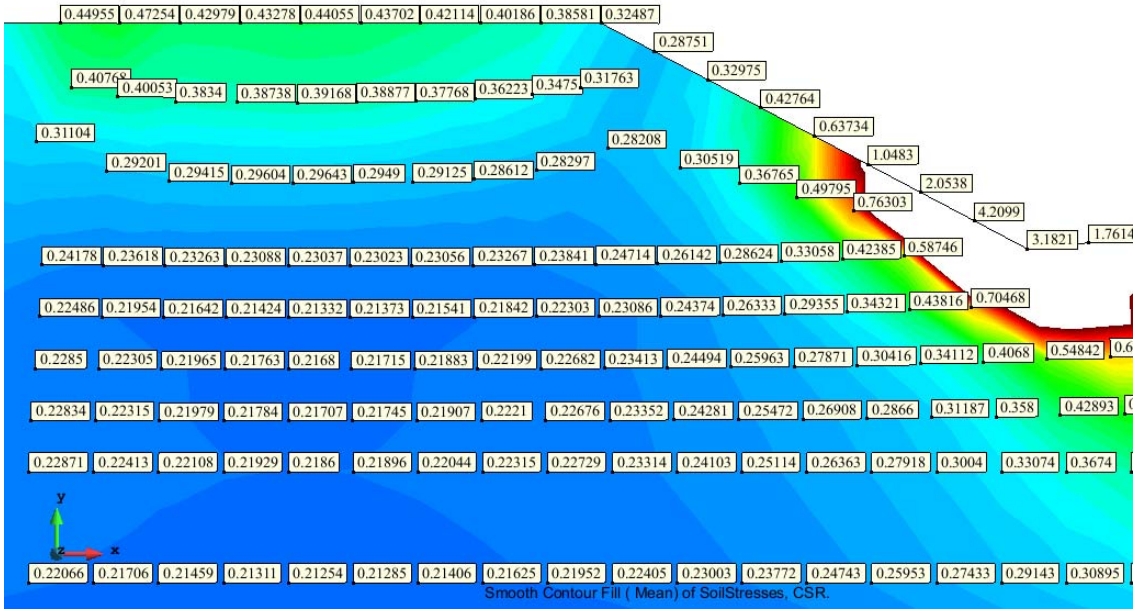

Fig. 5.47: CSR Contour of stiff crust over soft peat. Motion Scaled to PHA = 0.3g at levee crest

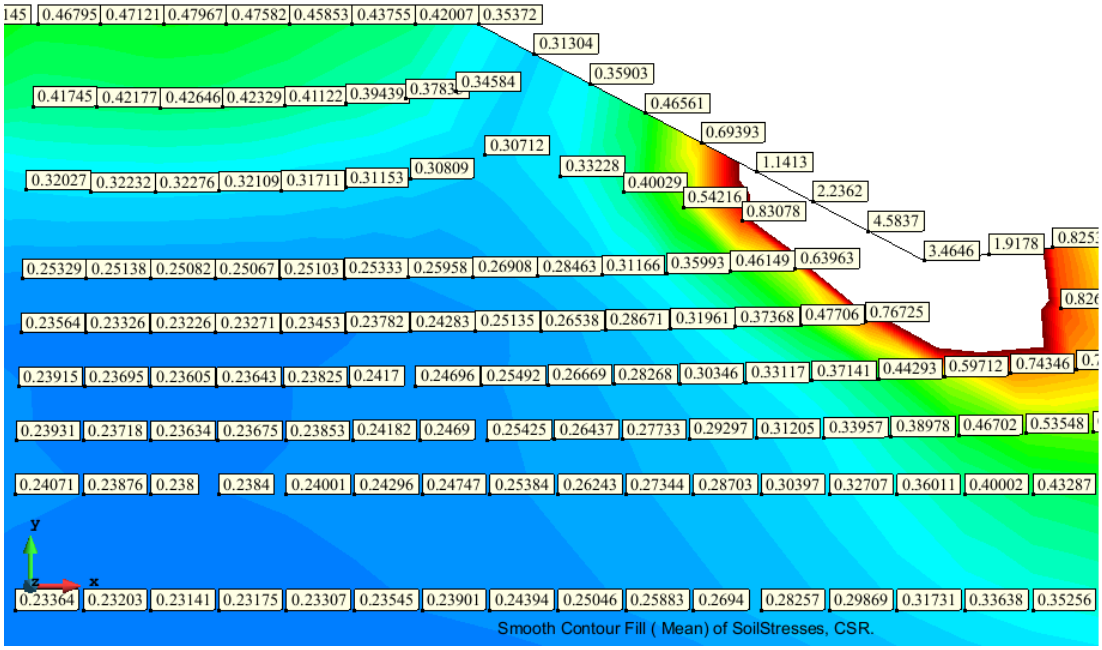

Fig. 5.48: CSR Contour of stiff crust over soft peat. PHA = 0.3g at levee base.

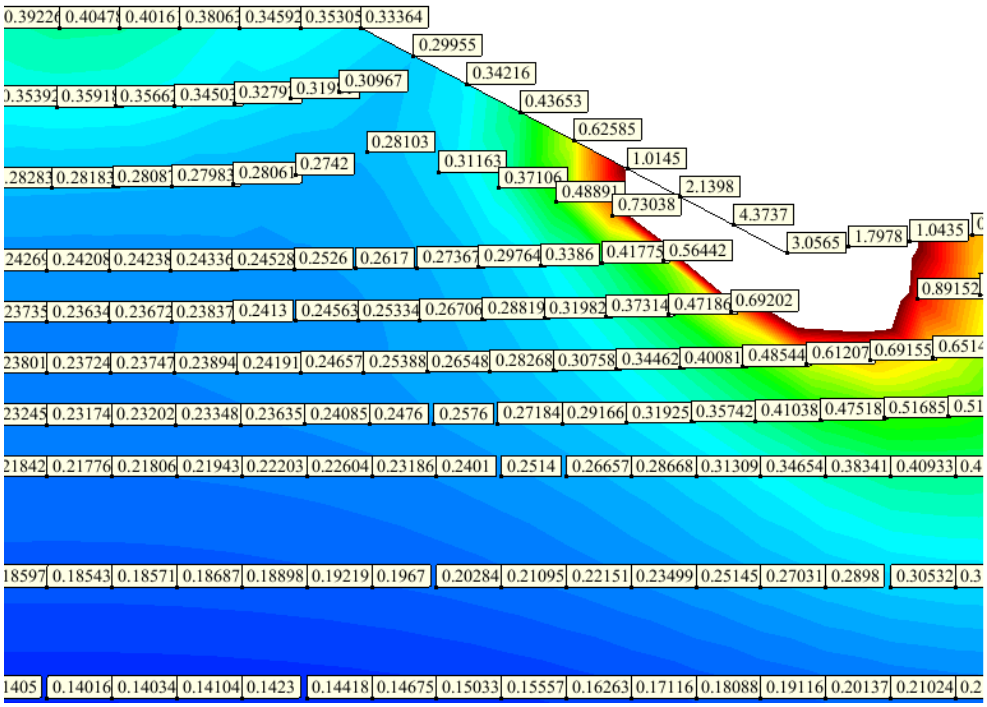

Fig. 5.49: CSR Contour of soft peat. Motion Scaled to PHA = 0.3g at levee crest

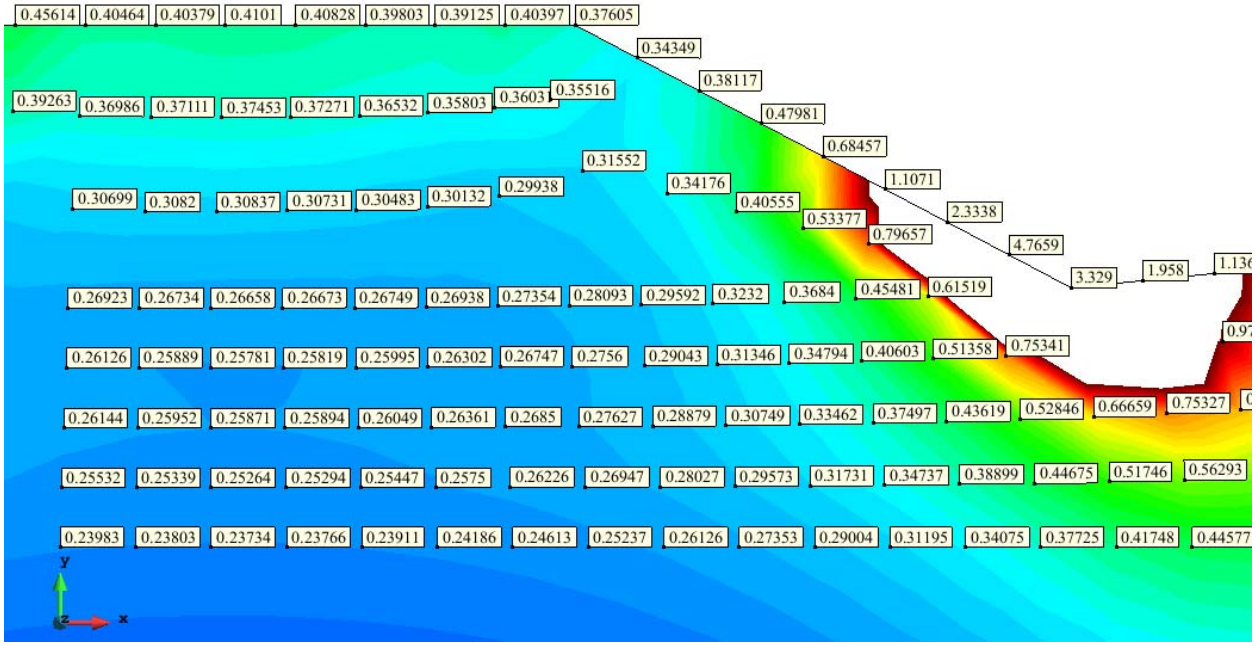

Fig. 5.50: CSR Contour of soft peat. PHA = 0.3g at levee base.

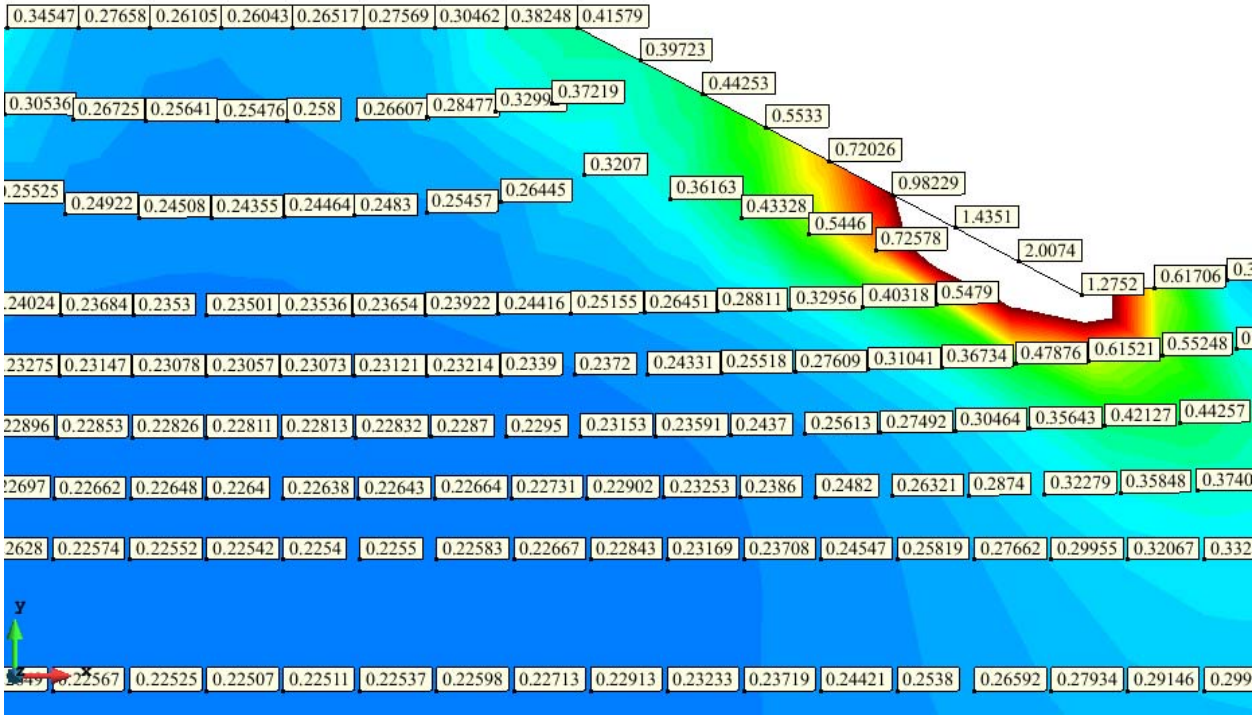

Fig. 5.51: CSR Contour of uniform soil. Motion Scaled to PHA = 0.3g at levee crest

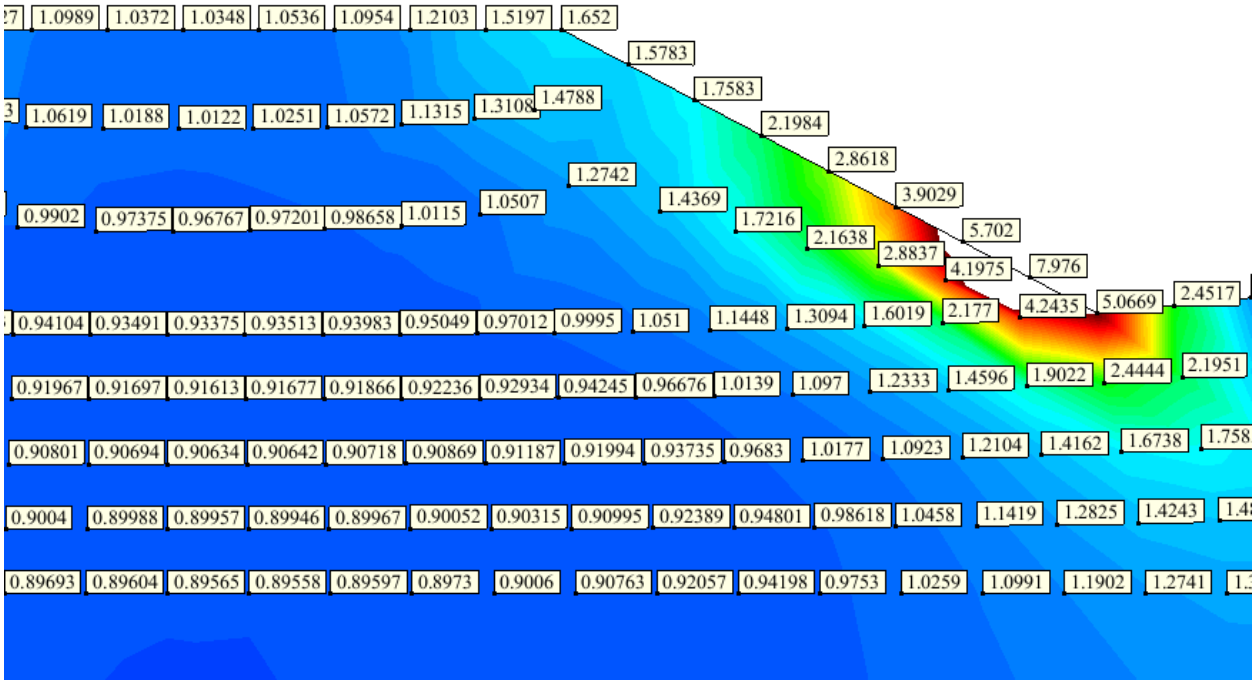

Fig. 5.52: CSR Contour of uniform soil. PHA = 0.3g at levee base.

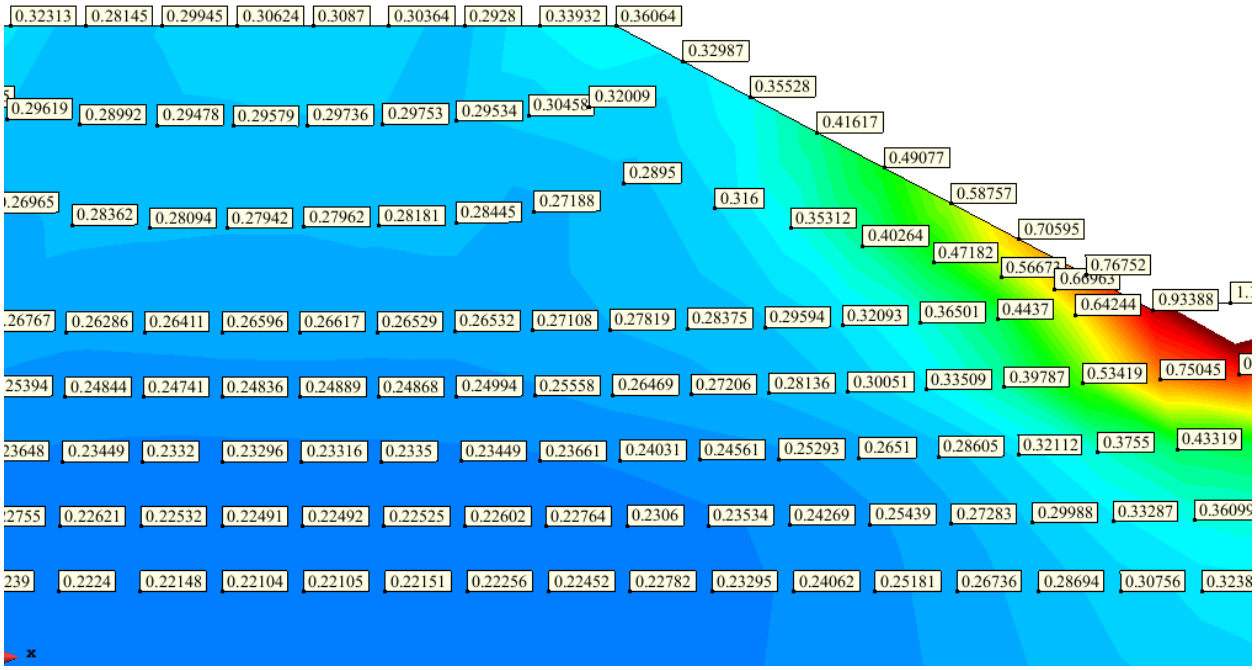

Fig. 5.53: CSR Contour of stiff soil. Motion Scaled to PHA = 0.3g at levee crest

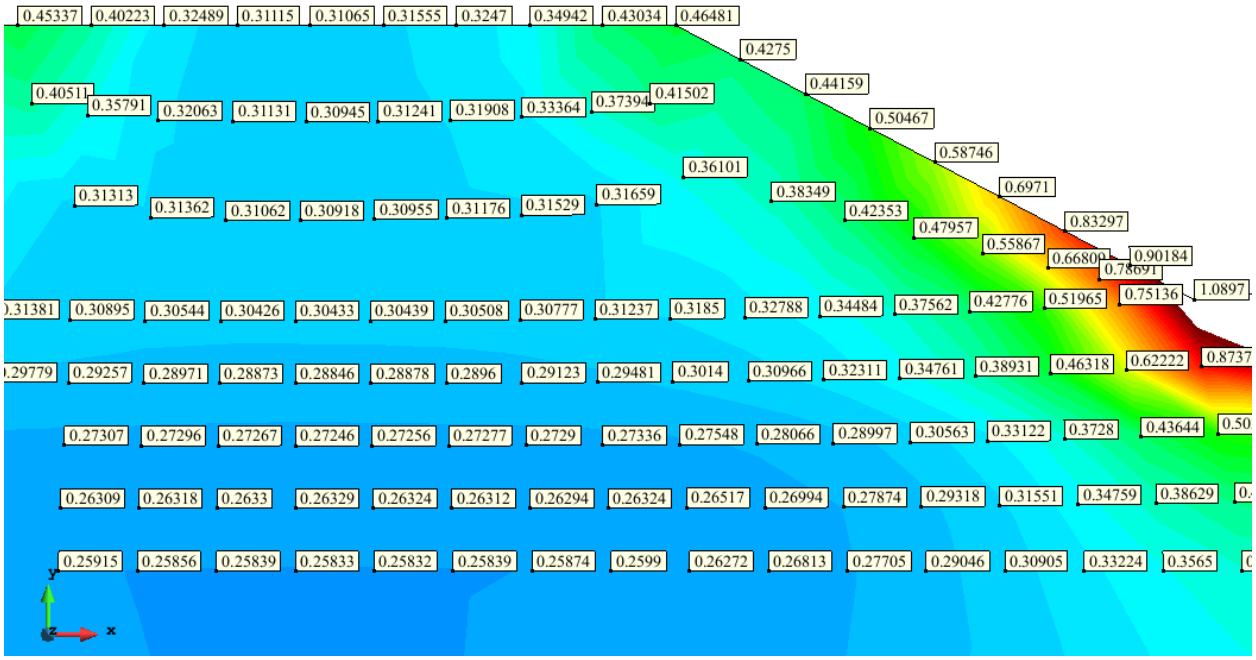

Fig. 5.54: CSR Contour of stiff soil. PHA = 0.3g at levee base.

Chapter 6: Summary and Conclusions

This dissertation has described a series of tasks and investigations that centered around the dynamic shake testing of a model levee founded on peaty organic soil in the Sacramento-San Joaquin Delta. With this in mind, this chapter will be divided into three sections summarizing: 1) the geotechnical and geophysical investigations performed at the Sherman Island test site, 2) the model levee's design, construction, remote monitoring, and dynamic shake testing, and 3) the interpretation of test data to learn about the dynamic behavior of Delta levees founded on peaty organic soil. This project only began to explore several important topics that will require additional research to resolve. Therefore, some recommendations for future research that center around several unresolved issues related to this project are also presented.

6.1. Geotechnical and Geophysical Investigations at the Sherman Island Test Site

- Geophysical investigations performed at the site were intended to measure shear wave velocity to characterize the site and establish estimates of ground motions imposed on the Sherman Island levees during the cyclic field test. . The March 2010 geophysical investigation concluded that the shear wave velocity of the soft free-field peat was 30 m/s, and the site frequency was 2.6 Hz. Based on estimates of geometric spreading and small-strain damping, shake testing of the model levee performed at the site was predicted to attenuate to levels below that of ambient noise for nearby levees. SASW performed one year later at the site verified that the soft saturated peat had a very low shear wave velocity, and further identified the shear wave velocity of a desiccated, unsaturated peaty crust overlaying the soft peat to be 60 m/s. An inversion to obtain a velocity profile from the dispersion curve was not performed because the dispersion

curve is believe to consist of many different modes of vibration, whereas most inversion algorithms assume the measured dispersion curve corresponds to the first mode.

- Geotechnical site investigations consisting of hand auger borings and piston sampling revealed the existence of an unsaturated peaty crust of about 2 meters thickness resting atop a soft, saturated, fibrous peaty organic soil. The hand auger borings were advanced to a depth of approximately 6m, and the bottom of the peat was not encountered in these borings. Undisturbed sampling was performed using a hand piston sampler and Shelby tube samples, and full recovery was achieved for sampling. Laboratory samples were subsequently tested by my colleague, Ali Shafiee, who found that the peat undergoes post-cyclic volume change (a previously unidentified mechanism).
- CPT soundings revealed the sand was encountered at a depth of 11m under the soft peat. We interpret this sand to be Pleistocene or early Holocene, as peat deposition began approximately 6000 years ago. The peat was found to be fairly permeable based on CPTu dissipation tests. The water level of the nearby Sacramento River is about 7 meters higher than the ground level of Sherman Island, which is hydraulically connected to the island via the underlying sand. Hence, artesian pressures exist in the saturated peat and sand, with the effective stress at the bottom of the peat layer being approximately zero.

6.2. Design, Construction, Monitoring, and Testing of the Model Levee.

- The model levee and timber shaker frame was designed to withstand dynamic forces from the NEES@UCLA MK-15 shaker and transmit cyclic stress ratios of up to 0.35 into the peat underlying the levee. The amount of force at the levee crest required to impose the desired cyclic stress ratio was predicted using two-dimensional finite element

simulations. With that in mind, the model levee and shaker frame were designed to withstand up to 190 kN of dynamic forces generated by the shaker. Eigen-analysis indicated that the two main modes of shaking would be in translation and rocking.

- The levee was constructed from 6 lifts of compacted clayey sand reinforced with 6 geogrids lined with geotextile. The geogrids were wrapped to form 0.3m (1ft) tall lifts forming a vertical face on the sides of the levee. A sturdy timber frame was embedded in the upper 3 lifts, and the MK-15 shaker was attached to this frame during shaking.
- The model levee was monitored by an array of piezometers and a horizontal slope inclinometer consisting of in-place MEMS accelerometers to measure pore pressure dissipation and settlement during construction, before, and after dynamic shake tests. Data was sent to a server remotely so it could be viewed on a website. During construction, pore pressures were observed to dissipate within a matter of days and noticeable immediate settlement and consolidation settlement was measured. The model levee continued settling long after construction and testing due to the high secondary compression, which is a characteristic property of peat soils.
- Shake tests consisted of a series of frequency sweeps performed by the NEES@UCLA MK-15 eccentric mass shaker. Tests were performed in 2011 and again in 2012 after flooding the desiccated crust in the vicinity of the levee. High intensity shakes during the 2011 tests caused a gap to form in between the levee fill and the timber shaker base, and the levee showed evidence of cracking. Prior to the 2012 test, the upper half of the model levee was removed and recompacted, and the shaker frame was fitted with footings to provide extra uplift resistance for the shaker base to reduce pounding. Although pounding occurred in the second year's tests, significant cracking did not occur in the levee fill.

6.3. Interpretation of Dynamic Test Data

- Calculation of the input shaker force required significant data processing. Raw recorded data included voltage spikes from two proximity sensors (one with 10 pulses per revolution to obtain rotation rate, and the other with 1 pulse per revolution to obtain position), and accelerometers on the shaker base. Alignment of two separate data acquisition systems was achieved using frequency domain cross-correlation. The inertial effects of the shaker base were taken into account and were found to be fairly significant at high intensities. Cosine sweep interpolation was used to preserve the sinusoidal nature of the sweep motions, as opposed to linear interpolation.
- All of the recorded data, including some interpreted data quantities such as shaker force, were uploaded to the NEEShub data repository. This dataset has been curated and is publicly available. The curated dataset can be found at http://nees.org/warehouse/project/644.
- Base shear, base moment, average displacement, and rotation were computed from sixteen triaxial accelerometers mounted on the model levee. These quantities were then used to compute impedance relations and complex-valued impedance functions. The impedance relations show an increase in damping as the shaking intensity increases, though it is impossible to separate the contributions from hysteretic and radiation damping. However, at frequencies approaching 3Hz, the shear-displacement loops become essentially circular, indicating that the base shear and base translation are 90^{o} out of phase, indicative of first-mode resonance, which agrees with the site frequency

obtained from geophysical investigations. The real and imaginary components of the impedance functions were compared to analytical solutions for a rigid foundation on elastic halfspace. There was little agreement in the solutions, as the levee is on a flexible foundation.

- Dynamic shear strains were measured from displacement gradients between subsurface accelerometer records. Peak measured strains were up to 0.4% underneath the toe. Comparison of maximum shear strains beneath the levee toe and levee crest for the 2011 tests generally show the shear strains beneath the toe to be greater due to the rocking motion of the levee. However, the pounding of the shaker base against the levee fill showed characteristic spikes that led some high-intensity tests to have larger shear strains beneath the levee crest, rather than the levee toe. Comparisons of shear strains beneath the levee crest between the 2011 and 2012 show that shear strains developed during the 2012 tests were approximately double those from the 2011 tests of similar shaker force amplitude. It is speculated that this may be due to softening of the levee crust due to the saturation in the three weeks prior to the 2012 tests.
- Residual pore pressures were generated in the peat underneath the levee during shaking for some of the tests. A clear trend in residual pore pressures was observed with increasing shaking intensity. When compared to a series of cyclic triaxial tests on peat, however, the increase in residual pore pressure from the field tests was much smaller than the laboratory tests. It is believed that pore pressure dissipation in the field tests during the time of shaking caused a reduction in excess pore pressure compared to the lab tests, which were undrained.

- Overall, the performance model levee presented in this dissertation should not be considered as fully representative of levees in reality for three reasons. The first is that conditions at real levees consist of saturated soils, whereas the model test levee was founded on a layer of stiff desiccated crust over the soft saturated peat. Levees hold back water and this levee did not, but was more intended to represent a cross section. The second reason is that actual Delta levees are composed of different materials than the model test levee. As mentioned in Chapter 2, real levees have been constructed of unengineered local fill, whereas the model test levee was constructed of compacted sandy clay reinforced with geogrids. The final reason is the loading in real earthquakes as opposed to the loading of the model levee. Real earthquakes emanate from the ground up, causing large overall vibrations in the Delta. However, the model test levee was loaded from the top down, and stresses, strains, and pore pressures only develop in a concentrated area underneath the model levee. These reasons are important to understand when attempting to extrapolate the results of these field tests to the performance of real Delta levees.

6.4. Finite Element Simulations

- A series of dynamic finite element simulations were performed to validate the field test results as well as test out other hypothetical scenarios, including different soil properties and different loading configurations, meant to resemble a real earthquake. Soil materials were modeled using elastic isotropic material models. The finite element simulations were two-dimensional, while the levee test was three-dimensional, which limits direct comparisons with the test data but permits several important conclusions despite this

limitation. Shear strains in the peat from simulated top-down loading was within the range of shear strains observed from field tests, and strains were greater in regions of the soft peat that were deeper than regions where measurements were made. Therefore, mobilized shear strains were likely about twice as large as measured shear strains. Shear strains within the peat were observed to be much greater for uniform base excitation when compared to the coupled top-down loading due to the superposition of site response stresses with those induced by inertial interaction with the levee. Only inertial interaction is present for top-down shaking.

- The finite element simulations were also utilized to study cyclic shear stresses mobilized within the levee fill and in the peat beneath the levee. Shear stresses in the region near the toe of the levee were found to be higher than those predicted for a simple shear stress path due to the rotation of principle stresses within the levee fill and underlying peat. This observation has implications to the calculation of cyclic shear ratios in liquefaction triggering analysis, which inherently assume simple shear loading conditions associated with vertically propagating shear waves in level ground.

6.5. Recommendations for Future Research

While the site investigations, dynamic testing, and analysis of test data may have shed some light on the dynamic behavior of Delta levees founded on peaty organic soils, there are still several issues that have yet to be resolved that are beyond the scope of this dissertation. However, these unresolved issues are good launching points for future research, and several potential topics of future research are discussed here.

- The presence of artesian conditions on Sherman Island and other Delta islands are a cause of concern. As the elevation of Delta islands still continue to drop due to biodegradation and wind erosion of the peat and artesian pressures increase due to sea level rise, pumping operations may be inadequate to drain regions of some islands and more land may become too wet to farm. This scenario may also lead to further weakening of Delta levees. Further research is needed to see how the artesian pressures, and the zero effective stress condition that exists between the peat-sand interface, affects the stability of Delta levees.
- Interpretation of the levee response in a soil-structure interaction framework provides a unique perspective that requires more research to fully flesh out. Elastic SSI solutions for rigid foundations did not agree well with measured impedance functions from the field tests. A program of 2D and 3D finite element simulations of model levees with flexible foundations may lead to a better idea of how flexible foundations influence SSI. Finite element simulations showed that the stiffness of the soil underlying the levees has an influence on mobilized cyclic stresses, with higher cyclic stresses mobilized for soft soils due to increased vertical accelerations associated with rocking. This is a potentially important mechanism, but more work is needed to more fully parameterize this effect and develop corrections to traditional liquefaction triggering evaluation procedures.
- Dynamic finite element simulations clearly showed that, for a constant crest acceleration, shear strains mobilized beneath levees were larger in amplitude and spatial extent for bottom-up shaking than for top-down forced vibration. Additional research is required to assess whether these strains would be large enough to result in post-cyclic levee settlement. No settlement was measured during the top-down loading, but it is currently

unclear whether bottom-up shaking during an earthquake would case measurable settlement.

- The OPENSEES finite element modeling only investigated elastic isotropic soils. Additional research should be performed using suitable plasticity models, preferably ones capable of capturing the settlement caused by cyclic straining. Equivalent linear simulations may also prove useful within the context of a simplified framework for estimating levee settlement.
- A great amount of data was collected during the field testing, and not all of it could be analyzed and interpreted. In this case, no extra work was done with the Atom Ant shake test data. The Atom Ant shaker shook the test levee at frequencies of up to 100 Hz. Future work with the Atom Ant data could help generate more meaningful impedance functions at frequencies higher than 3 Hz. Also, the Atom Ant shaker shook in the vertical, rather than the transverse direction. Since ground motions don't necessarily act in one direction, some work with the Atom Ant data could help engineers better understand vertical shaking of the Delta levees.

Bibliography

2007 Working Group on California Earthquake Probabilities, (WGCEP 2008), The Uniform California Earthquake Rupture Forecast, Version 2 (UCERF 2): U.S. Geological Survey Open-File Report 2007-1437 and California Geological Survey Special Report 203 [http://pubs.usgs.gov/of/2007/1091/].

American Society of Testing and Materials (ASTM). ASTM D2974-07a: Standard Test Methods for Moisture, Ash, and Organic Matter of Peat and Other Organic Soils

Athanasopoulos-Zekkos, A., Seed, R.B. (2013), Simplified Methodology for Consideration of Two-Dimensional Dynamic Response of Levees in Liquefaction-Triggering Evaluation. ASCE Journal of Geotechnical and Geoenvironmental Engineering, Vol. 139, No. 11. Nov. 1, 2013.

Boulanger, R., R. Arulnathan, et al. (2008). "Dynamic Properties of Sherman Island Peat." Journal of Geotechnical and Geoenvironmental Engineering. 124.1 (1998): 12-20. Print.

Brandenberg, S.J., Nigbor, R., Reinert, E., Levulett, D., Stewart, J.P., Moss, R. (2010). "Geophysical Testing to Determine Safe Vibration Limits and Spatial Attenuation of Vibrations on Sherman Island. Unpublished Manuscript. [http://nees.ucla.edu/neesrii/ShermanGeophysicalReport.pdf]

Brocher et al. (2008). "The Hayward Fault—Is It Due for a Repeat of the Powerful 1868 Earthquake?" US Geological Survey Fact Sheet 2008-3019. [http://pubs.usgs.gov/fs/2008/3019/]

California Department of Water Resources (CDWR 1992). "Seismic Stability Evaluation of the Sacramento-San Joaquin Delta Levees." 1992.

Casagrande, A. (1938) “Notes on Soil Mechanics – First Semester,” Harvard University (unpublished), 129 pp.

Chopra, A. Dynamics of Structures, Pearson Prentice Hall, Upper Saddle River, NJ, 2007.

Deverel, S., and Hart, C. (2012). “What is the future of farming on organic soils in the Sacramento-San Joaquin Delta.” HydroFocus, Inc. 36 p.

Dowding, C.H. (1996). Construction Vibrations. Prentice Hall, Upper Saddle River, New Jersey, 610 p.

Federal Highway Administration (FHWA 2001). "Design and Construction of Mechanically Stabilized Earth Walls and Reinforced Soil Slopes - Volumes I and II" (FHWA-NHI-10-024 and FHWA-NHI-10-025).

Finch,M. "Estimated Performance of Twichell Island Levee System, Sacramento-San Joaquin Delta, Under Maximum Credible Earthquake Conditions." Bulletin of the Association of Endineering Geologists. 25.2 (1988): 207-17. Print.

Foott, R., Sisson, R., and Bell,R. (1992). "Threatened Levees on Sherman Island." Stability and Performance of Slopes and Embankments-II. Ed. Seed and Ed. Boulanger. New York: ASCE, 1992. 756-74. Print.

GeoVision (2000). "Department of Water Resources Boreholes DHP-4D and DHP-5J3 Suspension P&S Velocities." Report 0297-01, June 30, 2000

Gere, J.M., Timoshenko, S.P., Mechanics of Materials, 4th ed. PWS Publishing Company, 1997.

Isenberg, P., Florian, M., Frank, R.M., McKeman, T., McPeak, S.W., Reilly, W.K., and Seed, R. (2008). "Delta Vision Final Report." Blue Ribbon Task Force Report.

Jones & Stokes. (2004) "Transportation- and Construction-Induced Vibration Guidance Manual." J&S 02-039. Prepared for California Department of Transportation, Noise, Vibration, and Hazardous Waste Management Office, Sacramento, CA.

Kishida, T., T. Wehling, et al. "Dynamic Properties of Highly Organic Soils from Montezuma Slough and Clifton Court." Journal of Geotechnical and Geoenvironmental Engineering. 135.4 (2009a)

Kishida, T., Boulanger, R., Abrahamson, N., Driller, M., Wehling, T. "Seismic Response of Levees in the Sacramento-San Joaquin Delta." *Earthquake Spectra,* Volume 25, No. 3, pages 557–582, August 2009; (2009b)

Kramer, S. (1996). Geotechnical Earthquake Engineering. Prentice-Hall. Upper Saddle River, NJ. Print.

Lund, J., E. Hanak, W. Fleenor, R. Howitt, J. Mount, and P. Moyle, Envisioning Futures for the Sacramento–San Joaquin Delta, Public Policy Institute of California, San Francisco, California, February 2007.

Lysmer, J., and Kuhlenmeyer, R.L., "Finite dynamic model for infinite media," Journal of the Engineering Mechanics Division, Proc. ASCE, Vol. 95, no. EM4, pp. 859-876, 1969

Marachi, N. D., Dayton, D. J., and Dare, C. T. (1983). "Geotechnical properties of peat in San Joaquin delta." Testing of peat and organic soils, STP 820, ASTM, West Conshohocken, Pa., 207–217.

Mesri, G., and M. Ajlouni. "Engineering Properties of Fibrous Peats." Journal of Geotechnical and Geoenvironmental Engineering. 133.7 (2008): 850-66. Print.

Mesri, G., Stark, T.D., Ajlouni, M.A., and Chen, C.S. (1997). “Secondary compression of peat with or without surcharge.” *J. Geotech. and Geoenviron. Eng.*, 123(5): 411-421.

Mount, J., and Twiss, R. (2005) "Subsidence, sea level rise, seismicity in the Sacramento-San Joaquin Delta." San Francisco Estuary and Watershed Science. Vol. 3, Issue 1 (March 2005), Article 5. http://repositories.cdlib.org/jmie/sfews/vol3/iss1/art5

National Institute of Standards and Technology (NIST (2012)). Soil-Structure Interaction for Building Structures. NIST GCR 12-917-21, September 2012.

Pais, A and E Kausel (1988). “Approximate formulas for dynamic stiffnesses of rigid foundations,” Soil Dyn. & Eqk. Engrg., 7(4), 213-227.

Reinert, E.T., Brandenberg, S.J., Stewart, J.P., Moss, R.E.S. (2012). “Dynamic Field Test of a Model Levee Founded on Peaty Organic Soil Using an Eccentric Mass Shaker.” 15th World Congress on Earthquake Engineering, Lisbon, Portugal. September 2012.

Reinert, E.T., Brandenberg, S.J., Stewart, J.P. (2013) "Measurements of Translational and Rotational Dynamic Stiffness for a Model Levee on Peat." 10th International Conference on Urban Earthquake Engineering, Tokyo Institure of Technology, Japan. March 2013.

Reinert, E.T., Lemke, J., Stewart, J.P., Brandenberg, S.J. (2013a). “Remote Monitoring of a Model Levee Constructed of Soft Peaty Organic Soil.” 2013 Geo Congress, San Diego.

Robertson, P.K., Sully, J.P., Woeller, D.J., Lunne, T., Powell, J.J.M., and Gillespie, D.G. (1992). "Estimating the coefficient of consolidation from piezocone tests." *Canadian Geotechnical Journal*, 29(4), 551-557.

Sacramento Area Flood Control Agency. Website: www.safca.org. (2008)

Santamarina, J., Fratta, D., (1998). Introduction to Discrete Signals and Inverse Problems in Civil Engineering. ASCE Press. Reston, VA. Print.

Sasaki, Y. (2009). "River dike failures during the 1993 Kushiro-oki earthquake and the 2003 Tokachi-oki earthquake," Earthquake geotechnical case histories for performance-based design - Kokusho (ed), 2009 Taylor & Francis Group, London, pp. 131-157, 2009

Seed, H.B., and Idriss, I.M., (1971). "Simplified procedure for evaluating liquefaction potential," Journal of the Soil Mechanics and Foundations Division, ASCE, Vol. 107, No. SM9, pp. 1249-1274

Shafiee, A., Brandenberg, S.J., and Stewart, J.P. (2013). "Laboratory investigation of the pre- and post-cyclic volume change properties of Sherman Island peat," 2013 Geo Congress, San Diego.

Skempton, A.W., and Bjerrum, L., (1957). “A contribution to settlement analysis of foundations in clay.” *Geotechnique*, 7(4), 168-178

Stewart, J.P., Brandenberg, S.J., Shafiee, A. (2013). "Laboratory evaluation of seismic failure mechanisms of levees on peat." UCLA-SGEL 2013/04, Structural and Geotechnical Engineering Laboratory, Civil and Environmental Engineering Department, UCLA.

Tileylioglu, S, JP Stewart, and RL Nigbor (2011). “Dynamic stiffness and damping of a shallow foundation from forced vibration of a field test structure,” J. Geotech. & Geoenv. Engrg., 137 (4), 344-353.

Tokimatsu, K., Sekiguchi, T. "Effects of Nonlinear Properties of Surface Soils on Strong Gound Motions Recorded in Ojiya During 2004 Mid Niigata Prefecture Earthquake." Soils and Foundations. 46.6 (2006): 765-775. Print.

Torres, R. A., et al., (2000). *Seismic Vulnerability of the Sacramento–San Joaquin Delta Levees,* report of Levees and Channels Technical Team, Seismic Vulnerability Sub-Team, to CALFED Bay-Delta Program, Sacramento, California, 2000.

URS Corporation, Jack R. Benjamin and Associates. (DRMS Phase 1 2009). "Delta Risk Management Strategy (DRMS) Phase 1 Report." California Department of Water Resources. 2009. http://www.water.ca.gov/floodmgmt/dsmo/sab/drmsp/phase1_information.cfm

Vucetic, M., and Dobry, R. "Effect of soil plasticity on cyclic response." Journal of Geotechnical and Geoenvironmental Engineering. 117.1 (1991), 89-107. Print.

Wehling, T., R. Boulanger, et al. "Nonlinear Dynamic Properties of a Fibrous Organic Soil." Journal of Geotechnical and Geoenvironmental Engineering. 129.10 (2003): 929-39. Print.

Yang, Z., Lu, J., Elgamal, A. (2008). OpenSees Soil Models and Solid-Fluid Fully Coupled Elements User's Manual. University of California, San Diego. Department of Structural Engineering. http://cyclic.ucsd.edu/opensees October 2008.